Modeling and Robust Control of Cable-Driven Parallel Robots for Industrial Applications

Etienne Picard

UNIVERSITE BRETAGNE SCIENCES LOIRE POUR L'INGENIEUR

CENTRALE NANTES

THESE DE DOCTORAT DE

L'ÉCOLE CENTRALE DE NANTES
COMUE UNIVERSITE BRETAGNE LOIRE

ECOLE DOCTORALE N° 602
Sciences pour l'Ingénieur
Spécialité : Robotique – Mécanique

Par
Etienne PICARD

Modeling and Robust Control of Cable-Driven Parallel Robots for Industrial Applications

Thèse présentée et soutenue à Bouguenais, le 17/12/2019
Unité de recherche : UMR 6004, Laboratoire des Sciences du Numérique de Nantes (LS2N)

Rapporteurs avant soutenance :

Edouard Laroche	Professeur des Universités, ICUBE - Université de Strasbourg
David Daney	Senior Inria Researcher, Inria

Composition du Jury :

Président :	Marco Carricato	Associate Professor, Università di Bologna
Examinateur :	Claire Dumas	Chargée de projets - Experte robotique, DAHER
Rapporteurs :	Edouard Laroche	Professeur des Universités, ICUBE - Université de Strasbourg
	David Daney	Senior Inria Researcher, Inria
Dir. de thèse :	Stéphane Caro	Directeur de recherche CNRS, Centrale Nantes
Co-dir. :	Franck Plestan	Professeur, Centrale Nantes
Co-encadrant :	Fabien Claveau	Enseignant-Chercheur
Invité :	Yves Guillermit	Ingénieur, Chantiers de l'Atlantique

Modeling and Robust Control of Cable-Driven Parallel Robots for Industrial Applications

ROCKET project

Etienne Picard

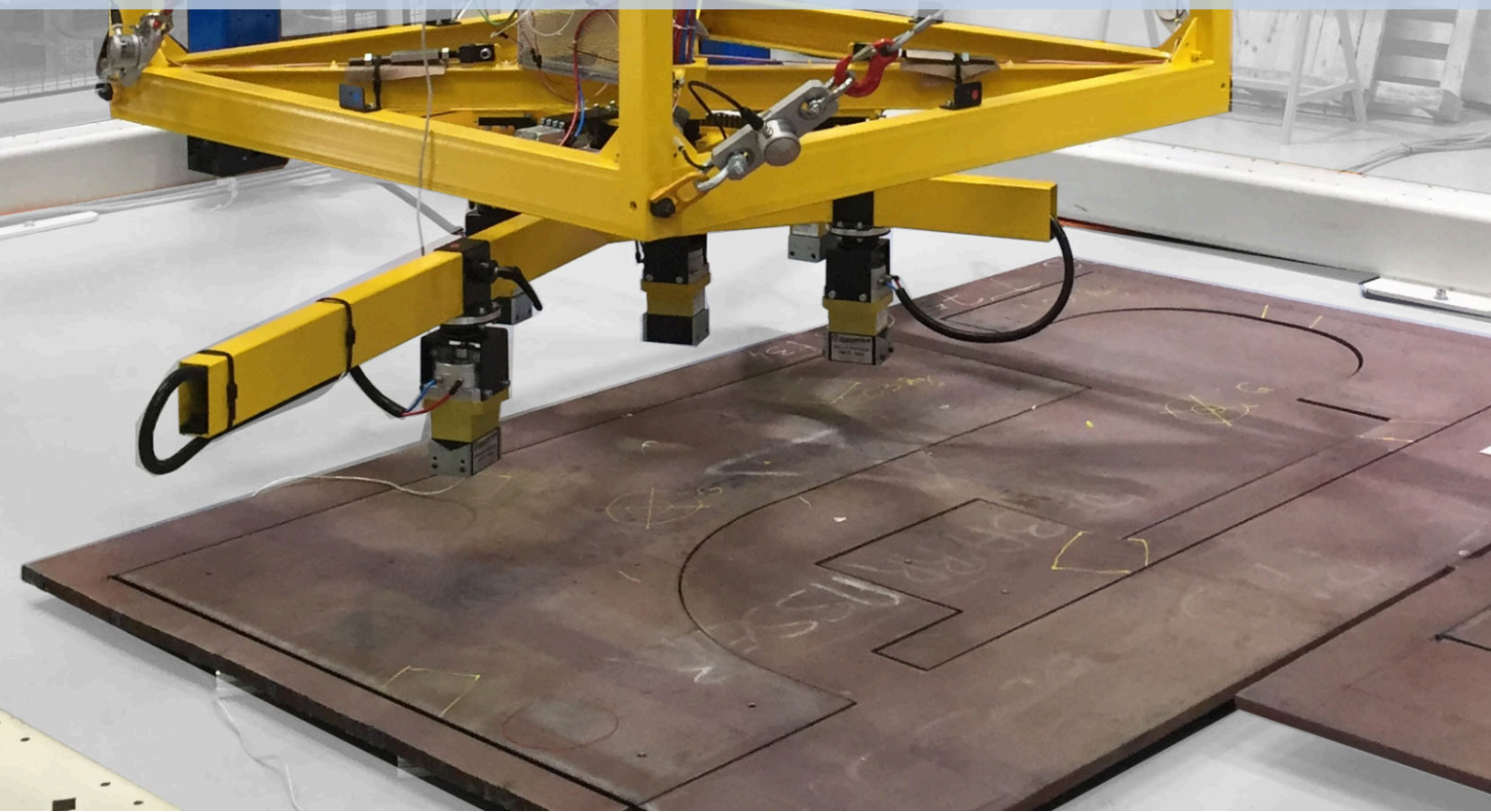

Contents

Appendix

List of Figures

List of Tables

General introduction

1. Context

In this chapter, Section 1.1 presents the concept of cable-driven parallel robots; existing prototypes and current applications of CDPRs, before going into more details about unique characteristics of this type robot. Section 1.2 puts in context the ROCKET project and the thesis work. Then, two CDPRs developed at IRT Jules Verne for the project are detailed in Section 1.3. Finally, Section 1.4 describes the experimental setup and test trajectories used to analyze the performance of the CDPRs under study.

1.1 Cable-driven parallel robots

The following definitions about serial and parallel mechanisms are extracted from [Mer06] and [Gos88]. A *link* is a rigid body and its *connection degree* is the number of rigid bodies attached to this link by a joint. A *simple kinematic chain* is a set of links in which each link has a connection degree of 2, except for the base and end-effector which have a connection degree of 1. On the other hand, a *closed loop kinematic chain* has one link - other than the base - with a connection degree of 3 or more. Fig. 1.1 presents serial and parallel mechanisms. On the left, the serial mechanism is composed of a single simple kinematic chain of n links and its end-effector has a connection degree of 1. On the right, a parallel mechanism is composed of m legs of n links and an end-effector with a connection degree of m. The end-effector is usually composed of a moving-platform on which is mounted a tool depending on the targeted application.

A well known parallel manipulator is the Gough-Stewart platform composed of six UPS limbs as shown in Fig. 1.2. U, P and S stand for Universal, Prismatic and

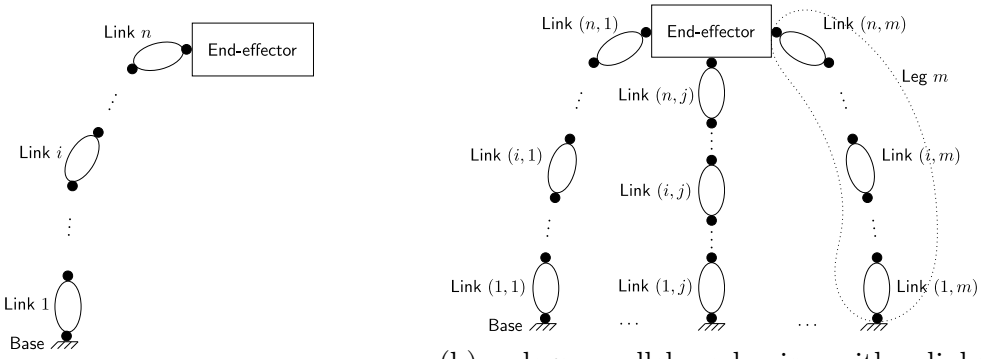

(a) n-links serial mechanism.

(b) m-legs parallel mechanism with n-links per leg.

Figure 1.1: Serial and parallel mechanisms.

Spherical joints. The prismatic joint within each limb is actuated. This type of robot was proposed by Gough in 1954 [GW62], but its concept has since been applied to different applications such as the AMiBA telescope [Raf+04] in Hawaii, for motion simulators [KJ75] or medical devices [Mer01].

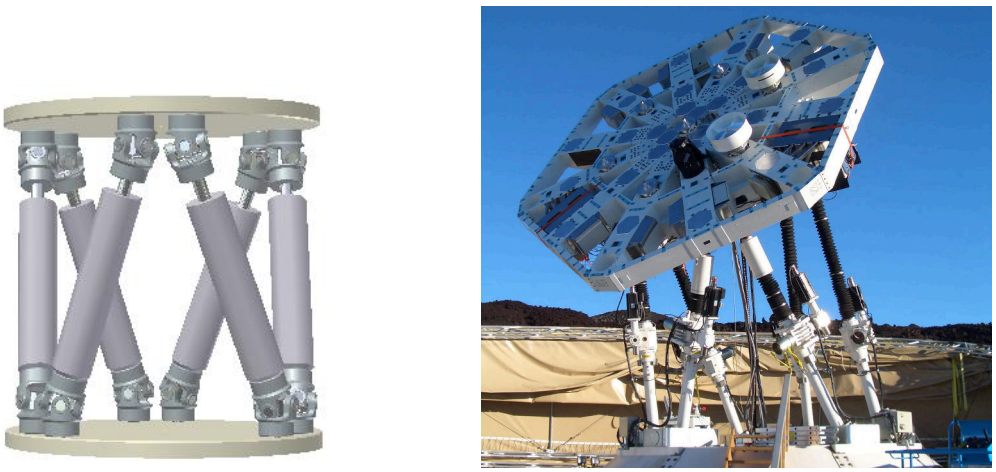

Figure 1.2: Gough-Stewart platform 3D model (left) and the AMiBA telescope (right).

Cable-Driven Parallel Robots (CDPRs) form a particular class of parallel robots whose moving platform is connected to a fixed frame by cables, as illustrated in Figure 1.4a. The cables are coiled on motorized winches. Passive pulleys may guide the cables from the winches to the cable exit points. Accordingly, the motion of the moving platform is controlled by modifying the cable lengths. Figure 1.3 shows a CDPR and its core elements.

The use of cables instead of rigid links leads to characteristics such as low mass of the moving parts, as only the moving-platform and cables are in motion. The gearmotors and winches used to control the cable lengths can be remotely mounted on the ground and are stationary during operation, which greatly reduces the load in motion. Cable weight is also low compared to the rigid links of classical parallel mechanisms (Delta, Gough-Stewart, etc.).

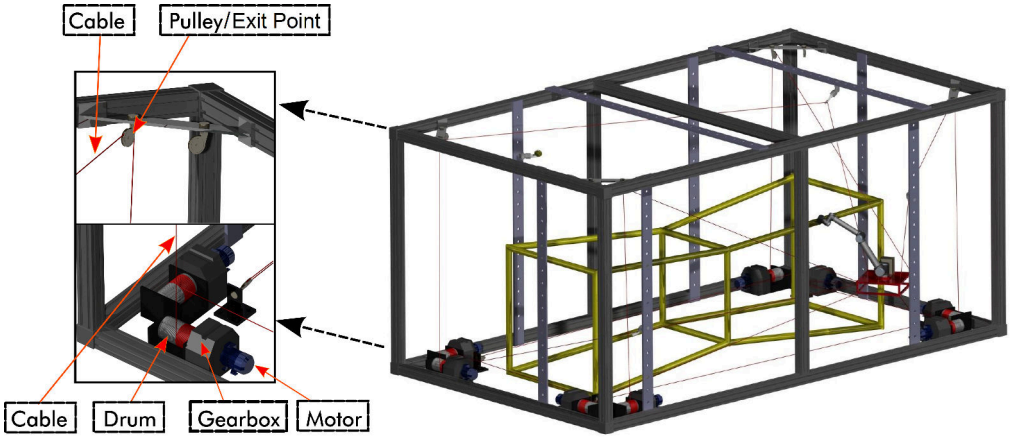

Figure 1.3: CDPR used for sandblasting and painting operations [GGC18].

A direct consequence of the low weight in motion is the possibility of achieving high dynamics of the end-effector. The scalability of CDPRs is also an advantage, as cable lengths can easily be increased to fit a larger structure, compared to rigid links, and reach large workspaces. This flexibility of CDPR also allows their concept to be applied in various ranges of dimensions and degrees of freedom.

Another specificity of CDPRs is the possibility of reconfiguration. By displacing the pulleys onto the frame, a new robot configuration can be quickly achieved, better suited for a particular task. The robot footprint can be modified to avoid cable collisions with the environment or to work around objects of awkward shapes. Recent works on this topic include [Gag+15] for painting and sandblasting applications illustrated in Fig. 1.3, where the robot configuration is modified to adapt the workspace, and [SRB15] in the medical field and in industry.

It should be noted that CDPRs can be more appropriate for accurate pick-and-place operations of large parts than overhead cranes as they suffer less from load swinging than the later. Moreover, CDPRs can control both the position and the orientation of the object to some degree depending on the robot configuration, which extends their application range.

Nevertheless, CDPRs have some drawbacks as well. CDPRs are nonlinear, possibly redundant systems, which leads to complication in their modeling. Hypotheses are usually made to simplify the geometric model of CDPRs, such as the consideration of massless, inelastic, straight cables. [Gag+15] However in reality, cables present elasticity, sagging or slackness [Irv92; Bak+17] which significantly complicates the modeling and control of CDPRs, and can be detrimental to their accuracy and stiffness. Depending on the prototype size, configuration and application, the necessity of a model which takes these behaviors into account might be necessary to achieve the desired precision and repeatability.

CDPRs usually have a lower maximum load capacity than standard or overhead crane, with a typical maximum load of 1 ton for an 8 cables CDPR [Pot+13]. As

the platform reaches the upper limits of the CDPR structure, cables tensions can become infinitely high, which imposes limits on the feasible workspace of CDPRs based on their hardware limitations.

1.1.1 Workspace

The workspace of a CDPR is the total volume that can be reached by its moving-platform. CDPRs can work in one, two or three dimensions and can have up to 6 degrees of freedom. Different types of workspace are considered, depending on the conditions in which they are accessible [EUV04].

The *wrench closure workspace* is the set of platform poses where a set of positive cable tensions can be found to satisfy the platform static equilibrium. However in this workspace, the cable tensions leading to the static equilibrium can have values too large to be feasible by the robot hardware. The *wrench feasible workspace* is the set of platform poses where the static equilibrium of the platform can be achieved with a set of cable tensions respecting the hardware upper and lower tensions limits. Finally, the *dynamic feasible workspace* is the set of platform poses where a range of platform accelerations can be achieved through a set of acceptable cable tensions. The maximum acceleration must be defined to study this workspace, a higher value of desired acceleration usually leading to a smaller dynamic feasible workspace. The feasibility of CDPR workspace is still an ongoing research subject, with recent publications such as [Gag16; GGC18; GG16; PK16].

1.1.2 CDPR configuration

The CDPR configuration is a function of the cable arrangement onto the moving-platform and the base. The configuration has a great importance on the CDPR behavior. It can be optimized to prioritize some aspects such as mobility, feasible workspace, stability or stiffness.

Suspended and fully-constrained configurations

Cable configuration can be put in two categories: suspended and fully-constrained.

In a *suspended configuration* (Fig. 1.4a) the platform is only held by cables coming from the top of the structure. This configuration minimizes the risks of collision between the cables and elements in the workspace. This type of robot can achieve the full 6 degrees of freedom but cannot apply a downward force greater than its own weight under gravity.

On the other hand in a *Fully-constrained configuration* (Fig. 1.4b) cables are pulling from both the top and the bottom of the structure, allowing the platform and its end-effector to exert a force in every direction of the workspace, included in the vertical axis directed to the ground. However, downward pulling cables can be problematic in a cluttered environment as they increase the risk of collision.

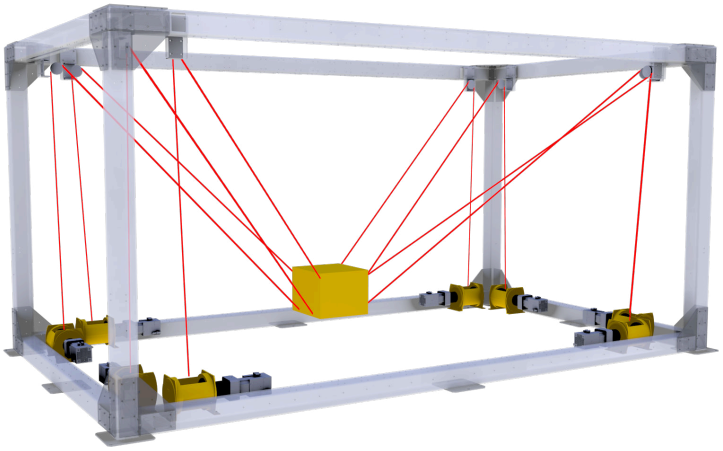

(a) Suspended configuration.

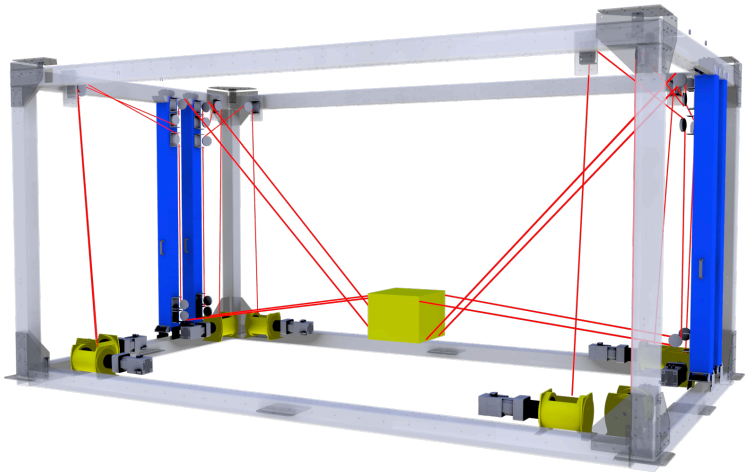

(b) Fully-constrained configuration.

Figure 1.4: Two Cable-Driven Parallel Robot configurations.

Both suspended and fully constrained configurations can allow for orientation of the platform. The rotation limits depend on the geometry of the structure and the platform, but also on the location of the cable anchor points on the moving-platform and of the cable exit points on the base. The typical range of feasible platform orientation is of 30 degrees about an axis using the CoGiRo cable configuration [Lam+13].

Actuation redundancy

Let m be the number of cables of a CDPR, and n the number of degrees of freedom (DoF) of the platform. There is actuation redundancy when $m > n$, that is when there are more cables than degrees of freedom. The *Degree of Redundancy* (DoR) r is then defined as $r = m - n$.

Redundancy is a necessity for fully-constrained CDPR, while in the case of suspended cable robots the gravity can act as an additional cable. CDPRs usually have a DoR of 1 or 2, as it is a good compromise between the benefits of redundancy, such as improved feasible workspace, and modeling and control complexity [Gou+15].

This thesis is focused on CDPRs with 6 degrees of freedom and 8 cables ($r = 2$) a popular configuration for its large homogeneous workspace and symmetrical frame.

1.1.3 Existing CDPRs

One of the first CDPR prototypes was developped by Kawamura *et al* from Ritsumeikan University, who designed in 1995 the FALCON, a 6 DoF cable robot with 7 cables [Kaw+95] aiming at achieving high speed for assembly operations.

CDPRs can be used in several applications such as heavy payload handling and airplane painting [ABD92], cargo handling [HC04], warehouse applications [HK09], large-scale assembly and handling operations [PMV10], and fast pick-and-place operations [Kaw+00]. Other possible applications include haptic devices [RGM07], support structures for giant telescopes [Yao+10], and search and rescue deployable platforms [Mer08b; MD10]. Some recent works at IRT Jules Verne have dealt with the design and reconfiguration planning of reconfigurable CDPRs that can be used in cluttered industrial environments for painting and sandblasting large structures [Gag+15] (Fig. 1.3).

The Skycam shown in Fig. 1.5 is the most widespread CDPR currently in use. It is used to displace a camera for the broadcasting of sporting events. It can bring video-game-like camera angles to television sports coverage and can provide a more immersive view to the remote viewer than still cameras. Two well known brands are Skycam [1] and Spidercam [2]. A typical skycam camera weighs around 14 kg and can travel up to 13 m/s. Skycams use a suspended configuration with four cables and

[1] Skycam website (link)
[2] Spidercam website (link)

three degrees of freedom.

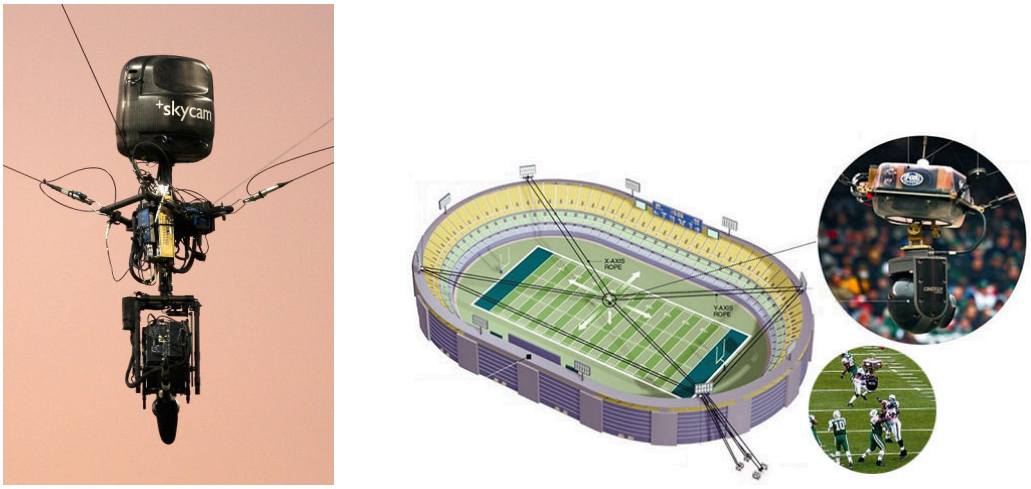

Figure 1.5: Skycam in a football stadium in the USA.

Similarly to Gough-Stewart platforms, CDPRs are good candidates for motion simulator, as proved by the CableRobot Simulator [Mie+16] built by Fraunhofer IPA in Stuttgart, Germany, and shown in figure 1.6. The work on industrial CDPR at Fraunhofer started with the IPAnema robot family [Pot+13].

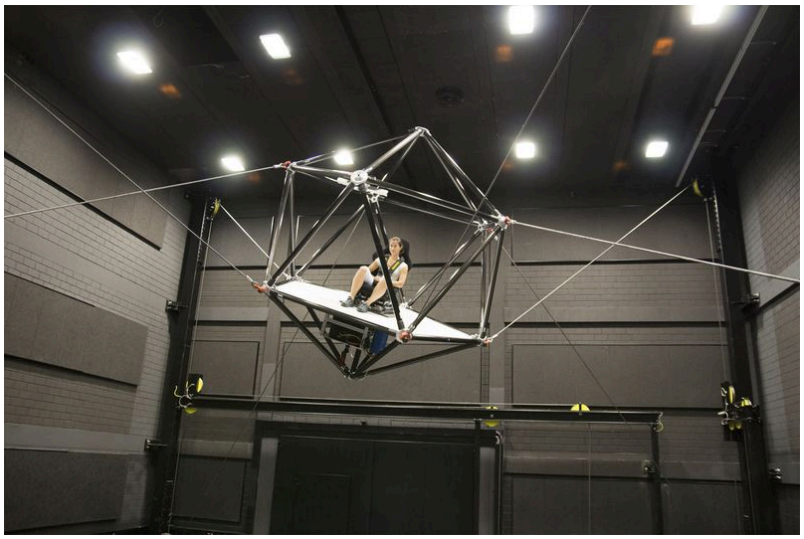

Figure 1.6: Fraunhofer CableRobot Simulator.

With the development of virtual reality, systems that allow humans to interact with a computer through bodily sensations and movements are also on the rise. These are called haptic interfaces and refers to human-computer interface technologies that encompasses tactile feedback or other bodily sensations to perform actions on a computing device. CDPRs are also being developed as haptic interfaces, for example at Université Laval, Québec, Canada [FCCG14a]. The prototype developed at "The Laboratoire de Robotique" of Laval University is shown in Fig. 1.7a is a 3 DoF haptic interface with a handle which allows the user to feel interaction with virtual objects

such as collisions. Similarly, [Kam+16] used a six DoF CDPR to apply external loads on an industrial serial arm during its elasto-geometrical calibration with a laser tracker, as shown in Fig.1.7b.

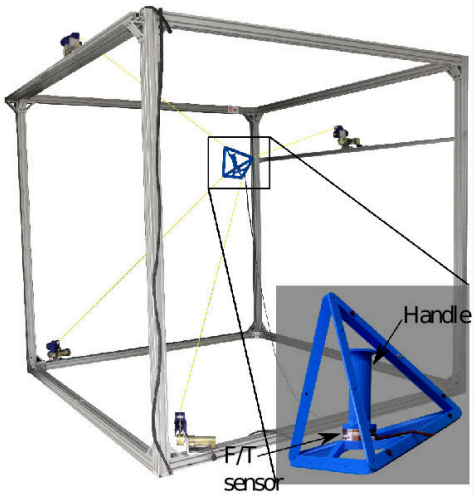

(a) 3 DoF haptic interface [FCCG14b].

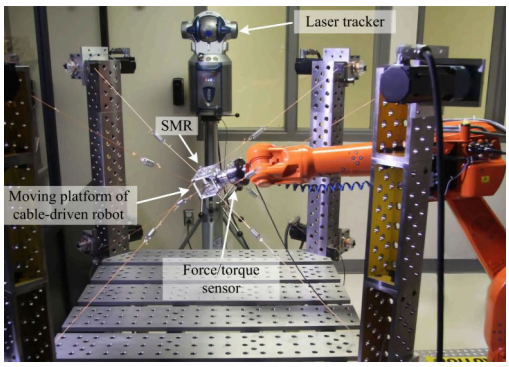

(b) CDPR for serial arm calibration [Kam+16].

Figure 1.7: CDPR used as haptic interfaces.

In France, the company Haption started the commercialization of a CDPR based haptic interface named as Inca [3]. The ICube laboratory in Strabsourg uses an *Inca 6D*, visible in Fig.1.8, in the frame of project PEPS IDRAC for developments in CDPR identification [Che+13] and control [Lar+13]; including vision-based control thanks to six infra-red cameras [CCL15; CCL17].

The *Laboratoire d'Informatique, de Robotique et de Microélectronique de Montpellier* (LIRMM) built a prototype for the COGIRO project [Gou+15] of size $15\times11\times6m$ with a payload capacity equal to 500 kg. This prototype visible in Fig. 1.9 is composed of eight cables and has a suspended configuration. The cable arrangement was optimized to find a good compromise between stability and mobility.

At high speed and acceleration, cable robots can exhibit vibrations due to the flexibility of the cables that can be harmful to the robot's performance, precision and stability. [Kaw+95] made use of cable actuation redundancy to increase the robot stiffness and reduce vibrations. Others research are made to counteract this effects, such as using reaction wheels in [WCG15]. However in this thesis, the dynamic of the platform should be low enough to not experience this kind of behavior.

1.2 ROCKET project

Launched in 2016 for a duration of three years, the IRT JV ROCKET project focused on two applications: *i)* metal plates handling and *ii)* cleaning of cruise ship facades.

[3] Haption Inca product page (link)

Figure 1.8: Haption *INCA 6D* at ICube laboratory [CCL17].

Figure 1.9: The COGIRO prototype developed at LIRMM [Gou+15].

1.2.1 First application: metal plate handling

The project aimed at developing an industrial CDPR for handling and sorting of metal parts by means of a human machine interface (HMI) with augmented reality. Some metal plates shown in Fig. 1.10 constitutes factual cruise ship parts provided by Chantier de l'Atlantique. ROCKET project specification sheet and final poster are available in the Appendices.

The metal handling application was validated on the semi-industrial prototype CAROCA at IRT Jules Verne using a specially built platform, with the ultimate goal of assembling a full-scale industrial CDPR at Chantier de l'Atlantique, as illustrated in Figure 1.11.

Figure 1.10: Metal plates with of different shapes and masses.

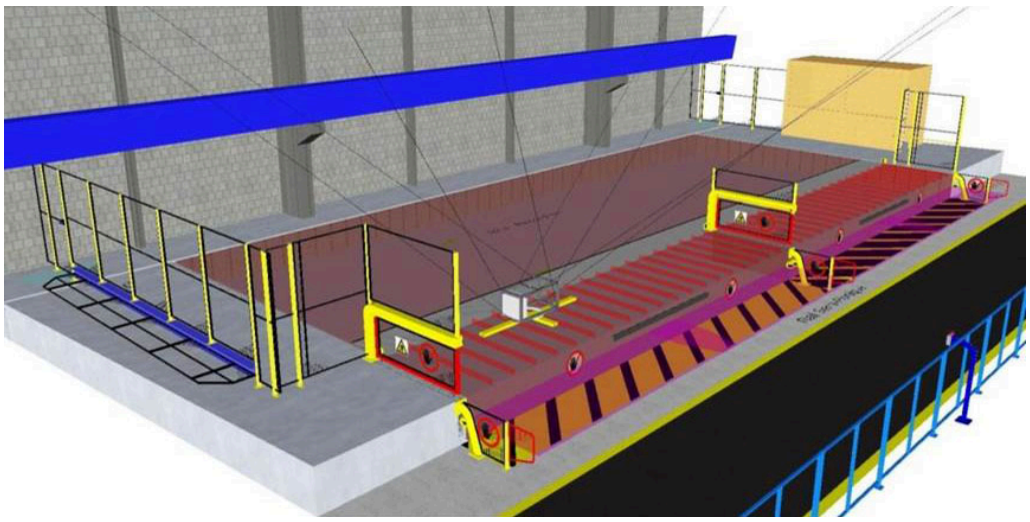

Figure 1.11: Possible CDPR implementation for metal parts handling in an industrial environment.

The main technical and economic impacts of the project are cost reduction, as CDPRs are typically twice cheaper than standard systems, fast handling of parts

and better control of the parts compared to other systems in terms of positioning, orientation and traceability. CDPRs are complementary to the classical six-revolute industrial serial robots in terms of workspace size, stiffness, dynamic performance and heavy payload capacity.

The project presents innovative features compared to traditional cranes. Augmented reality is integrated in the man/machine interface, allowing the operator to use intuitively the technology, with a color code for parts categories, and improve traceability as well as ergonomics. The use of a CDPR will provide improved maintenance of the system as mechanical and electronic components such as motors, gearboxes and winches are mounted to the floor, offering better accessibility.

The industrial partners of the ROCKET project are IRT Jules Verne, Chantiers de l'Atlantique, Clemessy, LS2N (UMR CNRS, Centrale Nantes, Université de Nantes, IMT Atlantique), B&R Automation and Clarté. At the end of the project, the prototype confirmed the proof of concept for handling and storing parts efficiently in a plant. The human machine interface shown in Figure 1.12 allows the operator to pilot the CDPR through and embedded camera on the platform, with augmented reality elements to show the position and status of ss located under the platform.

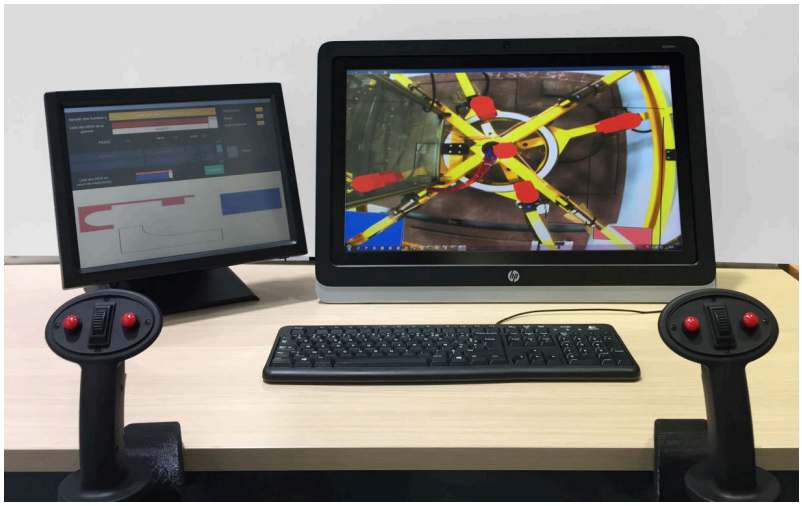

Figure 1.12: ROCKET Human Machine Interface (HMI) with augmented reality. A camera installed on the platform shows the magnets status while the operator controls the platform motion with joysticks.

1.2.2 Second application: window cleaning

The second use case of IRT ROCKET lies in the (window) cleaning of cruise ship facades. Large boats (Fig. 1.13) require rinsing of the outer shell to prevent degradation from salt. Existing systems are based on rails attached to the side of the ship. The main problems with the current installation are the necessity of one rail system per level to clean and the limited range of each machine, as it can only cover a single level of windows. Moreover, the system must be stored when not in

use, sometimes in front a window, obstructing passenger view as visible in the figure on the right.

In this application, the main benefits of CDPR are their large possible workspace, reconfigurability and low moving weight. The project goal is to design a fully-constrained redundant CDPR able to replace the current system by superseding its range and reducing the total number of robots through the use of a single CDPR to cover multiple levels.

On of the main challenges of this application is to cover different depths. The external surface of the ship is not flat as levels can present stairs-like arrangement, as visible in the left picture of Fig. 1.13. In addition, brackets supporting the upper level bridges can also restrain access to the windows. Accordingly, a multi-level mock-up of the ship facade was assembled for the project in order to simulate a surface of different levels, as shown in Fig. 1.26.

This second application was experimented in june and july 2019 on a planar fully-constrained CDPR prototype specially assembled for the project and denoted as ROWC (**RO**CKET **W**indow **C**leaning), presented in Sec. 1.3.2. It is equipped with a deployable axis to deal with the different depths of the ship surface.

Figure 1.13: **Left.** Side view of a cruise ship, which requires regular rinsing of the outer shell and windows. **Right.** Current solution on rails.

1.3 CDPR prototypes at IRT Jules Verne

Several CDPR prototypes have been developped at IRT Jules Verne in previous research projects, including IRT Jules Verne CAROCA [Gag+15] and FASTKIT [Ras+18] projects. These two robots have been upgraded and used in the framework of ROCKET for experimental demonstrations and validations.

1.3.1 ROMP prototype

The **RO**CKET **M**etal **P**late handling prototype (ROMP) is based on the CAROCA cell [Gag+15] and a new platform for the metal plate handling specifically developed

for the application.

Hardware

CAROCA is a reconfigurable CDPR cell developed at IRT Jules Verne for industrial applications experimentation such as photogrammetry, sandblasting and painting simulation, multi-robot collaboration and pick and place operations. Videos of applications tested on IRT Jules Verne prototypes, including CAROCA, are available[4].

The frame of CAROCA is presented in Fig. 1.14. The prototype is 7 m long, 4 m wide and 3 m high. It is composed of eight cables coiled around 120 mm diameter Huchez^{TM} winches, which are pulling a moving-platform (MP). The winches are actuated by synchronous motors of nominal speed and nominal torque equal to 2200 rpm and 15.34 Nm, respectively. A two-stage gearbox of reduction ratio equal to 40 is mounted between each motor and each winch. As a consequence, the prototype is capable of lifting up to one ton. The prototype has pulleys of radius 150 mm with two degrees of freedom that can be displaced in a discrete manner on its frame. Thanks to its reconfigurability, the robot can be assembled both in a suspended or fully-constrained configuration depending on the application at hand.

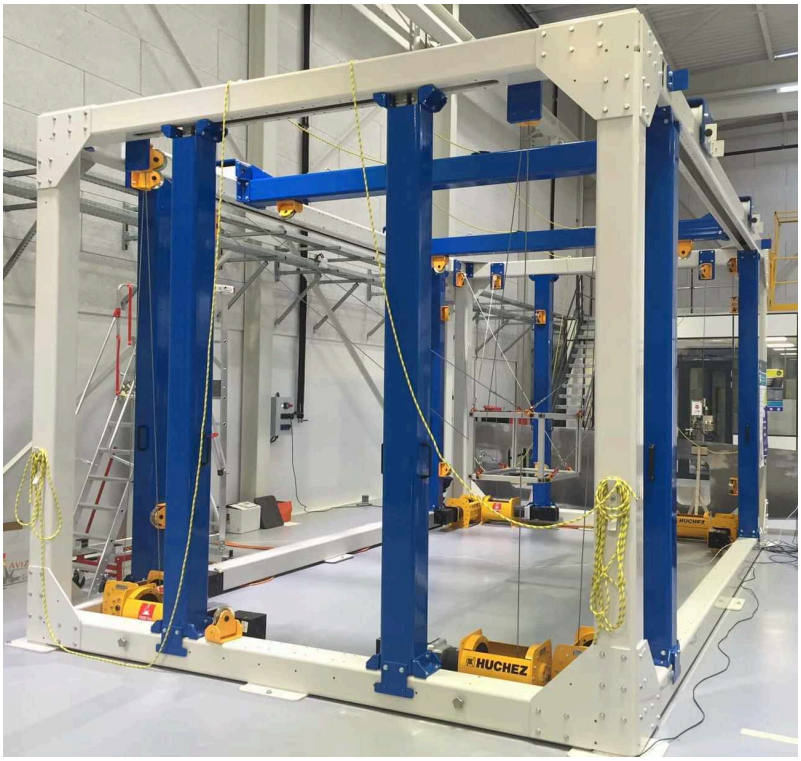

Figure 1.14: CAROCA cell at IRT Jules Verne (Technocampus Ocean).

A specific platform was designed for ROCKET, equipped with five magnets for the metal plates handling application and force sensors located at the cable anchor points on the platform. The robot equipped with this specific platform and working in a suspended configuration constitutes the ROMP prototype, shown in

[4]Cable Driven Parallel Robots at the Jules Verne Institute (link)

Fig. 1.15. Table 1.1 gives the Cartesian coordinates of the cable exit points in the base frame $\mathscr{F}_b$ and the Cartesian coordinates of the cable anchor points expressed in the moving-platform frame $\mathcal{F}_p$. The MP size is 1.5 m×1.5 m×1 m and its mass equals to 366 kg (Fig. 1.15). Five magnets are embedded under the moving platform to pick metal parts. A close-up view of a magnet and a force sensor are illustrated in Fig. 1.16. Each magnet can lift up to 147 kg and weighs 6 kg.

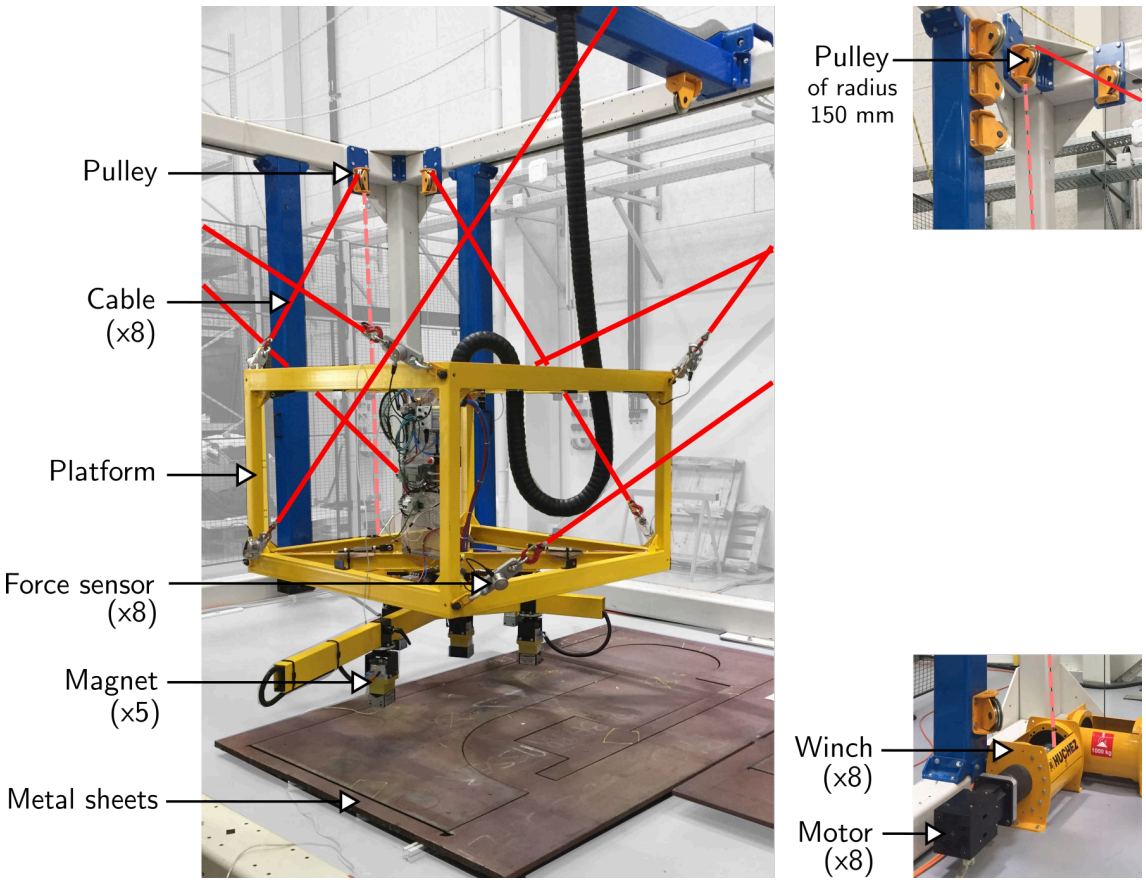

Figure 1.15: ROMP prototype **Top.** The moving-platform (MP) equipped with five magnets to pick metal parts and eight dynamometers to measure cable tensions. **Bottom.** A motor, a winch and a pulley.

Figure 1.16: Close-up view of **Left.** A Magswitch® magnet under ROMP platform **Right.** A Tractel® force sensor located between a cable and an anchor point.

	X (m)	Y (m)	Z (m)
A_1	1.659	-2.850	3.221
A_2	1.350	-3.159	3.221
A_3	-1.350	-3.159	3.221
A_4	-1.659	-2.850	3.221
A_5	-1.659	2.850	3.221
A_6	-1.350	3.159	3.221
A_7	1.350	3.159	3.221
A_8	1.659	2.850	3.221

	X (m)	Y (m)	Z (m)
B_1	0.760	0.725	0.450
B_2	-0.725	-0.760	-0.450
B_3	0.725	-0.760	0.450
B_4	-0.760	0.725	-0.450
B_5	-0.760	-0.725	0.450
B_6	0.725	0.760	-0.450
B_7	-0.725	0.760	0.450
B_8	0.760	-0.725	-0.450

Table 1.1: Coordinates of ROMP cable exit points A_i on the frame and cable anchor points B_i on the platform, with $i = 1 \dots 8$ for a suspended CoGiRo configuration, when neglecting the pulleys geometry.

Table 1.2: ROMP cables properties.

Prototype	Cable material	Young modulus E (GPa)	Cross sectional area S (m^2)
ROMP	Metal	102.2	7.1675×10^{-06}

The cable properties are listed in Tab. 1.2. The prototype is equipped with typical industrial metal wires able to support an effort of up to one ton.

The components manufacturers are listed in Tab. 1.3. Commercial industrial hardware was chosen for all elements of the prototype in order to facilitate the transfer towards industrial partners of the project.

Manufacturers	Component
Europe Technologies	Custom reconfigurable frame
B&R Automation	Control bay, electronics and gearmotors
Huchez	Winches
Tractel	Force sensors
Magswitch	Permanent magnets

Table 1.3: Manufacturers and components.

ROMP static workspace was traced in Fig. 1.17 using the ARACHNIS software for the analysis and parametric design of CDPRs [Gua+14; Rui+15].

Software

The software architecture of ROMP is presented in Fig. 1.18. At the center is the control bay, powered by a B&R Automation® XCPU3586 processor which executes a Linux-based real-time operating system. The robot code can be run at up to 500 Hz (2 millisecond cyclics).

Most of the thesis work was done in MATLAB® and Simulink® (version R2016b), including the creation of a CDPR dynamic simulator, programming of trajectory generation, testing of control laws and data analysis.

B&R Automation® provides an integrated software development environment called Automation Studio® to develop codes compatible with its hardware (servo

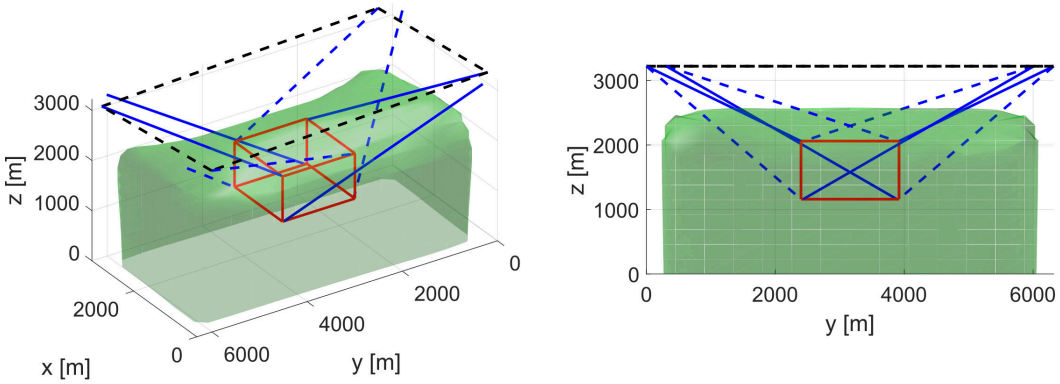

Figure 1.17: ROMP prototype static workspace for $t_{max} = 2667$ N.

drives, motors, coders). Programming of the robot was done in C/C++, although the software also supports Ladder, Instruction List, Structured Text and Sequential Function Chart. Version 4.3 of Automation Studio was used in the project for the final developments. A Simulink toolbox was purchased from B&R Automation for automatic code conversion from MATLAB to the hardware. This allowed to reduce implementation time and testing of new controls laws on the robot. Simulink Coder and Simulink Compiler toolboxes are required for the automatic code generation. Figure 1.19 presents the general flow and interaction of software and hardware for the robot control. Digital and analog inputs/outputs permits the connection of sensors and magnets to the control bay. All connections between the control bay and the platform transits through a *triflex® R* sheath from *igus®*.

1.3.2 ROWC prototype

The second prototype of the ROCKET project was assembled for the testing of a large scale **W**indow **C**leaning application (ROWC). This prototype is based on the frame of FASTKIT [Ras+18], a deployable autonomous CDPR developed in the context of the EU-funded project ECHORD++, for logistics applications in warehouses. It uses a fully-constrained cable configuration and has an almost planar workspace. A video of the window cleaning application is available[5].

Hardware and software

The prototype also uses B&R Automation hardware. As a consequence, the software is the same as ROMP and the system overall architecture is similar. This prototype is actuated by synchronous motors of nominal speed and nominal torque equal to 2100 rpm and 2.6 Nm. The motors are coupled to planetary gearboxes with a reduction ratio of 5, and its winches have a diameter of 80 mm. As such, the prototype can achieve maximum speed of up to 0.9 $\mathrm{m\,s^{-1}}$. However in the considered application of window cleaning, slower trajectories are considered. Contrarily to

[5]ROCKET window cleaning application video (link)

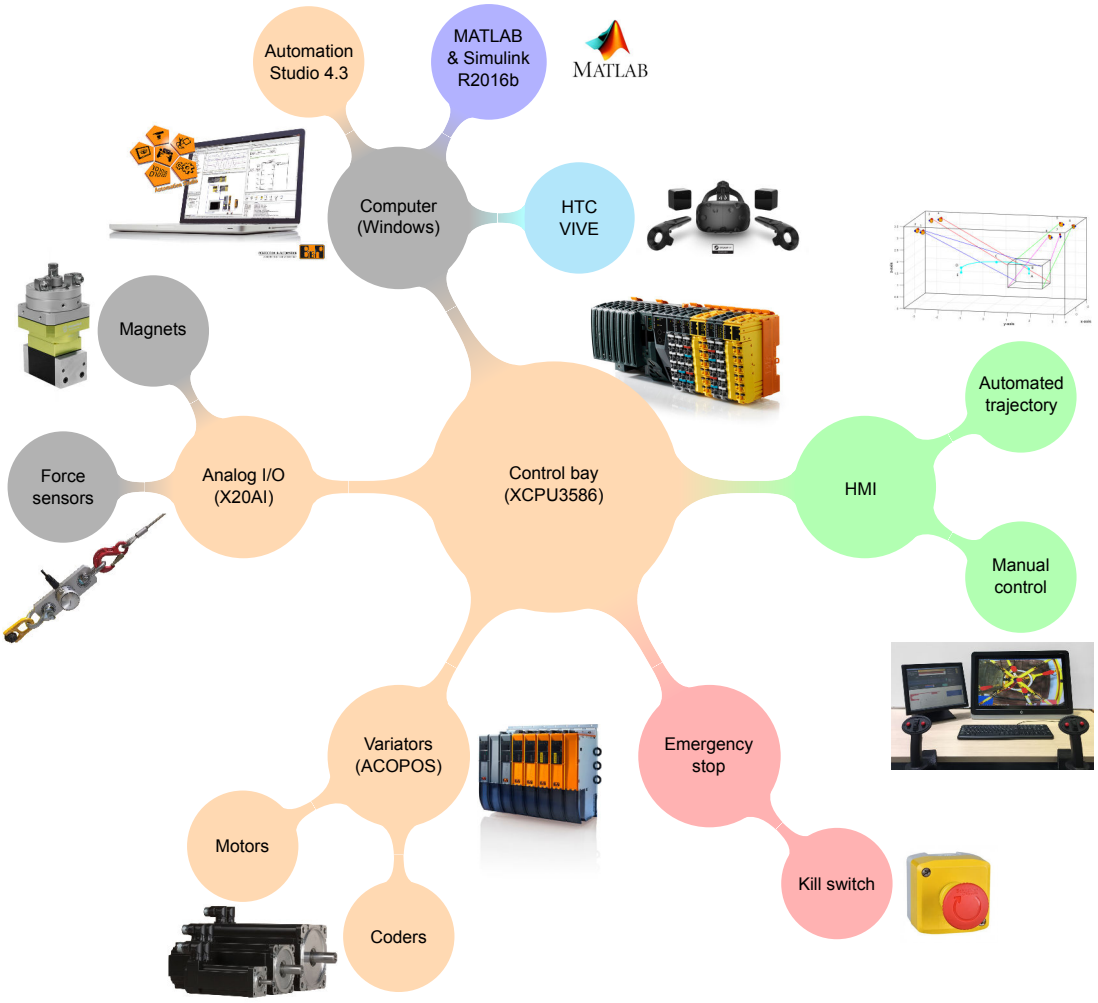

Figure 1.18: ROMP software architecture.

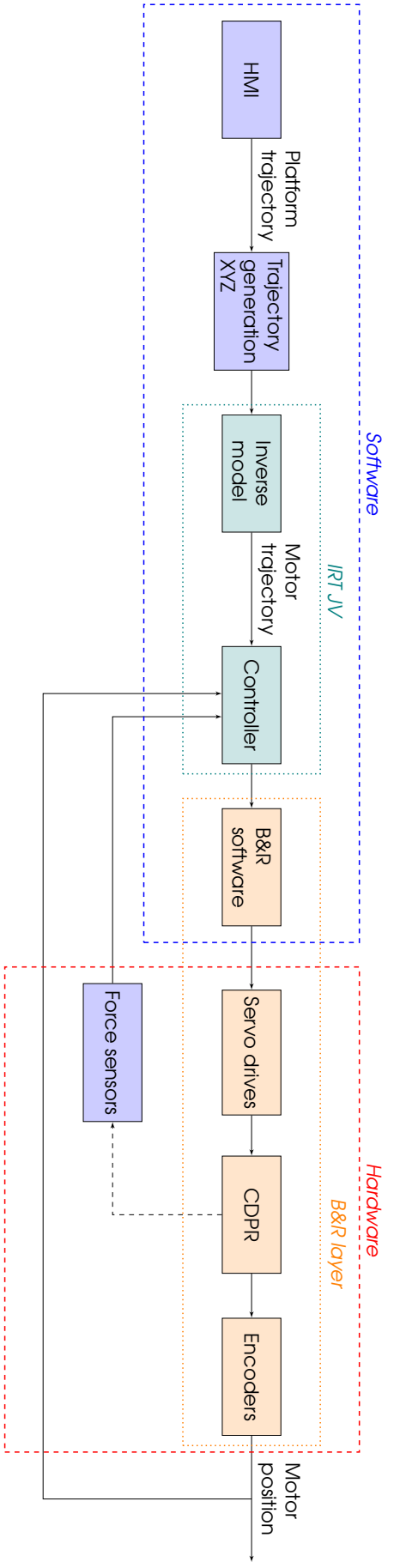

Figure 1.19: ROMP software and hardware interactions.

ROMP, the prototype is not equipped with force sensors, and cable tensions can only be estimated from motor torques. Figure 1.20 presents the real prototype projecting water onto a boat model.

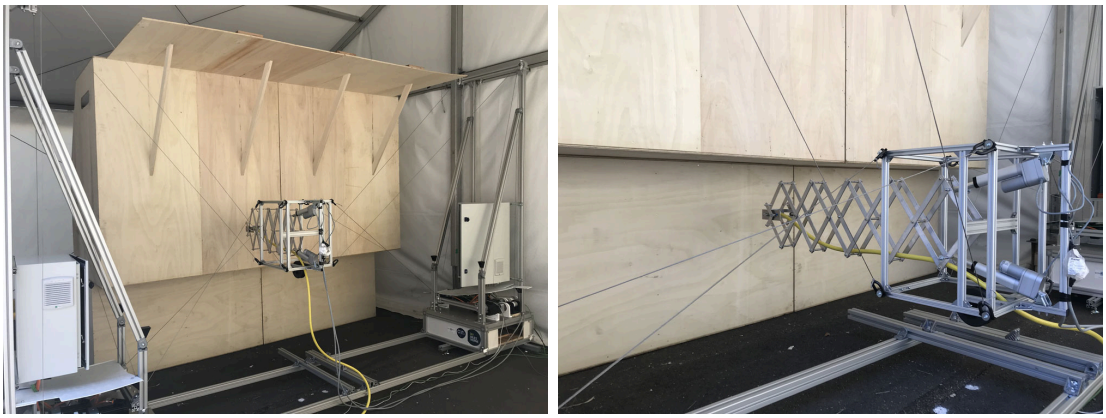

Figure 1.20: ROWC prototype projecting water on a boat model.

A specific platform was designed for the window cleaning application, equipped with a water nozzle placed at the extremity of a deployable mechanism. Since the robot configuration is close to planar, the platform cannot move towards the surfaces of variable depths. The deployable mechanisms, based on a pantograph linkage, can compensate for the distance differences between the surface and the robot workspace. The mechanism CAD model is presented in Fig. 1.21 and is actuated by two linear motors, for a total end-effector course of 900mm. The total weight of the platform equals 14 kg.

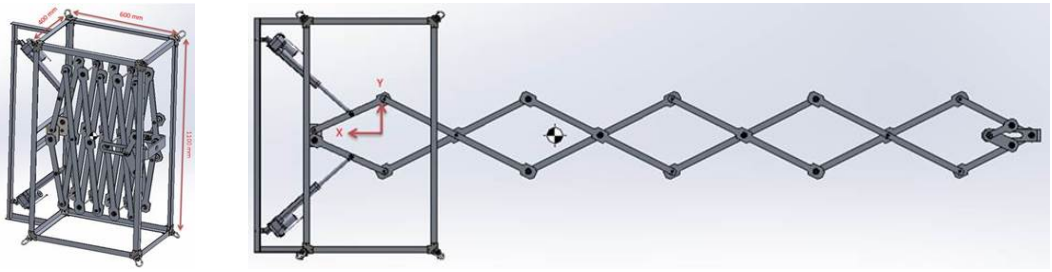

Figure 1.21: ROWC platform CAD model with retracted and deployed end-effector.

The workspace of the robot is presented in Fig. 1.22. The cable configuration of the prototype was chosen as a compromise between achieving the high platform rigidity and avoiding cable collisions. As such, only the lower cables are crossed and can effectively apply a force in the y axis of the robot.

The coordinates of ROWC cable exit points A_i on the frame and cable anchor points B_i on the platform, with $i = 1 \dots 8$ for a fully-constrained configuration with crossed-cables are written in Tab. 1.4 and Tab. 1.5.

ROWC uses polymer cables which are lighter than standard metal cables but still provide high stiffness. The Young modulus and cross sectional area of the cables are provided in Tab. 1.6.

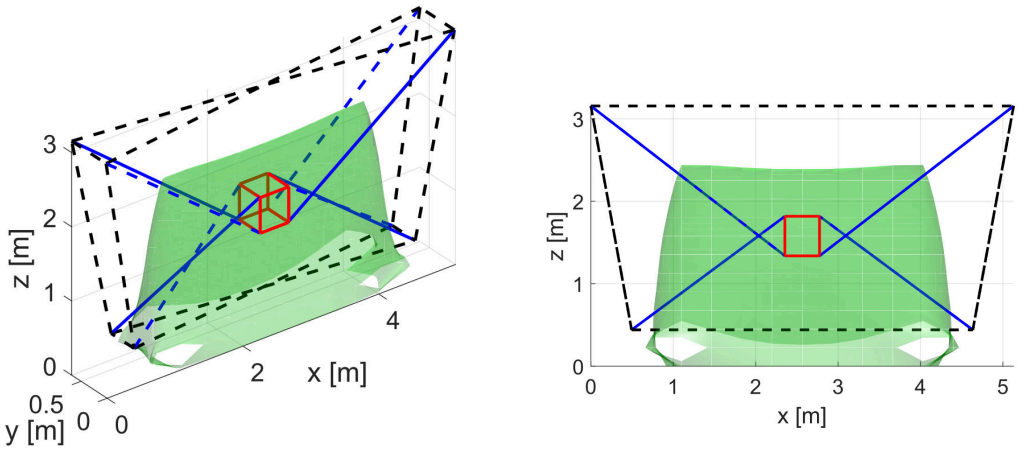

Figure 1.22: ROWC prototype wrench feasible workspace.

Table 1.4: ROWC cable exit points A (m).

A	A_1	A_2	A_3	A_4	A_5	A_6	A_7	A_8
x	-0.54	-0.08	-0.08	-0.54	3.41	2.95	2.95	3.41
y	0.02	0.13	0.57	0.68	0.68	0.57	0.13	0.02
z	2.71	0.44	0.44	2.71	2.71	0.44	0.44	2.71

Table 1.5: ROWC cable anchor points B (m).

B	B_1	B_2	B_3	B_4	B_5	B_6	B_7	B_8
x	-0.21	-0.21	-0.21	-0.21	0.21	0.21	0.21	0.21
y	0.19	0.19	-0.19	-0.19	-0.19	-0.19	0.19	0.19
z	-0.24	0.24	0.24	-0.24	-0.24	0.24	0.24	-0.24

Table 1.6: ROWC cables properties.

Prototype	Cable material	Young modulus E (GPa)	Cross sectional area S (m^2)
ROWC	Dyneema SK78	$109 - 132$	0.81×10^{-06}

1.4 Experimental setups

The experimental setup and test trajectory for the metal plate handling and window cleaning applications are described thereafter.

1.4.1 ROMP test trajectory

The trajectory presented in Fig. 1.23 and Fig. 1.24 simulates a typical pick-and-place operation corresponding to the metal plate handling application, and was used as a basis in the results presented thereafter.

The trajectory consists of the following sections:

1. AB: 200 mm vertical displacement up;
2. BC: arc along the diagonal of the base footprint, with simultaneous displacements of 300 mm up, 300 mm along the x-axis and 1400 mm along the y-axis;
3. CD: arc along the diagonal of the base footprint, with simultaneous displacements of 300 mm down, 300 mm along the x-axis and 1400 mm along the y-axis;
4. DE: 200 mm vertical displacement down;
5. EA: back to point A while following the same path.

The platform takes 30 seconds to move from point A to point E, then 30 seconds from E back to A.

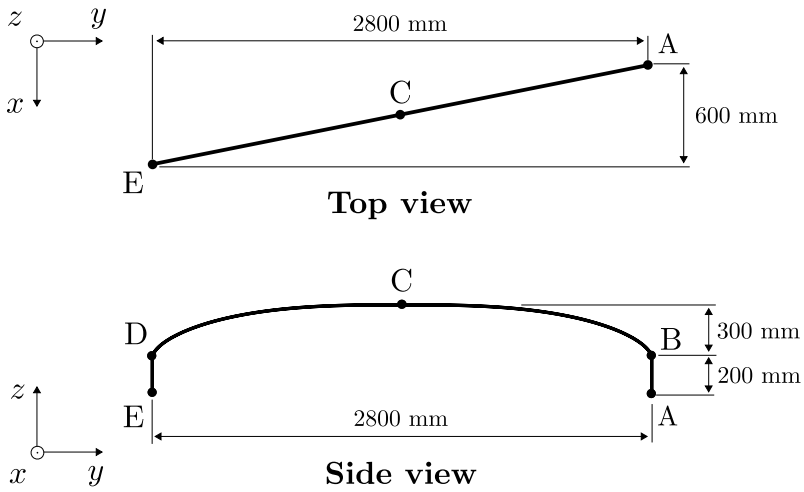

Figure 1.23: Top and side views of ROMP test trajectory.

The trajectory is generated using s-curves, which ensure continuous velocity and acceleration trajectory profiles [Ger+13]. The desired platform positions, speeds and accelerations are traced in 1.25.

1.4.2 ROWC Test trajectory

In the window cleaning application, the water jet must sweep the surface in a succession of horizontal and vertical motions. During the demonstration, the prototype must showcase its ability to deal with the different depths of the actual ship surface,

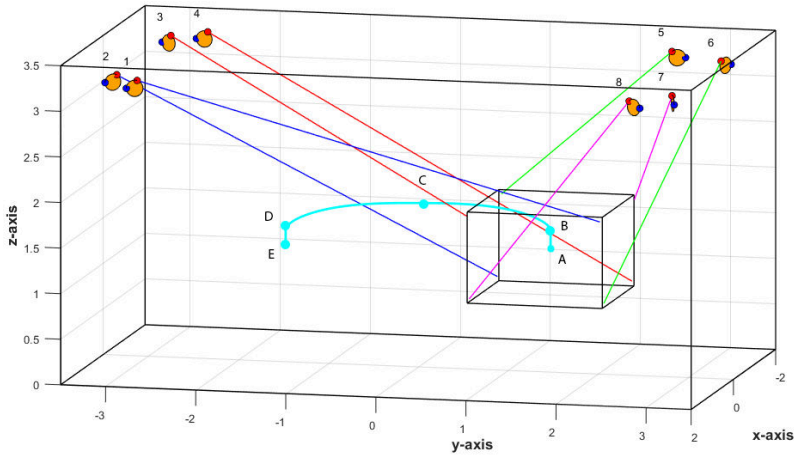

Figure 1.24: ROMP test trajectory in blue and CDPR prototype configuration with pulleys in orange.

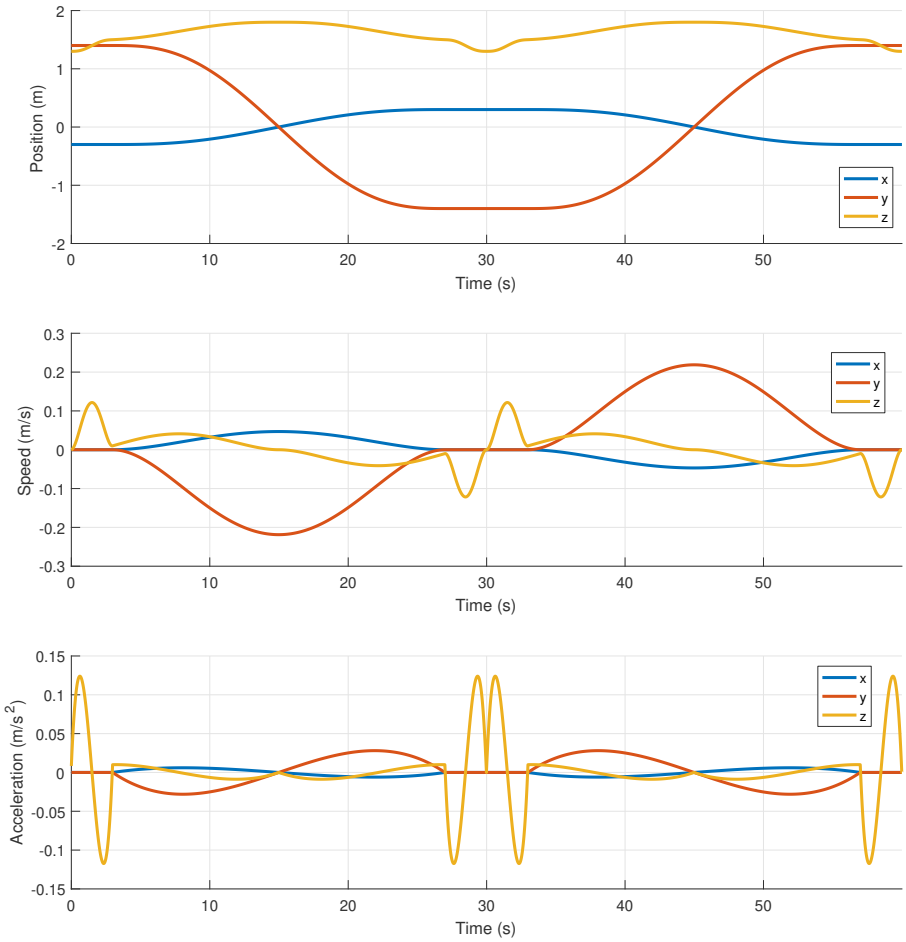

Figure 1.25: ROMP test trajectory desired position, speed and acceleration.

as discussed in Sec. 1.3.2 and visible in Fig. 1.13. The complete trajectory for validation of the prototype is shown in Fig. 1.26.

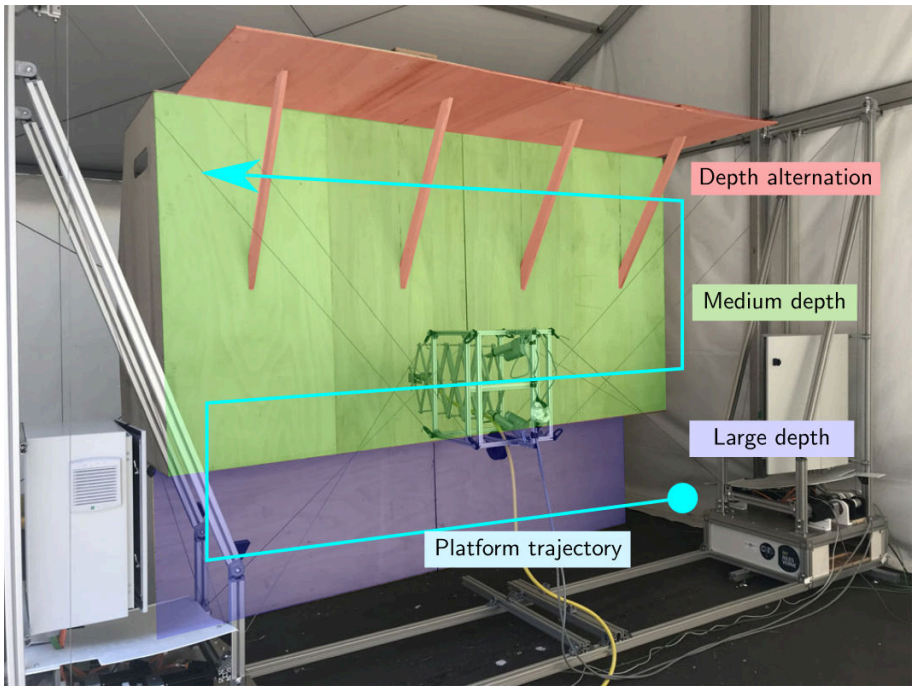

Figure 1.26: Trajectory for window cleaning.

Since the demonstration trajectory is purely constituted of a set of straight lines, the test trajectory considered for the design of ROWC control architecture is a straight line in the center of the workspace. The platform moves along the x axis at a constant orientation. Figure 1.27 shows the prototype, its configuration and the desired trajectory in cyan. The desired trajectory is centered in the workspace of the robot, at mid-height of the wrench feasible workspace. In the considered cable configuration, all cables are crossed so cables can apply a small force component along the y-axis.

The desired path is a simple linear motion along the x-axis at a constant height, representing a section of the window cleaning motion. The platform maximum desired speed is fixed at 0.1 m/s to allow the water jet to properly clean the surface. The trajectory is generated from *G-code*, a standard industrial trajectory programming language, then interpreted by B&R Automation numerical control (CNC) toolbox. The control bay realizes a linear interpolation between the way points written in a script. The top acceleration is fixed at 0.2 m/s^2 and the resulting desired pose along axis y is plotted as a function of time in Fig. 1.28.

1.4.3 Measurements

Internal sensors

On both ROMP and ROWC prototypes, hardware such as motors and control board are standard industrial components commercialized by B&R Automation^{TM}. Angular

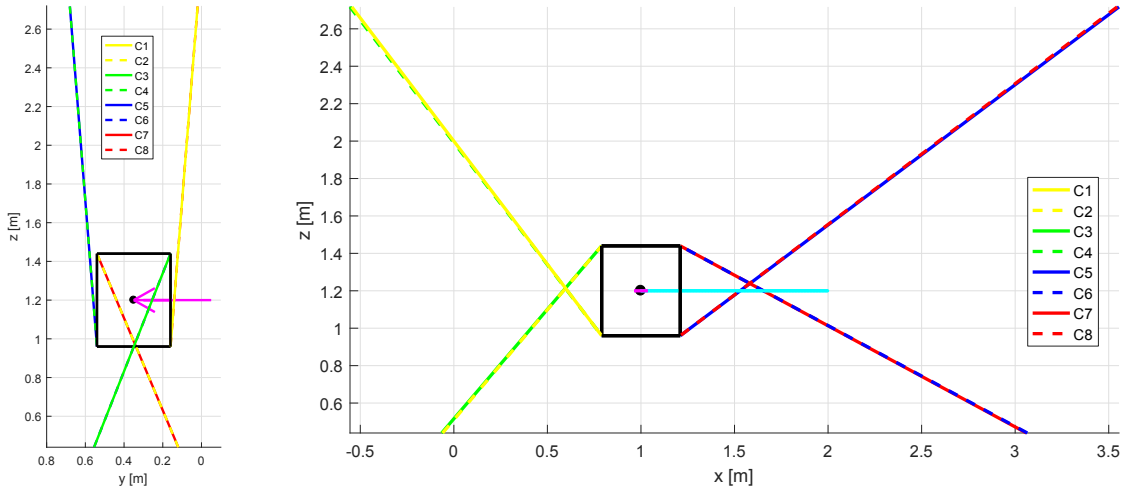

Figure 1.27: Simulated ROWC model, with trajectory portion (cyan) and external wrench due to water pressure (magenta).

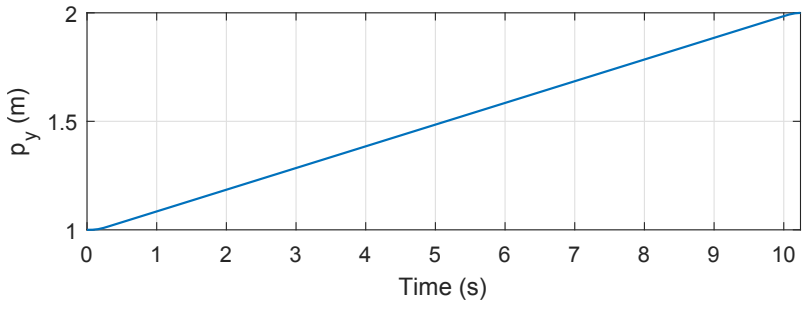

Figure 1.28: Desired pose along y axis for ROWC test trajectory.

position and velocity are available for each motor and the delivered torque is assessed from the motor current.

The ROMP prototype is equipped with Tractel^{TM} force sensors located between the cables and the anchor points of the platform to give a direct measurement of the efforts applied by the cables onto the platform, as shown in Fig. 1.15. These sensors output a current of magnitude between 4 and 20 mA proportional to the tension in the corresponding cable, up to 25000 N. They have been calibrated for the typical working range of the robot comprised between 0 and 5000 N while using a reference force sensor.

External sensors (ROMP)

In order to estimate the CDPR accuracy in the Cartesian space, a HTC VIVE was used to compute the position and orientation of ROMP platform about its six degrees of freedom. This systems relies on VIVE *base stations* which emits infrared light and VIVE *trackers* which are equipped with infrared sensors. A computer receives via WiFi the time data between laser swipes and detection, and computes the trackers poses by solving an optimization problem. In the experimental setup, two base stations and two trackers were used.

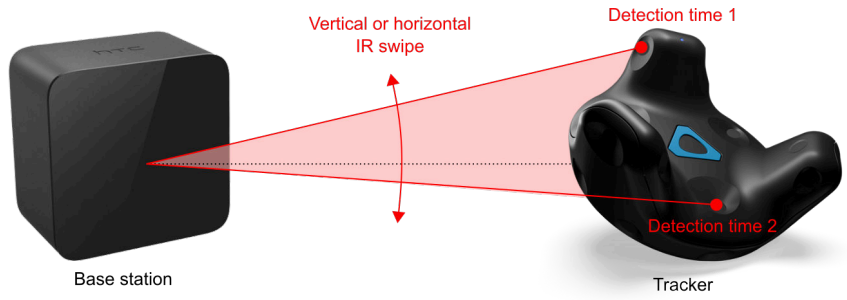

Figure 1.29: VIVE principle between a base station and a tracker.

To track the platform pose, one tracker is fixed to the robot frame and the other is attached to the platform. The trackers poses are recording along the trajectory and the data is treated out-of-the-loop. The platform position in the world frame is computed in MATLAB from the knowledge the trackers poses respectively to the world and platform reference frames. The different frames for one tracker and one base station are presented in Fig. 1.30 and the installation on ROMP in Fig. 1.31.

This system has several benefits compared to other vision based tracking systems. The VIVE does not rely on camera pixel precision but on the difference in laser impact time on the sensors of the tracker. Moreover, the absence of a light source is an advantage for the VIVE compared to cameras which often require high and homogeneous luminosity in the environment. Compared to inertia measurement units (IMU), the VIVE does not suffer from drift as it is a vision based system. While the VIVE can rely on internal inertia measurements to estimate the tracker

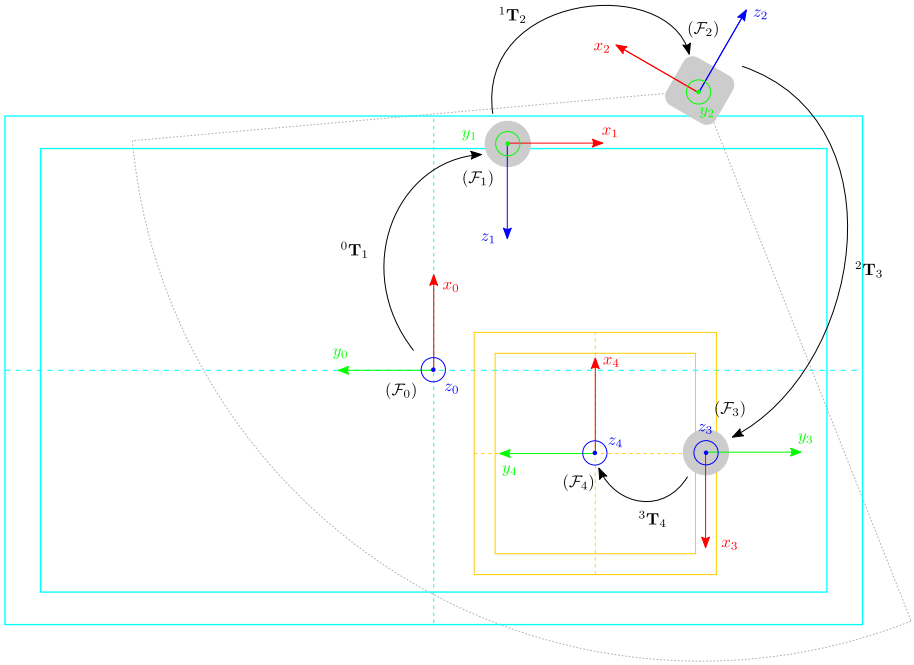

Figure 1.30: Reference frames involved in the platform (orange) tracking relatively to the frame (blue) using two VIVE trackers (grey circles) and a base station (grey square).

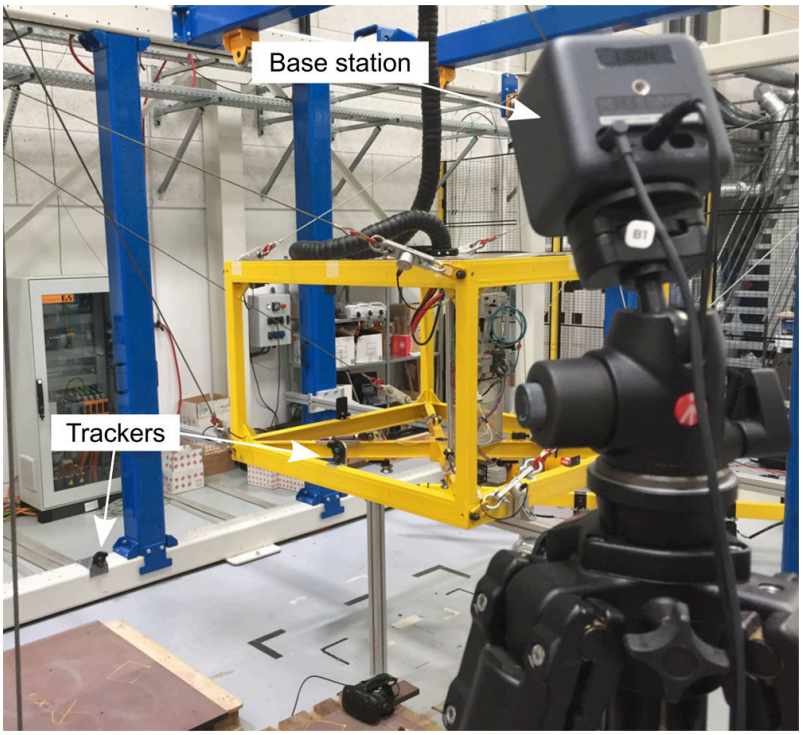

Figure 1.31: The two trackers and a base station.

position between two optical detection, a new absolute position measure is realized at each laser swipe. Due to its commercial ambitions, the VIVE is a very low cost and readily product, much more available than laser tracker and high resolution cameras. Finally, multiple trackers can be followed by the system at the same time. In the current experimental setup two VIVE trackers were used at the same time.

With an average accuracy of 0.3 mm in the plane perpendicular to the laser, and of 2 mm in the direction of the laser, the VIVE is not as precise as a laser tracker or similar professional measurement system. However, its availability at IRT Jules Verne made possible a large number or recordings on the prototypes. More information on the VIVE and recording setup are available in Appendix A.

1.5 Thesis objectives

The main objective of this doctoral thesis is the development of a suitable control method for the metal plate handling application and its implementation on a semi-industrial prototype.

Due to luminosity inconsistencies and dust in the industrial environment of ROMP, the use of visual control had to be set aside. As a consequence, only internal sensors are used in the control law. However, in addition to the usual motor readings, force sensors are available on the prototype to check cable tensions.

In order to achieve good trajectory tracking performance with the controller, aspects such as modeling and calibration must be considered. It also appeared during development that the case of an emergency stop should be considered in order to determine the maximum travel of the platform.

Metal plate handling application objectives

The main challenges for the metal plate handling application will be to ensure precision and repeatability of the platform positioning despite the mass variation. Consequently, the control architecture must be: *i)* **robust** and repeatable with respect to payload changes *ii)* **real-time compatible**, and *iii)* **stable**. It is expected that the largest error sources in the CDPR modeling will come from the consideration of the ROMP prototype large pulleys and cable elasticity.

Window cleaning application objectives

In the window washing application, platform rigidity in a planar configuration will be the most important control aspect as the robot stiffness is more important than absolute positioning accuracy. The goals are to: *i)* **ensure tension in all cables**, and *ii)* implement a **tension distribution algorithm** which maximizes the robot **stiffness** along the axis normal to the plane of motion of the moving-platform.

1.6 Plan

This first chapter presented the concept of cable-driven parallel robots and featured the large variety of existing CDPR applications. The ROCKET project which aimed at exploring handling of metal plates of various masses and sizes, and large scale window washing was presented. The context of the thesis and the prototypes at IRT Jules Verne were also detailed. Finally, the test trajectories and experimental setup for the next chapters were defined.

The rest of this document is organized in two parts: the first part is dedicated to the establishment of CDPR models for the prototypes at IRT Jules Verne, while the second part is focused on the development and testing of control architectures that are robust towards a wrench applied to the platform due to load variation or water pressure.

The modeling of CDPRs is detailed in Chapter 2, including the geometric, kinematic and dynamic models. At first, cables are considered to be straight, inelastic and massless and the geometry of the pulleys is neglected. A second modeling includes the geometry of ROMP two degrees of freedom pulleys. Then, a linear cable elasticity model is given, based on the identified properties of the metal cables of the ROMP prototype, and the elasto-static model of a CDPR is written. Under some hypotheses on the dynamics of the ROMP test trajectory, a method for mass and center of gravity estimation is presented. This information can be useful in the control a CDPRs, in a feedforward term in the control architecture or for safety purposes.

Chapter 3 presents the CDPR manual calibration procedure and details a method for self-calibration, which calculates the CDPR cable lengths and cable exit points locations based on internal sensors alone, such as motor coders and cable tension sensors. Simulation results are provided to compare the method precision depending on the models introduced in chapter 2.

Chapter 4 is dedicated to the control of CDPRs for the two targeted applications. Two families of controllers have been implemented on ROMP for the metal plate handling application, based on either a proportional-derivative controller or a balancing sliding mode/linear controller. Three control architectures for platform position control have been implemented on the prototype and compared along the test trajectory. Their precision at the motor or at the platform position are studied and their overall robustness towards payload increments is observed. In order to improve platform precision and stability, two other control architectures are considered: cable elasticity compensation on ROMP and tension control on ROWC. A novel criteria is proposed for a tension distribution algorithm (TDA) based on the feasible polygon of the CDPR and its the stiffness matrix. This stiffness oriented tension distribution algorithm (SOTDA) was implemented on the ROWC prototype. Simulation and

experimental results are provided in a static pose and along a test trajectory. Using the SOTDA, the platform displacement due to an external wrench was reduced compared to the classical barycenter method.

CDPRs safety is still a challenge for their expansion in the industry. Chapter 5 initiates a discussion on the emergency stop of CDPRs, and provides experimental results on the behavior of the Jules Verne IRT prototypes, based on the proposed control architectures. On ROMP, the impact on the platform displacement and cable tensions of an immediate stop is compared to those of a controlled deceleration in 500 ms. In the case of ROWC, the application of an overwhelming force and its consequences on the tension distribution is observed.

Finally, conclusions are drawn and perspectives on future works are provided in a closing chapter.

1.7 Plan (Français)

Cette thèse a été réalisée à l'IRT Jules Verne dans le cadre du projet ROCKET, dont l'objectif est le développement de robots parallèles à câbles (RPC) pour deux applications industrielles dans le domaine naval: *i)* un RPC en configuration suspendue dédié à la manipulation de plaques métalliques et *ii)* une RPC en configuration pleinement-contrainte pour le lavage de vitres de paquebots. Deux prototypes ont été assemblés à l'IRT Jules Verne pour les développements de ces deux applications, dénommés ROMP (***RO****CKET* ***M****etal* ***P****late handling*) et ROWC (**RO**CKET **W**indow **C**leaning). Les objectifs de cette thèse sont le développement des modèles et lois de commandes nécessaires pour le contrôle précis et répétable de ces deux prototypes. Par conséquents, les hypothèses de modélisation de ces deux robots sont adaptés en fonction de leur configuration et géométrie.

Ce document est organisé en deux parties : la première partie est dédiée à l'établissement du modèle et à la calibration des prototypes de RPC présents développés à l'IRT Jules Verne. La deuxième partie est concentrée sur le développement et les essais expérimentaux de lois de contrôle robustes vis à vis de la variation de masse embarquée dans le cas du prototype ROMP, et de perturbations externes telles que le jet d'eau pressurisé dans le cas de ROWC.

Les RPC utilisent des câbles dont la longueur formant des chaines cinématiques parallèles pour déplacer une plateforme ou un effecteur dans l'espace. La longueur des câbles est contrôlée par un ensemble d'enrouleurs actionnés par des moteurs et des poulies sont utilisées pour acheminer les câbles jusqu'à la plateforme. Les RPC se distinguent des robots parallèles classiques à membres rigides par l'utilisation de câbles flexibles. Cette particularité fournit certains avantages tels qu'un poids réduit des parties en mouvement en opération et de potentiels très grands espaces de travail. Des contraintes spécifiques aux RPC sont cependant à prendre en compte tels que

leur générale redondance d'actionnement et l'impossibilité pour les câbles d'exercer un effort de poussée sur la plateforme.

Le chapitre 1 a d'abord introduit le concept de RPC, les termes associés et leurs caractéristiques. Les robots parallèles à câbles disposent d'un grand champ d'applications possibles, dont certaines sont présentées dans ce chapitre. Le projet ROCKET ensuite été présenté, ainsi que les deux prototypes assemblés pour les applications visées, ROMP et ROWC. Enfin, le chapitre a exposé le montage expérimental mis en place pour ROMP et des trajectoires définies pour l'étude des deux prototypes.

La modélisation des RPC est abordée dans le chapitre 2, y compris les modèles géométrique, cinématique et dynamique. Dans un premier temps, le cas d'un RPC aux câbles droits, sans masse et inélastiques est considéré. Ces hypothèses sont souvent réalisées dans l'étude des RPC et sont en particulier vraies pour les robots de petite dimensions tels que souvent développés en laboratoires. Dans cette modélisation, les poulies redirigeant les câbles vers la plateforme sont considérées ponctuelles. Cependant, dans le cas de ROMP les poulies ont une dimension autour desquelles le câble s'enroule en fonction de la position de la plateforme dans l'espace. De plus, les poulies sont équipées d'un second axe de rotation vertical qui leur permet de suivre la plateforme lors de ses déplacements latéraux, afin d'être toujours orientée dans l'axe du câble. Ainsi, une seconde modélisation considérant la géométrie des poulies est détaillée pour prendre en compte leur effet sur les longueurs de câbles à générer pour contrôler avec précision le robot. Bien que les hypothèses de câbles inélastiques soient répandues dans l'analyse des RPC, les câbles réels ont une élasticité et subissent un allongement en fonction de leur tension. La modélisation des câbles élastique est discutée et le modèle linéaire de l'élasticité des câbles est rappelé. A partir de ce modèle, la matrice de raideur d'un RPC peut être exprimée. Elle permet de lier un petit effort extérieur appliqué sur la plateforme à son petit déplacement engendré, et sera utilisée dans le cas de ROWC pour minimiser le déplacement de la plateforme du au jet d'eau latéral. Enfin, à partir du modèle dynamique et de la connaissance des tensions dans les câbles de ROMP, une méthode est présentée pour réaliser l'estimation de la masse embarquée et du centre de gravité de l'ensemble composé de la plateforme et de sa charge. L'impact sur ces estimations de la considération de la géométrie des poulies dans le modèle est étudié, ainsi qu'une comparaison entre les résultats obtenus par l'estimation des tensions depuis les courants moteurs ou via l'utilisation de capteurs d'efforts mesurant directement les tensions des câbles.

Le chapitre 3 est dédié à la calibration des RPC. Afin de pouvoir débuter une trajectoire, la position initiale des éléments du système et en particulier de la plateforme doivent être connus. La procédure de calibration manuelle de ROMP est d'abord présentée, puis la calibration automatique des RPC est discutée. La calibration automatique consiste à retrouver la pose (position et orientation) de la

plateforme ainsi que les longueurs de câbles correspondantes, voir à reconstituer le modèle géométrique complet du robot. Pour cela, des méthodes basées sur des capteurs externes (caméras, lasers, etc.) ont été développées, mais aussi des méthodes d'auto-calibration internes, uniquement basées sur les capteurs proprioceptifs du RPC (codeurs moteurs et capteurs d'effort). Dans ce chapitre, une méthode d'auto-calibration interne est appliquée en simulation à partir de trois modélisations du robot: la modélisation basique, la modélisation considérant les poulies, et la modélisation considérant les poulies et incluant l'allongement des câbles par élasticité. Les résultats obtenus sont comparés en fonction du modèle ayant servi à la génération des données simulaées et celui utilisé pour la reconstruction du modèle du robot afin d'observer leur impact sur les résultats.

Le chapitre 4 concerne le contrôle des RPC appliqué aux prototypes ROMP et ROWC. Dans le cas de ROMP, l'objectif principal est d'assurer la précision et la répétabilité du robot malgré la variation de charge de la plateforme due à la masse des plaques métalliques. À cette fin, plusieurs architectures sont expérimentalement testés sur le prototype. ROMP ne disposant pas de capteurs extéroceptifs et devant être compatible avec une implémentation en temps réel pour un cadre industriel, les méthodes proposées sont basées sur le contrôle dans l'espace articulaire des moteurs. Au centre de ces architectures, deux contrôleurs sont comparés : un contrôleur basé proportionnel dérivée et un contrôleur alternant entre un comportement basé modes glissants et un comportement linéaire récemment proposé dans la littérature. Ces contrôleurs permettent d'obtenir de bonnes performances de suivi de consignes au niveau de positions motrices, mais la plateforme subit toujours les effets de l'allongement des câbles dû à la masse. Une architecture supplémentaire est alors implémentée, intégrant une boucle de compensation en temps réel de l'allongement des câbles, basée sur les mesures de tensions effectuées par les capteurs d'effort du prototype et le modèle de câble élastique linéaire. Cette architecture permet d'augmenter la répétabilité du robot vis à vis de l'augmentation de masse. ROWC est un RPC pleinement contraint et requiert par conséquent une gestion des tensions dans les câbles pour éviter tout risque de surtensions de câbles opposés, et une éventuelle casse de câble. Un algorithme de distribution de tensions, ou TDA (***T****ension* ***D****istribution* ***A****lgorithm*) doit alors être inclut dans l'architecture de contrôle afin d'assurer la bonne répartition des tensions dans les câbles et leur faisabilité. À partir d'un algorithme basé sur le polygone de faisabilité, un nouveau critère de sélection des tensions est proposé, basé sur la matrice de raideur du robot. Parmi un ensemble de tensions réalisables assurant l'équilibre statique de la plateforme, le *stiffness oriented* TDA (SOTDA) proposé permet de sélectionner le set de tensions minimisant le déplacement de la plateforme dû à la force exercée par le jet d'eau sous pression. Des résultats obtenus en simulation et expérimentalement sur ROWC sont présentés et comparés à ceux obtenus via la sélection des tensions par la méthode du

barycentre.

Enfin, le chapitre 5 constitue une ouverture vers l'étude de l'arrêt d'urgence et de l'aspect sécurité des RPC. L'un des freins à l'implémentation des RPC dans l'industrie en France semble provenir du manque de recul et de normes sur les aspects de sécurité des RPC. Dans ce chapitre, des stratégies d'arrêt d'urgences identifiées à l'IRT Jules Verne sont proposées. Ces stratégies diffèrent selon la configuration du robot et la gravité de l'arrêt d'urgence. Puis, un essai expérimental est réalisé sur le prototype ROMP pour comparer le comportement de la plateforme lors d'un blocage immédiat des moteurs par rapport à une décélération progressive en 500 millisecondes de la plateforme. Enfin l'évolution de la tension des câbles de ROWC avec le SOTDA est observée lorsqu'une force en dehors des limites du prototype est appliquée sur la plateforme.

Pour terminer, une conclusion générale sur les développements réalisés autour de cette thèse est tirée, et les perspectives sont présentées concernant les futurs travaux identifiés autour des RPC à l'IRT Jules Verne.

Part I: Modeling and Calibration

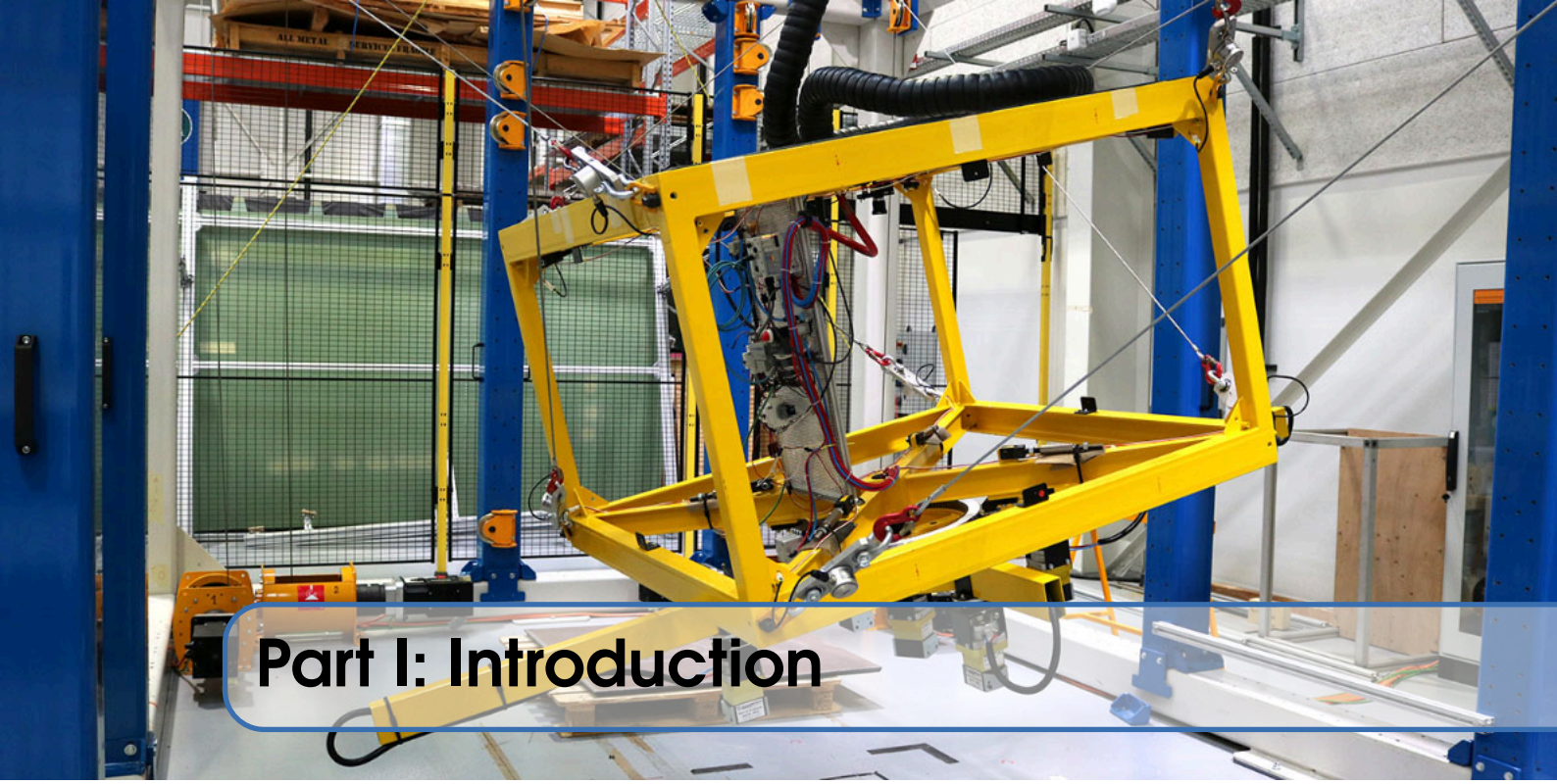

Part I: Introduction

This first part is devoted to the modeling of cable-driven parallel robots and their calibration. These models will later be used in calculations such as trajectory generation, anticipation of the platform dynamics or tension distribution. As a consequence, it is essential to design a model that is the closest to reality in order to achieve good control performances.

CDPR modeling

In the literature, CDPR inverse models are typically based on the same hypotheses as classical parallel mechanisms with rigid links, since the resulting model is simple and computationally efficient. In the simplest modeling, cable are considered straight, inelastic and massless. The dynamic model presented in chapter 2 is based on the formulation expressed in [Gag16].

In reality the use of cable to move and end-effector leads to two main consequences: cables cannot push onto the platform at the risk of becoming slack, and cables present elongation and sagging due to their mass and elasticity.

Due to possible cable slackness and actuation redundancy, solving the direct geometric model of a CDPR can be a challenge, as a set of cable lengths does not equate to a singular position of the platform. Moreover, even in the case of perfectly straight cables, there exists more than one solution to the forward kinematic of CDPRs, and in the case of redundant CDPRs all cables might not be in tension at the same time [Mer15]. Under these conditions, a common way of solving the direct geometric model is through the resolution by a Least Square Method, based on the cable loop closure equations. Recent works are focused on the real-time compatibility of solving the forward kinematics of CDPRs [Pot10].

Cable elasticity

Cable elasticity can lead to nonlinearities between uncoiled cable lengths and platform position. In particular, in the case of very large CDPRs, heavy objects handling and cables of non-negligible mass the sagging should be modeled [Mer08a; Mer15; Ars13]. [KZW06] realized a static analysis of CDPR with non-negligible cable mass. The most widely used formulation of cable sagging was defined in [Irv92], although attempts at simplifying this model for CDPRs exists under some hypotheses [Ngu+13] and other cable modeling techniques are actively being developed [Tem+19]. While lightweight cables might have a negligible mass, a low stiffness can lead to vibrations which should be addressed [WCG15]. Both linear and non-linear cable elasticity model are considered to study the behavior of CDPRs [Bak+17] and oscillatory motions of the platform. From these cable models, it is possible to write the CDPR elasto-static model and stiffness matrix, which correlates the wrench applied onto the platform to its displacement [BCC18]. Based on interval analysis, [STD13] proposed a method to check the validity of common assumptions realized in the modeling of CDPRs, such as massless inelastic cables. In the proposed examples, the simplifications were deemed acceptable for the lightweight prototype ReelAx8, but not CoGiRo.

Finally, in the design of CDPRs the pulleys which redirect the cables from winches towards the platform often have a second degree of freedom to be able to follow the platform as it moves horizontally in the workspace. Depending of their size, the two degrees of freedom pulleys geometry should be considered in the modeling [GGC18; IMC19], or can be neglected without significantly impact the platform positioning accuracy [Pot12].

In the ROCKET project, the geometry of the pulleys was found to be non-negligible on the CAROCA cell and therefore the ROMP prototype designed for the metal plate handling application. In the case of ROWC, the pulleys can be neglected according to [Pot12] since their geometry is less impacting on the cable length than on ROMP.

Load estimation

In order to improve robustness, it is interesting to provide an information on the platform mass to the control law, especially if the objects in the considered applications have highly various shapes, sizes and weights. A practical solution consists in using the measurements of the force sensors located between each cable and the platform. As a consequence, one can directly estimate the efforts applied to the platform. A relationship between the tension of the cables and the payload characteristics was proposed in [Kra+13] for a position based control method able to compensate for cable elasticity, and tested on up to 40 kg payloads. From hypotheses along the test trajectory such as low dynamics and no external wrench, a mass estimation method is experimented on ROMP for orientation and displacement of the platform.

In the scope of this thesis, a study was realized on the impact of the consideration of the pulleys geometry onto the estimated load, as well as a comparison between the use of force sensors versus motor torques to assess the cable tension and the load [Pic+18a]. This mass estimation can then be used to update the feedforward term of a controller and improve the accuracy of the CDPR for the metal plate handling application [Pic+18b], as discussed in Part II.

Calibration

Calibration is important for accurate and precise CDPR control, especially in the absence of external sensors to measure in real-time the platform pose (position and orientation). The robot geometry is typically supposed to be perfectly known and relies on the 3D model realized with *Computer Aided Design* (CAD) software. However, the prototype does not perfectly match its CAD model, leading to some positioning errors of its moving-platform. For a reconfigurable CDPR, geometry errors can appear because of pulley misplacement or backlash between the mobile elements of the structure. In the case of a deployable CDPR, ground leveling and base orientations can quickly lead to an overall deformation of the CDPR compared to its theoretical model. To the extreme, a CDPR could start in an entirely unknown initial position and structure geometry. Even static CDPRs suffer from model errors due to manufacturing defects and wear of parts. These errors can be difficult to assess and change over time, especially in an industrial environment with vibrations and long uninterrupted periods of operation. It is thus of interest to implement calibration procedures, which are able to quickly compute the geometric model based on sensor data. To this end, methods have been developed to automatically calibrate a CDPR using the least possible number of sensors. Two categories of automatic calibration can be considered: *auto*-calibration based on external sensors (cameras, tracking systems, lasers, etc.) and *self*-calibration solely based on internal sensors (motor encoders, cable force sensors, etc.).

Auto-calibration methods specific to CDPRs have been developed. The calibration of fully constrained CDPRs is discussed in [San+12; ADG13], including methods for automatic calibration based on internal sensor data, such as motor encoders, and external sensor data to measure the platform position in the Cartesian space. [DS13] implemented *interval programming* in order to propose a certified calibration of CDPRs, based on laser tracker measurements of the platform pose. It can be noted that while laser tracker are still widely used for their very high accuracy, methods based on more affordable external sensors have been developed such as in [Jin+18], based a single one-dimensional laser distance sensor.

A self-calibration method based the cable loop closure equations defininig Least Square Fitting problem was presented in [FCCG14b] for a CDPR with 4 cables and 3 degrees of freedom. This method only relies on the motor encoders, which

renders it applicable to almost any CDPR. Assuming the positions of the cable exit points as known, some self-calibration methods are dedicated to the estimation of the initial cable lengths only: [Lau18] applied such a method in simulation to a suspended CDPR with the CoGiRo prototype model. More recently, [IMC19] considered the pulleys geometry for the initial pose and cable lengths estimation of suspended under-actuated CDPRs.

In Chapter 3, the method presented in [FCCG14b] is extended to the case of a 6 degrees of freedom CDPR with 8 cables, with the consideration of *i)* the pulleys geometry in the model and *ii)* the cable elongation due to elasticity, as force sensors data could be used to consider the cable elongation in the resolution of the calibration problem. Simulation results are provided in Sec. 3.3 based on ROMP model. Input data for the method is generated based on each model, then the self-calibration is applied with either the same model, or with a different model to observe the impact of the chosen model on the output results.

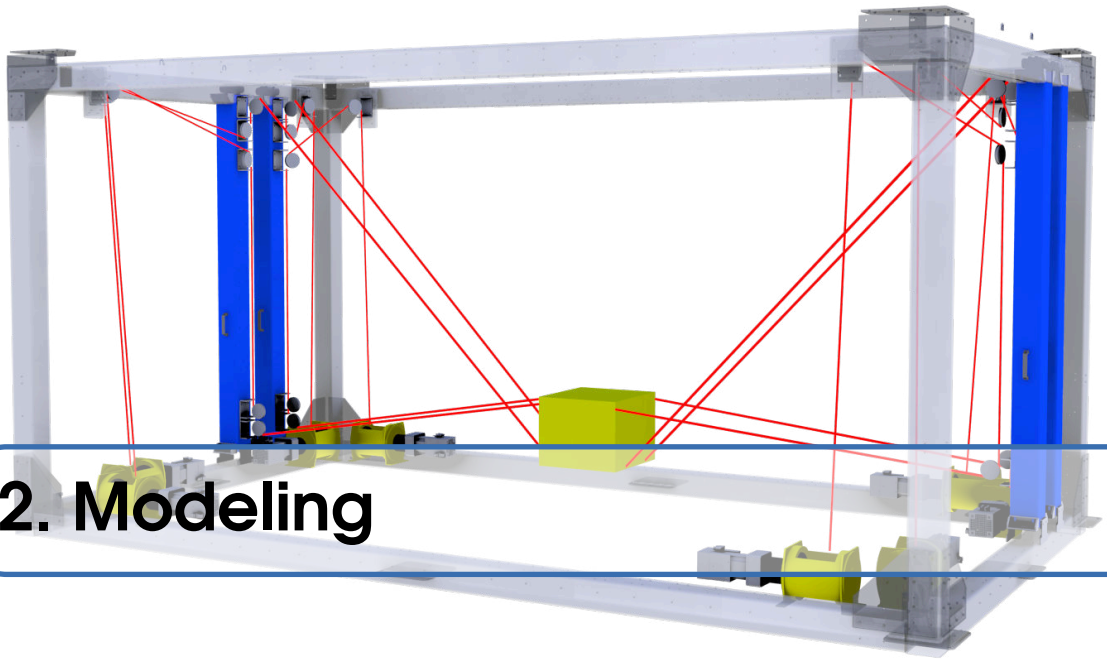

2. Modeling

The geometric, kinematic and dynamic modeling of cable-driven parallel robots is described in this chapter. The models are obtained while considering the pulleys and without taking them into account. Cable elasticity and sagging are discussed. The elasto-geometric model of a CDPR is presented too. From these models, a mass and center of gravity estimation method is described and implemented on the ROMP prototype in real-time. Experiments are carried out to test the precision of the estimation. As a closing remark, a comparison is made between cable tension measurement from force sensors and cable tensions assessed from motor torques. Finally, the impact of cable tension measurement on the quality of the mass estimation is studied.

2.1 Geometrico-static modeling

The geometric model links the pose of the platform in the *Cartesian space* (position and orientation) to the position of the motors in the *joint space* (angular position). The *Inverse Geometric Model* (IGM) of a CDPR expresses the cable length vector $\mathbf{l}$ as a function of the moving-platform pose (position and orientation) $\mathbf{X}$. The *Direct Geometric Model* (DGM), or *forward kinematics* of a CDPR, is used for the inverse operation to obtain the platform pose from the motor positions. Figure 2.1 summarizes the transformations operated by the direct and inverse kinematics.

The expression of the IGM and DGM depends on the hypotheses made on the cables. In this section, cables are considered straight, inelastic and massless. As a

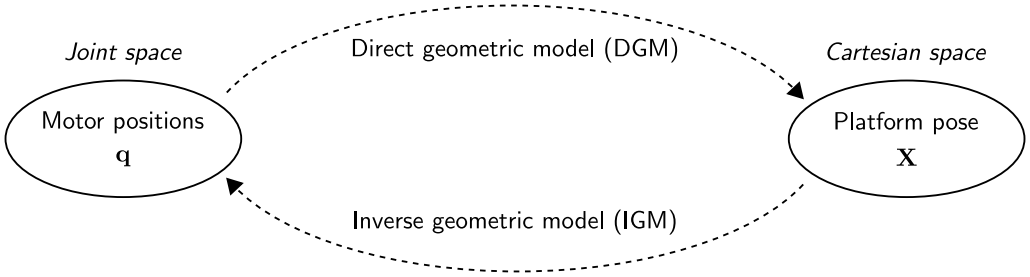

Figure 2.1: Direct and inverse geometric models input/output.

result, the motor positions $\mathbf{q}$ are directly proportional to the cable lengths $\mathbf{l}$:

$$\mathbf{l} = r_w \mathbf{q} \tag{2.1}$$

with r_w the radius of the winches cables are coiled onto.

2.1.1 Basic inverse geometric model (IGM I)

In a simplified model, CDPR pulleys are often treated as points and considered fixed in the frame $\mathcal{F}_b$. Such a modeling is represented in Fig. 2.2.

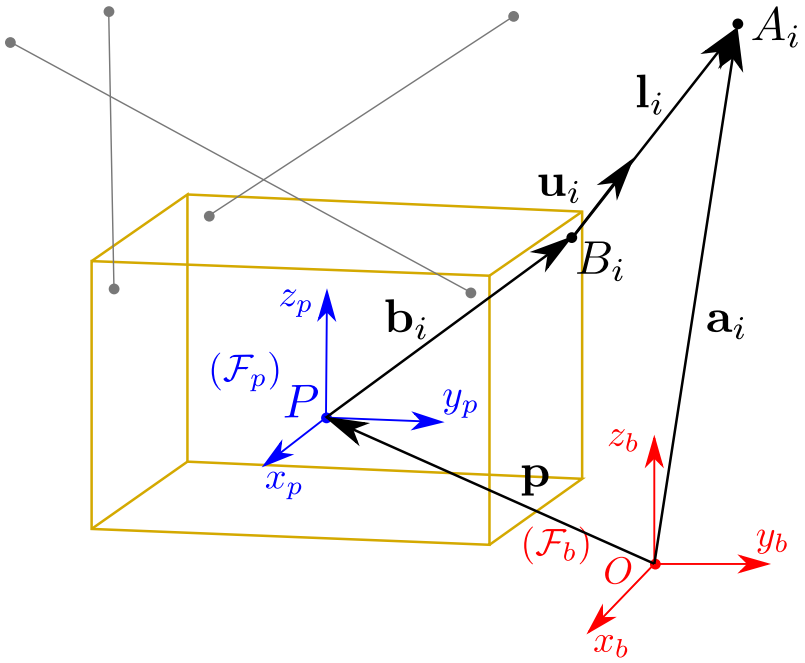

Figure 2.2: CDPR geometric parametrization.

Figure 2.2 depicts the main geometric parameters of a CDPR and its i^{th} loop-closure equation, $i \in \{1, \ldots, m\}$, m being the number of cables attached to the MP. $\mathscr{F}_b$ is the robot base frame, and $\mathscr{F}_p$ is the MP frame.

Cable exit points on the pulleys are denoted as A_i, while cable anchor points on the platform are denoted as B_i. Vector ${}^b\mathbf{a}_i$ points from point O to point A_i and is expressed in frame $\mathcal{F}_b$. Vector ${}^p\mathbf{b}_i$ point from point P to point B_i and is expressed

in frame $\mathscr{F}_p$. Vector ${}^b\mathbf{p}$ is the position vector of point P, the MP geometric center, expressed in $\mathcal{F}_b$.

Vector $\mathbf{l}_i$ represents the i^{th} cable vector and points from B_i to A_i:

$$ {}^b\mathbf{l}_i = l_i {}^b\mathbf{u}_i = {}^b\mathbf{a}_i - {}^b\mathbf{p} - {}^b\mathbf{R}_p {}^p\mathbf{b_i} = {}^b\mathbf{a}_i - {}^b\mathbf{p} - {}^b\mathbf{b_i} \tag{2.2} $$

with ${}^b\mathbf{R}_p$ the rotation matrix from frame $\mathcal{F}_b$ to frame $\mathcal{F}_p$. l_i is the length of the i^{th} cable and $\mathbf{u}_i$ is the unit vector of the i^{th} cable vector, defined as

$$ l_i = \|\mathbf{l}_i\|_2 \qquad {}^b\mathbf{u}_i = \frac{{}^b\mathbf{l}_i}{\|{}^b\mathbf{l}_i\|_2} \tag{2.3} $$

where $\|.\|_2$ denotes the Euclidean norm of a vector.

2.1.2 Static equilibrium

The static equilibrium of the platform takes the form:

$$ \mathbf{W}\mathbf{t} + \mathbf{w}_e + \mathbf{w}_g = 0 \tag{2.4} $$

$\mathbf{W}$ being named as the wrench matrix of the robot. In the basic modeling, this matrix is denoted as $\mathbf{W}_I$ [GGC18] and expressed as

$$ \mathbf{W}_I = \begin{bmatrix} {}^b\mathbf{u}_1 & \dots & {}^b\mathbf{u}_i & \dots & {}^b\mathbf{u}_m \\ {}^b\mathbf{b}_1 \times {}^b\mathbf{u}_1 & \dots & {}^b\mathbf{b}_i \times {}^b\mathbf{u}_i & \dots & {}^b\mathbf{b}_m \times {}^b\mathbf{u}_m \end{bmatrix} \tag{2.5} $$

$\mathbf{t}$ is the cable tension vector, $\mathbf{w}_g$ is the wrench applied to the platform due to gravity and $\mathbf{w}_e$ is an external wrench expressed in the fixed reference frame $\mathscr{F}_b$ defined as:

$$ \mathbf{w}_e = \begin{bmatrix} \mathbf{f}_e{}^T & \mathbf{m}_e{}^T \end{bmatrix}^T = \begin{bmatrix} f_x & f_y & f_z & m_x & m_y & m_z \end{bmatrix}^T \tag{2.6} $$

where f_x, f_y and f_z are the components of the external force vector $\mathbf{f}_e$, and m_x, m_y and m_z are the components of the external moment vector $\mathbf{m}_e$. The components of the external wrench $\mathbf{w}_e$ are assumed to be bounded.

2.1.3 Inverse geometric model including the pulleys geometry (IGM II)

In reality, the cable exit points on the pulleys are not fixed, but can move along the pulley sheave. The impact of this displacement depends on the design of the CDPR and the size ratio between pulley diameter and average cable length [Pot12]. When pulley size becomes important, pulley geometry influence on the CDPR modeling

will generate cable length differences of up to several centimeters. Pulleys of both ROMP and ROWC prototypes are respectively shown in Fig. 2.3 and 2.4. The two prototypes have two DoF pulleys, which can rotate about a vertical axis so the cable can follow the direction of the anchor point on the platform as it travels in the workspace. The main differences between the pulley geometries are:

1. A 150 mm diameter for ROMP pulleys versus a 20 mm diameter for ROWC pulleys
2. A smaller distance between the rotation and revolution axis in the case of ROWC upper pulleys (10 mm) than for ROMP pulleys (75 mm)
3. Intersection between rotation and revolution axis for ROWC lower pulleys

Considering the cable exit point as the tangent point between the cable and the pulley sheave, a rotation of ROMP pulleys about the vertical axis will result in a non-negligible displacement of the exit point position in space. On the contrary, ROWC pulleys rotation impact on the cable exit point is much smaller. As a consequence, in the thesis the pulleys geometry is considered for ROMP modeling, but neglected for ROWC.

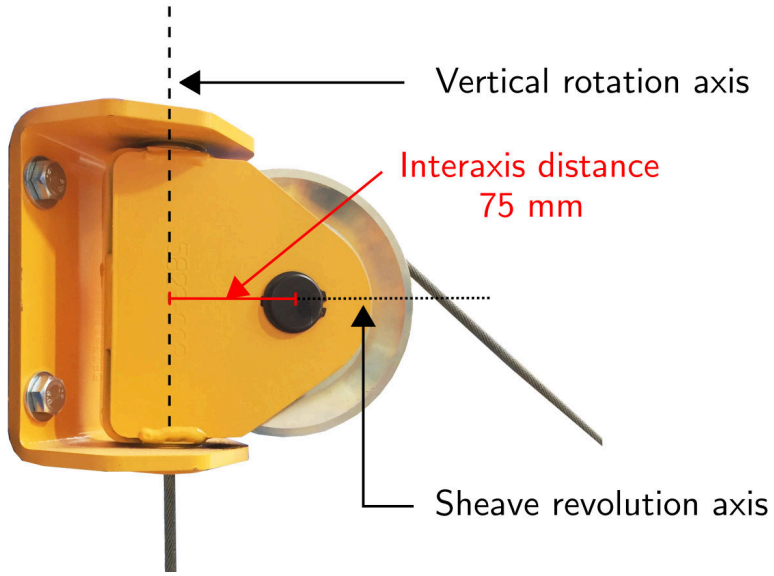

Figure 2.3: ROMP pulley of diameter 150 mm.

To take into consideration the pulleys geometry, the moving cable exit point onto the pulley sheave is introduced as A_i'. The parameterization for a two-DoF pulley is described in Fig. 2.5. The i^{th} cable is tangent to its pulley at point A_i'. l_{ci} is the distance between point A_i' and point B_i. l_{pi} is the length of the i^{th} cable part embracing the shape of the i^{th} pulley sheave. Point A_i is the intersection point between the vertical rotation axis of the i^{th} pulley and the horizontal plane containing the axis of its sheave.

The total cable length from A_i to B_i equals:

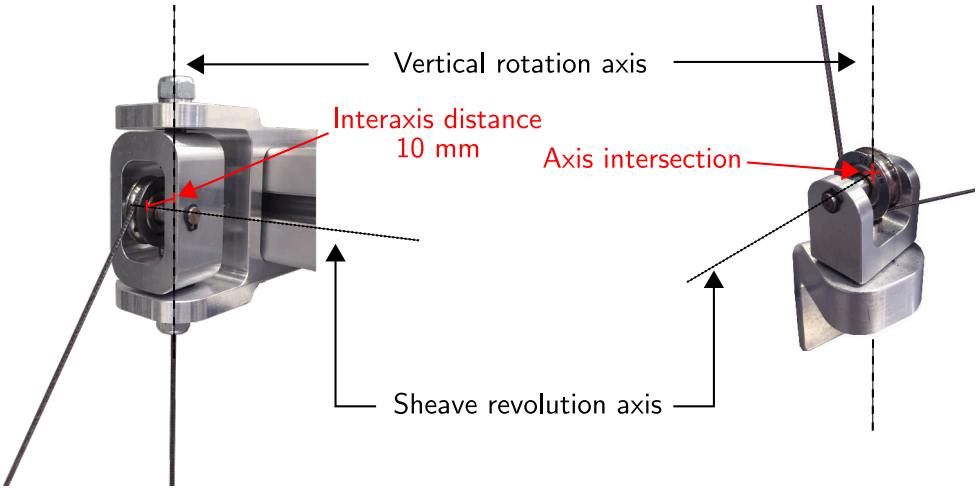

Figure 2.4: ROWC upper (left) and lower (right) pulleys of diameter 20 mm.

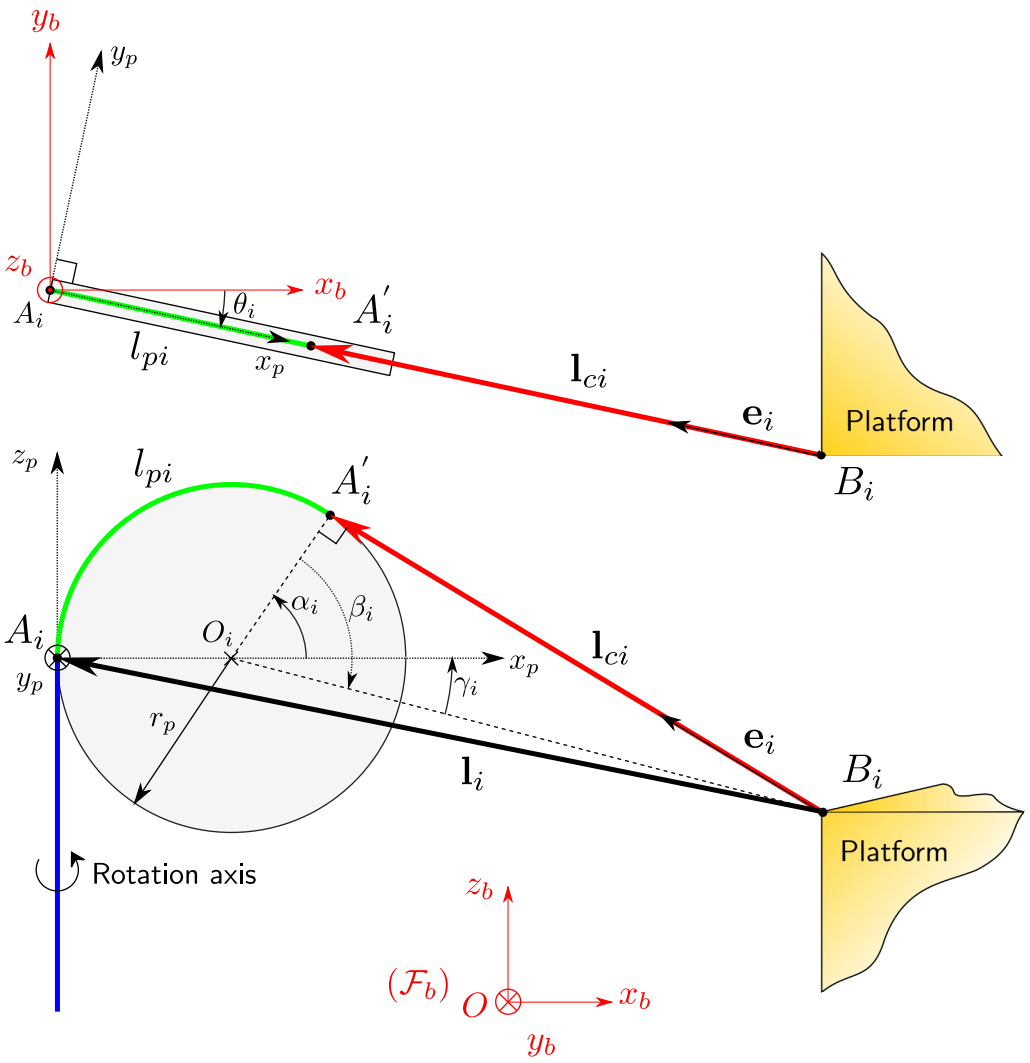

Figure 2.5: Top and side views of a two-DoF pulley.

$$l_i = l_{c,i} + l_{p,i} \tag{2.7}$$

where l_{ci} is the cable length and l_{pi} is the cable length in contact with the pulley.

The center of the ith sheave ${}^b\mathbf{o}_i$ is defined as:

$${}^b\mathbf{o}_i = {}^b\mathbf{a}_i + r_p {}^b\mathbf{x}_p \qquad \text{with} \qquad {}^b\mathbf{x}_p = {}^b\mathbf{R}_{pulley}\, {}^{pulley}\mathbf{x}_p \tag{2.8}$$

with ${}^b\mathbf{R}_{pulley}$ the rotation matrix between $\mathcal{F}_b$ and a new frame $\mathcal{F}_{pulley} = \{\mathbf{x}_p, \mathbf{y}_p, \mathbf{z}_p\}$ attached to the pulley. r_p is the inner radius of the sheave groove. Here, ${}^b\mathbf{R}_{pulley}$ consists of a rotation of angle θ_i about the axis $\mathbf{z}_i^b$, which gives:

$${}^b\mathbf{R}_{pulley} = \begin{bmatrix} \cos\theta_i & -\sin\theta_i & 0 \\ \sin\theta_i & \cos\theta_i & 0 \\ 0 & 0 & 1 \end{bmatrix} \tag{2.9}$$

The angle of the moving cable exit point A_i' about the pulley sheave equals

$$\alpha_i = \beta_i - \gamma_i \tag{2.10}$$

with

$$\sin\gamma_i = -\frac{\left(\mathbf{b}_i^b - \mathbf{o}_i^b\right)^{\mathrm{T}} \mathbf{z}_i^b}{\|\mathbf{b}_i^b - \mathbf{o}_i^b\|_2}, \qquad -\frac{\pi}{2} < \alpha_{i,1} < \frac{\pi}{2} \tag{2.11}$$

$$\cos\beta_i = -\frac{r_p}{\|\mathbf{b}_i^b - \mathbf{o}_i^b\|_2}, \qquad 0 < \alpha_{i,2} < \frac{\pi}{2} \tag{2.12}$$

By including the pulleys geometry, a new wrench matrix $\mathbf{W}_{II}$ is obtained:

$$\mathbf{W}_{II} = \begin{bmatrix} {}^b\mathbf{e}_1 & \dots & {}^b\mathbf{e}_i & \dots & {}^b\mathbf{e}_m \\ {}^b\mathbf{b}_1 \times {}^b\mathbf{e}_1 & \dots & {}^b\mathbf{b}_i \times {}^b\mathbf{e}_i & \dots & {}^b\mathbf{b}_m \times {}^b\mathbf{e}_m \end{bmatrix} \tag{2.13}$$

where $\mathbf{e}_i$ is the new unit vector of the i^{th} cable vector, defined as:

$$l_{c,i} = \|\mathbf{l}_{c,i}\|_2 \qquad {}^b\mathbf{e}_i = \frac{{}^b\mathbf{l}_{c,i}}{\|{}^b\mathbf{l}_{c,i}\|_2} \tag{2.14}$$

with the cable vector ${}^b\mathbf{l}_{ci}$ pointing from A_i' to B_i

$${}^b\mathbf{l}_{ci} = {}^b\mathbf{a}_i + r_p\left({}^b\mathbf{x}_p + {}^b\mathbf{O}\mathbf{A}_i'\right) - {}^b\mathbf{O}\mathbf{B}_i = {}^b\mathbf{a}_i - r_p\left({}^b\mathbf{z}_p + {}^b\mathbf{e}_i\right) \times {}^b\mathbf{y}_p - {}^b\mathbf{O}\mathbf{B}_i \tag{2.15}$$

2.2 Inverse Kinematic Model (IKM)

For CDPRs, the forward Jacobian matrix $\mathbf{A}$ links the speed of the platform to the cable unwinding velocities:

$$\mathbf{A}\mathbf{v} = \dot{\mathbf{l}} \qquad \text{with} \qquad \mathbf{v} = \begin{bmatrix} {}^b\dot{\mathbf{p}} & {}^b\boldsymbol{\omega} \end{bmatrix}^T \tag{2.16}$$

${}^b\mathbf{p}$ being the Cartesian position of MP and ${}^b\boldsymbol{\omega}$ its angular velocity, expressed in $\mathcal{F}_b$.

$\mathbf{A}$ and $\mathbf{W}$ are related by the equation:

$$\mathbf{W} = -\mathbf{A}^T \tag{2.17}$$

In the remainder of this thesis, the wrench matrix $\mathbf{W}$ either equals $\mathbf{W}_I$ corresponding to the modeling neglecting the pulleys, or $\mathbf{W}_{II}$ considering their geometry, depending on the model used.

2.3 Dynamic Model

From [GGC18], the dynamic model of a CDPR can be written as

$$\mathbf{W}\mathbf{t} - \mathbb{I}_p\dot{\mathbf{v}} - \mathbf{C}\mathbf{v} + \mathbf{w}_e + \mathbf{w}_g = 0 \tag{2.18}$$

with $\mathbf{t}$ the cable tensions vector, $\mathbb{I}_p$ the spatial inertia of the platform and $\mathbf{C}$ the matrix of the centrifugal and Coriolis wrenches.

Given that the center of mass of the platform, denoted as G, does not coincide with the origin of frame $\mathscr{F}_p$, the wrench $\mathbf{w}_g$ due to the gravity acceleration $\mathbf{g} = [0,\ 0,\ -g]$ is defined as

$$\mathbf{w}_g = \begin{bmatrix} m\mathbf{I}_3 \\ \mathbf{M}\hat{\mathbf{S}}_p \end{bmatrix} \mathbf{g} \tag{2.19}$$

with m the mass of the platform, $g = 9.81\ m.s^{-2}$, $\mathbf{I}_3$ the 3×3 identity matrix. $\mathbf{MS}_p = {}^b\mathbf{R}_p \left[mx_p, my_p, mz_p\right]^{\mathrm{T}}$ is the first momentum of the moving platform defined with respect to frame $\mathscr{F}_b$. The vector $\mathbf{s}_p = \left[x_p, y_p, z_p\right]^{\mathrm{T}}$ is the position vector of point G in $\mathscr{F}_p$. $\hat{\mathbf{MS}}_p$ is the skew-symmetric matrix associated to $\mathbf{MS}_p$:

$$\hat{\mathbf{MS}}_p = \begin{bmatrix} 0 & -\mathbf{MS}_{p,z} & \mathbf{MS}_{p,y} \\ \mathbf{MS}_{p,z} & 0 & -\mathbf{MS}_{p,x} \\ -\mathbf{MS}_{p,y} & \mathbf{MS}_{p,x} & 0 \end{bmatrix} \tag{2.20}$$

$\mathbb{I}_p$ represents the spatial inertia of the platform, and reads as

$$\mathbb{I}_p = \begin{bmatrix} M\mathbf{I}_3 & -\hat{\mathbf{M}}\mathbf{S}_p \\ \hat{\mathbf{M}}\mathbf{S}_p & \mathbf{I}_p \end{bmatrix} \tag{2.21}$$

with $\mathbf{I}_p$ the inertia tensor matrix of the platform, which can be computed from the platform's inertia tensor $\mathbf{I}_g$, using the Huygens-Steiner theorem

$$\mathbf{I}_p = {}^b\mathbf{R}_p \, \mathbf{I}_g \, {}^b\mathbf{R}_p^{\mathrm{T}} - \frac{\hat{\mathbf{M}}\mathbf{S}_p\hat{\mathbf{M}}\mathbf{S}_p}{M} \tag{2.22}$$

${}^b\mathbf{R}_p$ is the rotation matrix defining the platform orientation and $\mathbf{C}$ is the matrix of the centrifugal and Coriolis wrenches defined as

$$\mathbf{C}\mathbf{v} = \begin{bmatrix} {}^b\hat{\boldsymbol{\omega}}\,{}^b\hat{\boldsymbol{\omega}}\mathbf{M}\mathbf{S}_p \\ {}^b\hat{\boldsymbol{\omega}}\mathbf{I}_p\,{}^b\boldsymbol{\omega} \end{bmatrix} \tag{2.23}$$

with ${}^b\hat{\boldsymbol{\omega}}$ the skew-symmetric matrix associated to ${}^b\boldsymbol{\omega}$, defined as

$${}^b\hat{\omega} = \begin{bmatrix} 0 & -{}^b\omega_z & {}^b\omega_y \\ {}^b\omega_z & 0 & -{}^b\omega_x \\ -{}^b\omega_y & {}^b\omega_x & 0 \end{bmatrix} \tag{2.24}$$

2.4 Cable modeling

In addition, actual cables are elastic and have a linear mass. Therefore they are subject to elongation and sagging, which affects both the static and dynamic behavior of the CDPR. Comprehensive cable modelings include both cable elongation due to elasticity and cable sagging under cable weight. A well known sagging cable model was introduced in [Irv92; Mer15]. Cable can also be represented by linear and nonlinear elasticity models, and their effect on oscillatory motions have been studied in works such as [Bak+17; Mer08a]. In the scope of this thesis, the objective is to use the proper cable model to obtain good accuracy of the moving-platform positioning of ROMP and ROWC in a static case. Due to the low dynamics of the moving-platform in the considered applications, the cable effect on the dynamic model of the CDPR are neglected.

Different cable behaviors are represented in Fig. 2.6 to illustrate these effects, and four cases are described here.

Straight and inelastic cables

Cables can be considered straight and inelastic, as in Sec. 2.1. The resolution of the IGM and DGM are similar to those of rigid parallel mechanisms. The total cable

length from the cable exit point A on the robot frame to the anchor point B on the platform is equal to l.

Straight and elastic cables

Cables are still considered straight but elongation due to elasticity appears. The total cable length from the cable exit point A on the robot frame to the anchor point B on the platform is equal to:

$$l = l_N + \Delta l_e \tag{2.25}$$

where l_N is the cable unstrained length and Δl_e is the cable elongation due to elasticity.

Linear and nonlinear cable elasticity model can be considered to calculate the elongation [Bak+17; BCC18].

Sagging and inelastic cables

Cable sagging appears when the cable linear mass becomes important. Sagging cables are often visible on construction relying on heavy cables such as high voltage power lines, cable cars and suspended bridges. The total cable length is denoted here as l_s and its most widely used formulation was introduced in [Irv92].

Sagging and elastic cables

The most realistic cable modeling should take into account both the effect of sagging and elongation due to elasticity. This extension of the sagging model is detailed in [KZW06] for cable-driven manipulators. In the case of a sagging and elastic cable, the total cable length is equal to:

$$l = l_{Ns} + \Delta l_{es} \tag{2.26}$$

where l_{Ns} is the unstrained sagging cable length and Δl_{es} is the elongation due to elasticity, also affected by sagging.

However the complete model can be computationally intensive and requires either a good knowledge of the cable properties or additional sensors to obtain all the necessary information for its use. In particular in this modeling, the force applied by the cable onto the platform depends on the direction of cable tangent at the anchor point on the platform.

2.4.1 ROMP and ROWC cables

Figure. 2.7 shows the cables of ROMP and ROWC in operation, with straight lines overlaid in red to evaluate cable straightness. It can be observed that sagging appears as negligible on both prototype. Cable elongation due to elasticity cannot be evaluated from a picture, but was visible in practice, as the addition of load on

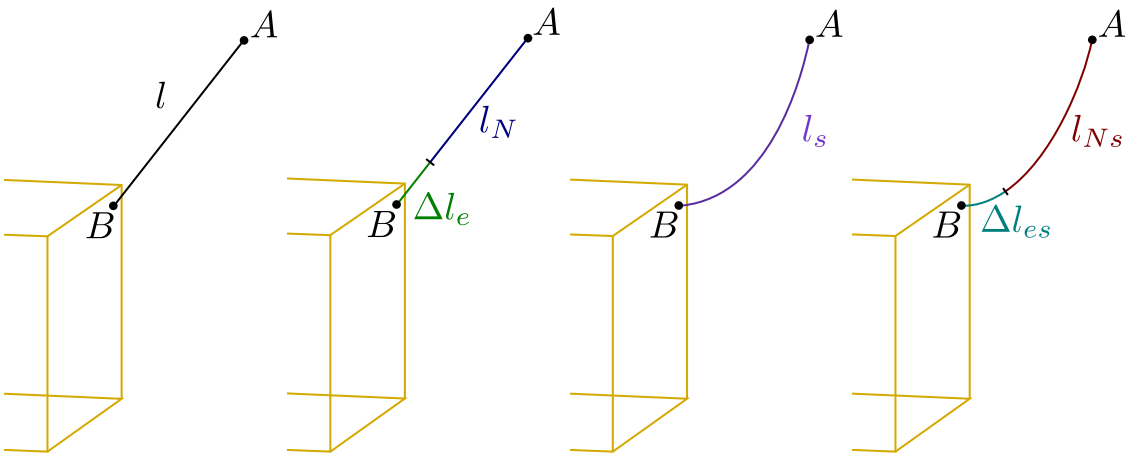

(a) Straight inelastic. (b) Straight elastic. (c) Sagging inelastic. (d) Sagging elastic

Figure 2.6: Usual cable modelings.

the platforms led to a platform downward displacement at constant motor position.

Figure 2.7: The two prototypes cables with straight lines overlaid for comparison **Left.** ROMP cables **Right.** ROWC cables.

ROMP and ROWC cable properties were given in Tab. 1.2 and Tab. 1.6. ROMP cables are typical industrial metal cables with a Young modulus experimentally evaluated at 102.2 GPa [BCC18]. While the total mass of a metal cable can reach several kilograms for a CDPR of this size, ROMP platform is significantly heavier with a mass equal to 366 kg, thus cable mass is considered negligible on this prototype.

ROWC uses SK78 Dyneema® polymer cables which offer a low weight and high stiffness, with a high resistance to abrasion. The yield strength of these cable are

comparable to high-strength steel cables and the Young modulus of SK78 is comprised between 109 and 132 GPa. Thanks to the much lower linear density of polymer compared to metal, the mass of Dyneema cables can be considered negligible as well with regards to the platform weight of 14 kg.

As a consequence, from the absence of visible cable sag on both prototypes, the straight elastic model is selected in this thesis to consider cable elasticity in the static case of CDPR.

2.4.2 Linear cable elasticity model

In order to take into account elasticity, a linear cable elasticity model considered. It is defined as:

$$t_i = k\Delta l_i + t_{i,0} = \frac{ES}{l_i}\Delta l_i + t_{i,0} \qquad \text{for} \qquad i \in \{1, \dots, m\} \tag{2.27}$$

t_i and $t_{i,}$ are the i^{th} current and initial cable tensions, Δl_i the cable elongation and k_i the cable stiffness coefficient, which equals $k_i = \frac{ES}{l_i}$, where l_i the corresponding cable length, E the cable Young modulus and S its cross-sectional area.

In this equation, the cable length l_i should be the total uncoiled cable length from the winch to the platform. As a consequence, the cable length from the winch to the cable exit point should also be considered in the formula:

$$l_i = l_{c,i} + l_{p,i} + l_{WA,i} \tag{2.28}$$

with $l_{c,i}$ the cable length from the exit point A' on the pulley to the anchor point B on the platform, $l_{p,i}$ the cable length in contact of the pulley sheave and l_{WAi} the cable length between winch and anchor point A_i. If pulleys are not considered in the modeling, the term $l_{p,i}$ representing the cable length in contact equals to zero.

This model will be used in this part for the establishment of the elasto-static model of a CDPR, in the design of a self-calibration method considering elasticity, and in the control part of this thesis to compensation for cable elongation.

2.5 Forward kinematics of CDPRs

For industrial applications, the knowledge of the platform pose in real-time can be an important information from safety and control perspectives. The goal of the direct forward kinematics or direct geometric model (DGM) is to compute the platform position in the Cartesian space knowing the motor position in the joint space. However solving the forward kinematics of CDPRs can be a challenge due to their parallel structure, actuation redundancy and the nature of cables.

The forward kinematics of parallel robots with rigid links such as the Gough-Stewart platform can present up to 40 solutions [Hus96]. Moreover contrarily to rigid parallel robots, the cables of a CDPR might become slack and the length of the corresponding cable will have no consequence on the pose of the platform, introducing errors in the resolution of the DGM. As a consequence it is difficult to analytically solve the DGM of CDPRs.

The direct geometrico-static problem (DGP) consists of the calculation of the platform pose and cable tensions based on the knowledge of the static load and cable lengths. The direct geometrico-static problem of suspended under-constrained CDPRs with three cables is solved in its analytical form in [CM11]. With this method, up to 156 complex solution were found, although constraints on the sign of cable tension and static equilibrium can reduce this number. In [AC15] a method to numerically solve the DGP of under-constrained CDPRs of $m \leq 6$ cables is presented. More recently, interval analysis based methods have been experimented in [BMC16] to provide robust and guaranteed solutions, including constraints on cable tension positiveness.

Numerical methods have been developed In order to overcome the issues of solving CDPRs forward kinematics. A common method is based on the resolution of set of non-linear equations issued from the cable loop closure equations, solved using a *Nonlinear Least Square Method* (NLLS) with the MATLAB function *lsqnonlin* for example.

The optimization problem is then defined as follows. A similar approach is used in this thesis for the self-calibration of CDPRs, presented in Sec. 3.3.

Let $\mathbf{X}$ be the real platform pose:

$$\mathbf{X} = \begin{bmatrix} \mathbf{p} & \boldsymbol{\phi} \end{bmatrix}^{\mathrm{T}} \tag{2.29}$$

where $\mathbf{p}$ is the platform Cartesian position and $\boldsymbol{\phi} = [\phi_x, \phi_y, \phi_z]$ the platform Cartesian orientation, represented as Euler angles .

The goal is to find an estimated platform pose $\mathbf{X}^* = [\mathbf{p}^*, \boldsymbol{\phi}^*]$ in which the difference between the corresponding cable length estimation $\mathbf{l}^*$ and the real cable lengths $\mathbf{l}$ are inferior than a desired precision.

The objective to minimize is then:

$$f(i) = l_i^* - l_i \tag{2.30}$$

Using a NLLS method to solve the optimization problem gives the following

complete formulation:

$$\mathbf{X}^* \rightarrow \min_{\mathbf{p}^*,\ \boldsymbol{\phi}^*} \sum_{i=1}^{m} (l_i^* - l_i)^2 \tag{2.31}$$

An initial solution must be given at the start of the algorithm, usually based on the current pose estimation of the platform or the estimated pose at the previous time.

Both the real and estimated cable lengths values $\mathbf{l}$ and $\mathbf{l}^*$ depend on the geometric and cable elasticity models used in the modeling of the CDPR. The estimated cable lengths $\mathbf{l}^*$ are evaluated at each iteration step of the algorithm from the current value of $\mathbf{X}^*$ based on the chosen geometric model.

For straight inelastic cables, the real cable lengths $\mathbf{l}$ can simply be computed from the motor positions as in Eq. (2.1), and the expression of the objective function becomes:

$$f(i) = l_i^*(\mathbf{p}^*, \boldsymbol{\phi}^*) - l_i = \|{}^b\mathbf{a}_i - ({}^b\mathbf{p}^* + {}^b\mathbf{R}(\boldsymbol{\phi}^*)_p {}^p\mathbf{b_i})\|_2^2 - r_w q(i) \tag{2.32}$$

Such a method is presented in [Pot10], along with a real-time compatible implementation algorithm. Cable elasticity is however not considered, which will lead to differences between the estimated and real position of the platform. These differences are expected to be non-negligible in the case of ROMP due to the metal plates weight.

2.6 CDPR Elasto-static model

One of the thesis objectives is to implement a tension distribution algorithm maximizing the stiffness of the ROWC prototype, for a given platform position and external wrench. Tension distribution algorithms and the proposed solution are detailed in Sec. 4.3. To this end, the elasto-static model must be written in order to analyze the CDPR stiffness. This is done by computing the CDPR stiffness matrix. As ROWC pulleys are considered very small in comparison to the cable lengths, the following model is established from the geometric modeling neglecting the pulleys and is based on the linear cable elasticity model written in 2.27.

From [Beh06] and [Gag16], the CDPR stiffness matrix $\mathbf{K}$ can be defined as:

$$\mathbf{K} = \frac{\mathrm{d}\mathbf{w_e}}{\mathrm{d}\mathbf{X}} \tag{2.33}$$

where $\mathrm{d}\mathbf{w_e}$ is a small external wrench applied onto the moving-platform and $\mathrm{d}\mathbf{X}$ the corresponding small displacement of the platform.

Considering a sole external wrench applied to the platform, the static equilibrium

from Eq. (2.4) is written as:

$$\mathbf{W}\mathbf{t} + \mathbf{w}_e = 0 \tag{2.34}$$

By replacing the expression of the external wrench $\mathbf{w}_e$ in Eq. (2.33), one obtains:

$$\mathbf{K} = \frac{\mathrm{d}\mathbf{w_e}}{\mathrm{d}\mathbf{X}} = -\frac{\mathrm{d}\mathbf{W}\mathbf{t}}{\mathrm{d}\mathbf{X}} = -\frac{\mathrm{d}\mathbf{W}}{\mathrm{d}\mathbf{X}}\mathbf{t} - \mathbf{W}\frac{\mathrm{d}\mathbf{t}}{\mathrm{d}\mathbf{X}} \tag{2.35}$$

The stiffness matrix can then be divided in two parts, a passive and an active stiffness matrix, denoted as $\mathbf{K}_p$ and $\mathbf{K}_a$ respectively:

$$\mathbf{K} = \mathbf{K}_p + \mathbf{K}_a \quad \text{with} \quad \mathbf{K}_p = -\mathbf{W}\frac{\mathrm{d}\mathbf{t}}{\mathrm{d}\mathbf{X}} \quad \text{and} \quad \mathbf{K}_a = -\frac{\mathrm{d}\mathbf{W}}{\mathrm{d}\mathbf{X}}\mathbf{t} \tag{2.36}$$

The passive stiffness matrix $\mathbf{K}_p$ corresponds to the stiffness component due to cable elasticity, while the active stiffness matrix is the part due to cable tensions

Passive Stiffness Matrix

In order to develop the expression of the passive stiffness matrix $\mathbf{K}_p$, the linear cable model proposed in Sec. 2.4 is rewritten as

$$\mathbf{t} = \mathbf{K}_l \Delta\mathbf{l} \tag{2.37}$$

where $\mathbf{K}_l = \mathrm{diag}(k_1, k_2, \ldots, k_m)$ is the diagonal matrix of the cable elastic coefficients.

This expression can then be inserted in Eq. (2.37) which gives:

$$\mathbf{K}_p = -\mathbf{W}\mathbf{K}_l\frac{\mathrm{d}\mathbf{l}}{\mathrm{d}\mathbf{X}} \tag{2.38}$$

From the inverse kinematic model presented in Sec. 2.2, matrix $\mathbf{K}_p$ takes the form:

$$\mathbf{K}_p = \mathbf{W}\mathbf{K}_l\mathbf{W}^{\mathrm{T}} \qquad \text{with} \qquad \mathbf{W}^{\mathrm{T}} = -\frac{\mathrm{d}\mathbf{l}}{\mathrm{d}\mathbf{X}} \tag{2.39}$$

Matrix $\mathbf{K}_p$ can be expressed a function of cable unit vector $\mathbf{u}_i$, Cartesian coordinate vectors of anchor points B_i and cable elasticity as follows:

$$\mathbf{K}_p = \sum_{i=1}^{m} k_i \begin{bmatrix} {}^b\mathbf{u}_i\,{}^b\mathbf{u}_i^{\mathrm{T}} & {}^b\mathbf{u}_i\,{}^b\mathbf{u}_i^{\mathrm{T}}\,{}^b\hat{\mathbf{b}}_i^{\mathrm{T}} \\ {}^b\hat{\mathbf{b}}_i\,{}^b\mathbf{u}_i\,{}^b\mathbf{u}_i^{\mathrm{T}} & {}^b\hat{\mathbf{b}}_i\,{}^b\mathbf{u}_i\,{}^b\mathbf{u}_i^{\mathrm{T}}\,{}^b\hat{\mathbf{b}}_i^{\mathrm{T}} \end{bmatrix} \tag{2.40}$$

with ${}^b\mathbf{u}_i$ the unitary vector of the i^{th} cable expressed in frame $\mathscr{F}_b$ and $\hat{\mathbf{b}}_i^b$ the cross

product matrix of vector ${}^b\mathbf{b}_i = [{}^b b_{i,x}, {}^b b_{i,y}, {}^b b_{i,z}]^{\mathrm{T}}$:

$$ {}^b\hat{\mathbf{b}}_i = \begin{bmatrix} 0 & -{}^b b_{i,z} & {}^b b_{i,y} \\ {}^b b_{i,z} & 0 & -{}^b b_{i,x} \\ -{}^b b_{i,y} & {}^b b_{i,x} & 0 \end{bmatrix} \tag{2.41} $$

Active Stiffness Matrix

The active stiffness matrix, $\mathbf{K}_a$ is developed as:

$$ \mathbf{K}_a = -\frac{\mathrm{d}\mathbf{W}}{\mathrm{d}\mathbf{X}}\mathbf{t} = -\sum_{i=1}^{m} \frac{\mathrm{d}\mathbf{w}_i}{\mathrm{d}\mathbf{X}} t_i \tag{2.42} $$

The Jacobian matrix $\dfrac{\mathrm{d}\mathbf{w}_i}{\mathrm{d}\mathbf{X}}$ can be expanded as:

$$ \frac{\mathrm{d}\mathbf{w}_i}{\mathrm{d}\mathbf{X}} = \begin{bmatrix} \dfrac{\mathrm{d}^b\mathbf{u}_i}{\mathrm{d}\mathbf{p}} & \dfrac{\mathrm{d}^b\mathbf{u}_i}{\mathrm{d}\phi} \\ \dfrac{\mathrm{d}\left({}^b\mathbf{b}_i \times {}^b\mathbf{u}_i\right)}{\mathrm{d}\mathbf{p}} & \dfrac{\mathrm{d}\left({}^b\mathbf{b}_i \times {}^b\mathbf{u}_i\right)}{\mathrm{d}\phi} \end{bmatrix} \tag{2.43} $$

From Eq. (2.2), the differential form of ${}^b\mathbf{l}_i$ is written:

$$ \mathrm{d}^b\mathbf{l}_i = -\mathrm{d}^b\mathbf{p} - \mathrm{d}^b\mathbf{b}_i = -\mathrm{d}^b\mathbf{p} + {}^b\mathbf{b}_i \times \mathrm{d}\phi = -\mathrm{d}^b\mathbf{OB}_i \tag{2.44} $$

Or alternatively as:

$$ \mathrm{d}^b\mathbf{l}_i = \mathrm{d}\left(l_i {}^b\mathbf{u}_i\right) = \mathrm{d}l_i {}^b\mathbf{u}_i + l_i \mathrm{d}^b\mathbf{u}_i \tag{2.45} $$

Reminding that $l_i^2 = {}^b\mathbf{l}_i^{\mathrm{T}} {}^b\mathbf{l}_i$ then $2l_i\mathrm{d}l_i = 2{}^b\mathbf{l}_i{}^{\mathrm{T}}\mathrm{d}^b\mathbf{l}_i$.

Which gives:

$$ \mathrm{d}l_i = \frac{{}^b\mathbf{l}_i{}^{\mathrm{T}}}{l_i}\mathrm{d}^b\mathbf{l}_i = {}^b\mathbf{u}_i{}^{\mathrm{T}}\mathrm{d}^b\mathbf{l}_i = {}^b\mathbf{u}_i{}^{\mathrm{T}}\left(-\mathrm{d}\mathbf{p} + {}^b\mathbf{b}_i \times \mathrm{d}\phi\right) = -{}^b\mathbf{u}_i{}^{\mathrm{T}}\mathrm{d}^b\mathbf{OB}_i \tag{2.46} $$

From Eqs. (2.44) and (2.45) the following expression is obtained:

$$ -\mathrm{d}^b\mathbf{OB}_i = -{}^b\mathbf{u}_i{}^{\mathrm{T}}\mathrm{d}^b\mathbf{OB}_i {}^b\mathbf{u}_i + l_i\mathrm{d}^b\mathbf{u}_i \tag{2.47} $$

which gives the expression of the first components of matrix $\mathbf{K}_a$:

$$ \mathrm{d}^b\mathbf{u}_i = -\frac{1}{l_i}\left(\mathbf{I}_3 - {}^b\mathbf{u}_i {}^b\mathbf{u}_i{}^{\mathrm{T}}\right)\mathrm{d}^b\mathbf{OB}_i = -\frac{1}{l_i}\left(\mathbf{I}_3 - {}^b\mathbf{u}_i {}^b\mathbf{u}_i{}^{\mathrm{T}}\right)\left(\mathrm{d}\mathbf{t} - {}^b\mathbf{b}_i \times \mathrm{d}\phi\right) \tag{2.48} $$

$$\frac{\mathrm{d}^b\mathbf{u}_i}{\mathrm{d}\mathbf{p}} = -\frac{1}{l_i}\left(\mathbf{I}_3 - {}^b\mathbf{u}_i {}^b\mathbf{u}_i{}^{\mathrm{T}}\right) \tag{2.49}$$

$$\frac{\mathrm{d}^b\mathbf{u}_i}{\mathrm{d}\phi} = \frac{1}{l_i}\left(\mathbf{I}_3 - {}^b\mathbf{u}_i {}^b\mathbf{u}_i{}^{\mathrm{T}}\right) {}^b\hat{\mathbf{b}}_i \tag{2.50}$$

The rest of the active stiffness matrix $\mathbf{K}_a$ in 2.43 is obtained by differentiating ${}^b\mathbf{b}_i \times \mathbf{u}_i$:

$$\begin{aligned}\mathrm{d}\left({}^b\mathbf{b}_i \times {}^b\mathbf{u}_i\right) &= \mathrm{d}^b\mathbf{b}_i \times {}^b\mathbf{u}_i + {}^b\mathbf{b}_i \times \mathrm{d}^b\mathbf{u}_i = \left(\mathrm{d}\phi \times {}^b\mathbf{b}_i\right) \times {}^b\mathbf{u}_i + {}^b\mathbf{b}_i \times \mathrm{d}^b\mathbf{u}_i \\ &= {}^b\mathbf{u}_i \times {}^b\mathbf{b}_i \times \mathrm{d}\phi - \frac{1}{l_i} {}^b\mathbf{b}_i \times \left(\mathbf{I}_3 - {}^b\mathbf{u}_i {}^b\mathbf{u}_i{}^{\mathrm{T}}\right)\left(\mathrm{d}\mathbf{p} - {}^b\mathbf{b}_i \times \mathrm{d}\phi\right)\end{aligned} \tag{2.51}$$

This raises:

$$\frac{\mathrm{d}\left({}^b\mathbf{b}_i \times {}^b\mathbf{u}_i\right)}{\mathrm{d}\mathbf{p}} = -\frac{1}{l_i} {}^b\hat{\mathbf{b}}_i \left(\mathbf{I}_3 - {}^b\mathbf{u}_i {}^b\mathbf{u}_i{}^{\mathrm{T}}\right) \tag{2.52}$$

$$\frac{\mathrm{d}\left({}^b\mathbf{b}_i \times {}^b\mathbf{u}_i\right)}{\mathrm{d}\phi} = \left[{}^b\hat{\mathbf{u}}_i + \frac{{}^b\hat{\mathbf{b}}_i}{l_i}\left(\mathbf{I}_3 - {}^b\mathbf{u}_i {}^b\mathbf{u}_i{}^{\mathrm{T}}\right)\right] {}^b\hat{\mathbf{b}}_i \tag{2.53}$$

where ${}^b\hat{\mathbf{u}}_i$ is the cross product matrix of vector ${}^b\mathbf{u}_i$.

The active stiffness matrix $\mathbf{K}_a$ is then expressed as:

$$\mathbf{K}_a = -\sum_{i=1}^{m} \tau_i \begin{bmatrix} -\frac{1}{l_i}\left(\mathbf{I}_3 - {}^b\mathbf{u}_i {}^b\mathbf{u}_i{}^{\mathrm{T}}\right) & \frac{1}{l_i}\left(\mathbf{I}_3 - {}^b\mathbf{u}_i {}^b\mathbf{u}_i{}^{\mathrm{T}}\right) {}^b\hat{\mathbf{b}}_i \\ -\frac{1}{l_i} {}^b\hat{\mathbf{b}}_i \left(\mathbf{I}_3 - {}^b\mathbf{u}_i {}^b\mathbf{u}_i{}^{\mathrm{T}}\right) & \left[{}^b\hat{\mathbf{u}}_i + \frac{{}^b\hat{\mathbf{b}}_i}{l_i}\left(\mathbf{I}_3 - {}^b\mathbf{u}_i {}^b\mathbf{u}_i{}^{\mathrm{T}}\right)\right] {}^b\hat{\mathbf{b}}_i \end{bmatrix} \tag{2.54}$$

Thus the full expression of $\mathbf{K}$ is written:

$$\begin{aligned}\mathbf{K} &= \mathbf{K}_p + \mathbf{K}_a \\ &= \sum_{i=1}^{m} k_i \begin{bmatrix} {}^b\mathbf{u}_i {}^b\mathbf{u}_i^{\mathrm{T}} & {}^b\mathbf{u}_i {}^b\mathbf{u}_i^{\mathrm{T}} {}^b\hat{\mathbf{b}}_i^{\mathrm{T}} \\ {}^b\hat{\mathbf{b}}_i {}^b\mathbf{u}_i {}^b\mathbf{u}_i^{\mathrm{T}} & {}^b\hat{\mathbf{b}}_i {}^b\mathbf{u}_i {}^b\mathbf{u}_i^{\mathrm{T}} {}^b\hat{\mathbf{b}}_i^{\mathrm{T}} \end{bmatrix} \\ &\quad - \sum_{i=1}^{m} \tau_i \begin{bmatrix} -\frac{1}{l_i}\left(\mathbf{I}_3 - {}^b\mathbf{u}_i {}^b\mathbf{u}_i{}^{\mathrm{T}}\right) & \frac{1}{l_i}\left(\mathbf{I}_3 - {}^b\mathbf{u}_i {}^b\mathbf{u}_i{}^{\mathrm{T}}\right) {}^b\hat{\mathbf{b}}_i \\ -\frac{1}{l_i} {}^b\hat{\mathbf{b}}_i \left(\mathbf{I}_3 - {}^b\mathbf{u}_i {}^b\mathbf{u}_i{}^{\mathrm{T}}\right) & \left[{}^b\hat{\mathbf{u}}_i + \frac{{}^b\hat{\mathbf{b}}_i}{l_i}\left(\mathbf{I}_3 - {}^b\mathbf{u}_i {}^b\mathbf{u}_i{}^{\mathrm{T}}\right)\right] {}^b\hat{\mathbf{b}}_i \end{bmatrix}\end{aligned} \tag{2.55}$$

The stiffness matrix of the CDPR can then be used to compute the displacement of the platform under a small external wrench. It can then be used to for study of the CDPR behavior under load, or to evaluate this displacement for compensation in a control architecture. In this thesis, the stiffness matrix is used in Sec. 4.3 in a tension distribution algorithm to select the set of feasible cable tensions minimizing the platform displacement in the desired direction. In the case of the ROWC prototype, this corresponds for example to finding the cable tension which will reduce the impact

of the pressured water jet onto the platform position in order to improve its stability and repeatability.

2.7 Payload mass and center of mass estimation

In pick and place applications, the knowledge of the payload mass and center of gravity is benefit for the control of the platform pose, especially for heavy loads: the mass can be used to evaluate the platform displacement using the stiffness matrix, to evaluate the position of the center of gravity for security purposes, or as in Sec. 4.2.2 to implement a feedforward term in the control architecture which will calculate the necessary motor torques ensuring the static equilibrium of the platform.

The CDPR dynamic model presented in Sec. 2.3 linked the cables tensions to the wrenches applied to the platform. In the event where the only wrench applied to the platform is due to gravity, the platform mass and center of gravity position can be expressed as a function of the CDPR cable tension and wrench matrix.

The ROMP prototype is equipped with 8 force sensors located between cable extremities and anchor points, as visible in Figs. 1.15 and 1.16. The position of the force sensors is favorable as they return a direct reading of the forces applied by the cable onto the platform. Since cable tensions measurements are readily available on the ROMP prototype, the method described thereafter was implemented to estimate in real-time the platform mass and its load. The influence of the modeling and force sensors on the mass estimation have been studied in [Pic+18a] and will be detailed afterwards.

2.7.1 Hypotheses and equations

The hypotheses and computation of the platform mass are presented thereafter. It should be noted that a similar approach is presented in [Kra+13], but with cables in polymer and payloads of up to 40 kg. These assumptions are acceptable in the heavy parts pick-and-place application of ROMP, where it is desirable to keep the platform leveled and the dynamics of the trajectories low.

Only wrench is due to gravity

The only wrench applied to the platform is due to the carried payload, namely, the metal plate. No external perturbation is applied to the platform, or need to be evaluated.

Low dynamics of the platform

The accelerations of the moving-platform are low and the associated wrench are negligible compared to gravity. This is true for the pick and place of heavy objects, where the maximum linear velocity of the platform is limited for security purposes and hardware limitations. In the case of ROMP, the mass of the metal plates require

slow trajectories so as not to risk an involuntary drop of the platform by the magnets.

Cables are straight

For the cable tension measurement obtained with the force sensors to be precise, cable sagging must be negligible on the prototype. In the case of important cable sag, the force in the cable is not directed towards the cable exit point on the pulleys but in the tangent to the cable at the anchor point. This angle depends on the cable mass and properties. In Sec. 2.4, ROMP cables were considered straight and elastic. In the following, cable elasticity was neglected since it has no impact on the tension amplitude and the cable angle difference was considered small. Its consideration should however further improve the mass estimation. The inclusion of the pulleys geometry in the modeling is however studied in Sec. 2.7.2.

Equation (2.18) can then be rewritten as:

$$\mathbf{W}\mathbf{t} + \mathbf{w}_g = 0 \tag{2.56}$$

From Eqs. (2.19) and (2.56), $\mathbf{w}_g$ can be expressed as:

$$\mathbf{w}_g = \begin{bmatrix} 0 \\ 0 \\ -mg \\ -mgy_G \\ mgx_G \\ 0 \end{bmatrix} = -\mathbf{W}\mathbf{t} = -\mathbf{W} \begin{bmatrix} t_1 \\ \vdots \\ t_i \\ \vdots \\ t_8 \end{bmatrix} \tag{2.57}$$

Knowing the tensions $\mathbf{t}$ in each cable and the wrench matrix $\mathbf{W}$, it is then possible to calculate the payload mass m and the Cartesian coordinates x_G and y_G of the center of mass of the set composed of the MP and the carried payload, expressed in frame $\mathcal{F}_p$.

Cable tensions can be either measured using force sensors or estimated from the motor currents as discussed in Sec. 2.7.2. The wrench matrix $\mathbf{W}$ depends from the platform position. As explained in Sec. 2.5 it is only possible to estimate the MP pose by solving the direct geometric model with Least Squares Method. However, the computation cost and the uncertainties can be detrimental for a real-time mass estimation method. As a consequence, in this method the errors between real and desired platform pose are supposed to be small enough along the trajectory in order to use the desired positions in the calculation of $\mathbf{W}$. In the same manner, cable elasticity was not considered for the mass estimation, but its inclusion should further improve accuracy.

2.7.2 Experimental results on ROMP

The mass estimation method was applied on ROMP with three payloads: the MP alone of mass 366 kg, the MP and a 122 kg metal plate M_1 and the MP and a 249 kg metal plate M_2. The total payload reaches 488 kg for the set MP+M_1 and 615 kg for MP+M_2. The mass variation is significant, namely +33% and +68% with respect to the MP mass, respectively.

This section also analyzes the effect of the pulleys geometric parameters onto the payload estimation as well as the comparison between force sensors and motor currents for cable tension and payload estimation. In what remains, Model I stands for the inverse geometric model neglecting the pulleys presented in Sec. 2.1.1 and Model II stands for the inverse geometric model considering the pulleys presented in Sec. 2.1.3.

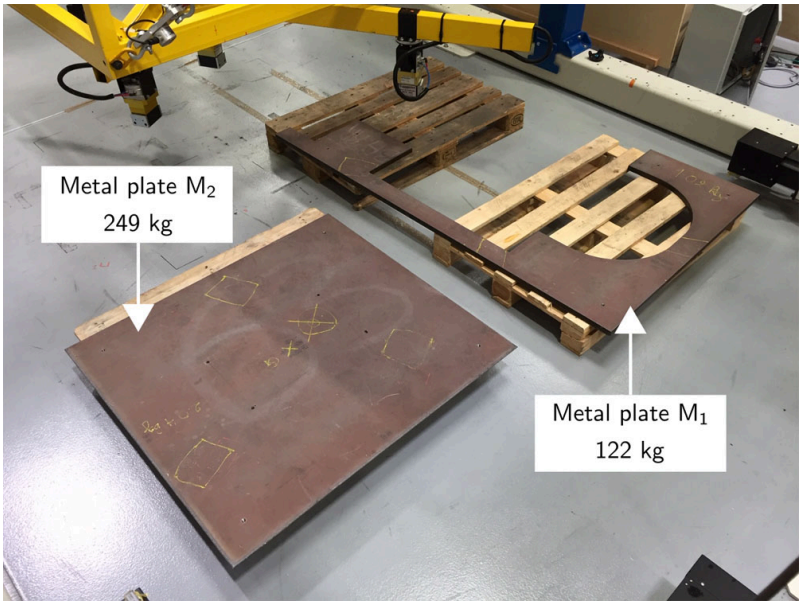

Figure 2.8: Metal plates M_1 (122 kg) and M_2 (249 kg).

Pulley effect onto payload estimation

The study of the effect of the pulleys geometry inclusion in the modeling onto the payload estimation is realized along the test trajectory described in Sec. 1.4.1 using the cable tensions measurements from the force sensors. Since the objective is to establish a method that is compatible with real-time computation, the wrench matrix of the platform is computed using the desired poses of the platform. If the processor can solve the direct geometric model fast enough or if external sensors are available the mass estimation from the estimated position will be further improved.

Figure 2.9 presents the estimated mass of the payload along the trajectory for the three different payloads with both the basic model, Model I, and the model including the geometry of the pulleys, Model II. It is noteworthy that the payload mass estimation is better with the model including the geometry of the pulleys than

with the model which does not consider the pulleys. The changes in the estimation can be explained by the new wrench matrix and computed cable angles from the MP to the exit points on the pulleys. This leads to higher and more stable values for the mass estimations along the trajectory. As shown in Tab. 2.1 and Fig. 2.10, the average mass estimation error drops from 4.5% to around 1% when considering the pulleys and the standard deviation is reduced by more than 20%. As a consequence, the consideration of the pulleys in the modeling is beneficial to the mass estimation. It should still be noted that even when neglecting the pulleys geometry, the average mass estimation error is still good, which motivates the use of the mass estimation in a control strategy. The variations in the estimation from $t = 0$ s to $t = 5$ s, $t = 25$ s to $t = 35$ s and $t = 55$ s to $t = 60$ s are due to the acceleration of the MP in the upward and downward phases and to vibrations which caused cable tensions fluctuations. The consideration of the desired platform acceleration in these phases could help in reducing these unwanted variations.

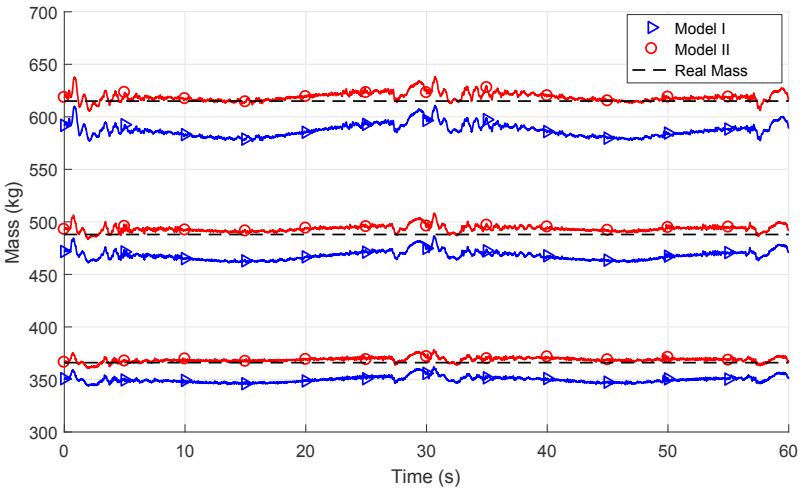

Figure 2.9: Estimated mass (kg) with the two models defined in Sec. III.A and III.B and for the three payloads along the test trajectory; the cable tensions are measured with force sensors.

The position of the center of mass along the x-axis and the y-axis of the MP frame $\mathscr{F}_p$ have been calculated with Models I and II and are illustrated in Fig. 2.11 for the heaviest payload, i.e., with mass M_2. An offset of the estimated total center of mass is noticeable in Fig. 2.12, especially along the y-axis of the platform reference frame. The estimated center of gravity position is estimated around 9 cm along $\mathbf{x}_p$ and only 1 cm along $\mathbf{y}_p$. This observation is consistent with the real position of payload M_2 under the moving-platform as shown in Fig. 2.12

According to the complexity of the pulleys model, its use in the mass estimation is therefore of interest and Model II is used in the remainder.

Table 2.1: Estimated mass along the test trajectory with Models I and II.

Model	MP	MP+M_1	MP+M_2
Mean mass (kg)			
Real mass	366	488	615
Model I	349.8	468.0	587.1
Model II	368.9	493.5	619.1
Error (%)			
Model I	4.4	4.1	4.5
Model II	0.8	1.1	0.7
Standard deviation (kg)			
Model I	2.8	4.3	6.2
Model II	2.2	3.0	4.3

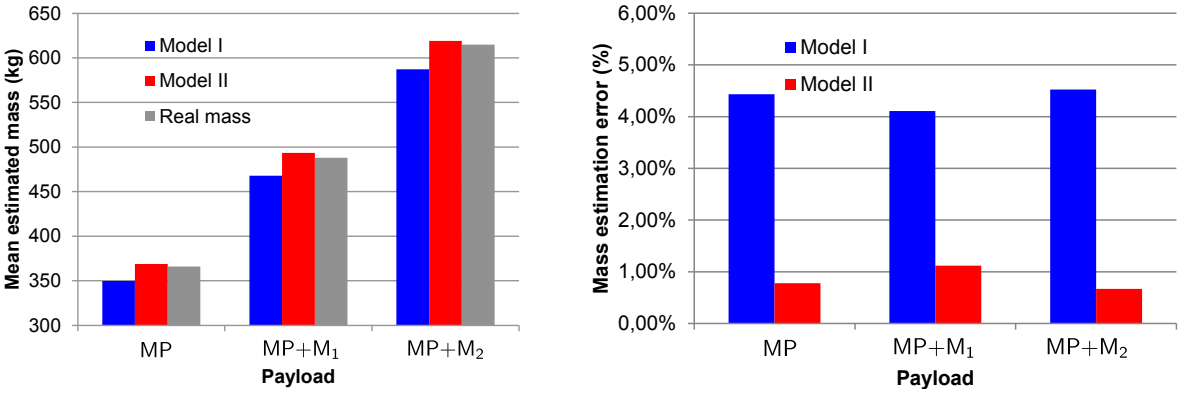

Figure 2.10: Comparison between estimated mass along ROMP test trajectory with Models I and II for the three payloads **Left.**Mean of mass estimation **Right.** Mean of mass estimation error.

(a) x_G Cartesian coordinate.

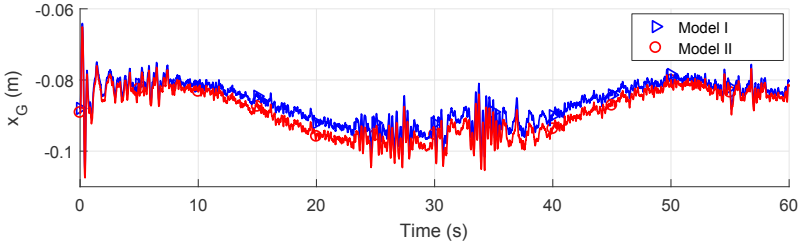

(b) y_G Cartesian coordinate.

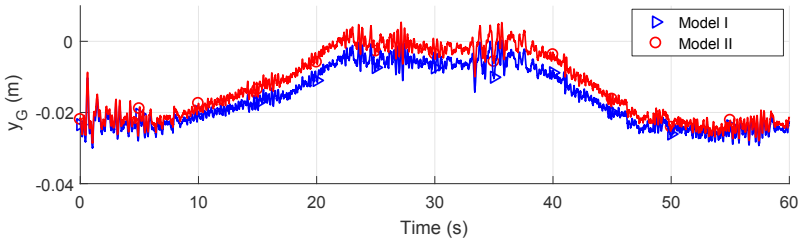

Figure 2.11: Center of mass position estimation in frame $\mathcal{F}_p$ for the heaviest payload MP+M_2 (615 kg) along the test trajectory with Models I and II **(Top).** along x-axis **(Bottom).** along y-axis.

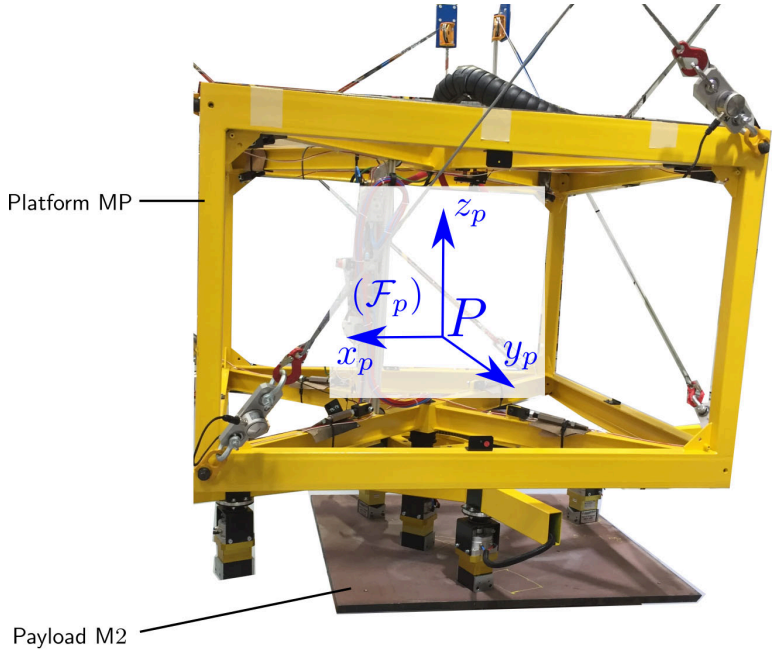

Figure 2.12: Moving platform (MP) displacing payload M_2. There is an offset between the center of mass of M_2 and axis z_p along axis x_p .

Tension estimations versus force sensor measurements

CDPRs are not all equipped with force sensors, since the integration of additional sensors might be expensive and complicated. However, it may be essential to implement a payload compensation method by estimating the cable tensions. Here, the influence of the cable tensions measurements on the payload estimation is studied. The experiments were made with the heaviest payload, i.e. MP+M_2 of 615kg, as illustrated in Fig. 2.12.

Motor torques, obtained from the motors currents, can be used to estimate the cable tensions, knowing the gearbox ratio and the drum radius. The cable tension estimations assessed from motor currents can be improved if a friction model of the motors is available, by subtracting the torque components due to friction in the gearbox and load inversion to the raw motor torque measurements. Figure 2.13 shows (i) the cable 1 tension measured by the force sensor located between the cable 1 exit point and the MP; (ii) the cable 1 tension assessed from the raw motor 1 torque, based on the motor current measurement; (iii) the cable 1 tension estimated from the raw motor 1 torque and the friction model expressed in (B.1), to reduce the perturbation caused by friction on the measure.

It first appears that the force sensor offers a measure with much less noise that the estimations from the raw motor torque. However, the estimation from the motor torque and the friction model are very close to the force sensor measurement when the velocity of the platform is almost constant, from $t = 5$ s to $t = 25$ s and $t = 35$ s to $t = 55$ s. The large discontinuities in the cable 1 tension profile obtained from the motor 1 torque are due to changes of motor 1 rotation direction. These results

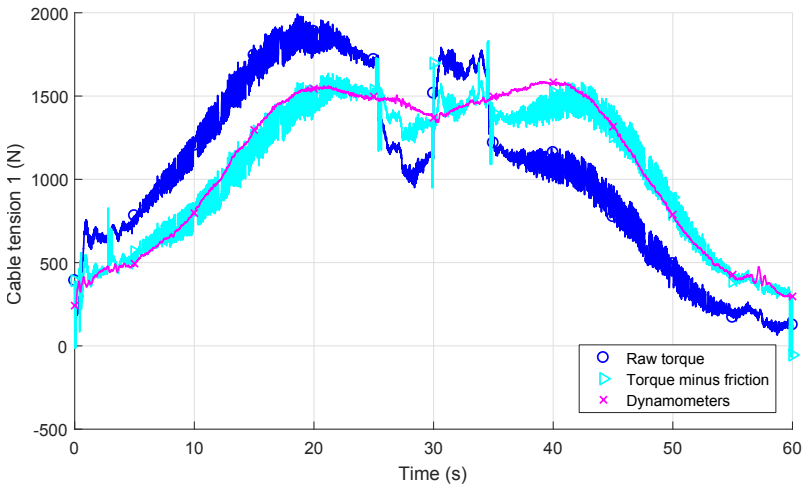

Figure 2.13: Cable tension 1 (N) with force sensors measurements, raw motor torque and torque minus frictions, for the heaviest payload MP+M_2 (615 kg) along the test trajectory.

confirm that the force sensors offer a cleaner measure of tension, but also highlight the possibility that with the proper filter and a better identification of the friction in the motors, motor torques could give a usable reading of the cable tension.

The mass estimation along the trajectory shown in Fig. 2.14 shows again that the estimation is the most accurate with the force sensor measurements. The impact of the noise in the cable tension estimation from motor torques is amplified in the mass estimation, as seen in Table 2.2. While the mean of the estimated mass error is smaller than 6% with both the raw torques and the torques minus the friction, the maximum error reaches respectively 57% and 30% of the payload mass with those measures. On the other hand the force sensors lead to a maximum error slightly above 4%. The largest errors occur along the vertical motion of the platform, in the acceleration phases and especially when the motors direction changes, for which the mass estimation error is suddenly inverted. In the central sections of the paths the mass estimation from the torques is closer to the force sensors results.

Finally, the center of mass is estimated for payload MP+M_2 and shown in Fig. 2.15. Here only the estimations from the force sensors to the motors torques minus friction are compared since it consistently offered better results than the raw torques. The same conclusions can be made than with the mass estimation as a more stable estimation was obtained from the force sensor measurements than with the torque, but with a fairly similar shape. A filter might lead to usable readings in the absence of force sensors.

Rotation of the platform

Although the pick and place trajectory does not contain orientations of the MP, the stability of the estimation was tested for rotations around the three axis, as illustrated in Fig. 2.16. Figure 2.17 presents the mass estimation while the platform,

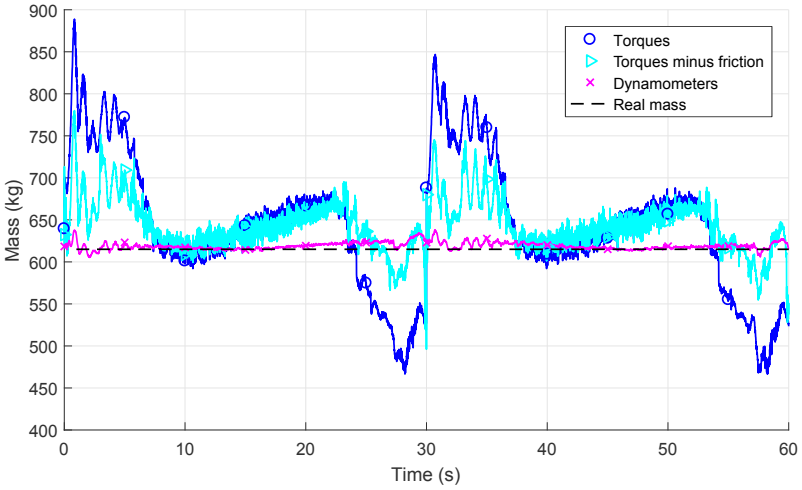

Figure 2.14: Estimated mass (kg) along the trajectory from force sensors measures, raw motor torques and motors torques minus friction model, for the heaviest payload MP+M_2 (615 kg).

Table 2.2: Estimated mass along the test trajectory with force sensor measurements and motor torques.

Measurements	**MP**	**MP+M_1**	**MP+M_2**
Real mass (kg)	366	488	615
Mean mass (kg)			
Raw torques	387.8	515.0	643.8
Torques minus friction	387.7	466.3	643.7
Force sensors	368.8	493.4	619.1
Mean error (%)			
Raw torques	5.97	5.54	4.7
Torques minus friction	5.93	5.51	4.7
Force sensors	0.8	1.1	0.7
Maximum error (%)			
Raw torques	56.58	48.1	44.5
Torques minus friction	30.1	28.1	26.8
Force sensors	3.4	4.2	3.7
Standard deviation (kg)			
Raw torques	66.5	71.9	78.5
Torques minus friction	20.2	25.1	31.3
Force sensors	2.2	3.0	4.3

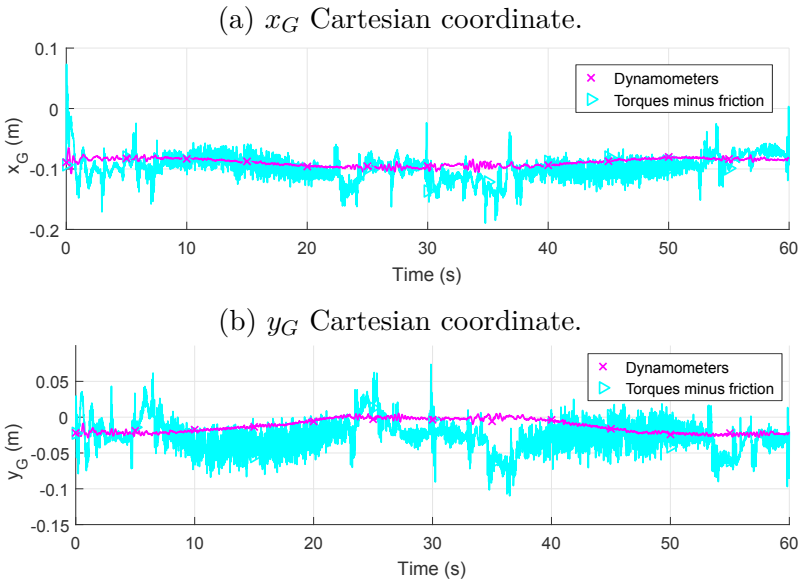

Figure 2.15: Center of mass position estimation in frame $\mathcal{F}_p$ for the heaviest payload MP+M_2 (615 kg) along the test trajectory from force sensor measurements and motor torques minus frictions **(Top).** along x-axis **(Bottom).** along y-axis.

placed in the center of the workspace, was successively rotated of 15 degrees around x, y then z. At 27 s, the platform was rotated of 10 degrees along the three axis simultaneously. Even if variations are visible at the start and end of each motion, due to vibrations in the platform and cables, it is visible that the mass estimation remained stable during these orientations, with a standard deviation of only 1.1 kg during this experiment.

Figure 2.16: MP with 15 degrees rotation about y-axis.

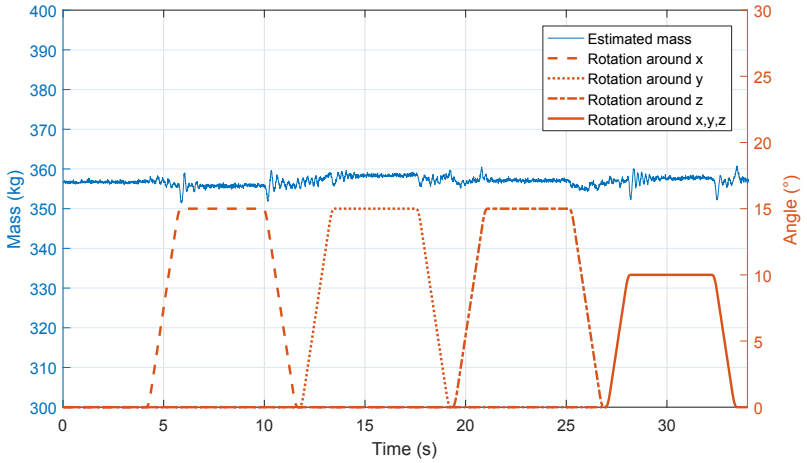

Figure 2.17: Estimated mass (kg) of MP during orientations.

Mass estimation during a drop

The control method should be robust with regard to quick payload changes during pick and place operations. Accordingly, the CDPR was loaded with the MP+M_2 and the mass M_2 was suddenly dropped during the tests. The recorded mass estimation is shown in Fig. 2.18. Oscillations can be observed as the platform vibrates once M_2 is released. This effect can be attributed to the cable elasticity, which is an ongoing subject of research [Bak+17] for the CDPR community. It can be noted that the oscillations are naturally damped in less than two seconds. It will be relevant to consider cable elasticity in future work to further improve the robustness of the proposed control method.

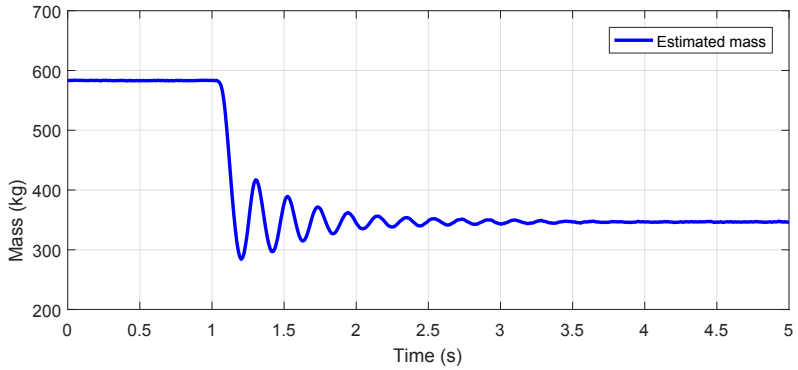

Figure 2.18: Starting with payload MP+M_2, estimated mass (kg) during a sudden drop of M_2.

2.8 Conclusion

This chapter presented the necessary CDPR modelings used in the thesis, including the inverse geometric, kinematic and dynamic models. At first, a simple modeling neglecting the pulleys geometry was considered. However, in the case of ROMP, due to the size of the pulleys this modeling can produce errors in the desired cable lengths computation of up to several centimeters, leading to unwanted platform pose errors, especially at the edges of the workspace. In order to improve the platform positioning accuracy, a second model considering the two DoF of the pulleys was implemented on the prototype, at a low additional computation cost, and compatible with a real-time implementation.

On both prototypes used in the scope of this doctorate thesis, cables appeared to be straight but elastic under the weight of the platform. From this observation, a linear cable elasticity model was considered and presented along with identified cable characteristics. One of the thesis objective is to optimize ROWC stiffness for the window cleaning application. The main disturbance along the trajectory is due to the water jet, which produces a force normal to the CDPR plane of motion, resulting in a displacement of the platform along the same direction. To this end the elasto-static model for CDPRs was described in order to evaluate this displacement based on the CDPR geometry, cable tensions and cable properties. The stiffness matrix was introduced and will be later used in the second part of the thesis to distribute the cable tensions to maximize the robot stiffness along a prescribed direction and reduces the moving-platform displacement due to water jet pressure.

Finally, for low dynamics trajectories a method to estimate the payload mass from cable tensions was presented. Thanks to force sensors located at the anchor points of the platform, a real-time reading of the platform and payload mass and center of gravity is possible. A comparison between measurement from motor torques and force sensors showed that the latter provided much cleaner readings all along the trajectory, free of the typical hysteresis in torque readings due to friction. ROMP being equipped with a force sensor at each anchor point of the platform is favorable for the application of the method, which yielded less than 5% of error in the mass estimation, further improved when using the geometric model considering the pulley geometry.

The main contributions of this chapter are the application of the mass estimation method and the corresponding sensitivity analysis on ROMP prototype. The mass estimation method will be further experimented with its real-time use in a control architecture in Part II. The improvement in the mass estimation thanks to the model including the pulleys geometry also motivates its use for the trajectory generation process. The next chapter deals with CDPR calibration, including a self-calibration method, where the geometry of the pulley is taken into account.

3. Calibration

This chapter is dedicated to the manual and automatic calibration of CDPRs. First, a brief state of the art on the calibration of CDPRs is presented in Sec. 3.1.

First, a simple approach for CDPR calibration is described step by step in Sec.3.2. The method consists in placing the moving-platform in a known reference pose, defined as the *home position* and to synchronize theoretical cable lengths and motor positions. In the home position, an hypothesis is made that all cables are straight and tensed in the calibration step.

In Sec. 3.3, a self-calibration method is experimented in simulation. An existing method uses the CDPR cable loop closure equations and a non linear least square solver to estimate the model of a six-DoF eight cables CDPR. The method only relies on the robot internal sensors, that is the motor encoders. In the scope of this thesis, the objective is to observe the impact on the calibration results of the CDPR theoretical model selected in the self-calibration. To that end, the method is written with models also taking into account the geometry of the pulleys and the cable elongation due to elasticity. As such, three geometric models are considered: *i)* model M1, neglecting both the pulleys geometry and cable elasticity ; *ii)* model M2, considering the pulleys geometry but neglecting cable elasticity *iii)* model M3, considering the pulleys geometry and the cable elasticity based on the linear model presented in Sec. 2.4. Simulated data is generated from each model, and the estimation results are compared, depending on the model used in the self-calibration.

3.1 State of the art

The calibration of parallel mechanisms was discussed in publications such as [VXM05] and [Maj+10], including processes based on internal and external sensors. However, these methods are adapted to mechanisms with rigid links and make the assumption that legs can push on the platform. With cables, the inability to push on the platform raises new constraints on the calibration problem: slack cables must be avoided and cable elongation should ideally be considered.

Two self-calibration approaches were proposed in [Bor+09a] for NIMS-PL, a deployable two DoF CDPR with four cables. First a tension based method is presented, based on the static equilibrium equation (2.4), where two cables have a constant length, a third cable tension is set and the impact on the fourth cable tension is measured. Secondly, a *jitter*-based method is used with two cables controlled in tension and their elongation is observed depending on the length of the other two cables.

The calibration of fully constrained CDPRs is discussed in [San+12; ADG13], including methods for automatic calibration based on internal sensor data, such as motor encoders, and external sensor data to measure the platform position in the Cartesian space. A laser tracker is typically used for this task.

A self-calibration method based on motor encoders and a Least Square Fitting problem was presented in [FCCG14b] and applied to a CDPR with 4 cables and 3 degrees of freedom, used as an haptic interface. Cables are considered straight, inelastic and massless, and the pulleys geometry is not considered. The resulting errors on the Cartesian coordinates of the anchor points averaged around one to two percent of the prototype dimensions. Under similar assumptions, [MPV12] introduces a method for over-constrained 6-DoF CDPRs distinguishing 6 cables as dependent, and $m-2$ cables as independent. The dependent cables lengths are used to position the platform and the independent cables lengths are used as measurement. [YZX19] generalized the method to redundant CDPRs with an arbitrary number of cables and provides an application example to a three DoF and four cables CDPR. In [SRB15], the method is applied to the case of reconfigurable CDPRs, including the pulleys geometry. A sensitivity analysis is also realized. However, cable elasticity is not considered as its consideration increases the self-calibration complexity and can lead to a local minimum. In [MP12] a method similar to the tension based approach of [Bor+09a] is presented. The least square problem is formulated around the static equilibrium from Eq. (2.4) and used force sensors to measure cables tensions in each pose. The objective function of the optimization problem is then the difference between estimated and measured cable tensions. Cable elasticity is considered based on the linear spring model and the cables stiffness coefficients are included in the parameters to optimize.

Some calibration methods are specific to the determination of the initial cable lengths while assuming the positions of the cable exit points as known, as in [Lau18] which applied the method in simulation to a suspended CDPR with the CoGiRo prototype model. More recently, [IMC19] also considered the pulleys geometry the cable length calibration for a suspended under-actuated CDPR.

External based calibration requires more sensors which are possibly costly in the case of a laser tracker for example. Camera based vision solutions increasingly being used due to the reduced cost of hardware, however their viewing distance, restrained field of view and possible visual distortion constitutes limits for very large CDPRs. For external sensors based calibration, [DS13] implemented *interval programming* [AH17] in order to propose a certified calibration of CDPRs, based on laser tracker measurements of the MP pose. [Ham+19] also uses a laser tracker in order to identify the geometric parameters of a reconfigurable three-DoF CDPR, through a procedure based on *radial basis functions*. It can be noted than while laser tracker are still widely used for their very high accuracy, methods based on more affordable external sensors have been developed. [Jin+18] introduced a calibration method based on a single one-dimensional laser distance sensor measuring the distance between the bottom of the platform and the ground. The geometry of the pulleys is considered in the model and cable elongation is assessed. [Tre+19] uses a camera embedded on the platform and a set of *markers*, or *tags*, placed randomly in the environment. A vision C++ library (*ArUco*) is used to detect and map the marks in space and subsequently locate the camera in the environment. This method proved to be more efficient than [FCCG14b], but requires a camera and the placement of markers, albeit temporarily.

3.2 Manual calibration

In this section, the calibration of ROMP is described, along with the corresponding dimensions and values. ROWC used a similar process. The objective is to place the platform in a known home position and apply a torque in each motor to straighten all cables. The cable tensions are recorded for computation of the pre-tension when considering cable elasticity in the control.

Figure 3.1 illustrates the following calibration process:

(a) two aluminum bars of square section 60×60mm and length 3.9 m are installed in the workspace. These bars will hold the MP and are each placed into two U-shape brackets on the robot frame. Each bar is supported in its center by a perpendicular vertical bar equipped with a leveling foot to compensate for ground leveling differences. This prevents the support bars from bending under the platform weight. With proper tuning of each feet elevation, the tilt of each bar at the center was measured at 0.25mm/m, which is equivalent to a 0.14° angle;

(b) the MP is placed on the support bars against three aluminum mechanical stops: one stop along the x-axis and two stops along the y-axis. The corresponding MP center home position is $\mathbf{X}_{Home} = [0; -0.120; 1.5175]^{\mathrm{T}}$ (m), obtained from the CAD model of the CDPR. The platform mass (366 kg) is sufficient to ensure that it will not move along the vertical axis z during calibration;

(c) with the MP in contact with all mechanical stops, a 1 N m torque command is applied in all motors, producing a 667 N force in each cable. This is close to, but not sufficient, to lift the MP;

(d) because of friction in the kinematic chain, actual cable tensions differ from their theoretical values. Using force sensors, cable tensions are recorded for their future consideration in the cable elasticity model, as the pre-tension. A record of cable tensions during the process raised the pre-tension values $\mathbf{t}_0 = [474; 538; 513; 483; 516; 501; 438; 522]^{\mathrm{T}}$ instead of 667 N;

(e) motor positions corresponding to the MP home position with tensed, straight cables are saved; the manual calibration is complete.

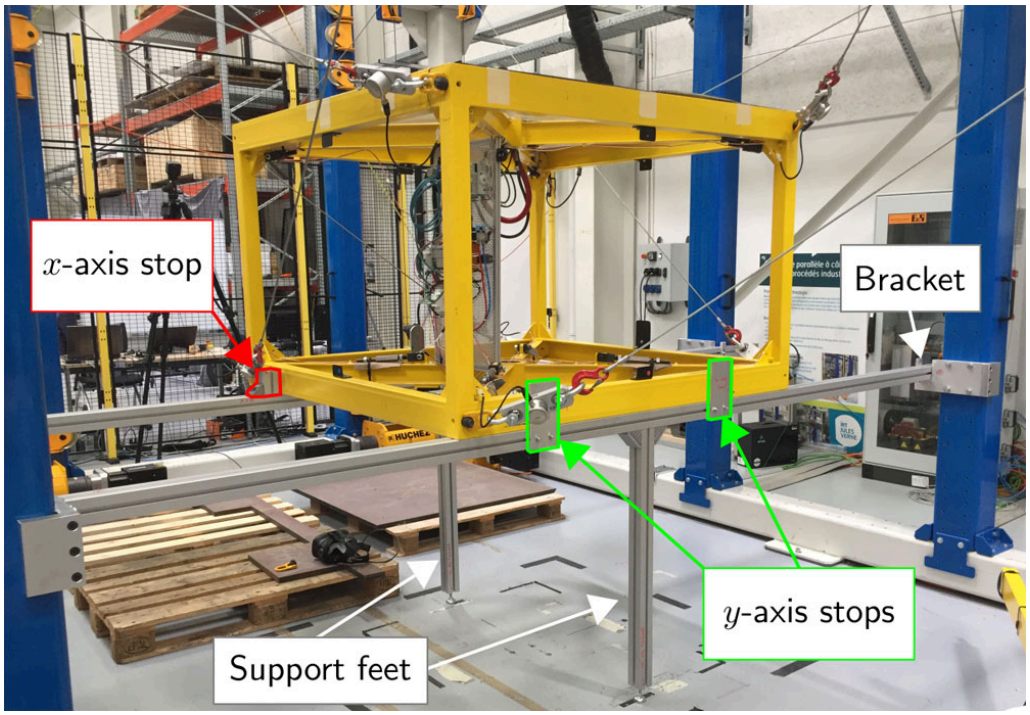

Figure 3.1: ROMP calibration support.

3.3 Self-calibration

The objective of the self-calibration is to estimate from internal sensor data the geometric parameters and the platform initial pose of a redundant 6 DoF CDPR ($m > 6$), with straight cables, as in Model I from Sec. 2.1.1. Input and outputs of the self-calibration are presented in Tab. 3.1. The inputs of the self-calibration depend on the model used, as cable tensions will only be considered with the model including

cable elasticity in the scope of this thesis. The goal is to compute the coordinates of the cable exit points A_i in the base frame $\mathscr{F}_b$ and the total cable lengths in an initial pose $L_{i,0}$, for $i = \{1, \ldots, m\}$. The only information available are the geometry of the platform, i.e. the position of the cable anchor points B_i in frame $\mathscr{F}_p$ and the internal sensor readings: the motor encoders giving an angular position q_i and the force sensors measuring the cable tensions t_i.

3.3.1 Principle

In a single position, the system does not give enough information to compute the desired parameters [FCCG14b]. However, by moving the platform in the workspace through a number of n static poses under the conditions that all cables are tensed during each measurement, a set of mn non-linear equations is formed and can be solved with a least square method.

Table 3.1: Input and outputs values .

Inputs			Outputs	
Cable anchor points	${}^p\mathbf{b}_i$		Cable exit points	${}^b\mathbf{a}_i$
Cable lengths variations	$\Delta\mathbf{l}$	$\longrightarrow$	Initial cable lengths	$\mathbf{l}_0$
Cable tensions (optional)	$\mathbf{t}_i$		MP poses	${}^b\mathbf{X}_j$

3.3.2 Problem formulation from model M1

Variables and equations

In what remains, V^* denotes the estimation of variable V through the self-calibration. In order to solve the self-calibration problem, the cable loop closure equation from Eq. (2.2) is used to compute the estimated cable length $l^*_{i,j}$:

$$l^*_{i,j} = \|{}^b\mathbf{a}^*_i - {}^b\mathbf{p}^*_j - {}^b\mathbf{R}^{*p}_p\mathbf{b_i}\|^2_2 \tag{3.1}$$

where ${}^b\mathbf{a}^*_i$ is the estimated position of the i^{th} cable exit point, ${}^b\mathbf{p}^*_j$ the estimated MP center position and ${}^b\mathbf{R}_j$ the estimated MP rotation matrix at the j^{th} pose. ${}^b\mathbf{R}^*_j$ is defined as

$${}^b\mathbf{R}^*_j = {}^b\mathbf{R}^{*b}_z\mathbf{R}^{*b}_y\mathbf{R}^*_x \tag{3.2}$$

with

$$ {}^{b}\mathbf{R}_x = \begin{bmatrix} 1 & 0 & 0 \\ 0 & \cos\left(\alpha^*_{Pj}\right) & -\sin\left(\alpha^*_{Pj}\right) \\ 0 & \sin\left(\alpha^*_{Pj}\right) & \cos\left(\alpha^*_{Pj}\right) \end{bmatrix} \quad , \quad {}^{b}\mathbf{R}_y = \begin{bmatrix} \cos\left(\beta^*_{Pj}\right) & 0 & sin(\beta^*_{Pj}) \\ 0 & 1 & 0 \\ -\sin\left(\beta^*_{Pj}\right) & 0 & cos(\beta^*_{Pj}) \end{bmatrix} \tag{3.3} $$

and

$$ {}^{b}\mathbf{R}_z = \begin{bmatrix} \cos\left(\gamma^*_{Pj}\right) & -\sin\left(\gamma^*_{Pj}\right) & 0 \\ \sin\left(\gamma^*_{Pj}\right) & \cos\left(\gamma^*_{Pj}\right) & 0 \\ 0 & 0 & 1 \end{bmatrix} \tag{3.4} $$

where α_{Pj}, β_{Pj} and γ_{Pj} are the rotation angles of the MP around axis x_b, y_b and z_b, respectively, at the j^{th} pose.

On the other hand, at each pose, the i^{th} real cable length equals:

$$ l_{i,j} = L_{i,0} + \Delta l_{i,j} \tag{3.5} $$

The calibration will be successful if the estimated and real cable lengths $\tilde{l}_{i,j}$ and $l_{i,j}$ are equal. From Eq. (3.5) and Eq. (3.1), the components of the objective function $f_{i,j}$ are:

$$ \begin{aligned} f_{i,j} &= l^*_{i,j} - l_{i,j} && (3.6) \\ &= \|{}^{b}\mathbf{a}^*_i - {}^{b}\mathbf{p}^* - {}^{b}\mathbf{R}^{*p}_{p}\mathbf{b_i}\|^2_2 - (L_{i,0} + \Delta l_{i,j}) && (3.7) \end{aligned} $$

so that

$$ f_{i,j} = 0 \qquad \text{if} \qquad l^*_{i,j} - l_{i,j} = 0 \tag{3.8} $$

This defines a set of equations that can then be solved by a *Non Linear Least Square* (*NLLS*) method. Let $\mathbf{x}$ be the vector containing the $4m + 6n - 6$ variables of the self-calibration, the solution to the problem is the vector $\mathbf{x}^* = [{}^{b}\mathbf{a}^*_1, \ldots, {}^{b}\mathbf{a}^*_1, \mathbf{l}^*_0, {}^{b}\mathbf{X}^*_m, \ldots, {}^{b}\mathbf{X}^*_n]$, which minimizes the optimization criterion:

$$ \min_{\mathbf{x}^*} \|\mathbf{F}(\mathbf{x})\|^2_2 = \min_{\mathbf{x}^*} \sum_{i=1}^{m} \sum_{j=1}^{n} (f_{i,j})^2 \tag{3.9} $$

with

$$\text{with} \quad \mathbf{F}(\mathbf{x}) = \begin{bmatrix} \mathbf{F_1}(\mathbf{x}) \\ \vdots \\ \mathbf{F_j}(\mathbf{x}) \\ \vdots \\ \mathbf{F_n}(\mathbf{x}) \end{bmatrix} \quad \text{and} \quad \mathbf{F_j}(\mathbf{x}) = [f_{i,1}(\mathbf{x}) \dots f_{i,j}(\mathbf{x}) \dots f_{i,m}(\mathbf{x})] \tag{3.10}$$

MATLAB Optimization Toolbox provides the *lsqnonlin* function to solve NLLS problems. The user can choose between two nonlinear least-squares algorithms in *lsqnonlin*: Levenberg-Marquardt and a trust-region-reflective method based on the interior-reflective Newton method [1]. The trust-region-reflective method accepts boundaries to the solution variables, which can be useful to restrain the set of possible solutions.

The unknown parameters to determine with the self-calibration are the $3m$ coordinates of the cable exit points on the pulleys A_i, the m initial cable lengths $l_{0,i}$ at the start of the calibration process and the $6n$ position and orientation components ${}^b\mathbf{X}_j$, with $i = \{1, \dots, m\}$ and $j = \{1, \dots, n\}$, in the base frame $\mathscr{F}_b$. This raises a total of $4m + 6n$ variables. The full expression of these parameters are detailed in Tab. 3.2.

Table 3.2: Unknown parameters in the self-calibration method.

Unknown parameters	Expression	Number of variables
Initial cable lengths	$\mathbf{l}_0 = [l_{1,0}, \dots, l_{m,0}]^{\mathrm{T}}$	m
Cable exit points	${}^b\mathbf{a}_i = \left[{}^bA_{i,x}, {}^bA_{i,y}, {}^bA_{i,z}\right]^{\mathrm{T}}$	$3m$
MP poses	${}^b\mathbf{X}_j = [p_{x,j}, p_{y,j}, p_{z,j}, \alpha_{P,j}, \beta_{P,j}, \gamma_{P,j}]^{\mathrm{T}}$	$6n$

However, in order to avoid an infinite number of solutions for a three dimensional CDPR, six cable exit points coordinates must be imposed so the problem is constrained in space. This is necessary to constitute a reference frame in which the Cartesian coordinates of the other points are expressed. As a result, three coordinates of one pulley, two coordinates of a second pulley and one coordinate of a third pulley are set, removing 6 variables from the problem. Then $4m + 6n - 6$ parameters must then be identified. In the case of ROMP, the chosen coordinates are $\{A_{x,2}, A_{y,2}, A_{z,2}, A_{x,3}, , A_{z,3}, A_{z,4}\}$, due to their symmetry and position in space as they define a set of orthogonal axis.

The known geometric parameters are the Cartesian coordinates of the cable anchor points B_i in the frame $\mathscr{F}_P$ and, assuming straight and inelastic cables, the

[1] MATLAB lsqnonlin online page: https://fr.mathworks.com/help/optim/ug/lsqnonlin.html

relative cable length difference $\Delta\mathbf{l}_{i,j}$ between the initial and, j^{th} MP pose, assessed from the corresponding motor positions:

$$\Delta\mathbf{l}_{i,j} = r_w \Delta\mathbf{q}_{i,j} \tag{3.11}$$

with $\Delta\mathbf{l}_{i,j}$ the i^{th} relative cable length in the j^{th} pose ${}^b\mathbf{X}_j$, r_w the winches radius and $\Delta\mathbf{q}_{i,j}$ the motor angular position in radian. These parameters are presented in Tab. 3.3

Table 3.3: Known parameters in the self calibration method.

Known parameters	Expression	Number of variables
Cable lengths variations	$\Delta\mathbf{l}_i = [\Delta l_{1,i}, \ldots, \Delta l_{m,i}]^{\mathrm{T}}$	mn
Cable anchor points	${}^p\mathbf{b}_i = [{}^p b_{i,x}, {}^p b_{i,y}, {}^p b_{i,z}]^{\mathrm{T}}$	$3m$

Resolution

The self-calibration problem consists in $4m + 6n$ variables minus 6 variables corresponding to the 6 fixed coordinates. On the other hand, for n MP poses, mn equations are provided by Eq. (3.8). In order to find a solution to the problem, n must satisfy the following inequality:

$$mn \geqslant 4m + 6n - 6 \tag{3.12}$$
$$mn - 6n \geqslant 4m - 6 \tag{3.13}$$
$$n \geqslant \frac{4m - 6}{m - 6} \tag{3.14}$$
$$\tag{3.15}$$

It means that for $m = 8$ cables, 13 poses are necessary for self-calibration.

3.3.3 Problem formulation from model M2

If the pulleys are considered in the modeling as in model M2 from Sec. 2.1.3, the total cable lengths from point A_i to B_i becomes:

$$l_{M2,i,j} = l_{c,i,j} + l_{p,i,j} \qquad \text{with} \qquad l_{p,i,j} = r_p(\pi - \alpha_{i,j}) \tag{3.16}$$

where $\alpha_{i,j}$ is the angle of the i^{th} pulley in the j^{th} MP pose, and r_p the pulley radius. $l_{c,i,j}$ is the straight cable section from B_i to the moving cable exit point on the pulley

A'_i as introduced in Sec. 2.1.3 and $l_{p,i,j}$ the cable length in contact of the pulley.

$$\min_{\mathbf{x}^*} \sum_{i=1}^{m} \sum_{j=1}^{n} (f_{M2,i,j})^2 \qquad \text{with} \qquad f_{M2,i,j} = l_{II,i,j} - (L_{i,0} + \Delta l_{i,j}) \tag{3.17}$$

In this case $L_{i,0}$ now also contains the cable length going around the pulley.

3.3.4 Problem formulation from model M3

In order to further improve the model, the cable elasticity is considered using the linear model introduced in Sec. 2.4.

$$l_{M3,i,j} = l_{M2,i,j} + r_{i,j} \tag{3.18}$$

with $r_{i,j}$ the cable elongation due to elasticity, defined by:

$$r_{i,j} = \frac{(l_{M2,i,j} + L_{WA,i})(t_{i,j} - t_{0,i})}{ES} \tag{3.19}$$

where $t_{i,j}$ is the cable measured tension, $t_{0,i}$ the cable pre-tension if considered, E the cable Young modulus and S the cable cross-sectional area. The cable length $L_{WA,i}$ is the constant cable length going from the cable exit point on the i^{th} winch to the point A_i. This length must also be taken into account to compute the total cable elongation. The coiled cable length around the winch and its possible elongation are however neglected here.

$$\min_{\mathbf{x}^*} \sum_{i=1}^{m} \sum_{j=1}^{n} (f_{M3,i,j})^2 \qquad \text{with} \qquad f_{M3,i,j} = l_{M3,i,j} - (L_{i,0} + \Delta l_{i,j}) \tag{3.20}$$

$L_{i,0}$ contains the total cable length from A_i to B_i in the initial position, including the cable length coiled onto the pulley and the elongation due to elasticity.

3.3.5 Simulation results

Setup

In order to test the self-calibration method and its three models, cable length differences and cable tensions must be simulated for each pose. The ROMP prototype model is used in this study. The nominal positions of cable exit points A_i, extracted from the CAD model of the robot, are given in Tab. 3.4. These values are used to generate the inputs of the method, and represent the real robot model. Then, an initial approximation of this model is defined as $\mathbf{A_{approx}}$ as a starting point for the optimization problem. This model simulates current approximate knowledge of the

	X (m)	Y (m)	Z (m)
A_1	1.659	-2.850	3.221
A_2	1.350	-3.159	3.221
A_3	-1.350	-3.159	3.221
A_4	-1.659	-2.850	3.221
A_5	-1.659	2.850	3.221
A_6	-1.350	3.159	3.221
A_7	1.350	3.159	3.221
A_8	1.659	2.850	3.221

	X (m)	Y (m)	Z (m)
$A_{0,1}$	1.8	-2.7	3.1
$A_{0,2}$	1.3	-3	3.1
$A_{0,3}$	-1.3	-3	3.1
$A_{0,4}$	-1.8	-2.7	3.1
$A_{0,5}$	-1.8	2.7	3.1
$A_{0,6}$	-1.3	3	3.1
$A_{0,7}$	1.3	3	3.1
$A_{0,8}$	1.8	2.7	3.1

Table 3.4: Perfect matrix of cable exit points $\mathbf{A}$ from ROMP CAD model and approximated matrix $\mathbf{A}_0$ used as a starting point in the optimization problem.

robot model. The values have been chosen to introduce significant errors of up to 159 mm compared to the nominal model $\mathbf{A}$. The values of $\mathbf{A_{approx}}$ are also provided in Tab. 3.4.

The initial solution $\mathbf{x}_0$ of size $4m + 6n - 6$ provided to the optimization problem is presented in Tab. 3.5. The platform pose estimations $\mathbf{X}_0$ are provided to the algorithm. In reality, these estimations can come from either a rough first calibration and the theoretical position of the platform in this first model, or from external sensors if available. In order to generate approximations of the platform poses in simulation, errors of up to 200 mm where introduced to the poses computed from the perfect model.

Table 3.5: Components of solution vector $\mathbf{X}$.

Initial solution index	Components
$x_0(1 : m-1)$	$\begin{bmatrix} A_{0,x,1} & A_{0,x,3} & A_{0,x,4} & A_{0,x,5} & A_{0,x,6} & A_{0,x,7} & A_{0,x,8} \end{bmatrix}$
$x_0(m : 2m-3)$	$\begin{bmatrix} A_{0,y,1} & A_{0,y,4} & A_{0,y,5} & A_{0,y,6} & A_{0,y,7} & A_{0,y,8} \end{bmatrix}$
$x_0(2m-2 : 3m-6)$	$\begin{bmatrix} A_{0,x,1} & A_{0,x,5} & A_{0,x,6} & A_{0,x,7} & A_{0,x,8} \end{bmatrix}$
$x_0(3m-5 : 3m-6+6n)$	$\mathbf{X_0} = \begin{bmatrix} p_{0,x,j} & p_{0,y,j} & p_{0,z,j} & \alpha_{0,P,j} & \beta_{0,P,j} & \gamma_{0,P,j} \end{bmatrix}$
$x_0(3m-5+6n : 4m-6+6n)$	$\mathbf{l}_0 = \begin{bmatrix} 4 & 4 & 4 & 4 & 4 & 4 & 4 & 4 \end{bmatrix}$

In order to compare the self-calibration results obtained with the three models, the following procedure was applied:

(a) n random poses are generated. To keep the problem simple, the orientation of the MP is assumed to be null. In practice, this would translate to choosing random poses in which the platform is almost level, eventually using a spirit level. The positions for the MP center are listed in Tab. 3.6. A total of $n = 30$ poses were generated, as a higher number of poses provides diminishing returns in accuracy [FCCG14b].

(b) For each pose, the cable lengths with model M1, M2 and M3 are generated.

(c) The static equilibrium is used to simulate cable tensions $t_{i,j}$ at pose $\mathbf{X}_{i,j}$ using the wrench matrix including the pulleys geometry $\mathbf{W}_{II}$.

Index	$\mathbf{X}_x$	$\mathbf{X}_y$	$\mathbf{X}_z$	Index	$\mathbf{X}_x$	$\mathbf{X}_y$	$\mathbf{X}_z$
1	0.500	0.500	0.500	16	-0.945	1.157	0.951
2	-0.166	1.513	1.761	17	0.341	-1.587	2.153
3	0.441	-1.607	1.960	18	-0.165	-0.208	1.416
4	-1.000	-0.316	0.884	19	0.117	1.634	0.998
5	-0.395	1.832	1.445	20	-0.719	-0.826	2.370
6	-0.706	0.133	1.950	21	-0.604	-0.849	1.326
7	-0.815	0.768	1.446	22	0.601	-1.480	2.051
8	-0.627	-0.738	0.790	23	0.937	-1.923	2.007
9	-0.309	0.746	1.665	24	-0.373	0.715	2.290
10	-0.206	1.339	1.895	25	0.385	-1.153	1.823
11	0.078	-1.927	1.627	26	0.753	-0.938	2.052
12	-0.162	1.001	2.400	27	0.789	-0.034	1.328
13	0.370	1.955	1.756	28	-0.830	-1.787	1.186
14	-0.591	0.993	2.326	29	-0.922	0.296	2.313
15	0.756	-0.878	0.947	30	-0.660	-1.413	1.471

Table 3.6: Randomly generated platform positions.

(d) The cable tensions $t_{i,j}$ are used in Eq. (3.19) to compute the total cable length including cable elongation due to elasticity for the resolution by model M3

(e) For each model, the corresponding $\Delta l_{i,j}$ which will be used as the input in the self-calibration method are obtained by subtracting the first cable length to the j^{th} cable length.

In steps (d) and (e), an assumption is made that the cable tensions in the generated MP pose with inelastic cables will be close to the cable tensions at the MP pose after considering cable elasticity. This simplification does not hold for large cable elongations, which would produce significant difference between theoretical cable tensions in poses $\mathbf{X}_{\text{inelastic}}$ and $\mathbf{X}_{\text{elastic}}$. If cable elasticity is high, the relation between cable tensions and generated position cannot be approximated using the wrench matrix $\mathbf{W}_{II}$ (Eq. 2.13). In this case, the elasto-static model could be used to compute the MP position displacement due to gravity while considering elasticity, from which more accurate cable tensions could be evaluated.

In order to study the self-calibration accuracy, differences between perfect and estimated parameters are defined as

$$\mathbf{D}_{A,i} = \mathbf{a}_i - \mathbf{a}_i^*, \quad \mathbf{D}_{l,i} = l_{0,i} - l_{0,i}^* \quad \text{and} \quad \mathbf{D}_{X,i,j} = \mathbf{X}_{i,j} - \mathbf{X}_{i,j}^* \tag{3.21}$$

$\mathbf{D}_{A,i}$ being the difference between perfect and estimated cable exit points, $\mathbf{D}_{l,i}$ between perfect and estimated initial cable lengths and $\mathbf{D}_{X,i,j}$ between perfect and estimated MP poses.

The difference between the perfect model used in the generation and the initial guess provided to the algorithm are shown in Fig. 3.2. The difference between the

two models for the fixed coordinates of cable exit points 2, 3 and 4 as these points were fixed in order to create a reference frame aligned with the base frame $\mathscr{F}_b$ of the CDPR for convenience. Alternatively, these coordinates could have been set to a zero, as in [FCCG14b], with the origin of the reference frame being set as the position of the exit point whose three coordinates are null.

The platform position errors introduced in the initial solution are also visible in the same figure, with a maximum error just above 200 mm for the y axis coordinate of pose number 25.

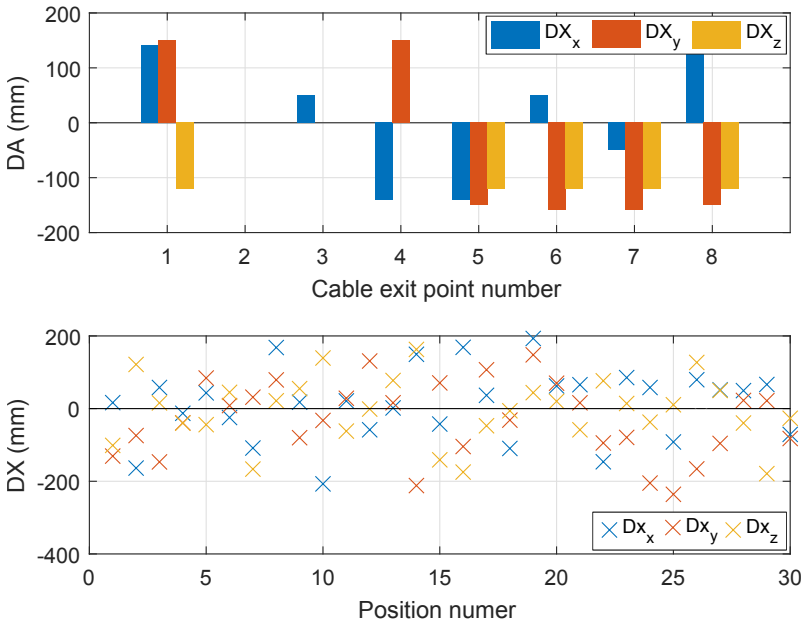

Figure 3.2: Errors introduced between perfect model and initial solution. $\mathbf{D}_A$ is the coordinate difference between $\mathbf{A}$ and $\mathbf{A}_0$, and $\mathbf{D}_X$ the pose difference between $\mathbf{X}$ and $\mathbf{X}_0$.

Simulated data from basic model M1

The above problem is solved using MATLAB *lsqnonlin* function with the Levenberg-Marquardt algorithm. As discussed earlier, an initial solution must be provided, however boundaries on the solution cannot be defined with this algorithm. As a consequence, the solutions are not bounded in space and the convergence is only due to the algorithm.

This first case considered is the self-calibration of a CDPR with massless, inelastic and straight cables with negligible pulleys. This case is similar to the prototype studied in [FCCG14b], although orientations of the platform are considered here.

Cable lengths are computed from model M1 and the self-calibration is applied based on the same model M1. Ideally, the method should be able to compute exactly the positions of the pulleys. However, the starting point $\mathbf{x}_0$ introduces errors in the model of the robot and in the initial cable lengths.

Figure 3.3 presents an overview of the generation poses in the space. The perfect

cable exit points A_i are represented as magenta asterisks, while the solution A_i^* as blue circles. The difference between $\mathbf{A}$ and $\mathbf{A}_{M1}^*$ are shown in Fig. 3.4a.

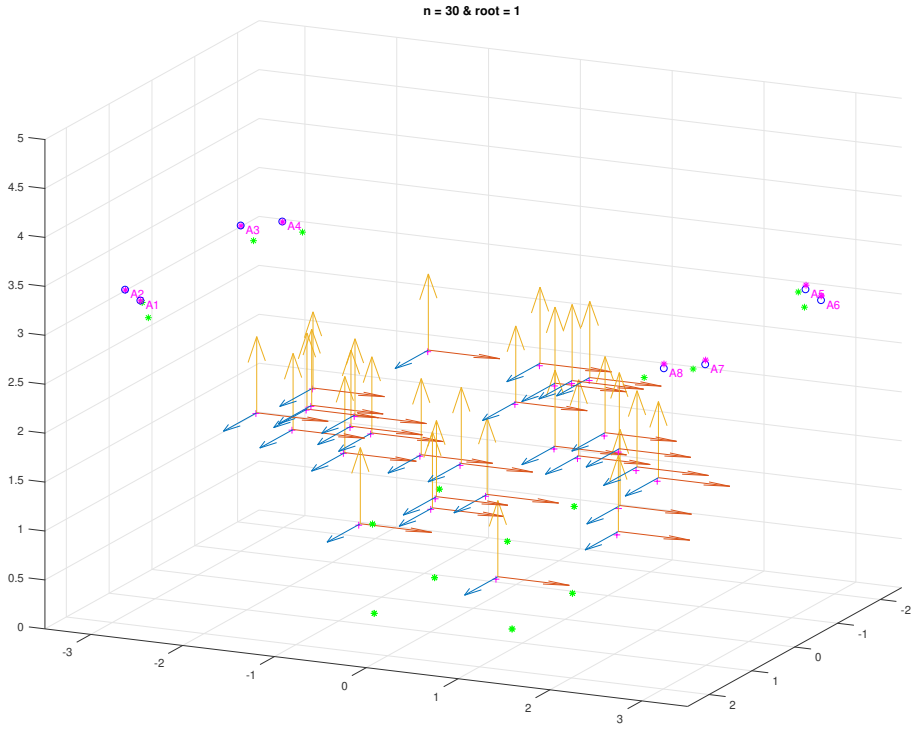

Figure 3.3: 3D view of of the 30 platform center poses represented by the frames, perfect A_i points as magenta asterisks and solution A_i^* as blue circles.

The maximum difference between $\mathbf{A}$ and $\mathbf{A}_{M1}$ reaches around 45 mm when applying the self-calibration. It can be observed that this error is achieved along the z axis, and only affects the last 4 points. Regarding the poses estimation, in this example the differences in pose estimation are almost null along the x axis, with an average error of around 2 mm. The largest difference in the estimation is found along the vertical axis z with a maximum error of 40 mm.

The initial cable length estimation is provided in Fig. 3.4b. Cable lengths are accurately estimated with this method, the difference between perfect model used in generation and solution obtained from the self-calibration being less than 10^{-7} mm.

Overall, the algorithms significantly improved the model estimation. Most of the cable exit points coordinates have been identified with an error lower than 5 mm. However, some errors remains on the z coordinates of cable exit points 5 to 8, possibly due to local minima.

These results were expected since the same model was used for the generation of the input data and as the base of the self-calibration method. This method should be applicable on a CDPR with negligible pulley diameters as in [FCCG14b], by ensuring that at each recorded position, cables can be considered as straight, inelastic and massless. However, these assumptions might not always be true and could impact the calibration results.

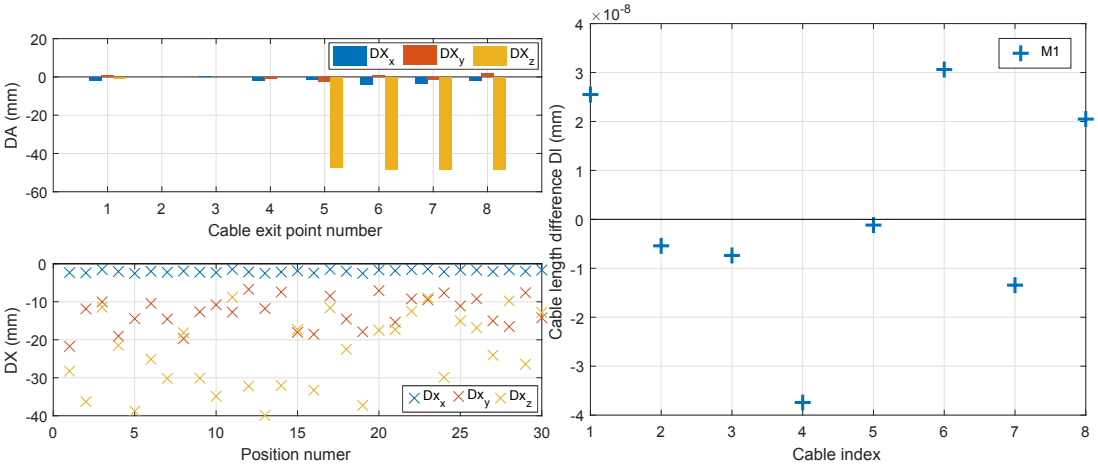

(a) $\mathbf{D}_A$ and $\mathbf{D}_X$ from model M1. (b) $\mathbf{D}_L$ from model M1.

Figure 3.4: $\mathbf{D}_A$, $\mathbf{D}_X$ and $\mathbf{D}_L$ obtained with self-calibration based on model M1, from input generated from model M1.

Simulated data from model including pulleys M2

In reality, on a CDPR with non-negligible pulleys, the cable lengths coiled onto the pulleys will have an impact on the total cable lengths at each pose, and consequently on the measured cable lengths variations. The objective of this second scenario is to evaluate the impact of the pulleys geometry consideration in the modeling on the self-calibration results. This time, the cable length variations $\Delta\mathbf{l}_{M2}$ provided as input to the algorithm are based on the cable length expression from Eq. (3.16). The self-calibration is then applied with either model M1, neglecting the pulleys, or model M2, which considers their geometry, and the results obtained are analyzed.

Figure 3.5a presents the cable exit point difference $\mathbf{D}_A$ obtained from model M1. It is apparent that the self-calibration led to large errors of up to 900 mm when solving for model M1. On the other hand, model M2 (Fig. 3.5b) provides a solution with a maximum difference of only 14 mm compared to the reference model used in the generation.

Criteria of the last iteration of the *lsqnonlin* solver using Levenberg-Marquardt are provided in Tab. 3.7. In the case of model M1, the algorithm reached the calculation limit with a residual of 1.52×10^{-5} m versus 7.89×10^{-27} m with model M2.

Model	Iter.	Fun. count	Residual (m)	F-O optimality (m)	Lambda	Norm of step (m)
M1	198	41290	1.52×10^{-05}	3.46×10^{-05}	1×10^{-06}	2.72×10^{-2}
M2	12	2692	7.90×10^{-27}	1.56×10^{-13}	1×10^{-12}	7.20×10^{-07}

Table 3.7: Output of *lsqnonlin* with models M1 and M2.

When providing $\Delta\mathbf{l}_{M2}$ as an input to the self calibration, model M1 leads to large errors in both the geometric model reconstruction and the platform poses estimations,

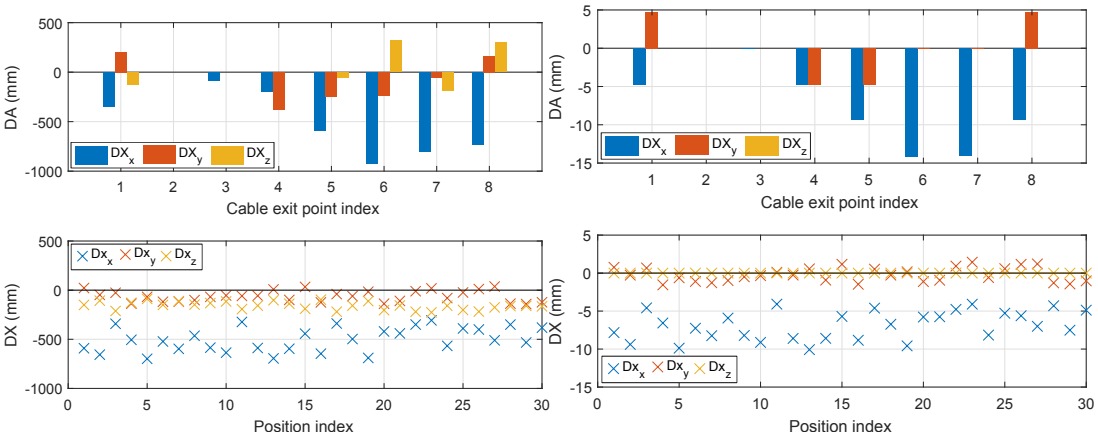

(a) $\mathbf{D}_A$ and $\mathbf{D}_X$ from model M1. (b) $\mathbf{D}_A$ and $\mathbf{D}_X$ from model M2.

Figure 3.5: $\mathbf{D}_A$ and $\mathbf{D}_X$ obtained with self-calibration based on models M1 and M2, from input generated with model M2.

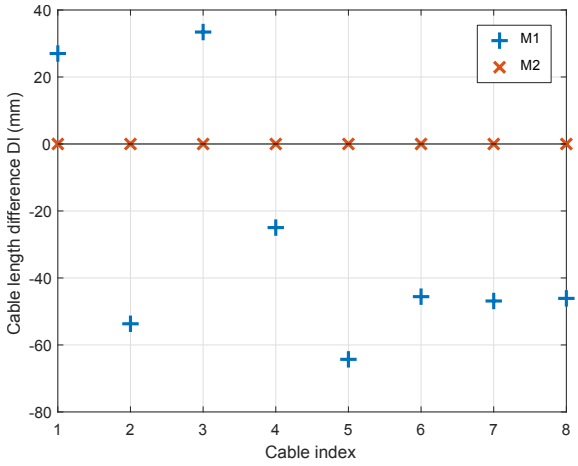

Figure 3.6: $\mathbf{D}_L$ obtained with self-calibration based on models M1 and M2, from input generated with model M2.

while model M2 shows a maximum of 14 mm in the difference between perfect and estimated cable exit point coordinates $\mathbf{D}_A$.

The initial cable lengths are also better estimated with model M2, but model M1 still provides good results. The largest difference between the cable lengths generated using models M1 and M2, denoted as $\Delta\mathbf{l}_{M1}$ and $\Delta\mathbf{l}_{M2}$ respectively, is equal to 63 mm. The average mean difference, mean$(\Delta\mathbf{l}_{M1} - \Delta\mathbf{l}_{M2})$, is equal to 26 mm which represents only 0.65% of an average cable length, evaluated at 4.02 m from the considered set of platform poses. As a consequence, the difference between the cable lengths variations $\Delta\mathbf{l}_{M1}$ and $\Delta\mathbf{l}_{M2}$ seems to have a large impact on the results of the self-calibration, even though they appear to be small relatively to the total cable lengths.

Predictably, model M2 appears significantly more adapted than model M1 for the self-calibration based on the data generated with model M2, of a CDPR with non-negligible pulleys. It can be noted that the model used in the self-calibration has a large impact on the positions of the cable anchor points, while the initial cable lengths estimations were still close with both models. Thus some parameters seem to have a better identifiability than others.

If the method is to be applied to a CDPR with non-negligible pulleys and very low cable elasticity, model M2 should provide a better estimation of the model. On the other hand, it seems that the use of the self-calibration based on the simple model M1 could quickly lead to large estimation errors of the cable anchor points. In order to avoid cable elongation during the calibration in the case of ROMP and respect the assumptions made in model M2, a lightweight platform could be used to exert the least possible effort on the cable, but sagging might then be a problem if the platform is too light compared to the the cable mass.

Simulated data from model including pulleys and elasticity M3

In the case of a CDPR with a heavy platform, elasticity will have an impact on the actual position of the cable lengths corresponding to a platform pose, and on the measured cable lengths variations. For example with ROMP cable elongation can reach several centimeters with the heaviest total load (MP+M_2). In addition to the consideration of the pulleys geometry in the model, this last case also considers the cable elongation due to elasticity. From Eq. (3.19), here the hypothesis is made that the initial cable length $L_{0,M3}$ includes both the cable length coiled onto the pulley and the total cable elongation. As a result, the measured coiled or uncoiled cable length variation $\Delta\mathbf{l}_{M3}$ also includes cable elongation due to elasticity.

The simulation results presented afterwards are based on a platform mass of 1000 kg, which raises an average cable elongation r of 25.1 mm. The impact on cable length of elasticity appears to be lower than the inclusion of the pulleys in the geometry, which raised an average cable length variation of 77.9 mm.

Criteria of the last iteration of the *lsqnonlin* are presented in Tab. 3.8 with the three models. As expected, model M3 is the only model to find a solution before reaching the function count limit, with a residual of 6.26×10^{-21} m.

Model	Iter.	Fun. count	Residual (m)	F-O optimality (m)	Lambda	Norm of step (m)
M1	198	41290	1.53×10^{-05}	6.91×10^{-05}	1×10^{-07}	2.65×10^{-2}
M2	198	41290	4.51×10^{-06}	1.09×10^{-05}	1×10^{-06}	7.20×10^{-3}
M3	11	2484	6.26×10^{-21}	2.66×10^{-10}	1×10^{-13}	2.25×10^{-05}

Table 3.8: Output criteria of *lsqnonlin* with models M1, M2 and M3.

Figure 3.7 presents the values differences to the perfect model, from the solution obtained with models M1, M2 and M3. From Figs. 3.7a to 3.7c, it is apparent that the model M3 is the best suited for the self-calibration based on $\Delta \mathbf{l}_{M3}$, as expected. Model M1 leads to the largest differences in the found solution compared to the perfect model. It can be noted that model M2 slightly improved the estimation of some cable exit points and platform poses compared to the initial solution provided to the algorithm. Moreover, the initial cable length estimation obtained from all models greatly improved over the initial cable length estimation, even in the case of model M1.

It is noteworthy that the solution present a similar shape in Fig. 3.5a, Fig.3.5b, Fig. 3.7b and Fig. 3.7d. These similarities should be further studied in future work on self-calibration, but could possibly be attributed to the formulation of the problem and the choice of the three cable exit point fixed (A_2, A_3 and A_4), which are all located on the same side of the CDPR.

Overall, it can be concluded again that the model used in both the input data generation and in the self-calibration provided the best results, as could be expected. At this point, it is recommended to use the model which is closest to the real robot modeling hypotheses in order to obtain the best results. It can however be noted that some parameters are less affected than others by the model choice in the self-calibration method, namely the initial cable lengths differences. An analysis of the parameters identifiability should be realized in the future to better understand the current difficulties of the method, and possibly focus on the parameters which can yield robust estimation.

3.4 Conclusion

This final chapter of the modeling part presented the manual calibration of the prototype and preliminary work on the extension of a self-calibration method.

The objective of the manual calibration is to put the platform in a known position

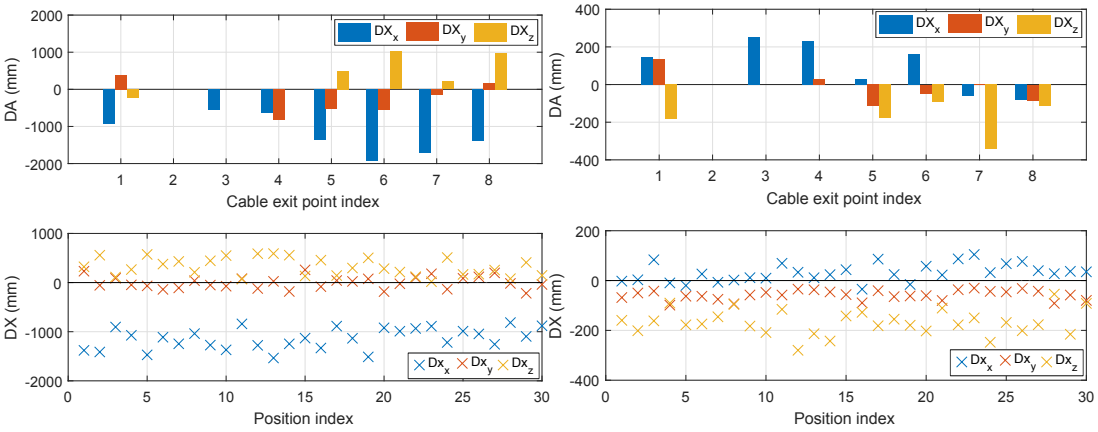

(a) $\mathbf{D}_A$ and $\mathbf{D}_X$ from model M1.

(b) $\mathbf{D}_A$ and $\mathbf{D}_X$ from model M2.

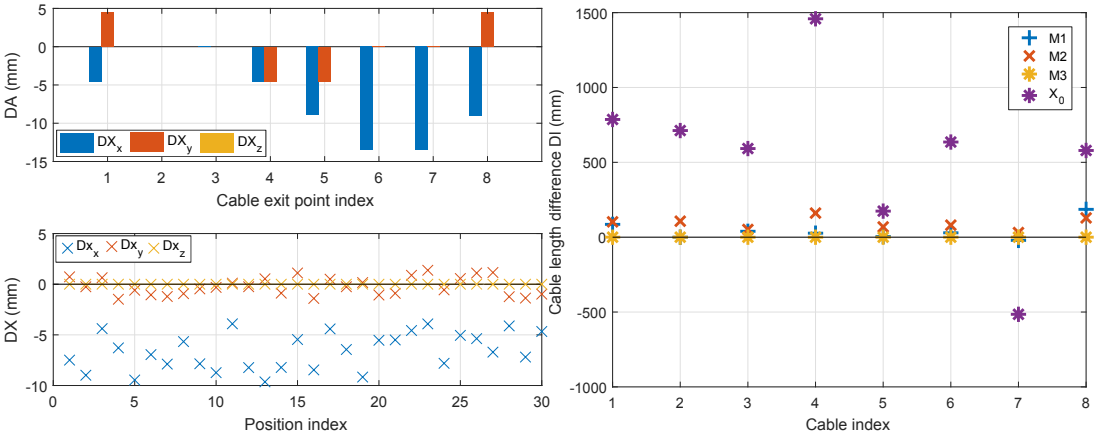

(c) $\mathbf{D}_A$ and $\mathbf{D}_X$ from model M3.

(d) $\mathbf{D}_L$ from models M1, M2, M3 and X0.

Figure 3.7: Results with generation from M3 and self-calibration based on model M1, M2 and M3.

and to ensure that all cables are tensed in order to approach the assumptions made in Chapter 2. Cable tension measurements can also be useful if a cable elasticity compensation method is to be applied, as presented in Chapter 4.

Self-calibration methods aim to automatically obtain the model of the CDPR and the initial pose of the platform from internal sensors only. An existing method based on the simplest modeling of a CDPR, where cables are considered straight and inelastic, was presented. The self-calibration consists in the resolution of a set of nonlinear equations established from the cable loop closure equations with a least square optimization method. In the scope of this thesis, an attempt is made to extend this method to CDPRs whose pulley geometry and cable elasticity are not negligible.

In this chapter, the cable lengths equations are written from the basic CDPR model (M1), the model including the pulleys geometry (M2), and with a third model including linear elastic cable model (M3). Input data is generated in simulation with each model. Then, the self-calibration method is applied based on each model as well, and the results are observed. An initial guess of the robot parameters is provided based on an approximate model with errors in the range of 20 centimeters.

From the simulation experiments it was found that, although the generated cable lengths in the input data are only slightly affected by the model used for the generation, the choice of model greatly impacts the reconstruction of some parameters, such as cable exit points. When simulating cable lengths from the basic model, M1, and applying the self-calibration based on the same M1 model, the solution greatly improved estimation of the model over the initial guess, with errors of a few millimeters to a few centimeters on the coordinates of the cable exit points. However, if the method is applied based on input data generated from a model which considers the pulleys geometry, such as M2, and is solved using the simple model M1, large errors in the self-calibration results appear. As expected, the resolution with the corresponding model M2 was much more accurate, with again an error in the range of a centimeter for the cable exit points estimations. Similarly, the generation of input data from of cable elasticity in model M3 in the generation of the cable lengths variations also leads to high errors in the solution obtained with both previous models, M1 and M2. The geometric model reconstruction obtained from M1 is clearly erroneous with differences in the range of meters for the exit points and platform poses, while model M2 provided mixed results.

On the other hand, the estimation vector of initial cable lengths was much improved over the provided initial solution with all three models. Indeed, even model M1 could be used to gain a rough estimate of the initial cable lengths, although the use of a more elaborate model is recommended.

The initial results on the self-calibration method presented in this chapter will require further study before the method is applicable to an industrial robot. In

particular, a parameter identifiability analysis should be realized to obtain a better understanding of the problem and adjust expectations depending on the parameters one desires to estimate. Finally, when cable tension sensors are available on the prototype as on ROMP, the self-calibration method would also benefit from the inclusion of the static equilibrium equation inside the optimization problem, and should be experimented in future work.

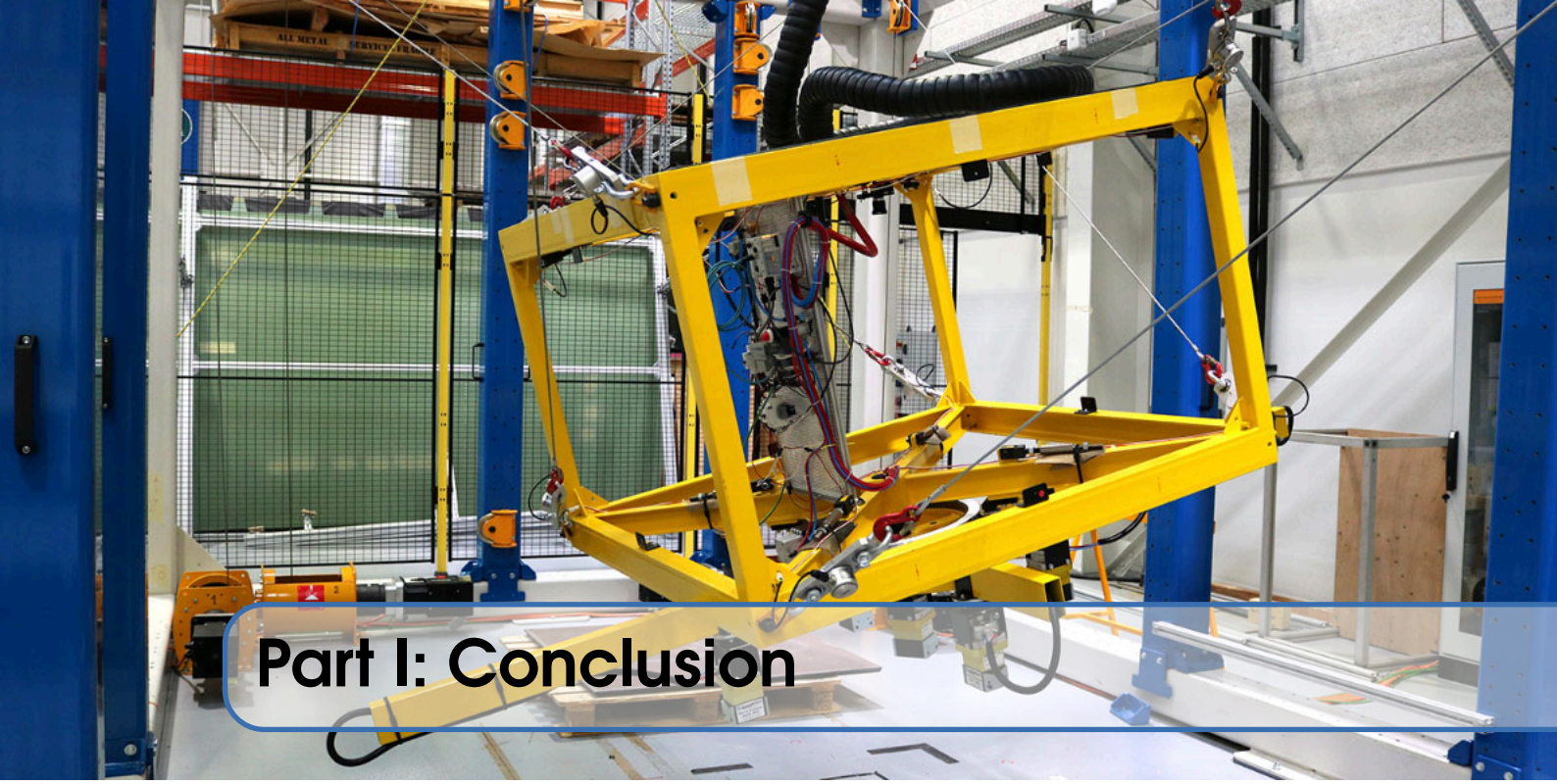

Part I: Conclusion

This part first introduced the concept of cable-driven parallel robots (CDPRs) and the context of this thesis, the modeling of CDPRs and their calibration. The modelings presented here are necessary for the study and control of CDPRs and form the necessary basis for their control, considered in the second part of this thesis.

In order to understand and control CDPRs, their modeling was addressed in Chapter 2. At first cables were considered straight, massless and inelastic and the geometry of CDPRs were reduced to the most basic elements by neglecting the pulleys geometry. However, the two DoF pulleys of ROMP have a non-negligible impact on the computation of cable lengths. As such, the modeling of CDPRs including the pulleys geometry was written. From the geometric models, the platform static equilibrium can be expressed by introducing the wrench matrix of the robot, which links the Cartesian twist of the platform to the joint velocities. This matrix is prevalent in the study and control of CDPRs and is impacted by the consideration of the new cable exit point introduced by the consideration of the pulleys.

Cables are often considered as massless and inelastic in the study of CDPRs but this hypothesis does not hold true in the case of heavy loads or CDPRs of very large dimension. While cable sagging was considered negligible on the two prototypes studied in this thesis, due to the low total cable mass compared to the platform weight, cable elasticity should be considered, especially for ROMP which is designed to lift loads of up to 1 ton. As such a linear cable elasticity model was considered, based on the identified cable properties of the two prototypes. In the case of ROMP, this model will be used in Sec. 4.2.4 to evaluate cable elongations due to cable forces and introduce a real-time compensation in the control architecture to ensure the platform positioning repeatability despite load changes. From the linear cable

elasticity model, it is also possible to write the stiffness matrix of the robot, which can be used to compute the platform small displacement under a small external wrench. This information can be leveraged in a tension distribution strategy to find the set of feasible cable tensions which improves the robot stiffness along a desired direction. The proposed control architecture for the ROWC prototype which includes this criteria to minimize the platform displacement due to the activation of the water jet is presented in Sec. 4.3.

Then from the modeling of CDPRs, calculations to obtain the mass and center of gravity of the set composed of the platform and its load were detailed along a trajectory of low dynamics. Availability of cable tensions measurements on the ROMP prototype motivated the real-time estimation of the load to update its value in a compensation term for the control law proposed in Sec. 4.2.4. The influence of the pulleys and force sensors on the payload estimation of CDPRs was analyzed. The effect of the pulleys onto the payload estimation was experimentally evaluated and it could be be noted that the consideration of the pulleys into the geometric model of the robot improves the mass and center of mass estimations of the payload, at a low computational cost. The cable tension values were found to be much more accurate when they are measured with force sensors instead of being assessed from the motor torques. A better friction model of the transmission systems and a filter are required to get a better estimation of the cable tensions from the motor currents.

Finally, Chapter 3 dealt with the calibration of CDPRs, a necessary step to initialize the system before its control. First, the manual process of calibrating the prototypes was detailed, then a self-calibration method was applied in simulation to automatically compute the position of the cable exit points and initial cable lengths of the prototype, from an unknown initial position and approximate model. Based on an existing method, a small contribution was realized in this chapter by observing the impact of the model used in the self-calibration on the results. While the initial method only used the basic modeling of CDPRs, the self-calibration was expressed while also considering the effect of pulleys geometry and cable elasticity on the cable loop closure equations. The simulation results have shown that all parameters do not have the same identifiability with this method. While the estimation of the initial cable lengths was improved with all models compared to the provided approximation, the accurate estimation of cable anchor points was greatly affected by the model used in the self-calibration. Further work is necessary before the method can be implemented in an industrial settings, but the initial results are still encouraging and should be experimented on IRT Jules Verne prototypes in the future.

The second part of this thesis will now focus on the control of CDPRs, based on the hypotheses and models introduced in Chapter 2.

II Part II: Robust Control

Part II: Introduction

The fine modeling previously introduced can be leveraged in a number of ways, by enhancing the understanding of Cable-driven parallels robots (CDPRs) inner working through simulation, but also for direct use in the control of the robot for calibration, trajectory generation or in-line estimation of some variable parameters. Although a fairly detailed model of the robot is available, it is not sufficient to ensure accurate and especially robust control. As a consequence, a closed-loop control architecture must be designed. Concretely, the second part of this thesis is dedicated to the robust control of CDPRs for two targeted applications: pick-and-place of metal plates in a suspended configuration (ROMP), and window cleaning in a fully-constrained configuration (ROWC).

Redundant nonlinear systems

CDPRs, which have more actuators than degrees of freedom, are over-actuated nonlinear systems. In the case of suspended CDPRs, the redundancy is necessary to ensure control of all degrees of freedom since cables can only pull onto the platform [RGL98; Fan+04; Mik+08; OA05; OA06; Bor+09b]. In addition, redundancy increases the size of the feasible workspace [Lam+13]. However, actuation redundancy leads to modeling and control challenges. For a 6 DoF CDPR with 8 cables, the resolution of the robot forward kinematics leads to multiple possible solutions, usually solved numerically by an optimization problem (see Sec. 2.5). In the same manner, applying a specific wrench onto the platform can be achieved through an infinity of cable tensions sets. Moreover, contrarily to mechanisms with rigid legs, cables can only pull on the platform. As consequence, in order to apply a desired wrench onto the platform, a tension distribution algorithm must be implemented to find and

select a solution that ensure positiveness of cable tensions [Pot14; Gou+15; Sch+18; SCG19].

Uncertain systems

Secondly, CDPR control is affected by a number of uncertainties. Cables have elasticity and flexibility which can lead to a nonlinear behavior between motors and platform positions. Sagging cables will result in differences between anticipated and real force amplitude and direction at the anchor points while slack cables, which are equivalent to a missing leg for a parallel mechanism, will potentially lead to platform instability [Bak+17]. Finally, some parameters of the dynamic model of the robot can be unknown, as for example the mass of the transported object in a pick-and-place application or frictions in the motors [Kra+17; Lam+13]. Robust control methods should then be implemented to ensure that the CDPR performances are maintained despite these uncertainties.

Joint / Cartesian space

In what follows, a distinction is made between motors positions errors observed in the *joint space*, and platform position errors observed in the *Cartesian space*. Control architectures can be implemented based on a single space, or on the two which is sometimes referenced as *dual space* control [Lam+13]. If no measurement or estimation of the platform pose is available, implementing a controller in the joint space is usually simpler. However, accurate control in the joint space does not ensure a good platform positioning in the Cartesian space, due to the nonlinearity between the two spaces.

Position / force control

CDPR *position control* corresponds to the positioning of the platform through the control of cable lengths, via motor positions. On the other hand, in *force control* the platform positioning is realized through the forces applied by the cables onto the platform at the anchor points, and the resulting wrench exerted onto the platform.

The main advantage of position control is its simplicity of implementation. CDPRs motors are mainly equipped with encoders returning the motor positions, and eventually velocities. The desired cable lengths are directly generated using the inverse models of the robot. However, with position control, inaccurate computations of the desired cable lengths can lead to either slack cables or very high tensions. This is particularly true for fully-constrained CDPRs where each cable acts in opposition with one another.

In the case of fully-constrained CDPRs, force control is then preferred, combined with the implementation of a tension distribution algorithm that ensures the positiveness and limits on the cable tensions.

Centralized / decentralized control

CDPRs control architecture can be centralized or decentralized, the last solution being far more developed to the author's knowledge. Centralized architectures take into consideration the interactions between the cables and their interdependence. The wrench applied to the platform is computed for all actuators by a Multi Input Multi Output (MIMO) controller, taking into consideration all the available measurement signals (coder information, tension sensors, tracking position of the effector, etc.). Centralized architecture are not often implemented because of their higher complexity and necessity of a good knowledge of the CDPR model. The control laws proposed by Meunier et al. [MBN09] can be cited. Linearization by dynamic inversion, or Computed Torque Control, is also applied in [Hu+14]. More recently, a very interesting Model Predictive Control solution is proposed in [SCG19], assuming slow and smooth motion of the platform. However, at this time, the accuracy of the method must still be verified experimentally.

Decentralized control architecture are far more used in the literature. In a decentralized control architecture, all cables are separately driven by their own controller. Typically for CDPR control, decentralized architectures induce one individual Single Input Single Output (SISO) controller per motor which follows its own trajectory, resulting in the indirect motion control of the platform. Proportional-Integrate-Derivative (PID) control laws [Kaw+00] are widely used in the industry due of their easy programming and good performance when systems have not too important nonlinearities and uncertain perturbations [AH95]. Robust linear control methods have also been tested on CDPRs, such as H∞ theory [CLC14] or modal approaches [WCG15]. However, the application of such linear control methods is delicate due to their hands-on tuning methods, risk of instability and reduced performances, and given that CDPR are highly nonlinear.

Decentralized control: robust approaches based on sliding mode theory

Nonlinear control methods include the more recent development of sliding-mode controllers, particularly interesting due to their robustness to uncertainties and perturbations [ES98]. Sliding mode control has been increasingly considered for CDPR control in several applications [ZK10; AV12; EGGC15; SBM15; SCG19] both in simulation and experimentally, with good performances against perturbations. The drawback of sliding mode control is the existence of discontinuities in the control input due to the use of the sign function [BT01]. As a consequence, the *chattering* phenomenon appears: it is a high frequency oscillation that engenders vibrations on the actuators and can prematurely deteriorate gearmotors and other mobile parts in the kinematic chains. Higher order and gain adaptive sliding mode control methods have been developed to reduce chattering such as [EP14; STP12], and have been implemented in [Sch+18]. Very recently, new control methods based on linear and

sliding mode algorithms have been developed to achieve both lower chattering and energy consumption compared to pure sliding mode controllers [Tah+18b]. The controller then balances between the two control types to get a good compromise between robustness and smoothness of the control output.

Design of control architectures for ROMP and ROWC

In Chapter 4, control architectures are studied for both the metal plate picking application (ROMP) and the window cleaning application (ROWC). Both CDPRs are redundant; however their configurations, the available sensors, their dimensions and the maximum load are different. As a consequence, different architectures are considered for each application and the reasons for their choice are detailed in the following.

The ROMP prototype has a suspended configuration with non-negligible 2 DoF pulley geometries, lifts loads of up to 615 kg and is equipped with 8 force sensors which provide additional information for its control. The two main challenges on this prototype are: the robustness of control despite load variations, and the consideration of cable elasticity. For this application, position control (PC) is considered for its simplicity and low computation cost, which are valuable advantages for an industrial implementation in a real-time environment. Experiments have been realized with architectures based on either a standard PD controller or a novel controller balancing between sliding mode and linear algorithms (SML). The payload mass estimation from Sec. 2.7 was considered in a feedforward term to compensate for the current payload. Then, based on the force sensors and the best performing architecture, a cable elasticity feedback loop is introduced to improve positioning repeatability in spite of cables elongations. The resulting control architecture (PCE) is easy to implement and provides good repeatability of the platform positioning for the targeted application.

ROWC has negligible pulley geometries and a 14 kg platform. However, it uses a fully-constrained configuration, meaning that a tension distribution algorithm (TDA) is necessary to avoid cable slackness or over-tension. In addition, in the window cleaning application, the robot stiffness should be maximized in order to reduce the eventual displacement of the platform when subjected to a lateral wrench (due to water pressure, wind, etc.). The chosen architecture places the tension distribution after the sum of the feedforward and control block output to distribute the total resulting force on the platform onto all cables. The selected tension distribution method is based on the *feasible polygon* of the CDPR [Gou+15]. For a CDPR with an actuation redundancy of two, this polygon defines the 2D space of possible cable tensions solutions ensuring the static equilibrium of the platform while taking into account the minimum and maximum admissible cable tensions. A usual method for selecting a solution in the feasible polygon is based on the calculation of its

barycenter. Based on the stiffness matrix of the CDPR, a novel solution selection criterion is proposed, in order to maximize the robot stiffness in the direction of the external wrench. Simulation and experimental comparison between the platform displacement and cable tensions selected with the barycenter method and the stiffness oriented TDA are provided.

Emergency stops of CDPRs

Chapter 5 contains a study of the particular case of the emergency stop for an industrial purpose. The security and safety of CDPRs are actively being investigated for their industrialization, such as very recently the application of emergency strategies in the case of cable breaks studied in [BB19]. In this chapter, the objective is to discuss emergency stop strategies for industrial CDPRs, and to quantify the behavior of the platform during a classical emergency stop on the ROMP prototype. The evolution of cable tensions is also observed in the case of an overwhelming lateral wrench on ROWC. These values will be used at IRT as first reference towards the design of safety measures for CDPRs in an industrial environment.

4. Control

The goal of Chapter 4 is to design control architectures suited to the configurations and objectives of ROMP and ROWC.

For the metal plate handling application of ROMP, robust control scheme must be designed in order to keep high level of performances for a large range of masses and trajectories. Control architectures are proposed in the sequel and the stability, accuracy and repeatability of each method are compared experimentally on the prototype. Firstly, several decentralized position control schemes (PC) are successively presented in Sec. 4.2, including a feedforward term for the platform mass compensation, and the real-time estimation of the platform load presented in Sec. 2.7. In order to improve repeatability of the platform positioning in spite of the load changes and cable elasticity, a control architecture that compensates for cable elongation (PCE) is presented in Sec. 4.2.4 and implemented, by using force sensors.

In the case of the fully-constrained configuration of ROWC, miscalculations of cable lengths due to modeling simplifications can either lead to very high cable tensions, or sagging cables. For the window cleaning application (ROWC), the inclusion of a tension distribution algorithm (TDA) in the control architecture is recommended to ensure operational safety. After a presentation of suitable control architectures, a novel tension distribution selection criterion is introduced in Sec. 4.3, with the objective of computing the set of tensions that maximizes the robot stiffness. Based on the feasible polygon of the CDPR [Gou+15], the stiffness matrix is computed to find the set of cable tensions that leads to the smallest platform displacement under an external wrench.

At the center of all these control schemes, two controller types, proportional-derivative (PD) and novel sliding mode (SML) [Tah+18b] controllers have been

considered.

Experimental results for theh PC and PCE control architectures are provided for ROMP in Sec. 4.5, along the test trajectory defined in Section 1.4.1. For each architecture, the performances between PD and SML controllers are compared, and conclusions are drawn on the best performing architectures towards robustness and accuracy. Simulation and experimental results of the proposed stiffness oriented tension distribution algorithm (SOTDA) for ROWC are given in Secs. 4.6 and 4.7, in a static pose and along the test trajectory defined in Sec. 1.4.2. The results are discussed and compared to the solution obtained with the barycenter selection method with regards to the obtained cable tensions and estimated platform displacement

4.1 Control design

4.1.1 System input and outputs

Figure 4.1 presents the input, outputs and perturbations. Solid arrows represent components that are generic to any typical CDPR while dashed arrows are situational and depend on the robot hardware and the considered operating conditions.

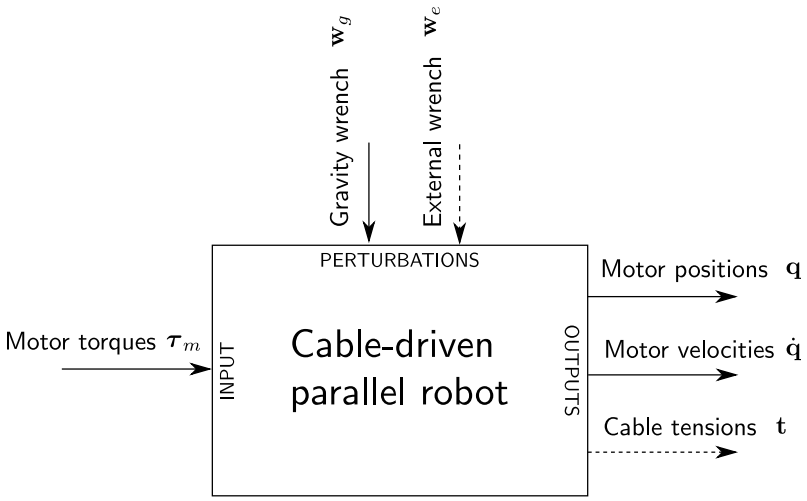

Figure 4.1: System input, outputs and perturbations.

The system input is the vector of motor torques $\boldsymbol{\tau}_m$. The usual outputs of the system are the actual motor positions $\mathbf{q}$ and motor velocities $\dot{\mathbf{q}}$. Motor positions and velocities are obtained from the encoders. The actual motor torques can be derived from the motor current, although their are intrinsic to the system. The servo drives then perform the control loop between desired control input $\boldsymbol{\tau}_m$ and motor currents.

Cable tensions $\mathbf{t}$ can be directly measured using force sensors. ROMP is equipped with analogical Tractel® sensors which can return the cable tensions. ROWC is not currently equipped with such sensors and cable tensions can only be assessed from motor torques, whose measurements are noisy, mainly due to friction in the gearmotors.

Finally, the considered perturbations are the wrench due to gravity $\mathbf{w}_g$ applied onto the platform, which depends on its mass and the eventual additional load, and a possible external wrench $\mathbf{w}_e$. The only wrench considered for ROMP is the one due to gravity. For ROWC, the pressurized water jet generates an external wrench that will disturb the system, and that must be considered.

B&R Automation® hardware and software can provide proprietary control laws for motor position and velocity control. However, in order to have complete control of the robot, these functions are not used in the frame of this thesis.

4.1.2 Architecture choices

The overall goal of the control architectures is to control the platform pose along a desired trajectory, while ensuring stability and robustness towards perturbations. The developed architectures should ideally be compatible with a real-time computation and implementable on a programmable logic controller with limited processing power, such as ROMP Intel Atom based system (Sec. 1.3.1).

No direct information on the platform pose or motion is readily available from the system sensors, as seen in Fig. 4.1. Vision-based solutions have been discarded for ROMP due to their sensitivity to dust and lighting conditions, and currently considered not compatible with the industrial environment.

In the absence of direct measurement, the platform pose can only be estimated from the motor measured information and, eventually, cable tensions. As discussed in Chapter 2, solving the direct geometric model of a CDPR is not an easy task since more than one solution is possible from a fixed set of motor positions, even considering straight and inelastic cables. The accuracy of the platform pose estimation is also dependent on the quality of the model. The use of a simplified geometric model is expected to lead to inaccurate platform pose estimation due to the nonlinearities of the system (actuation redundancy, cable elasticity). In addition, the existence of multiple solutions to the forward kinematics could lead to discontinuities in the pose estimation, and potentially unstability of the closed-loop system. Finally, the developed architecture should also be compatible with real-time computation; however, the complexity of the geometric model used in the forward kinematics impacts the computational cost of a solution.

As a consequence, the following control architectures only rely on the system internal sensors and are based on the errors in the joint space of the robot, that is both the motor angular positions and velocities. Additional information such as cable tensions can be used to improve the control architecture performance, through mass or cable elongation estimation.

Decentralized control architectures have been considered in this chapter for their simplicity of implementation, with one controller separately tuned for each motor. In order to achieve robust and stable control, a novel controller balancing between

sliding mode and linear behavior (SML) is considered at the heart of the control architectures. Its performances are compared to those of a standard proportional-derivative (PD) controller, that is often used in robotics for both serial and parallel robots control [KD04], also serving as a performance benchmark.

4.2 CDPR position control

As presented in Chapter 1, the ROCKET project is the development of a robot for pick-and-place of more or less heavy metal plates in an industrial environment. The main control objectives for this application are the stability of the closed-loop system, its robustness and repeatability despite the load changes inducing different wrenches onto the platform. The developed architecture should also be compatible with real-time implementation. The resolution of the direct geometric model to estimate the platform pose could lead to longer computation time and the risk of discontinuities in the solution found by the optimization method. A simpler approach based on the control at the motor level only was then preferred for this particular application.

For fully-constrained CDPRs, underestimated cables lengths can lead to very high tensions in opposing cables. Centralized control architectures based on the control of the wrench applied by the cables onto the platform and implementing a tensions distribution strategy are then more appropriate. However in the case of suspended CDPRs, small errors in cable lengths computation should only induce platform pose errors. A decentralized position control architecture which compute a set of desired cable lengths is considered for the metal plate handling application.

Due to the parallel nature of CDPRs and the decentralized aspect of the control, all signals are treated as vectors in the following control schemes. Each actuation chain, from the motor to the cable, has its own controller that is using desired and measured motor positions, q_d and q, and motor velocities, $\dot{q}_d$ and $\dot{q}$. The signal provided by the controller is the desired motor torque $\boldsymbol{\tau}_m$.

4.2.1 PC1: Basic architecture

The first control architecture implemented in the sequel on ROMP, denoted as PC1, is presented in Fig. 4.2. The *controller* box at the center of the scheme is either the PD controller or SML controller presented in Sec. 4.4. The corresponding control architecture is then referenced as PC1-PD or PC1-SML accordingly.

In this scheme, $\mathbf{X}_d$ is the 6-dimensional vector containing the desired Cartesian position and orientation of the MP, $\mathbf{v}_d$ the desired MP twist (linear and angular platform velocities). $\mathbf{q}_d$, $\dot{\mathbf{q}}_d$ and $\boldsymbol{\tau}_m$ are the 8 vectors of desired motor angular positions, velocities and torques, respectively. In this first scheme, $\boldsymbol{\tau}_m$ is directly equal to the controller signal.

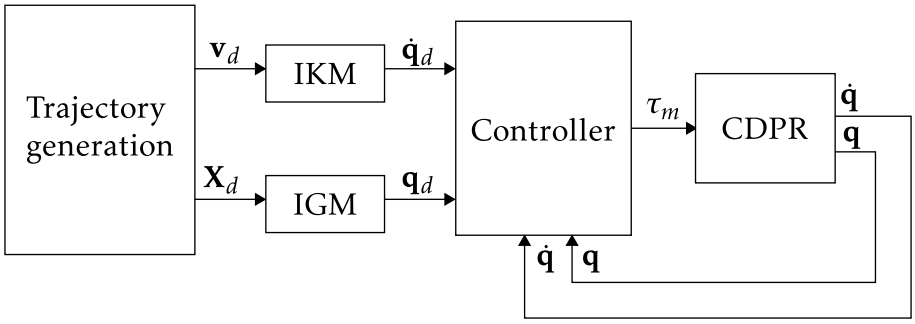

Figure 4.2: PC1 control architecture.

The MP Cartesian MP pose and twist are converted into desired motor positions and velocities using the CDPR inverse geometric (IGM) and kinematic (IKM) models based on the modeling considering the pulleys geometry from Sec. 2.1.3.

4.2.2 PC2: Control with feedforward

A feedforward term is commonly included in CDPR control strategies to predict the dynamics of the platform and improve the accuracy of the robot [Lam+13; VAT10]. The goal of this architecture is to compute in advance the necessary motor torques ensuring the dynamic equilibrium of the platform along the test trajectory.

Figure 4.3 presents the PC2 control architecture with feedforward, where $\dot{\mathbf{v}}_d$ contains the Cartesian acceleration and angular acceleration of the platform. $\boldsymbol{\tau}_c$ is a 8 vector receiving the signal of the controller.

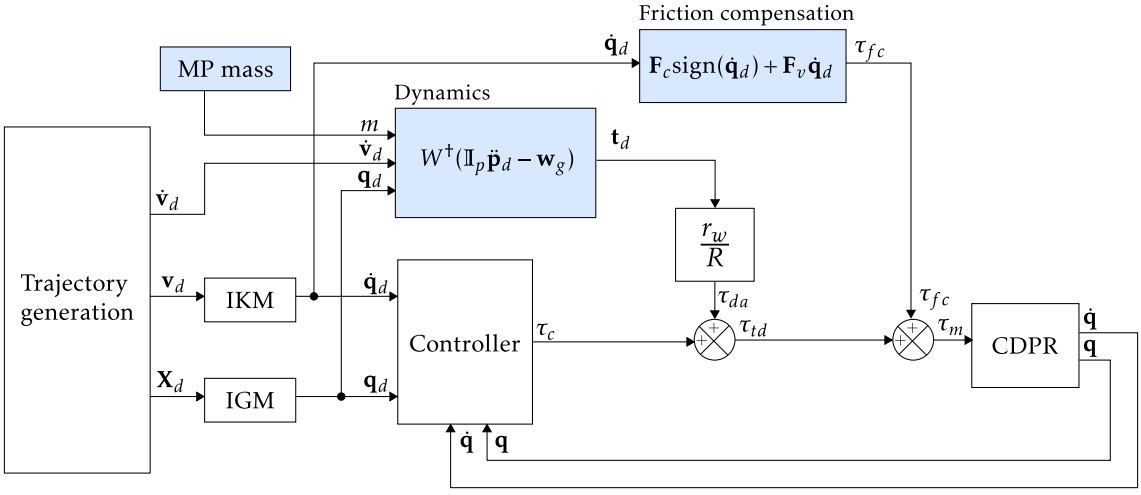

Figure 4.3: PC2 control architecture with feedforward terms.

Based on the dynamic model of the robot, it is possible to add a term to the controller that anticipates the MP dynamics and compensates for a given mass value along the trajectory. From Eq. (2.18), this feedforward term is defined as

$$\tau_{da} = \frac{r_w \mathbf{W}^{\dagger}(\mathbb{I}_p \dot{\mathbf{v}}_d \ - \mathbf{w}_g)}{R} \tag{4.1}$$

with τ_{da} the feedforward torque, $\mathbf{w}_g$ the wrench due to the gravity applied onto the platform to compensate, $\mathbf{g}$ the vector representing gravity in the base frame, r_w the radius of the winches and R the gearbox reduction. $\mathbf{W}^\dagger$ denotes the Moore-Penrose pseudo-inverse of $\mathbf{W}$.

The term $\mathbf{w}_g$ depends on the load mass. However, for the metal plate handling application of ROMP, the metal plates masses are considered unknown. As a result, only the mass of the platform is considered in the feedforward term.

Since m_{MP} is the mass of the platform, it equals 266 kg for the platform without the cross (MPNC), and 366 kg when the complete platform is used (MP, MPM1 and MPM2). This fact voluntarily introduces an error in the latter two cases, that is when metal plate M_1 or M_2 is carried, in order to quantify the control robustness.

$$\mathbf{w}_g = \begin{bmatrix} 0 & 0 & -m_{MP}g & -m_{MP}gy_G & m_{MP}gx_G & 0 \end{bmatrix}^{\mathrm{T}} \tag{4.2}$$

A linear friction model [KD04] has been implemented in each actuation chain to compensate the losses in the motors, gearbox and winches:

$$\boldsymbol{\tau}_{fc} = \mathbf{F}_c \mathrm{sign}(\dot{\mathbf{q}}_d) + \mathbf{F}_v \dot{\mathbf{q}}_d \tag{4.3}$$

with $\boldsymbol{\tau}_{fc}$ the friction compensation and $\dot{\mathbf{q}}_d$ the desired motor rate vector. $\mathbf{F}_c$ and $\mathbf{F}_v$ are respectively the vectors containing the static and viscous friction coefficients separately identified for each motor. More information on the friction estimation on the ROMP prototype are available in Appendix B.

This architecture can also reduce chattering and overshooting by allowing for smaller gains in both controllers, resulting in a smoother behavior of the robot. In the experimental results, the gains are kept the same as with PC1 architecture for a direct comparison of the two.

Total mass known: PC2$^+$ notation

The notation PC2$^+$ will be used in the case were the total mass is known, that is for both the platform and the metal plate. In this case, the term m_{MP} should be replaced by m_{tot}, which contains the complete load mass. This notation is used in the experimental section Sec. 4.5.6, where the benefits of a cable elasticity compensation term are studied in the most favorable control conditions.

4.2.3 PC3: Control with feedforward using real time mass estimation

Based on the mass estimation method presented in Sec. 2.7, a controller is designed, which updates the value of the mass in the feedforward term ; indeed $\mathbf{w}_g$ is now defined as:

$$\mathbf{w}_g = \begin{bmatrix} 0 & 0 & -m(t)g & -m(t)gy_G & m(t)gx_G & 0 \end{bmatrix}^{\mathrm{T}} \tag{4.4}$$

where $m(t)$ describes the current estimated total load, namely the MP and a possible metal plate. The control scheme of the PC3 architecture with real-time update of the feedforward term τ_{idm} is depicted in Fig. 4.4.

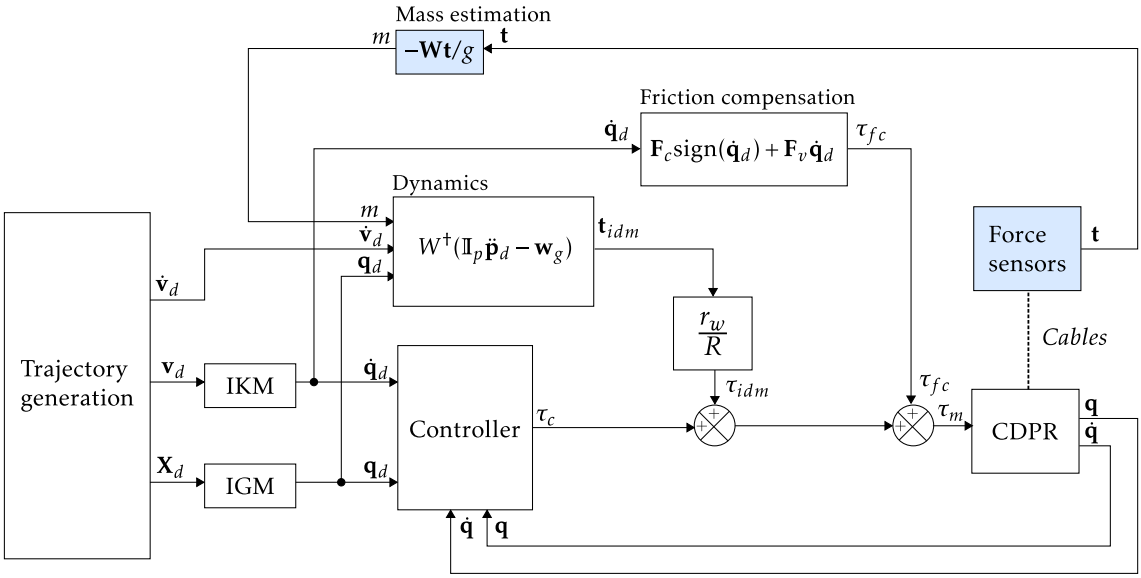

Figure 4.4: PC3 ontrol architecture real-time mass compensation.

4.2.4 PCE: Cable elasticity compensation

It is expected that with controllers in the joint space, even if a controller can achieve accuracy at the motor level, the platform might still subject to pose errors due to cable elasticity. Furthermore, this error depends on the carried load. As the ROMP prototype is not equipped with external sensors during operation, it is not possible to directly measure this position error for correction.

Figure 4.5 presents a Position Control architecture compensating for cable Elasticity (PCE), by implementing a cable elongation feedback loop.

Based on a cable elasticity model and the force sensors readings, it is possible at each time to calculate the necessary motor position correction $\delta\mathbf{q}_E$ to compensate for the cable elongation. From the linear cable elasticity model presented in Sec. 2.4, the cable tensions $\mathbf{t}$ is linked to the cable elongation $\delta\mathbf{l}_E$ by the equation:

$$\mathbf{t} = \frac{ES}{\mathbf{l}}\delta\mathbf{l}_E + \mathbf{t}_{Cal} = \frac{ES}{(r_w\mathbf{q}_d + \mathbf{L}_{WA})} r_w\delta\mathbf{q}_E + \mathbf{t}_{Cal} \tag{4.5}$$

with $\mathbf{l}$ the nominal cable length, $\mathbf{q}_d$ the nominal motor positions and $\delta\mathbf{q}_E$ the small motor position corresponding equivalent to the cable elongation. $\mathbf{t}_{Cal}$ is the cable tension measured in the calibration step (Sec. 3.2), r_w the winch radius and $\mathbf{L}_{WA}$ the

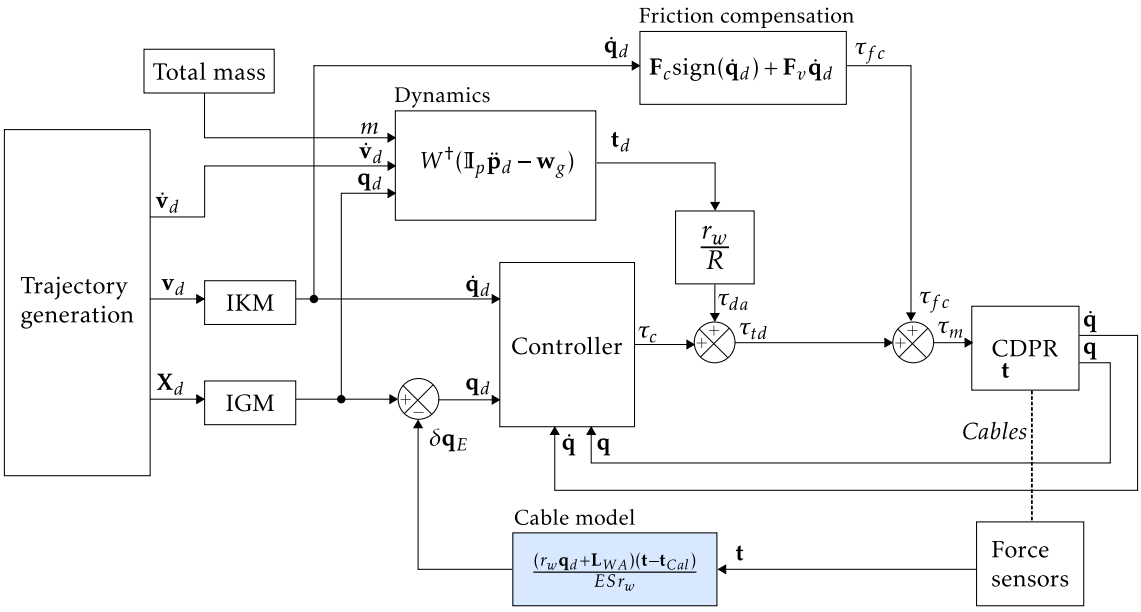

Figure 4.5: Position controller with cable elasticity compensation (PCE)

vector containing the cable dead lengths from the winches to the pulleys. $\mathbf{t}_{Cal}$ the cable pre-tension, that is the tension in the cables while the platform is in a known pose. For the ROMP prototype, $\mathbf{t}_{Cal}$ is measured during the prototype calibration.

The motor position correction term $\delta\mathbf{q}_E$ then equals:

$$\delta\mathbf{q}_E = \frac{(r_w\mathbf{q}_d + \mathbf{L}_{WA})(\mathbf{t} - \mathbf{t}_{Cal})}{ESr_w} \tag{4.6}$$

Note that the correction term only affects the desired position in the proposed architecture. The cable elasticity compensation should ideally also be applied to the desired speed. $\delta\mathbf{q}_E$ being relatively small, neglecting its variation along time seemed acceptable for now.

Also in order to evaluate the impact of the elasticity compensation term in Sec. 4.5.6, the total mass of the platform and its load are used in the calculation of the dynamics anticipation term, as in PC2$^+$.

4.3 CDPR control with tension distribution

Prototype ROWC is also composed of 8 cables and has a 6 DoF moving-platform. However contrary to ROMP it uses a fully-constrained cable configuration, with cables coming from both the top and the bottom of the frame. The control of such CDPRs requires more attention than purely suspended ones.

Small errors in the computation of the necessary cable lengths to achieve a desired position of the platform can either lead to overestimated cable lengths, resulting in slack cables and platform unstability, or underestimated cable lengths leading to higher tensions in the concerned cables. In the case of suspended platforms, these

small errors are not very impactful, although they can still lead to decreased robot stiffness, platform stability and inferior positioning accuracy. However in the case of fully-constrained configurations, the effects of modeling errors are amplified: if all cables lengths are overestimated, the cables coming from the bottom of the frame will be slack and the platform will be held by the 4 cables from the top. In the case of ROWC, the platform will then be under-constrained and will become unstable. On the other hand, if cable lengths are underestimated, since cables can have opposing effects in all directions, cable tensions will rise and could become dangerously high. A motor controller might also provide a negative tension in a cable, which means the cable attempts to push on the platform. While this latter situation could work on a robot with rigid legs like the Gough-Stewart platform, slack will appear in the concerned cables and might lead to unwanted load on the other cables.

In order to have control over the cable tensions during the motion of the platform, a tension distribution algorithm (TDA) must be implemented. The goal of tension distribution is to divide the overall effort on the platform between all cables, while maintaining the static or dynamic equilibrium of the platform. The TDA can also be employed to enforce boundaries on the cable tensions to avoid any danger.

In the sequel, control schemes integrating a TDA and considered for ROWC are presented. Then, from the computation of the CDPR feasible polygon, a novel stiffness oriented TDA is proposed, which aims at finding the set of tensions maximizing the robot stiffness against an external wrench.

4.3.1 Control architectures

The majority of CDPRs implementing a TDA use a dedicated computation step separated from the motor controllers. The TDA takes as an input the desired wrench to apply onto the platform and generates a set of desired cable tensions.

Two architectures have been experimented on ROWC depending on the position of the TDA, either through an external loop or directly at the input of the system.

TC1: Tension external loop

The control scheme presented in Figure 4.6 has an external tension loop based on the CDPR dynamic model. Based on the current desired platform pose $\mathbf{X}_d$ and wrenches applied onto the platform, a desired set of cable tensions $\mathbf{t}_d$ is given by the TDA. The information obtained from the force sensors $\mathbf{t}$ are then compared to these desired tensions. Therefore, a tension controller generates a motor position delta $\delta\mathbf{q}_t$ from the tension error $\mathbf{e}_t$. A similar architecture is proposed in [KD04] for the hybrid position/force control of serial robots.

The knowledge of the cable properties is beneficial to compute the necessary cable length difference that will correct the cable tension error. In [Kra+14] a similar approach has been proposed, using a PI controller with an anti-windup term for to

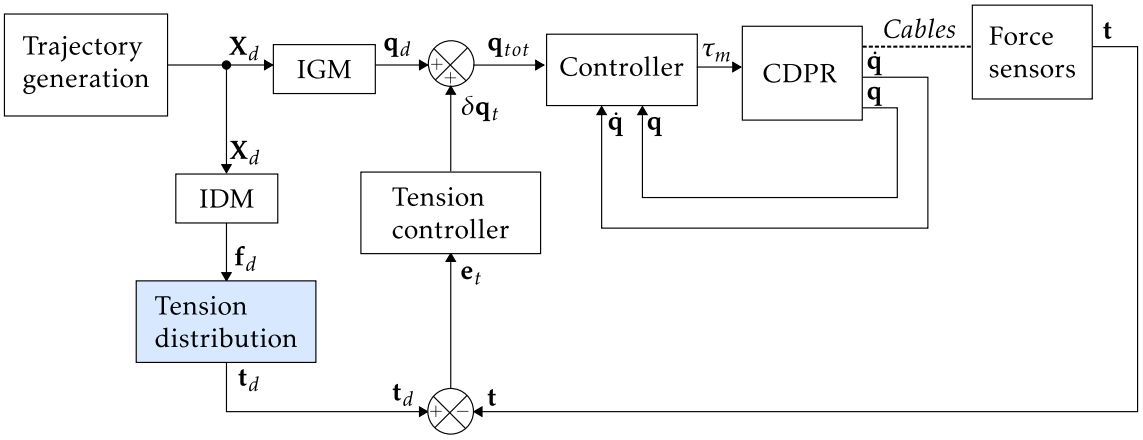

Figure 4.6: Controller architecture with TDA in external loop (TC1).

compute the correction.

A saturation should be applied to the term $\delta\mathbf{q}_t$ to restrain the correction of the desired position while maintaining a motor position $\mathbf{q}_{tot}$ that is close to $\mathbf{q}_d$. In case of drift, as $\delta\mathbf{q}_t$ increases, the platform can become closer to the desired cable tensions but will also deviate from the desired motor positions, leading to larger positioning and orientation errors. In addition, if the modeling of the CDPR is not sufficiently precise, large correction or drift of the platform is possible.

This architecture was considered for ROWC, however in practice, if the difference between the actual and desired set of tension were too large and the saturation is quickly reached. The CDPR modeling must then be precise in order to make this control scheme applicable.

TC2: Tension distribution in the loop

The effects of the location of the TDA in the control scheme have been studied in [Lam13]. If the TDA is applied to the controller signal $\boldsymbol{\tau}_c$ only, the addition of the dynamic anticipation term $\boldsymbol{\tau}_{da}$ could result in an infeasible set of tensions. On the other hand, by placing the TDA after the controller and the feedforward terms, if a solution to the distribution is found, the generated desired motor torques τ_m will satisfy the objectives of the TDA. As a consequence, the tension distribution should be to applied to both $\boldsymbol{\tau}_{da}$ and $\boldsymbol{\tau}_c$, as presented in Fig. 4.7.

It is visible however that additional nonlinearities are introduced between the controller signal and the system input. As a consequence, this architectures might degrade the positioning accuracy of the robot at the motor level.

4.3.2 Common tension distribution algorithms

From the multitude of tension distribution algorithms, one can cite in particular the Median method [Pot14] with its simple implementation or the barycenter method (BM), based on the computation of the CDPR feasible polygon, and which ensures the respect of tension upper and lower boundaries and a balanced selected tension

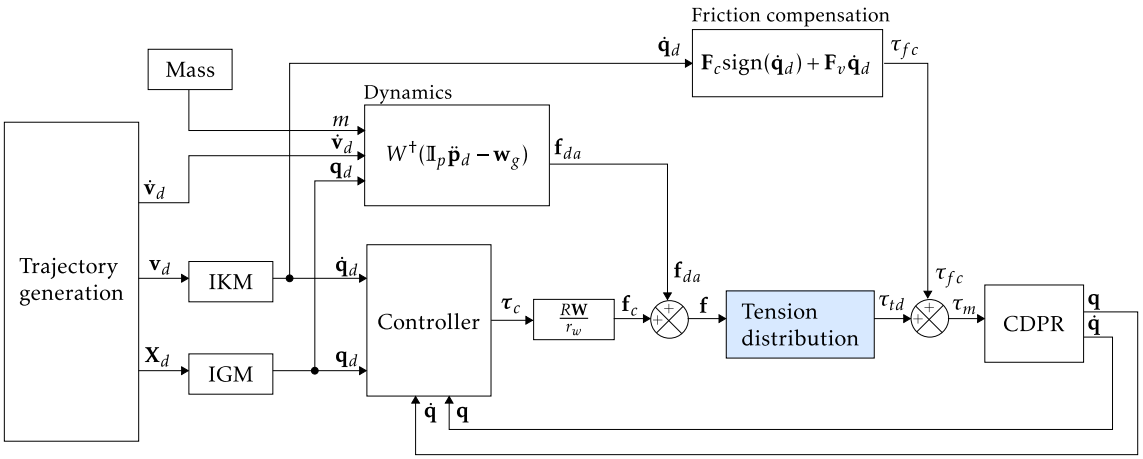

Figure 4.7: PC2 control scheme with tension distribution on feedforward and controller block outputs.

set between these limits [Gou+15].

From wrench matrix pseudo-inverse

In the absence of a specific tension distribution algorithm, a set of cable tensions for a MP static equilibrium can be directly computed from Eq. (2.56) using the pseudo-inverse of the wrench matrix $\mathbf{W}^\dagger$, as

$$\mathbf{t} = -\mathbf{W}^\dagger \mathbf{w}_e \tag{4.7}$$

This method was implicitly realized in the previous control architectures PC2, PC3 and PCE for the computation the feedforward term $\boldsymbol{\tau}_{da}$.

Median method

A simple method to distribute tension was proposed in [Pot14] by setting boundaries to cable tensions and by giving a solution around the median of the chosen interval.

From the dynamic model of the CDPR (Eq. (2.18)), the problem of tension distribution is written as

$$\mathbf{W}\mathbf{t} + \mathbf{w}_e + \mathbf{w}_g = 0 \quad \text{with} \mathbf{t} = \begin{bmatrix} t_1 & \dots & t_i & \dots & t_m \end{bmatrix}^T \tag{4.8}$$

The vector of median cable tensions $\mathbf{t}_m$ is defined by

$$\mathbf{t}_m = \frac{1}{2}(\mathbf{t}_{min} + \mathbf{t}_{max}) \quad \text{with} \quad 0 < t_{min} \leqslant t_i \leqslant t_{max} \tag{4.9}$$

The solution given using this method is

$$\mathbf{t} = \mathbf{t}_m + \mathbf{t}_v = \mathbf{t}_m - \mathbf{W}^\dagger(\mathbf{w}_e + \mathbf{w}_g + \mathbf{W}\mathbf{t}_m) \tag{4.10}$$

This algorithm has the advantage of taking very little computation time and provides continuous solutions which respect the lower limits, as long as $\mathbf{t}_v$ respects the criterion detailed in [Pot14].

However the fixed formula only depends on the force to distribute and the chosen upper and lower tension limits. In order to find the set of feasible cable tensions that maximizes the CDPR stiffness, a better knowledge of the space of possible solutions is necessary.

Feasible polygon and barycenter method

For over-constrained CDPRs with a redundancy degree equal to two such as ROMP and ROWC, solutions for tension distribution are based on the computation of a polygon of feasible tensions [HK11], from which a set of tensions satisfying the robot equilibrium can be selected. An implementation of such a TDA is described in [Gou+15], with a finite time convergence of the algorithm to ensure its compatibility with real-time software. TDA based on this method ensures that, if a solution to the static equilibrium is found, all tension constraints are respected. The definition of the *feasible polygon* [Gou+15] is presented thereafter.

A solution to the static equilibrium of the CDPR (Eq. (2.4)) can be written as

$$\mathbf{t} = \mathbf{W}^{\dagger}\mathbf{f} + \mathbf{N}\boldsymbol{\lambda} \quad \text{with} \quad \boldsymbol{\lambda} = \begin{bmatrix} \lambda_1 & \lambda_2 \end{bmatrix}^{\mathrm{T}} \tag{4.11}$$

where $\mathbf{N} = \mathrm{null}(\mathbf{W})$ is the null space of the wrench matrix $\mathbf{W}$, and $\boldsymbol{\lambda}$ is an arbitrary vector of coordinates λ_1 and λ_2.

Let Σ be the 2D space of solutions $\begin{bmatrix} \lambda_1 & \lambda_2 \end{bmatrix}^{\mathrm{T}}$ obtained from Eq. (4.11), and Ω the hypercube of feasible cable tensions $\Omega = \left\{ t \mid 0 \leqslant t_{min} \leqslant t_i \leqslant t_{max} \right\}$. Their intersection $\Lambda = \Sigma \cap \Omega$ is a 2D convex polytope of feasible cable tensions sets, obtained from the affine map $\mathscr{A} = (\mathbf{N}, \mathbf{t}_0)$:

$$\mathscr{A}^{-1}(\Lambda) = \left\{ \boldsymbol{\lambda} \in \mathbb{R}^2 \mid \mathbf{t}_{min} \leqslant \mathbf{t}_0 + \mathbf{N}\boldsymbol{\lambda} \leqslant \mathbf{t}_{max} \right\} \tag{4.12}$$

where $\mathbf{t}_0$ is the particular solution of the static equilibrium given by $\mathbf{t}_0 = \mathbf{W}^{\dagger}\mathbf{f}$. $\mathscr{A}^{-1}(\Lambda)$ is also a 2D convex polytope, defined as the feasible polygon.

An example of computation of the feasible polygon of ROWC is visible in Fig. 4.8 to compensate for the gravity at position $\mathbf{p} = \begin{Bmatrix} 1.5 & 0.350 & 0.590 \end{Bmatrix}^{\mathrm{T}}$.

A criterion must then be defined to select one solution from the feasible polygon: a common solution is the selection of the polygon barycenter, represented by the red point in Fig. 4.8. The resulting TDA will be denoted as the barycenter method (BM). This solution has the advantage of leading to a compromise between energy consumption and robot stiffness [Gou+15]. The next section will focus on selecting the set of tensions leading to the highest robot stiffness along the desired axis.

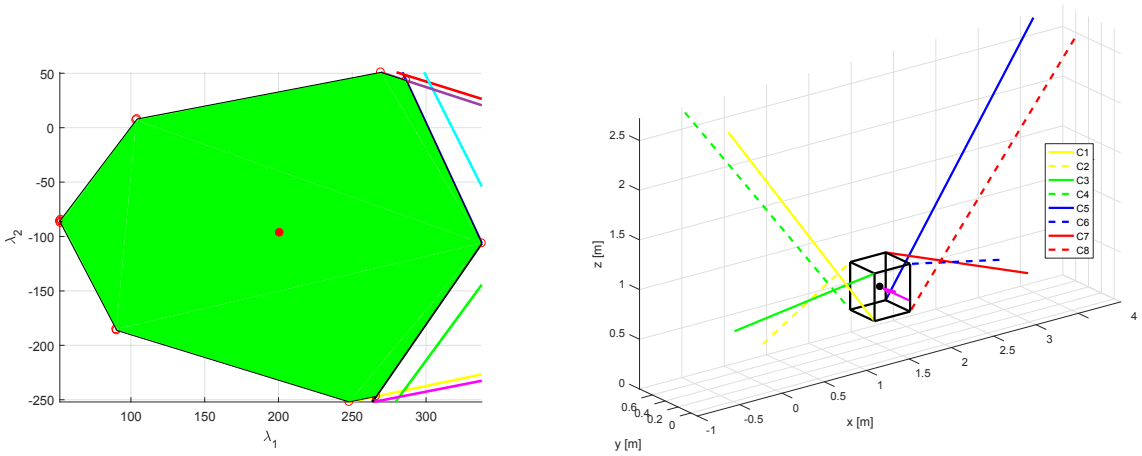

Figure 4.8: Polygon associated to feasible cable tensions in green (**Left**), for ROWC platform pose $\mathbf{p} = [1.5,\ 0.350,\ 0.590]^{\mathrm{T}}$ with platform mass $m = 14$ kg (**Right**)

4.3.3 Stiffness oriented tension distribution

In this section, the objective is to minimize the platform displacement $\delta\mathbf{p}$ in a particular direction due to an external wrench $\delta\mathbf{w}_e$ applied onto the platform. Additional steps to the barycenter method are proposed in order to select from the feasible polygon the set of cable tension satisfying this objective.

In the window cleaning application the moving-platform is equipped with a pressure washer hose. In operation, water is projected with a pressure of 3 bar onto the surface to clean, which creates a force in the opposite direction of the water flow. Due to cable elasticity, this external wrench induces a small displacement of the platform along the y axis, noted as δp_y. From the feasible polygon obtained with the previously described TDA, it would be interesting to find the feasible cable tensions which minimize this displacement. To do so, a novel *stiffness oriented tension distribution algorithm* (SOTDA) is proposed, based on the Cartesian stiffness matrix expressed in Sec. 2.6.

As a reminder the stiffness matrix $\mathbf{K}$ of the robot directly links a small external wrench $\delta\mathbf{w}_e$ to the corresponding small platform displacement $\delta\mathbf{p}$:

$$\delta\mathbf{X} = \mathbf{K}^{-1}(\mathbf{t})\delta\mathbf{w}_e \quad \text{with} \quad \delta\mathbf{X} = \begin{bmatrix}\delta\mathbf{p} & \delta\boldsymbol{\phi}\end{bmatrix}^{\mathrm{T}} \quad \text{and} \quad \delta\mathbf{p} = \begin{bmatrix}\delta p_x & \delta p_y & \delta p_z\end{bmatrix}^{\mathrm{T}} \tag{4.13}$$

In the following, the cable tension solution obtained from the BM will be denoted as $\mathbf{t}_{BM}$ and the solution corresponding to the SOTDA as $\mathbf{t}_{SO}$.

If the goal is to maximize the stiffness along axis y, the problem will aim to minimize the following objective function:

$$\min_{\mathbf{t}^*} |\delta p_y(\mathbf{t})| \quad \text{with} \quad \delta\mathbf{p}(\mathbf{t}) = \mathbf{K}^{-1}(\mathbf{t})\delta\mathbf{w}_e \tag{4.14}$$

where the vector of cable tensions $\mathbf{t}$ is a function of λ_1 and λ_2, and $\mathrm{d}\mathbf{w}_e$ is a small wrench in the same direction of the external wrench $\mathbf{w}_e$.

The corresponding optimization problem can be solved by different methods, such as a nonlinear least square method.

Algorithm 1 describes the proposed SOTDA, $\mathbf{t}_{SO}$ being the resulting cable tension vector.

Algorithm 1: Stiffness Oriented Tension Distribution Algorithm (SOTDA)

Input: Moving-platform pose $\mathbf{X}$, external wrench $\mathbf{w}_e$
Output: Stiffness oriented cable tensions $\mathbf{t}_{SO}$
Compute feasible polygon $\mathscr{A}^{-1}(\Lambda)$ at MP pose $\mathbf{X}$, the MP being subjected to external wrench $\mathbf{w}_e$
for $(\lambda_1,\ \lambda_2) \in \mathscr{A}^{-1}(\Lambda)$ **do**
  Compute corresponding cable tension vector $\mathbf{t} = \mathbf{t}(\lambda_1,\ \lambda_2)$
  Compute cable length vector $\mathbf{l} = \begin{bmatrix} l_1 & \dots & l_m \end{bmatrix}^{\mathrm{T}}$
  Compute cable elasticity coefficients $k_i = \frac{ES}{l_i}$
  Compute the stiffness matrix $\mathbf{K} = \mathbf{K}_{\mathrm{p}} + \mathbf{K}_{\mathrm{a}}$
  Compute the MP displacement screw $\delta\mathbf{X} = \mathbf{K}^{-1}\delta\mathbf{w}_e$
  Select the second component of $\delta\mathbf{X}$, i.e., the MP displacement along axis y_b, $\delta p_y(\mathbf{t})$
end
Select and apply the set of cable tensions that minimizes δp_y:
$\mathbf{t}_{SO} = \min_{\mathbf{t}} |\delta p_y(\mathbf{t}_j)|$

It should be noted that $\mathbf{l}$ must contain the total cable length, including the dead cable lengths from the drums to the platform.

In order to obtain a better view of the selection process, the feasible polygon can be discretized into a grid, using MATLAB *meshgrid* function for example, from which a number of sets of $(\lambda_1,\ \lambda_2)$ are tested. The maximum stiffness is obtained numerically by comparing the displacement of the platform $\delta\mathbf{p}$ for each considered point located in the feasible polygon. The result is a surface in which the coordinate along the vertical axis corresponds to the evaluated displacement of the platform under the small external wrench $\delta\mathbf{w}_e$. The output of the proposed stiffness oriented tension distribution was studied in simulation in 4.6 using such a grid function in a static pose and along a path.

It should be noted that the addition of the stiffness criterion does not introduces new cable tension sets, but selects one solution from the feasible polygon. As such, the solution have the same certification as any other solution computed from the feasible polygon.

In order to implement the SOTDA on the ROWC prototype, some adjustments are made to the selection of the solution.

Consideration of feasible polygon corners only

The SOTDA must be compatible with a real-time implementation on ROWC. The computation time of the SOTDA is directly related to the number of considered

solutions. In simulation in Sec. (4.6), the feasible polygon is divided into a grid in which all intersections were evaluated. While this method is useful to study the stiffness of the robot over the entire feasible polygon, it drastically increases the computation time of the final solution depending on the size of the grid. In order to implement the proposed TDA in a real-time compatible formulation, the computation time of the algorithm should be maintained low and the number of considered solutions must then be restrained.

In order to consider a very small number of solutions, a proposed implementation is to limit the set of candidates $(\lambda_1,\ \lambda_2)$ to the corners of the feasible polygon. Two assumptions must be made in order to justify this choice:

(1) The robot achieves maximum stiffness when at least one cable tension reaches the maximum admissible value

(2) A second cable should either reach the maximum or the minimum admissible tension

From the first assumption, the SOTDA solution should be located on the edges of the feasible polygon, more specifically along a vertex of maximum admissible tension. The second assumption depends on the direction of the external wrench, pose and mass of the platform, and on the configuration of the CDPR. Under these assumptions, the optimal solution would be located at the intersection of two vertices, that is in a corner of the feasible polygon. These assumptions seem acceptable according to the form of the solution displayed in Fig. 4.36.

If only the minimum and maximum tension constraints are considered, the feasible polygon is constituted of 16 vertices at most for an 8 cable CDPR with a redundancy of 2. As a consequence, in the worse case 16 sets (λ_1, λ_2) will be evaluated. One can note that even if the optimal solution is not among the considered set of solutions, the algorithm can at least find the best out of several extremes.

A comparison between the solution obtained from the SOTDA using the grid method and from the consideration of the polygon corners only is available in Appendix D.

Stiffness coefficient ν and intermediate solution

The SOTDA must ensure safe and feasible cable tensions during operation. In an industrial application a security margin must be taken into account in order to maintain physically feasible values of tensions in the cables, based on the robot hardware and security factors.

For the ROWC prototype, an emergency stop of the robot will be requested if no solution is found to the tension distribution problem, that is if the feasible polygon is empty. However, since the SOTDA selects a set of cable tensions at the edge of the feasible polygon, the robot is continuously working at its limits. Variations in the controller output torques $\boldsymbol{\tau}_c$ can lead to a sudden infeasible force $\mathbf{f}$ (Eq. (4.11)),

resulting in a security stop of the robot.

In order to select an improved stiffness solution while still leaving a security margin between desired and maximum admissible cable tensions, an Intermediate Solution (IS) is introduced by selecting a new point between the barycenter and the stiffness oriented solutions. This new solution is chosen based on the value of a stiffness coefficient ν comprised in the interval $[0, 1[$. The value 1 is excluded in order to avoid choosing a solution on the edge of the polygon.

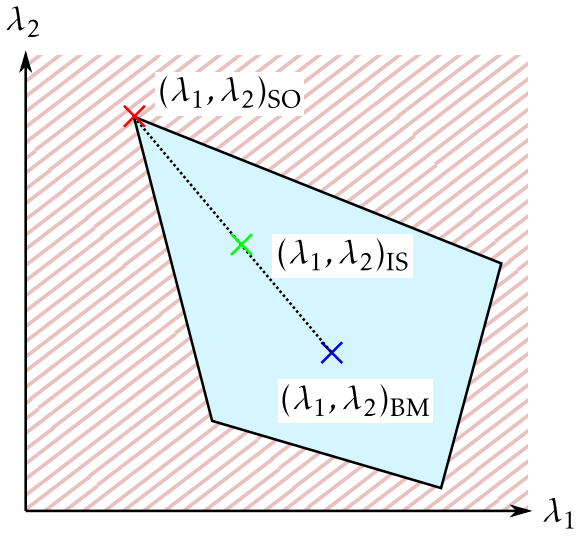

$$\lambda_{1,IS} = \nu(\lambda_{1,SO} - \lambda_{1,BM}) + \lambda_{1,BM}$$
$$\lambda_{2,IS} = \nu(\lambda_{2,SO} - \lambda_{2,BM}) + \lambda_{2,BM}$$
$$\nu \in [0, 1[$$

Figure 4.9: Representation of intermediate point (IS) inside the feasible polygon

If $\nu = 0$, the intermediate solution equals the solution found with the barycenter method $(\lambda_1, \lambda_2)_{BM}$. On the other hand, as ν tends towards 1, the solution approaches $(\lambda_1, \lambda_2)_{SO}$ and the maximum stiffness.

Experimental results of the SOTDA including the stiffness coefficient are provided in Sec. 4.6, in a static pose and along a path.

4.4 Controllers

This section covers the controllers considered for the *Controller* box of the previous control architectures. A similar controller is applied to the eight motors of the CDPR. Recall that the CDPR motors are controlled with a torque input, the internal control loop between desired torque and motor current being operated by the motor drivers. The control input is a torque (N m) applied by the B&R servo drives every 2 ms (500 Hz), which is the highest possible rate on the prototype hardware. The drives internal current/torque loop has a 50 µs cycle time (20 kHz). Motor encoders provide position and velocity feedback.

The test trajectory described in Section 1.4.1 gives the desired MP pose, *i.e.* MP position and orientation, which are converted into desired motor positions and velocities using the inverse CDPR geometric and kinematic models, from Eqs. (2.2) and (2.16).

Two families of controllers have been implemented and tested: proportional-derivative and new generation of sliding mode control. Concerning this latter [Tah+18b], its main feature is that it balances between linear and sliding mode control to take advantage of these two classes of control, that are robustness and accuracy for sliding mode control, and smoothness and reduced energy consumption for linear state feedback.

4.4.1 Proportional-derivative controller

Proportional-derivative (PD) controllers are already widely used in industry and machinery. Industrial motors are usually equipped with position sensors making the implementation of a PD controller particularly simple. The choice of a PD controller compared to the full PID is based here on its asymptotically stable [KD04]. Its main drawbacks are the static error between the desired and real position of the robot as well as a tuning that often requires iteration. In addition, this controller can be sensitive to noise and its settings are optimal only around an operating point. The scheme representation of the PD controller is presented in Fig. 4.10.

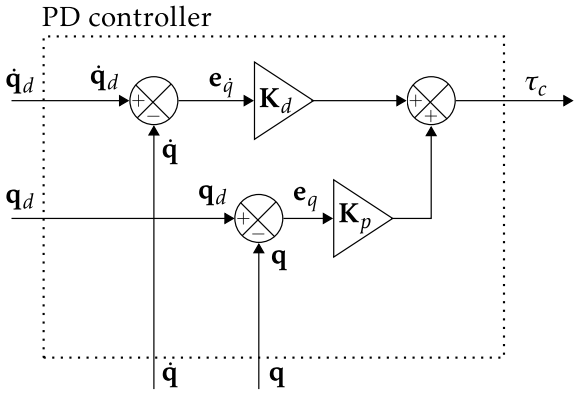

Figure 4.10: Internal structure of the PD controller.

The control input vector of motor torques $\boldsymbol{\tau}_{\mathrm{PD}}$ generated by the controller reads as

$$\boldsymbol{\tau}_{\mathrm{c}} = \mathbf{K}_{\mathrm{p}}\mathbf{e}_q + \mathbf{K}_{\mathrm{d}}\mathbf{e}_{\dot{q}} \tag{4.15}$$

with $\mathbf{e}_q$ the difference between the desired and actual motor positions and $\mathbf{e}_{\dot{q}}$ being the difference between the desired and actual motors velocities.

In a decentralized control architecture, each motor is independently controlled:

then, the matrices $\mathbf{K}_\mathrm{p}$ and $\mathbf{K}_\mathrm{d}$ are diagonal and read as

$$\mathbf{K}_\mathrm{p} = \mathrm{diag}(K_{\mathrm{p},1} \dots K_{\mathrm{p},i} \dots K_{\mathrm{p},m}) \quad \text{and} \quad \mathbf{K}_\mathrm{d} = \mathrm{diag}(K_{\mathrm{d},1} \dots K_{\mathrm{d},i} \dots K_{\mathrm{d},m}) \tag{4.16}$$

For simplicity and since the identified motor friction coefficients have been found to be similar across all motors, the eight decentralized controllers have been tuned by a similar manner: $K_p = K_{p,1} = K_{p,2} \dots$ and $K_d = K_{d,1} = K_{d,2} \dots$. However, it could be possible to independently adjust the gains of each motor accordingly to their typical error along the test trajectory or interdependence.

In the remainder of this thesis, K_p and K_d have been tuned so as the robot achieves accuracy and stability with the CDPR platform (MP), without external wrench or load. The values K_p and K_d for ROMP and ROWC are given in Table 4.1.

The PD controller was tuned using the standard Ziegler-Nichols method [ZN95], during which was determined the "critical" gain K_u, that is the ultimate gain producing oscillations of period T_u. Values of the proportional and derivative gains, K_p and K_d respectively, are then derived from Table 4.1. This method provides a good tuning starting point. However, since this method is applied along a single typical trajectory of the platform, these gains will probably not be optimal due to system nonlinearities (cables, motors, etc.).

Table 4.1: Ziegler-Nichols equations for PD control and chosen values.

Gain	Ziegler-Nichols (PD)	ROMP values	ROWC values
K_p	$0.8K_u$	0.3	0.008
K_d	$K_uT_u/10$	0.03	0.0012

4.4.2 Balancing sliding mode/linear controller

Sliding mode control is a nonlinear class of control laws that is particularly interesting for its accuracy, stability and robustness versus perturbations and uncertainties.

However, due to the presence of a sign function, discontinuity in the control can lead to an effect called *chattering*, *i.e.* that leads to high frequency oscillations of the actuator; these latter can lead to wear of mechanical elements. This phenomenon is particularly present for first order sliding mode control, and can be reduced by using higher order sliding mode methods [Lev93; Sht+14; EP14; YPP17], where the discontinuous functions can appear in higher order dynamics of the output of the system; as a consequence, the chattering is reduced. An other drawback of sliding mode control is that the power consumption is generally higher than for linear control methods as the system is constantly excited to achieve high tracking accuracy.

In [Tah+18a], a very recent and novel controller has been proposed to dynamically balance between a linear controller and a sliding mode one, this sway being based on

the accuracy of the closed-loop system. In the sequel, this controller is defined as the sliding mode/linear (SML) controller. The objective of the SML controller is to take advantage of both control strategies: *i)* reduced chattering and energy consumption compared to sliding mode control and *ii)* accuracy, stability and robustness in spite of perturbations and uncertainties. The SML controller equations for one motor are described thereafter.

The dynamics of the motors [LG13] are given by

$$\boldsymbol{\tau}_m = \mathbf{I}_q\ddot{\mathbf{q}} + \mathbf{F}_v\dot{\mathbf{q}} + \mathbf{F}_s\text{sign}(\dot{\mathbf{q}}) + \frac{R}{r_w}\mathbf{t} \tag{4.17}$$

where $\mathbf{I}_q$ is the diagonal matrix containing the moment of inertia of the gearmotors and winches associated to each motor, and $\mathbf{F}_c$ and $\mathbf{F}_v$ are respectively the diagonal matrices containing the static and viscous friction coefficients for each motor.

From the motor dynamic model (equation 4.17), the CDPR inverse kinematic model (equation (2.16)) and the CDPR dynamic model (equation (2.18)), defining the state vector as $\mathbf{x} = \begin{bmatrix}\mathbf{q} & \dot{\mathbf{q}}\end{bmatrix}^{\mathrm{T}}$ and the system input as $\mathbf{u} = \boldsymbol{\tau}_m$, the system can be represented as a standard nonlinear system of the form

$$\mathbf{x} = f(\mathbf{x}) + g(\mathbf{x})\mathbf{u} \tag{4.18}$$

The system is nonlinear and affine in the control input $\mathbf{u}$. Furthermore, $f(\mathbf{x})$ is uncertain due to the presence of $\mathbf{w}_e$ in (equation (2.18)).

The vector sliding mode variable $\boldsymbol{\sigma}$ is defined as

$$\boldsymbol{\sigma} = (\dot{\mathbf{q}}_d - \dot{\mathbf{q}}) + \lambda(\mathbf{q}_d - \mathbf{q}) \tag{4.19}$$

$$= \mathbf{e}_{\dot{q}} + \lambda\mathbf{e}_q \tag{4.20}$$

with $\mathbf{q}_d$ and $\mathbf{q}$ respectively the desired and current motor angular positions, $\dot{\mathbf{q}}_d$ and $\dot{\mathbf{q}}$ respectively the desired and current motor velocities, $\mathbf{e}_q$ and $\mathbf{e}_{\dot{q}}$ the corresponding tracking errors and λ a strictly positive parameter ($\lambda > 0$).

Similarly to the PD controller, eight individual SML controllers have been implemented. The control signal $\mathbf{u}$ and sliding variables $\boldsymbol{\sigma}$ are 8×1 vectors, and u_i and σ_i are the singletons representing the control input and the sliding variable of the i^{th} motor, respectively. All SML controllers were tuned in a similar manner. As such, parameter λ is the same for all motors.

Sliding mode control must ensure that the sliding variable reaches and is maintained at zero in a finite time [Utk92; Sht+14]: given the definition (4.19) of $\boldsymbol{\sigma}$, when the sliding variable of the i^{th} motor σ_i tends to zero, the convergence of $e_{q,i}$, the i^{th} component of $\mathbf{e}_q$, to zero is guaranteed exponentially with a rate depending on the parameter λ. This is described as the *transient phase*. Then, the controller is in the

steady state: the sliding variable σ_i is maintained around zero and the dynamic of the control is defined by the differential equation $e_{\dot{q},i} = -\lambda e_{q,i}$, as such the higher λ, the faster the correction. This is described as the *sliding phase*.

$\boldsymbol{\sigma}$ has a relative degree of one with respect to $\boldsymbol{\tau}_m$. The time derivative of the sliding variable equals

$$\dot{\boldsymbol{\sigma}} = \mathbf{e}_{\ddot{q}} + \lambda \mathbf{e}_{\dot{q}} \tag{4.21}$$
$$= (\ddot{\mathbf{q}}_d - \ddot{\mathbf{q}}) + \lambda(\dot{\mathbf{q}}_d - \dot{\mathbf{q}}) \tag{4.22}$$
$$= (\ddot{\mathbf{q}}_d + \lambda(\dot{\mathbf{q}}_d - \dot{\mathbf{q}})) - \ddot{\mathbf{q}} \tag{4.23}$$

$\ddot{\mathbf{q}}_d$ and $\ddot{\mathbf{q}}$ being the desired and actual motor acceleration vectors, respectively. $\ddot{\mathbf{q}}$ is correlated to the motor torques $\boldsymbol{\tau}_m$ by equation (4.17). $\dot{\boldsymbol{\sigma}}$ then takes the form

$$\dot{\boldsymbol{\sigma}} = a(\mathbf{q}) + b(\mathbf{q})\boldsymbol{\tau}_m \tag{4.24}$$

where $b(\mathbf{q}) \neq 0$.

In order to design the twisting algorithm, the sliding variable is derived a second time ; one gets:

$$\ddot{\boldsymbol{\sigma}} = (\dddot{\mathbf{q}}_d - \dddot{\mathbf{q}}) + \lambda(\ddot{\mathbf{q}}_d - \ddot{\mathbf{q}}) \tag{4.25}$$
$$= (\dddot{\mathbf{q}}_d + \lambda(\ddot{\mathbf{q}}_d - \ddot{\mathbf{q}})) - \dddot{\mathbf{q}} \tag{4.26}$$
$$= h(\mathbf{q}) + j(\mathbf{q})\dot{\boldsymbol{\tau}}_m \tag{4.27}$$

with $j(\mathbf{q}) \neq 0$.

Each component of $\dot{\boldsymbol{\tau}}_m$ [Tah+18a], is defined as

$$\dot{\tau}_{m,i} = -K_1 \lceil \sigma_i \rfloor^{\frac{\alpha}{2-\alpha}} - K_2 \lceil \dot{\sigma}_i \rfloor^{\alpha} \tag{4.28}$$

with $\dot{\tau}_{m,i}$ the i^{th} component of $\dot{\boldsymbol{\tau}}_m$ and

$$\lceil \sigma_i \rfloor^{\alpha} = |\sigma_i|^{\alpha} \text{sign}(\sigma_i) \tag{4.29}$$

K_1 and K_2 are the controller gains, and $\alpha \in \begin{bmatrix} 0 & 1 \end{bmatrix}$ based on the following adaptation law:

$$\alpha = \max\left(-\beta\left(\frac{|\sigma_i|}{|\sigma_i| + \epsilon_\sigma} + \frac{|\dot{\sigma}_i|}{|\dot{\sigma}_i| + \epsilon_{\dot{\sigma}}}\right) + 1, 0\right) \tag{4.30}$$

with β, ϵ_σ and $\epsilon_{\dot{\sigma}}$ constant parameters chosen such that $\beta > 1$ and $\epsilon_\sigma, \epsilon_{\dot{\sigma}} > 0$. Values of these parameters for the experiments are provided in table 4.2. The control input $\boldsymbol{\tau}_m$ is then obtained by integrating its time derivative from Eq. (4.28).

The principle of the SML controller (Eqs. (4.28)-(4.30)) is the following: the value

of the variable α depends on the current tracking errors. If the absolute values of $|\sigma|$ and $|\dot{\sigma}|$ are large, it means that the closed-loop system is not accurate: then, the controller should lean towards a robust controller, namely the sliding mode control. That is the case because in such a situation, $\alpha \to 0$, then from Eq. (4.28), the control becomes a twisting one [Lev93]:

$$\dot{u}_i = -K_1 \text{sign}(\sigma_i) - K_2 \text{sign}(\dot{\sigma}_i) \tag{4.31}$$

On the other hand, if these errors are small, in order to reduce chattering and energy consumption, the controller should lean towards the linear control behavior: that is the case because $\alpha \to 1$. The evolution of α regulates the compromise to maintain high accuracy while reducing chattering. $\dot{u}_i$ then tends towards the expression

$$\dot{u}_i = -K_1 \sigma_i - K_2 \dot{\sigma}_i \tag{4.32}$$

The control input u is then obtained by integrating its time derivative from Eq. (4.28). Figure 4.11 presents the internal structure of the controller.

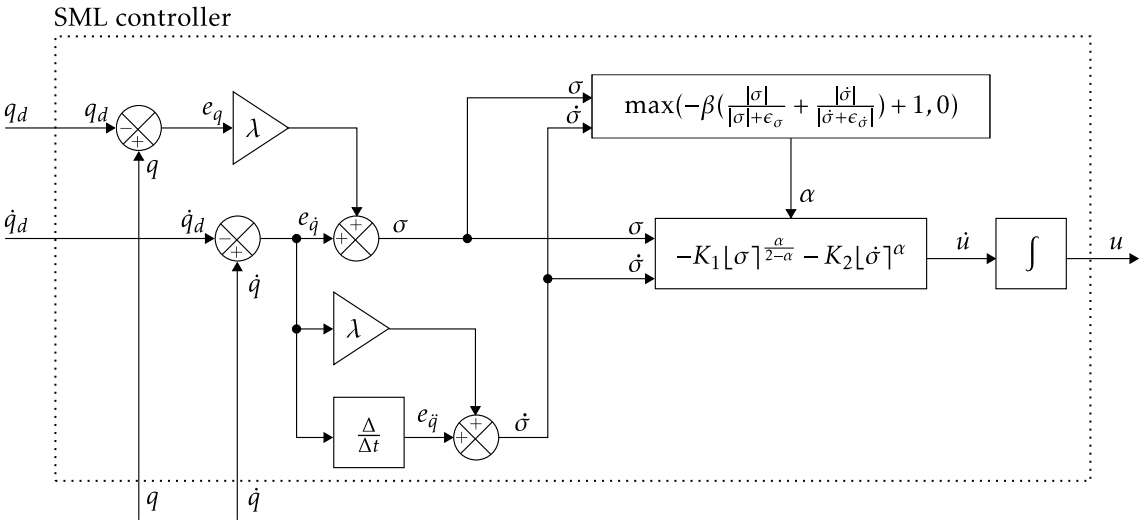

Figure 4.11: Internal structure of the SML controller for one motor.

In order to guarantee convergence of the closed-loop system, the gains K_1 and K_2 must be positive and follow the twisting condition [Lev93]:

$$\begin{aligned} K_1 > K_2 > 0, \quad & (K_1 - K_2) b_m > a_M \\ & (K_1 + K_2) b_m - a_M > (K_1 - K_2) b_m + a_M \end{aligned} \tag{4.33}$$

with a_M, b_m and b_M positive constants such that for each motor

$$\left|a_i(q)\right| \leqslant a_M \tag{4.34}$$

$$0 < b_m \leqslant b_i(q) \leqslant b_M \tag{4.35}$$

The reduced energy consumption of the SML controller compared to the twisting algorithm is ensured by the following condition [Tah+18a]:

$$K_1\epsilon_\sigma + K_2\epsilon_{\dot{\sigma}} < K_1 - K_2 \tag{4.36}$$

A first tuning has been obtained from a Simulink® model based on the inverse geometric, kinematic and dynamic models presented in Chapter 2.

Table 4.2: SML controller parameter values for ROMP.

Parameter	ROMP values
λ	0.15
β	1.01
ϵ_σ	4
$\epsilon_{\dot{\sigma}}$	80
K_1	4
K_2	2

The following proposes a tuning methodology to find initial working parameters:

1. select a value of $\lambda > 0$ in relation to the desired closed-loop dynamics and $\beta > 1$ with respect to the desired closed-loop accuracy;
2. set ϵ_σ to zero to force α to zero and achieve pure sliding mode control;
3. tune gains K_1 and K_2 to achieve good sliding mode control accuracy;
4. observe $\boldsymbol{\sigma}$ and $\dot{\boldsymbol{\sigma}}$ values, choose values for ϵ_σ and $\epsilon_{\dot{\sigma}}$ with the same proportionality as the average ratio between $\boldsymbol{\sigma}$ and $\dot{\boldsymbol{\sigma}}$;
5. adjust β, ϵ_σ and $\epsilon_{\dot{\sigma}}$ so that the variable α is not always equal to zero but evolves between $[0, 1]$;

After some iterations, the gains and parameters are set to obtain a good compromise between accuracy and evolution of α.

Recall that K_1 and K_2 are the gains of the controller: they must be chosen sufficiently large in order to counteract perturbations and uncertainties effects. β and ϵ_σ,$\epsilon_{\dot{\sigma}}$ have opposing effects on the evolution of α. These parameters should be chosen to calibrate the controller behavior with respect to the desired compromise between accuracy and chattering/consumption reduction: if β is increased or ϵ_σ,$\epsilon_{\dot{\sigma}}$ are decreased, the overall value of α decreases, the system leans towards sliding mode. As a consequence, the control accuracy is improved with higher energy consumption. On the other hand, if β is decreased or ϵ_σ,$\epsilon_{\dot{\sigma}}$ are increased, α increases, the chattering and energy consumption are reduced as the linear control contribution increases.

However, the robustness, and then the accuracy, are reduced.

The controller (Eqs. (4.28)-(4.30)) is implemented in a 500 Hz real-time loop. In addition to the choice of the control parameters and gains, the accuracy of the method also depends on the controller running frequency. In order to compute the control input at the fastest possible rate, the Euler integrate method is used. This numerical integration method choice is due to its very low computational cost and the fact that the controller and integration codes both run at the maximum frequency achievable on the hardware.

4.5 Position control experiments (ROMP)

Several control architectures have been tested experimentally on ROMP along the test trajectory described in Sec. 1.4.1, with the four loads visible in Fig. 4.12.

The three cases MP, MPM1 and MPM2 represent typical loads of ROMP: the moving-platform only (MP) with a mass $m_{MP} = 366$ kg, the platform carrying a metal plate M_1 for a total mass of $m_{MPM1} = 488$ kg (MPM1), and the platform carrying a metal plate M_2 for a total mass of $m_{MPM2} = 615$ kg (MPM2). The specific case of the platform without its cross/end-effector, of mass $m_{MPNC} = 266$ kg (MPNC), is also considered to benefit from a larger range of loads.

Table 4.3 summarizes the control architectures experimented on the prototype, along with the controller used.

Table 4.3: Control architectures experimented on prototype ROMP

Load	MPNC		MP		MPM1		MPM2	
Architecture	PD	SML	PD	SML	PD	SML	PD	SML
PC1	×	×	×	×	×	×	×	×
PC2	×	×	×	×	×	×	×	×
PC3	×	×	×	×	×	×	×	×
PCE				×		×		×

Recall that the robot follows the pick-and-place trajectory from points A to E between $t = 0$ s and $t = 30$ s, and back from points E to A between $t = 30$ s to $t = 60$ s. In the sequel, results are either presented for the totality of the trajectory in order to observe the behavior of the controller in the transient phase, or only for the second half of the trajectory ($t = 30$ s to $t = 60$ s), in which controllers reached steady state.

4.5.1 PC1 control architecture joint space results

Firstly, the behavior of all motors are observed in the worst case scenario in order to discuss the presentation of the results in the sequel. Figure 4.13 shows the eight motor position errors e_q (degrees) for the heaviest payload (615 kg). The transient

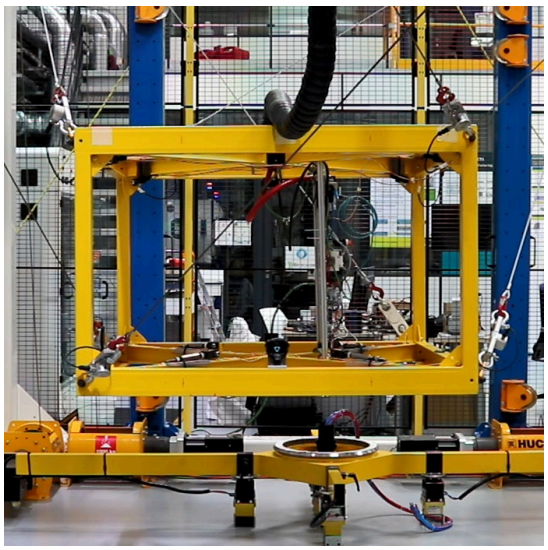

(a) Platform without cross (MPNC, 266 kg)

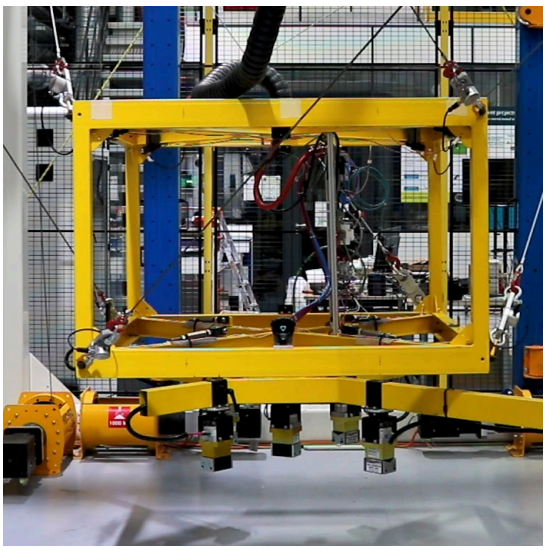

(b) Complete platform (MP, 366 kg)

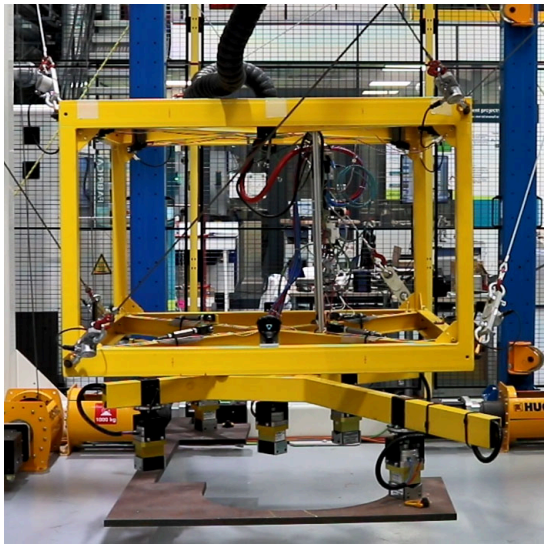

(c) Platform with plate M1 (MPM1, 488 kg)

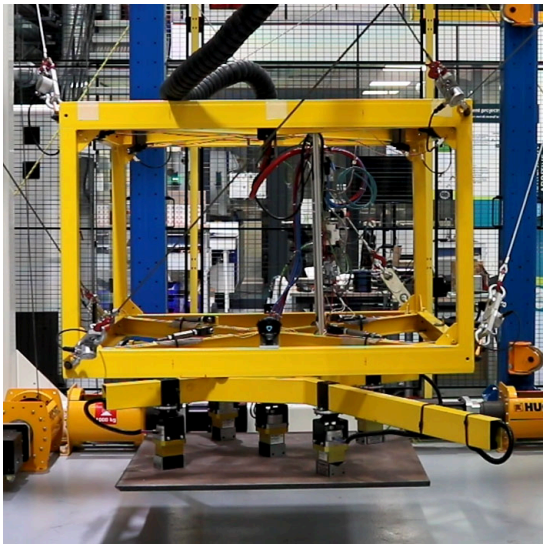

(d) Platform with plate M2 (MPM2, 615 kg)

Figure 4.12: The four loads experimented on prototype ROMP

phase of the SML controller is clearly visible here. It also appears that the motors do not have the same level of errors in the first half of the trajectory. Since the platform is closer to the corner of the workspace in which are located Motors 5 and 6, the latter must provide the largest effort to support the platform and its load. This is verified in Fig. 4.14 presenting the tensions in all cables along the trajectory, where Motors 5 and 6 present the highest starting cable tensions at around 2000 N. As such, Motor 6 suffers the largest error, up to 150 degrees with the SML controller. However, this error is corrected over the first half of the trajectory and by $t = 20$ s, once in steady state, the SML controller in the PC1 architecture (PC1-SML) reached low and stable levels of errors across all motors, consistently lower than those of the PC1 architecture with the PD controller (PC1-PD).

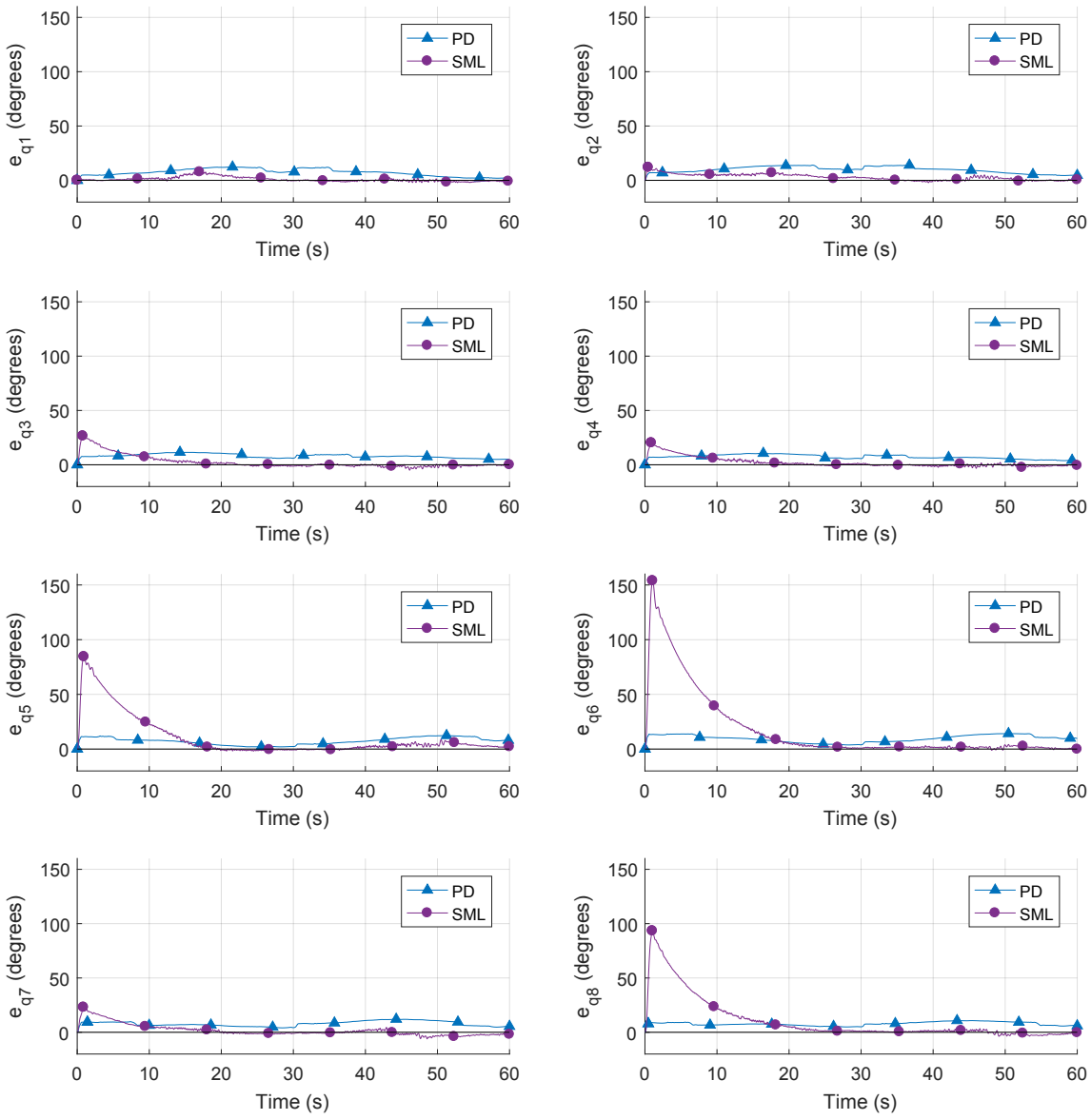

Figure 4.13: Position errors e_q (degrees) of the eight motors for the heaviest payload (615 kg) with PD and SML controllers.

As each motor is individually controlled, the angular position tracking errors

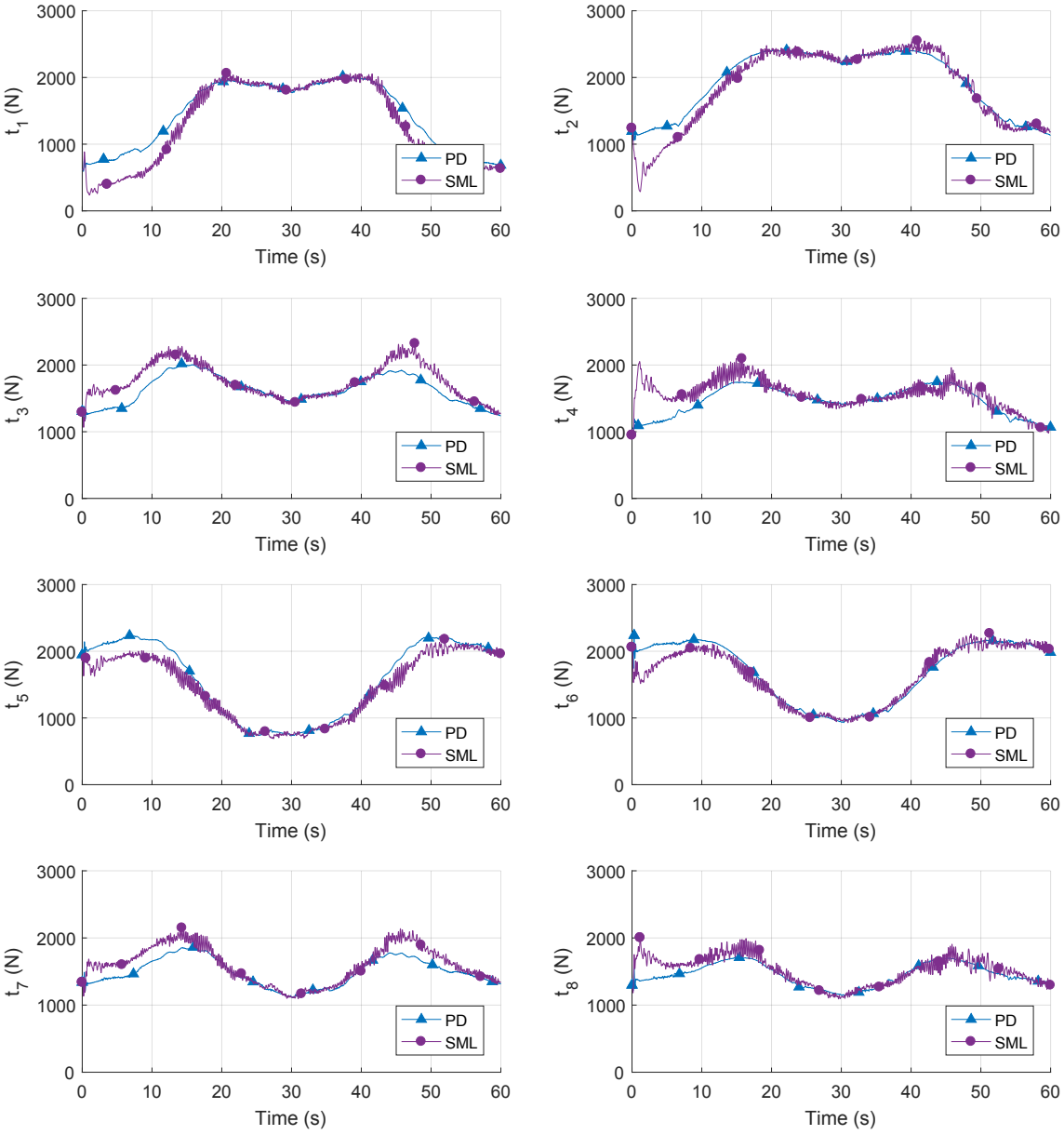

Figure 4.14: Cable tensions t (N) of the eight motors for the heaviest payload (615 kg) with PD and SML controllers.

depend on the considered motor. In order to keep the same vertical axis scale in all the figures of this section, and to improve readability, the observations must be focused on a single motor whose maximum errors is not too large. Otherwise, comparison between the different controllers in the steady state would be difficult. While Motor 6 shows the largest error out of any motor, the scale of the vertical axis renders the behavior of other controllers difficult to properly observe on the figures. Motor 4 is then selected in the sequel of this section for its smaller maximum error, but still visible, error in the transient phase, thus allowing for a smaller vertical axis limit. Standard Deviation (STD), Root Mean Square (RMS) and Maximum of the Absolute value (MAX ABS) for all motor tracking errors, along the second half of the trajectory in which all controllers are in steady state, are provided in Fig. 4.17 for PC1-PD and PC1-SML.

Accordingly, Fig. 4.15 presents Motor 4 angular error e_{q4} along the trajectory, with the four payloads. The PD controller is tuned for the nominal mass of the platform only, $m_{MP} = 366$ kg. As expected, PC1-PD presents a static error which increases with the mass, the maximum error being equal to 11 degrees for the heaviest payload (MPM2). In the case of PC1-SML, the motor position error oscillates more. However, once in steady state, the static error is around zero. The controller has been tuned for lightest load ($m_{\hat{\imath}MPNC} = 266$ kg. As a consequence the initial error is close to zero in this case. As the load increases, so does this initial error. It should be noted that this error was always corrected by the end of the first half of the trajectory ($t = 20\ s$). In continuous operation, the PC1-SML controller would then maintain the performances of the steady state.

Figure 4.16 presents the control input for Motor 4 along the test trajectory. As there is no knowledge of the mass at the beginning of the motion, the two controllers start from an initial null torque output, before reaching the necessary torque to control the motor despite the load on the platform and friction in the gearmotors. In steady state, both controller generate a similarly shaped control signal, although slight chattering is visible in the case of the sliding mode, as expected.

From Fig. 4.17, the increasing RMS and MAX of the motor position errors along with the mass increase can be clearly observed for PC1-PD, in particular for Motor 6 which presents an absolute maximum error of 7.1 degrees for load MPNC, and 14.1 degrees for load MPM2. On the other hand, once in steady state, PC1-SML gives more stable values across all criteria for all load levels, with a maximum of 8.9 degrees (motor 8), resulting in a reduction of 36% of the maximum error. It appears however that for each load, a single motor presents a significantly higher error than the other ones.

In summary for the PC1 control architecture, it appears that PC1-PD led to the expected static error, while PC1-SML suffered from a strong transient behavior in motor position error but removes the error by an efficient way over the course

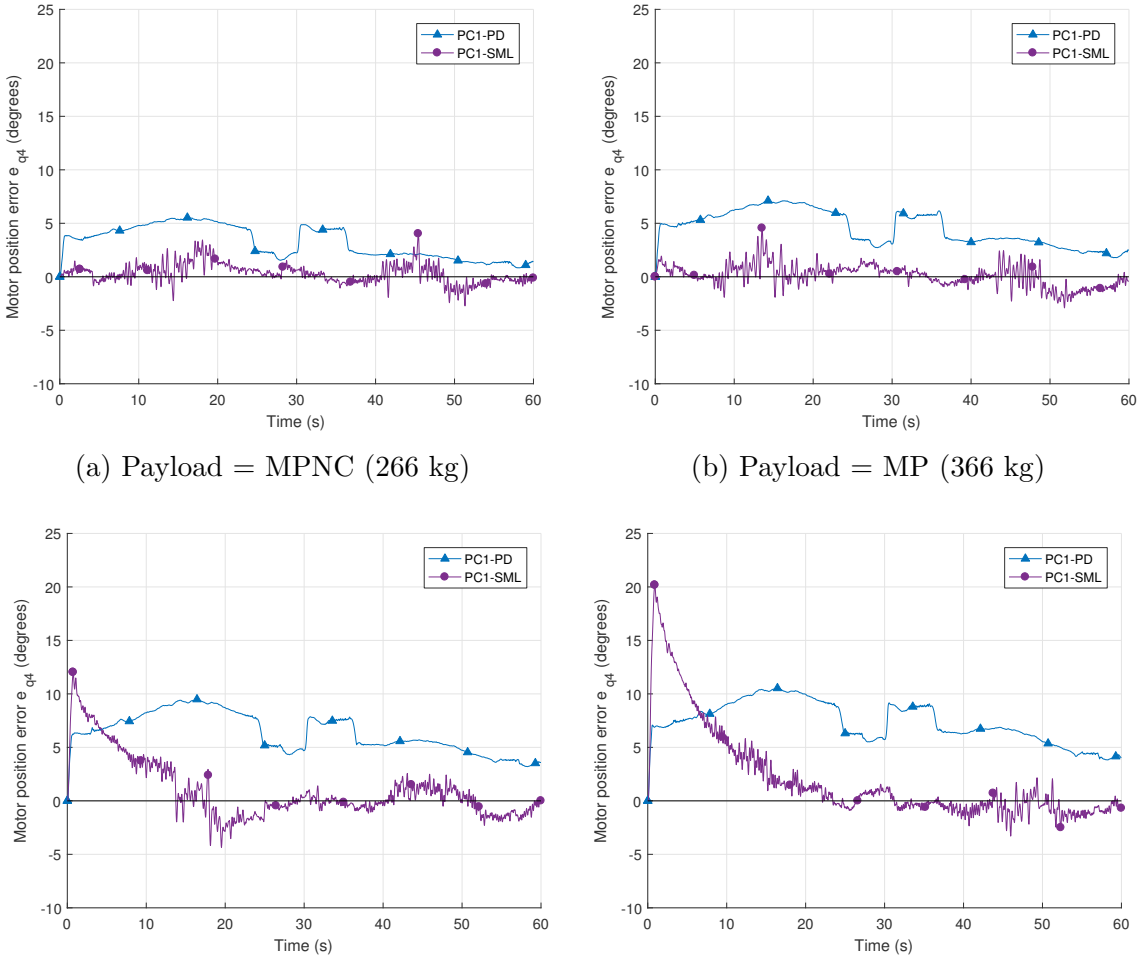

(a) Payload = MPNC (266 kg)

(b) Payload = MP (366 kg)

(c) Payload = MPM1 (488 kg)

(d) Payload = MPM2 (615 kg)

Figure 4.15: Motor 4 position error along trajectory for PC1 control scheme, with PD and SML controllers.

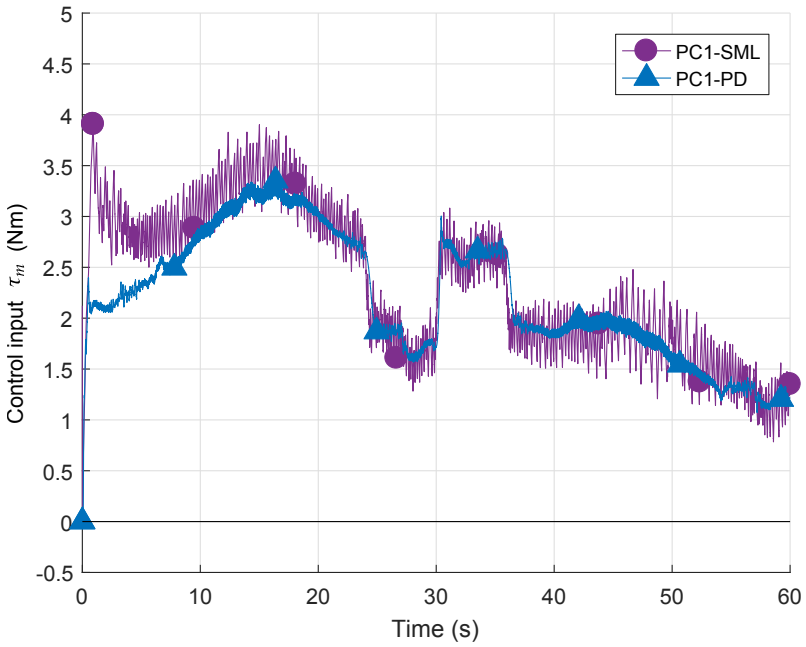

Figure 4.16: PC1 control input for Motor 4 with the heaviest load (MPM2).

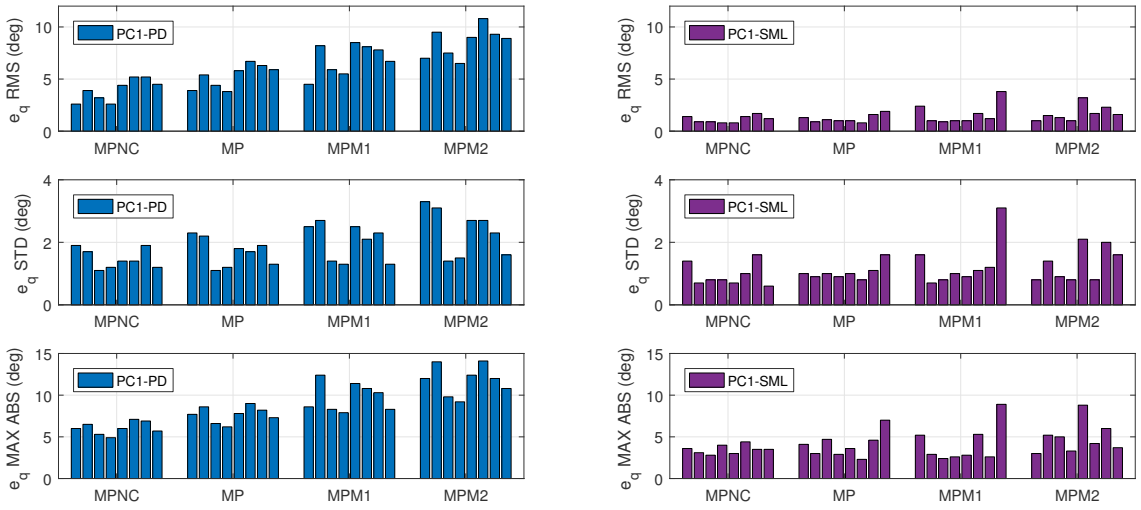

Figure 4.17: Analysis of $\mathbf{e}_q$ for Motors 1 to 8 (left to right), with PC1 along trajectory second half (degrees).

of the trajectory. The time taken to reduce the tracking error is determined by λ, with $\lambda = 0.15$ corresponding to a convergence time of around 20 seconds, which is observed in Fig. 4.15d. This value has been selected low in order to avoid high dynamics of the platform in these experiments, due to the large payload, but could have been increased to reduce the duration of the transient phase. However, once in steady state, the sliding mode controller error was consistently lower than with the PD control law.

4.5.2 PC2 control architecture joint space results

Motor 4 position errors along the trajectory are plotted in Figs. 4.18a–4.18d. Recall that the feedforward term for dynamic anticipation is based on the platform mass only, either equal to 266 kg in the case of MPNC (light version of the platform), or to 366 kg (complete platform) for cases MP, MPM1 and MPM2.

It is immediately visible that the errors are reduced compared to the PC1 results. For PC2-PD, it can be observed that when the motors only support the platform (MPNC and MP) and since the platform mass is perfectly known in these two instances, no static error is visible. From Fig. 4.19, the maximum error across all motors is equal to 1.4 degrees for both MPNC and MP (Motor 7). If the platform carries a metal plate of unknown mass, the static error naturally reappears but is reduced compared to PC1-PD, with a maximum error of 6.3 degrees for Motor 2. This error is also slightly lower than with PC1-SML for the heaviest load.

In the case of PC2-SML, it can be noted that the initial error observed with PC1-SML is eliminated. Some variations in the shape of the error curve are visible, but the general behavior is constant for all loads. The maximum error along the second half of the trajectory (Fig. 4.19) is reached for load MP, with 7.3 degrees. However, it appears that as the load increases, the maximum error for the heaviest

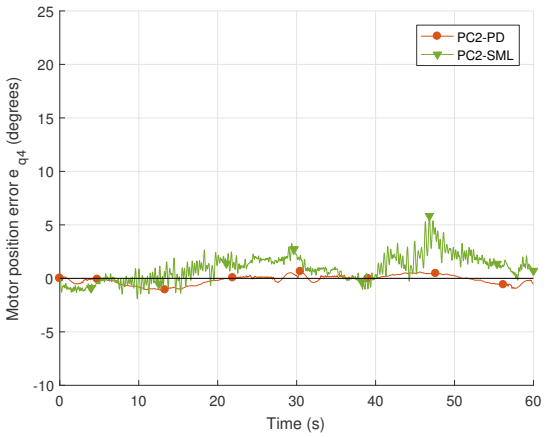

(a) Payload = MPNC (266 kg)

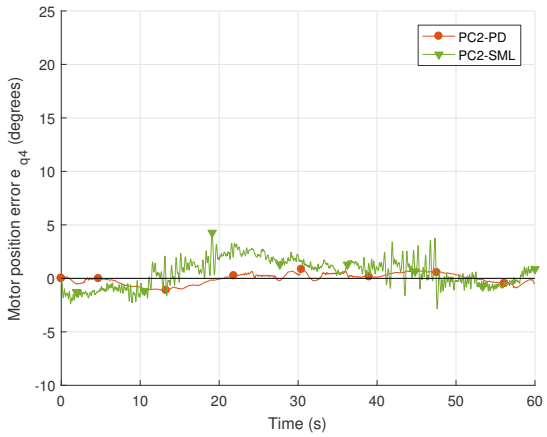

(b) Payload = MP (366 kg)

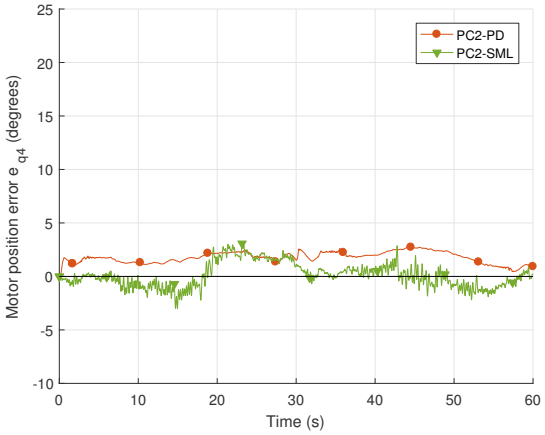

(c) Payload = MPM1 (488 kg)

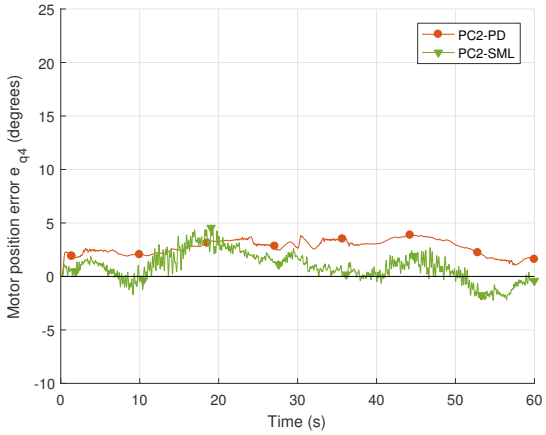

(d) Payload = MPM2 (615 kg)

Figure 4.18: Motor 4 position error along trajectory for PC2 control scheme, with PD and SML controllers

load MPM2 is reduced to 3.7 degrees. Further study will be necessary to determine the exact cause of this behavior. An initial guess is that the contribution of the feedforward and SML controller to the generated motor output torque are a this time not optimally balanced. Since the feedforward term compensates for most of the total load, the SML controller gains could be tuned differently, with lower gains for a smoother behavior.

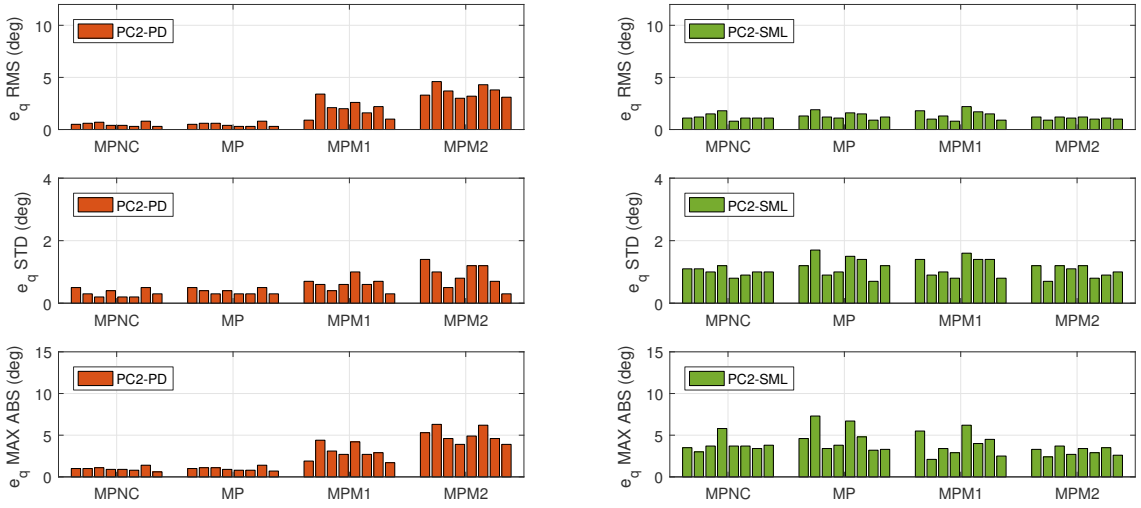

Figure 4.19: Analysis of $\mathbf{e}_q$ for Motors 1 to 8 (left to right), with PC2 along trajectory second half (degrees).

The torque $\boldsymbol{\tau}_m$ control input of Motor 4 in the case of the heaviest payload by PC2-PD and PC2-SML is shown in Fig. 4.20. The torque $\boldsymbol{\tau}_m$ is initially at around 1.5 N m, this value being generated by the feedforward terms. Each controller has to compute the remaining necessary torque to achieve the desired position. The motor orientation changes during upward or downward motions of the platform are also sharper, due the friction compensation term which effectively predicts the static friction sign change. The two control inputs are both very similar in their overall shape. Although the SML controller still presents slight chattering, no large transient is apparent. The STD of the PC1-SML tracking error are also more consistent across all loads and motors compared to PC1-SML.

The contribution of the feedforward terms for Motor 4 are presented in Fig. 4.21, with $\boldsymbol{\tau}_{ff} = \boldsymbol{\tau}_{da} + \boldsymbol{\tau}_{fc}$ corresponding to the sum of both the dynamic anticipation and friction compensation. The feedforward applied in the PC2 architecture is traced in red with square markers, and was computed based on the mass of the platform only. The initial starting torque of 1.5 N m as seen in Fig. 4.20 is recognizable. The computed feedforward represents more than half of the control input along the trajectory, even with the mass estimation error. For comparison, the blue line represents the value of the feedforward if the total mass of MPM2 is provided. The shape of the latter is very similar to the actual control output $\boldsymbol{\tau}_m$ for the heaviest load from Fig. 4.20. This confirms that a good anticipation of the motor torques is

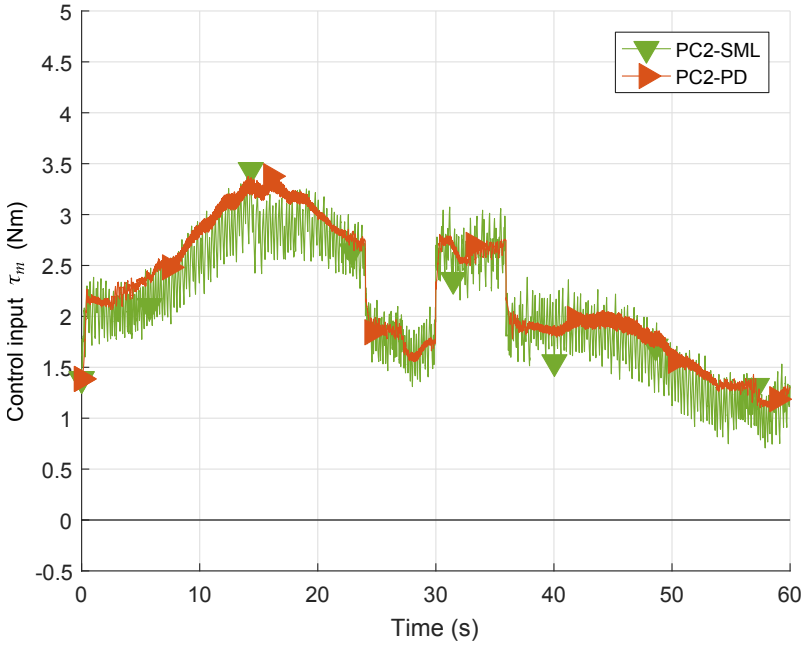

Figure 4.20: PC2 control input for Motor 4 with the heaviest load (MPM2).

possible with the current model, although $\boldsymbol{\tau}_{ff}$ is slightly overestimated for MPM2 around $t = 15$ s.

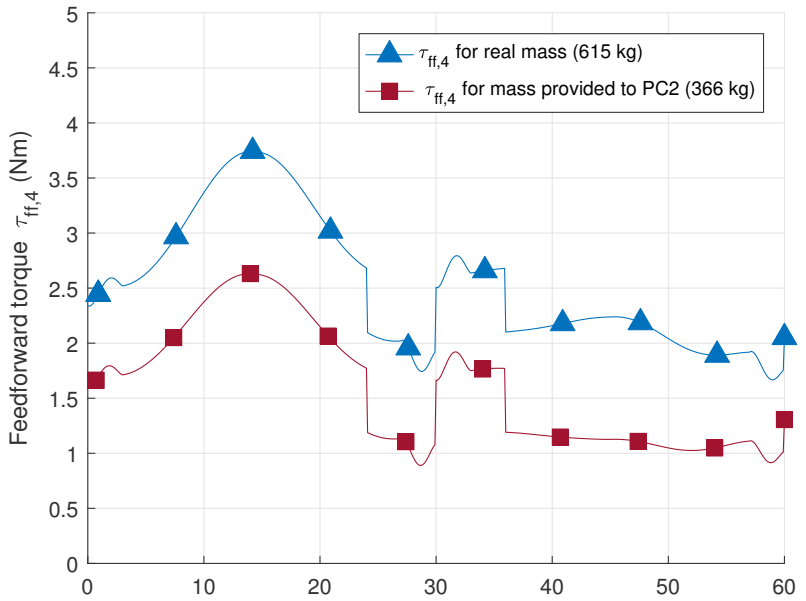

Figure 4.21: Torque of feedforward terms $\boldsymbol{\tau}_{ff}$ as a function of mass, in case MPM2.

With the PC2 architecture, the PD initial drop previously observed has been scaled down. The static errors appear to remain when a metal plate of unknown mass is carried (MPM1 and MPM2), although they are greatly reduced when the nominal mass is equal to the real mass (MPNC and MP). Regarding the SML controller, the transient phase is also significantly reduced with PC2-SML thanks to the feedforward, and its performances are very similar across all loads, including the standard deviation and maximum error. While the SML controller tuning could be

improved for intermediate loads, PC2-SML seems to be robust and an interesting possibility for the metal handling application.

4.5.3 PC3 control architecture joint space results

As previously, Motor 4 position error with PC3-PD and PC3-SML is presented in Figs. 4.22a–4.22d. Concerning the PC3-PD architecture, it is visible that with the real-time update of the mass term in the feedforward, the static error is strongly reduced for all loads, including MPM2. The error oscillates around zero all along the trajectory and provides the best accuracy (see Fig. 4.23), with a maximum error of 2.1 degrees for load MPM1, and 1.6 degrees for load MPM2. Recall it is obtained with the same PD tuning as in PC1-PD and PC2-PD, with the addition of the real-time mass estimation.

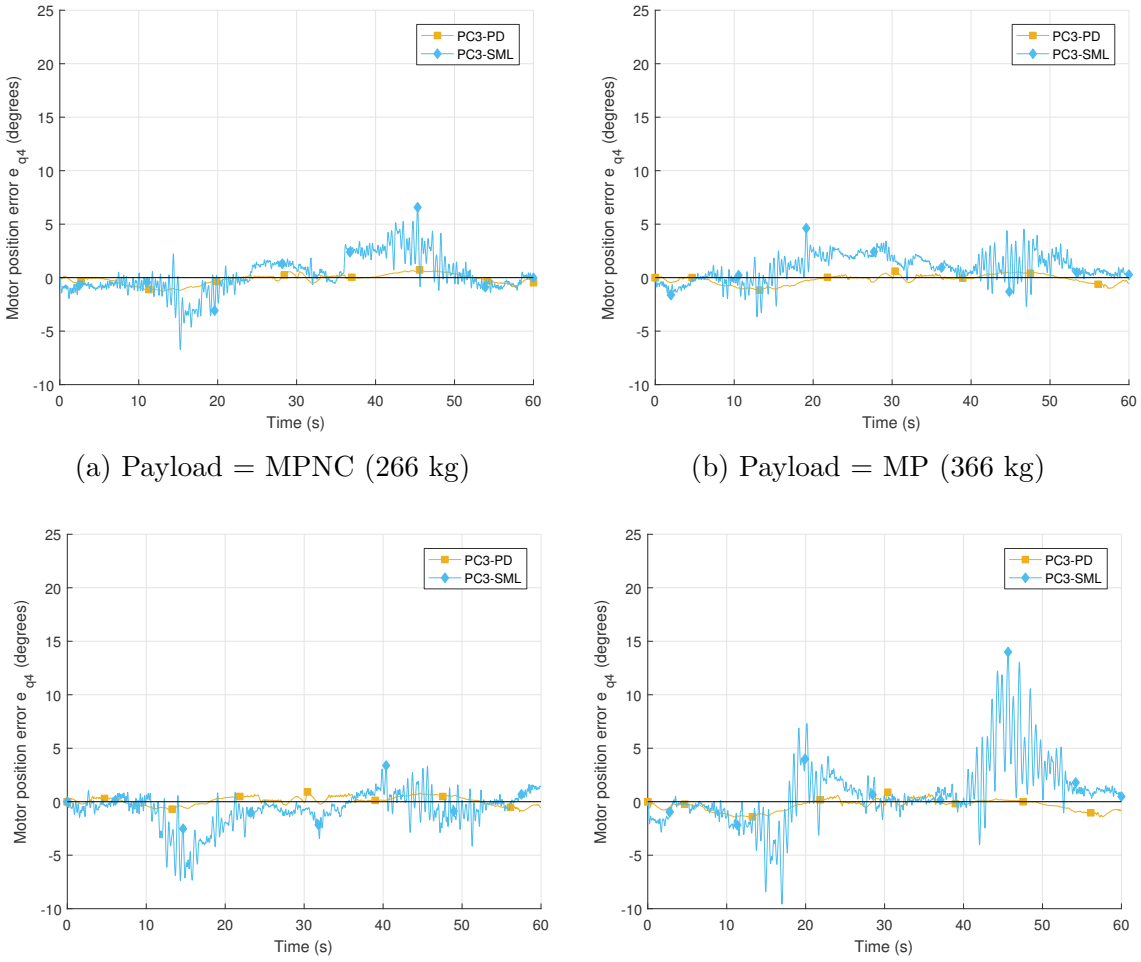

(a) Payload = MPNC (266 kg)

(b) Payload = MP (366 kg)

(c) Payload = MPM1 (488 kg)

(d) Payload = MPM2 (615 kg)

Figure 4.22: Motor 4 position error along trajectory for PC3 control scheme, with PD and SML controllers.

On the other hand, PC3-SML suffers from oscillations due to the real-time mass estimation in combination with the sliding mode control chattering. Chattering of the motor torque induces cable tensions variations, generating errors in the mass

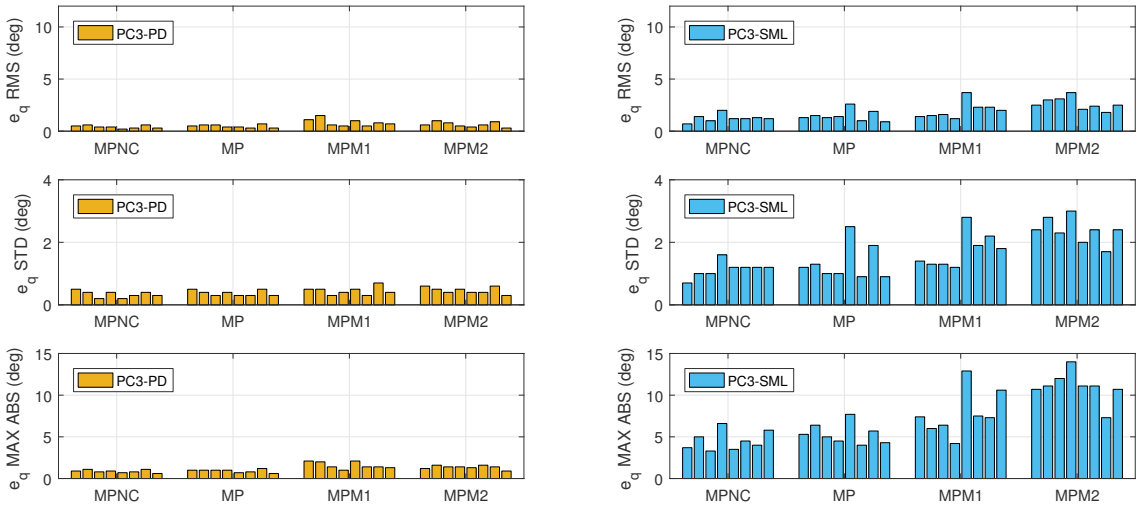

Figure 4.23: Analysis of $\mathbf{e}_q$ for Motors 1 to 8 (left to right), with PC3 along trajectory second half (degrees).

estimation. The errors in the mass estimation are clearly visible in Fig. 4.24 as oscillations with a frequency around 1 Hz, the amplitude of the variations increasing with the load. From Fig. 4.23, the maximum error with PC3-SML was reached for the heaviest load MPM2, at 14 degrees. As a consequence, it appears that the real-time mass estimation is not well suited as a direct feedback in the case of PC3-SML.

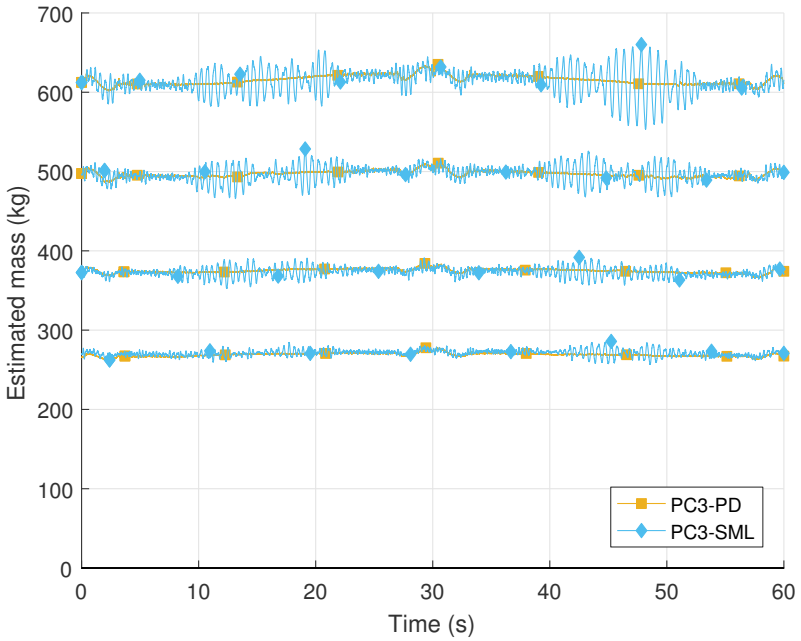

Figure 4.24: Estimated mass (kg) for the four payloads with PC3-PD and PC3-SML control schemes along trajectory.

Figure 4.25 shows the control input provided by PC3 for Motor 4 with the heaviest load MPM2. Oscillations affect PC3-SML control output, while PC3-PD maintains a low spread along the trajectory.

In this section, the use of real-time mass estimation as direct feedback and input

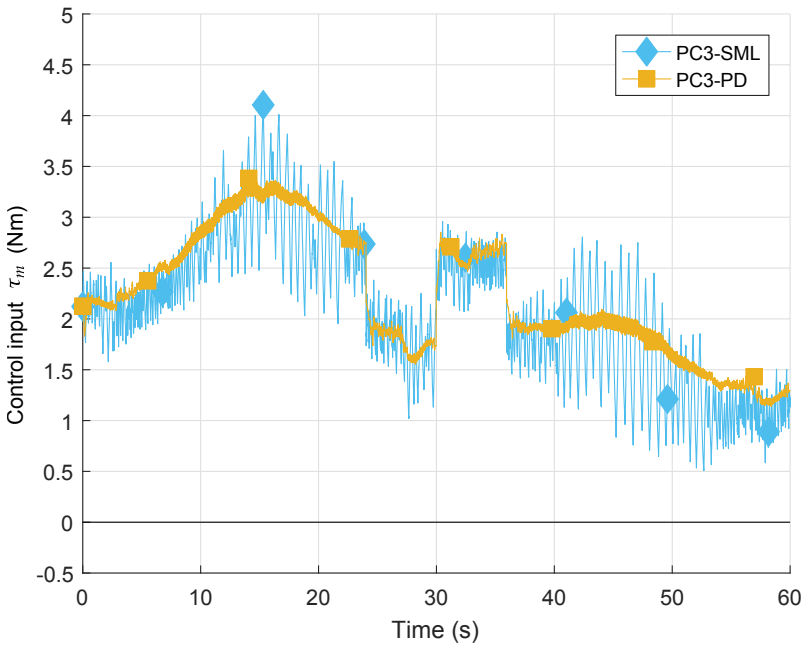

Figure 4.25: PC3 control input for Motor 4 with the heaviest load (MPM2)

has been experimented. Along the test trajectory, this additional information in the control scheme greatly improves the accuracy of the PD controller, even for the highest load. However, if the platform is disturbed, oscillation in the mass estimation can generate a sustaining oscillation. Combined with the residual chattering of the sliding mode controller, the overall performance is unfortunately decreased versus to PC2-SML. It is noteworthy than PC3-SML was still stable in spite of these strong oscillations.

In practice, real-time mass estimation would really be a benefit for continually changing loads (on-board tank emptying over time for example). In the metal plate handling application, the mass estimation could be made only once, just after picking a plate, and during a limited time; after this the mass is supposed known and this constant value is used in the controller. In this case, the expected performance are those of controllers PC2-PD and PC2-SML when the nominal mass equals the real mass.

4.5.4 PC1 to PC3 control architectures Cartesian errors

During the test trajectory, the platform pose is now captured using an HTC VIVE. The overall setup and inner working of the tracking are detailed in Sec. 1.4.3 and App. A. A tracker is attached on a side of the platform and is located inside the workspace using infrared lasers. This tracker has an offset in the base frame compared to the center of the platform P equal to $\begin{bmatrix}-0.001 & -0.330 & 0.695\end{bmatrix}^{\mathrm{T}}$ m, expressed in $\mathscr{F}_b$. In the sequel, the platform tracking error in the Cartesian space is calculated at the tracker level. The error is then calculated between the desired and measured tracker pose along the trajectory.

Cartesian error along z_b axis

The tracking errors along the axis z_b are discussed first, given that the vertical motions (along z_b) are the most affected by the load changes.

Figures 4.26a–4.26d display the position of the tracker attached to the platform along the test trajectory. The desired position of the tracker is the dashed black line. The impact of the global mass on the position accuracy is viewed by comparing the height of the tracker depending on the load.

While all controllers present similar behavior for MPNC, spread becomes apparent with MPM1 and MPM2. In particular, the transient phase of PC1-SML is visible in Fig. 4.26 corresponding to the heaviest load. It should also be noted that over the course of the trajectory, PC1-SML converges as PC2 and PC3 architectures, while PC1-PD maintains a steady static error.

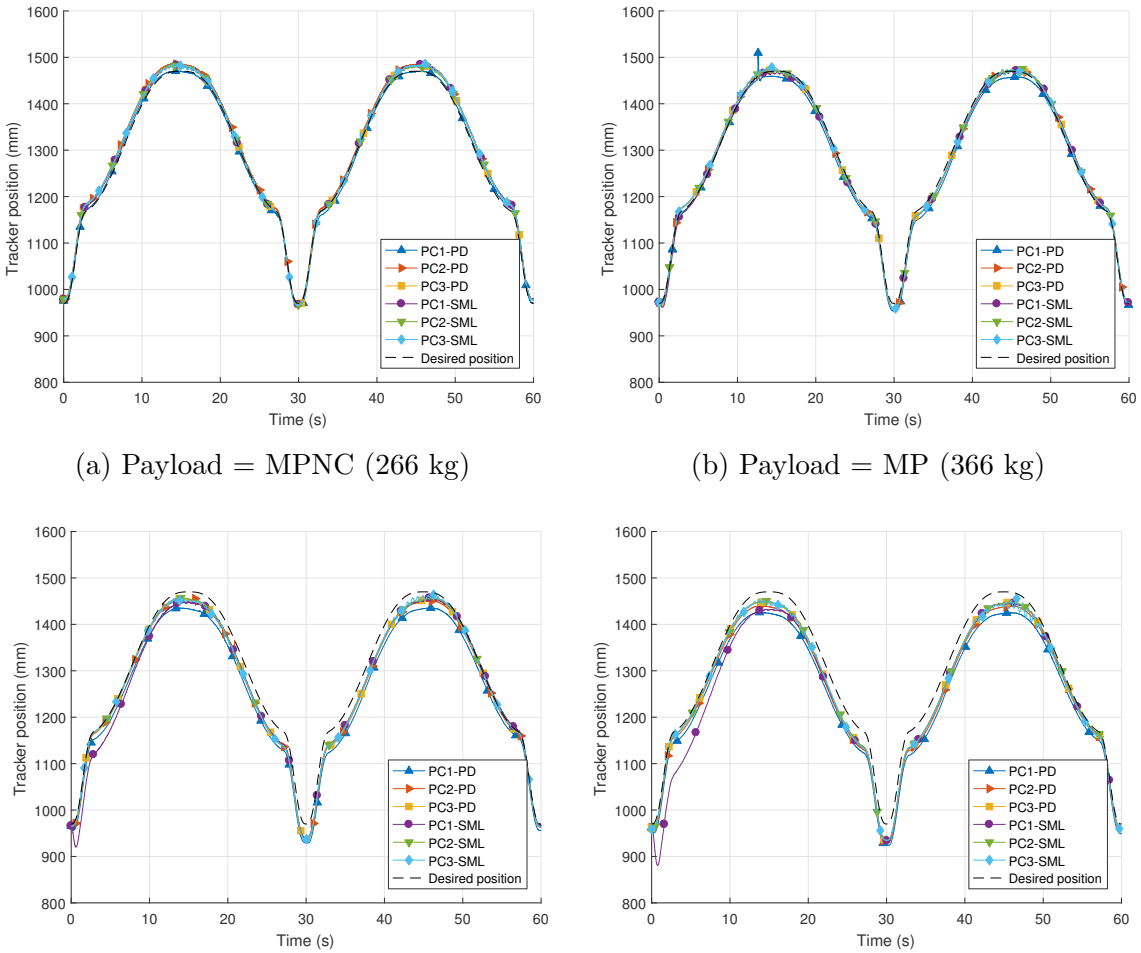

(a) Payload = MPNC (266 kg)

(b) Payload = MP (366 kg)

(c) Payload = MPM1 (488 kg)

(d) Payload = MPM2 (615 kg)

Figure 4.26: Cartesian position of tracker along z_b during trajectory

Figures 4.27a–4.27d present the Cartesian error between the desired and measured position of the tracker along the vertical axis z_b. The overall wave form of the Cartesian tracking error is mainly assumed to derive from a combination of platform orientation along the trajectory, CDPR modeling errors (and their consequence on

trajectory generation) and measurement tool inaccuracies. Nonetheless, despite this error it is possible to compare the controllers behaviors and accuracy relatively one to another. The downward trend of the average error is, on the other hand, directly due to mass augmentation and cable elasticity. This subject is discussed in Sec. 4.5.4.

As previously seen with the motor position error, the PC1 architecture suffers from an initial error, resulting in a drop of the platform. The static error of the PC1-PD architecture, and the initial error of PC1-SML are clearly visible on these figures.

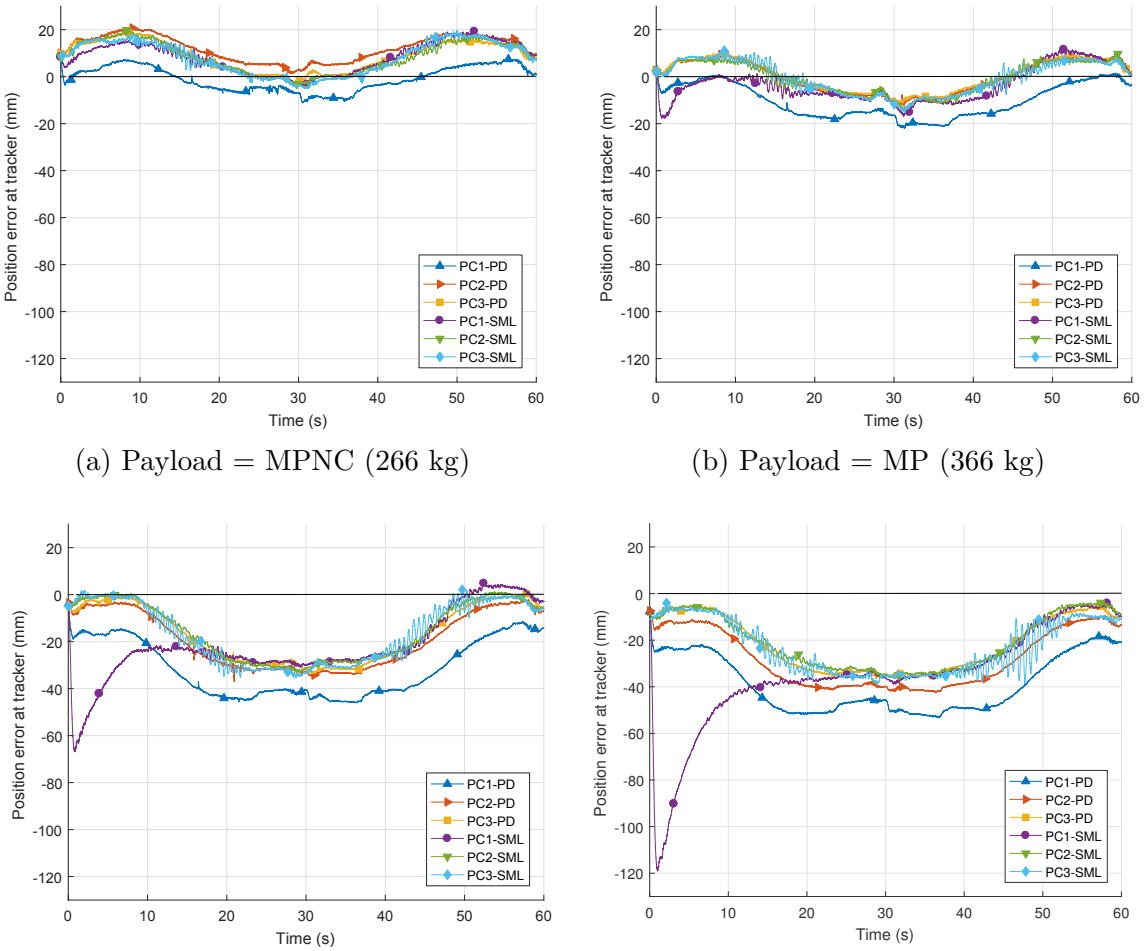

(a) Payload = MPNC (266 kg)

(b) Payload = MP (366 kg)

(c) Payload = MPM1 (488 kg)

(d) Payload = MPM2 (615 kg)

Figure 4.27: Cartesian error along axis z_b at tracker along test trajectory

Tables 4.4 and 4.5 contain respectively the position and orientation errors of the platform along the second half of the trajectory, once all controllers are in steady state. For an easier comparison, Fig. 4.28 displays the curve representing the value of average position error along axis z_b for all control architecture and loads. The effect of the mass augmentation onto the platform vertical position error is clearly visible and appears almost linear, with a 10 mm error per 100 kg added. It is possible to conclude that while some controllers where robust to mass changes in the joint space, errors in the platform positioning increases with the load. It is expected that

cable elasticity should be considered for the metal plate handling. This motivates the necessity for cable elasticity compensation in the control scheme, as presented in Sec. 4.2.4. It is noteworthy that the static error of PC1-PD is visible for all loads, as well as for with PC2-PD for the two heaviest loads. On the other hand, the SML based control schemes are very close performance wise.

Table 4.4: Position error along trajectory at tracker along axis z_b (mm) for trajectory second half ($t = 30$s to $t = 60$s)

Error	e_z	PC1-PD	PC2-PD	PC3-PD	PC1-SML	PC2-SML	PC3-SML
MPNC	RMS	5.8	12.9	10.2	11.7	10.2	11.2
	STD	5.7	4.8	5.5	7.0	6.4	7.4
	MEAN	-0.9	12.0	8.6	9.4	8.0	8.4
MP	RMS	13.3	7.1	6.8	9.2	7.4	7.1
	STD	7.7	7.1	6.8	9.0	7.4	7.0
	MEAN	-10.9	-0.2	0.4	-1.4	-0.9	-1.2
MPM1	RMS	33.8	22.7	20.7	19.1	19.3	19.3
	STD	12.2	11.9	12.3	13.0	11.8	12.0
	MEAN	-31.5	-19.3	-16.6	-13.9	-15.3	-15.1
MPM2	RMS	41.2	30.7	24.4	25.4	24.4	26.8
	STD	12.5	12.2	11.2	12.2	12.2	10.8
	MEAN	-39.3	-28.2	-21.7	-22.3	-21.2	-24.5

Table 4.5: Orientation error along trajectory at tracker about axis z_b (degrees) for trajectory second half ($t = 30$s to $t = 60$s)

Error	e_{Rz}	PC1-PD	PC2-PD	PC3-PD	PC1-SML	PC2-SML	PC3-SML
MPNC	RMS	1.6	1.6	1.6	1.6	1.6	1.7
	STD	1.5	1.6	1.6	1.6	1.5	1.7
	MEAN	0.4	0.3	0.3	0.3	0.2	0.3
MP	RMS	1.5	1.6	1.6	1.6	1.6	1.5
	STD	1.5	1.6	1.6	1.6	1.5	1.5
	MEAN	0.3	0.3	0.3	0.3	0.3	0.3
MPM1	RMS	1.5	1.5	1.5	1.6	1.6	1.5
	STD	1.5	1.5	1.5	1.6	1.6	1.5
	MEAN	0.0	-0.1	-0.1	0.1	0.1	0.0
MPM2	RMS	1.5	1.5	1.5	1.5	1.5	1.5
	STD	1.5	1.5	1.5	1.5	1.5	1.5
	MEAN	0.2	0.2	0.2	0.1	0.2	0.2

Overall, PC3-PD and PC2-SML are the most robust architectures, as PC1-SML once in steady state.

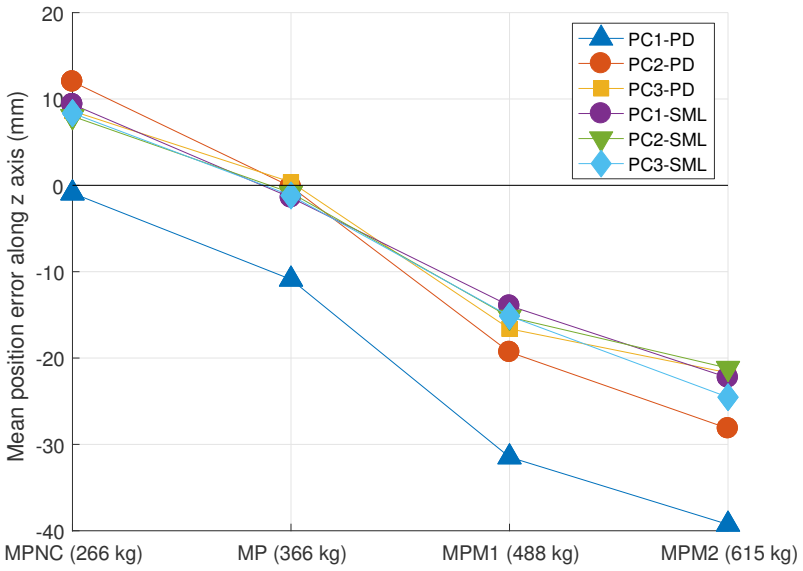

Figure 4.28: Mean position error along axis z_b for all controllers and loads (mm) for trajectory second half ($t = 30$s to $t = 60$s)

Cartesian error along x_b and y_b axes

The errors along the vertical axis z_b are the most representative, but for a full analysis errors along axis x_b and y_b are also observed. The Cartesian error along axis x_b is presented in Fig. 4.29. It appears that along this axis, most controllers have similar performances and behavior. Two controllers behaviors are noteworthy: the transient phase of PC1-SML as previously discussed, and controller PC3-SML for which the platform oscillations are visible.

Finally, Fig. 4.30a–4.30d show the tracking errors along the y_b axis. Since this axis corresponds to the longest travel distance of the platform, it is also the most affected by modeling errors. An initial 50 mm error has been recorded in the initial pose (trajectory point A) and a -30 mm error at the opposite side of the workspace (trajectory point E). It is also noteworthy that this axis was the one presenting the most measurement noise.

Observations on Cartesian errors

The main sources of error in the platform positioning are the orientation of the platform along the trajectory, the robot modeling errors, the calibration errors, and the precision of the measurement system.

Since the tracker is fixed on the side of the platform, a slight orientation of the platform gives a large displacement of the tracker: for example a 2 degrees orientation around axis x_b at the center of the platform generates a 24.5 mm shift of the platform along the z_b axis. As a consequence, the platform pose errors are amplified at the tracker level. Due to measurement noise in the orientation of the tracker, the estimation of the platform pose center P from the tracker pose would degrade.

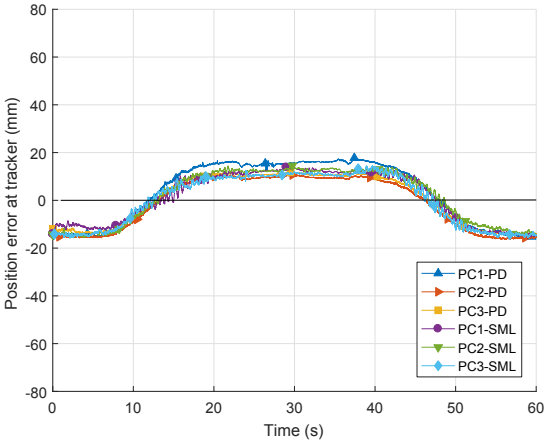

(a) Payload = MPNC (266 kg)

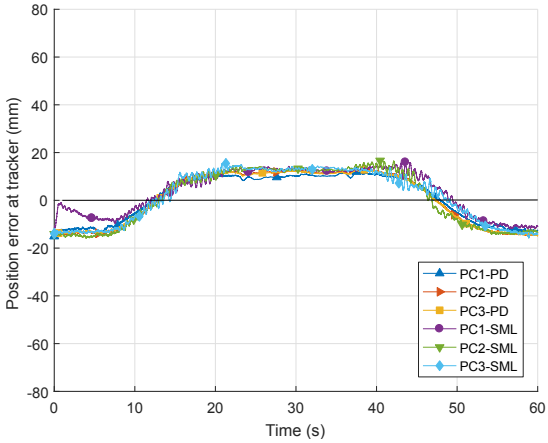

(b) Payload = MP (366 kg)

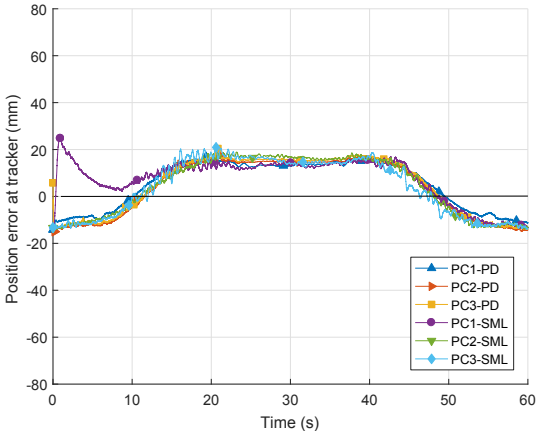

(c) Payload = MPM1 (488 kg)

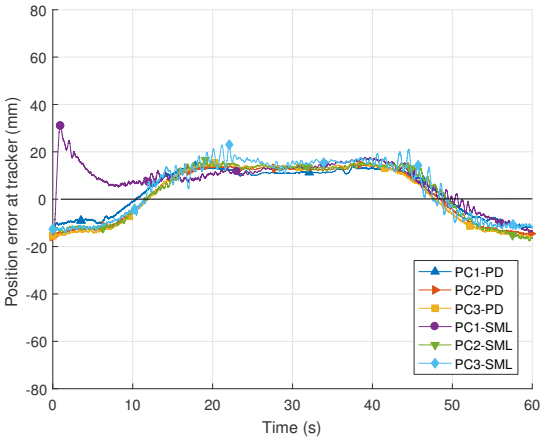

(d) Payload = MPM2 (615 kg)

Figure 4.29: Cartesian error along axis x_b at tracker along test trajectory

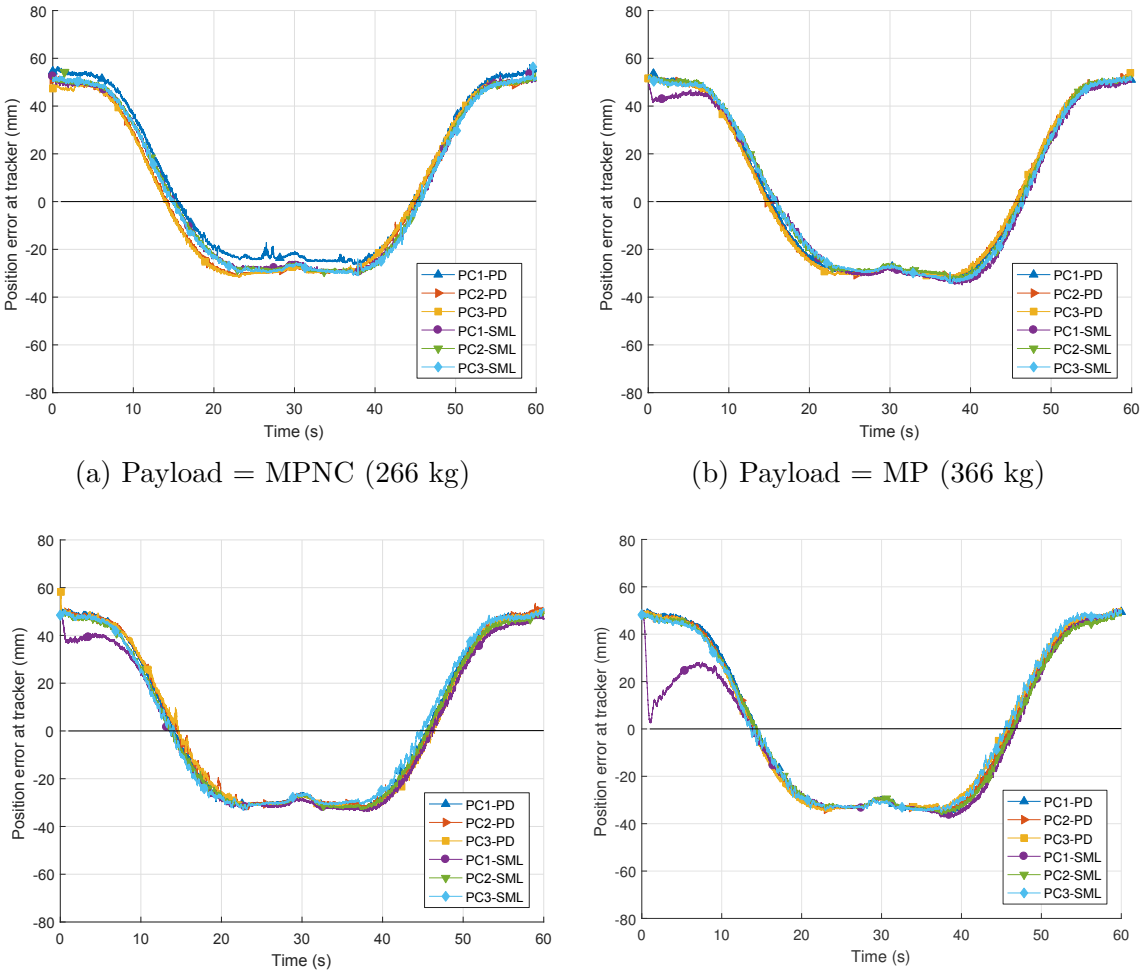

(a) Payload = MPNC (266 kg)

(b) Payload = MP (366 kg)

(c) Payload = MPM1 (488 kg)

(d) Payload = MPM2 (615 kg)

Figure 4.30: Cartesian error along axis y_b at tracker along test trajectory

The models used for the conversion of the desired Cartesian trajectory in to the motor desired positions and velocities did not take into account the cable elasticity. Therefore, errors due to cable elongations are not compensated. The positioning accuracy along the vertical axis is obviously the most impacted, but cable elasticity might also lead to slight orientations of the platform.

Calibration has been manually made in the center of the workspace, as explained in Sec. 3.2. However, small inaccuracies in the calibration process are amplified in the boundaries of the workspace, which is the case for the extremities of the test trajectory.

Finally, the VIVE measurement system used for the experiments does not have the same precision than conventional but costlier laser tracker systems. The VIVE accuracy is estimated between 1 and 10 mm, depending on the distance between the tracker and the center of the volume visible by the VIVE.

4.5.5 Evolution of parameter α in SML based controllers

The evolution of the variable α, the factor describing the balancing between the linear and nonlinear contribution of the SML controller, is observed and discussed in the sequel versus the payload increment and the chosen control architectures. The average value of α in the trajectory second half (steady state) is presented in Figure 4.31, for the eight controllers. It appears that the value of α decreases as the payload increases, which means that the controller leans towards sliding mode control. Notice also than the mean value of α is less than 0.2, meaning that globally the control is always close from sliding mode approach. PC3-SML gives the lowest average value of α for payload MPM2 due to the oscillations observed earlier.

By considering especially the results obtained by the PC1 architecture, figure 4.32 shows the evolution of the value versus time of α in each scenario for motor 4. Null values of α are used at the beginning of the trajectory, between $t = 0$ s and $t = 0.5$ s. This is due to a large initial motor error observed earlier with the higher payloads.

The SML controller gains have been tuned so that good performance is obtained with the sliding mode ($\alpha = 0$). However, it seems that these gains are not optimum for the linear control side. In order to improve control performance in future applications of this controller to CDPRs, it would be necessary to develop a tuning method that better takes into account the linear controller behavior.

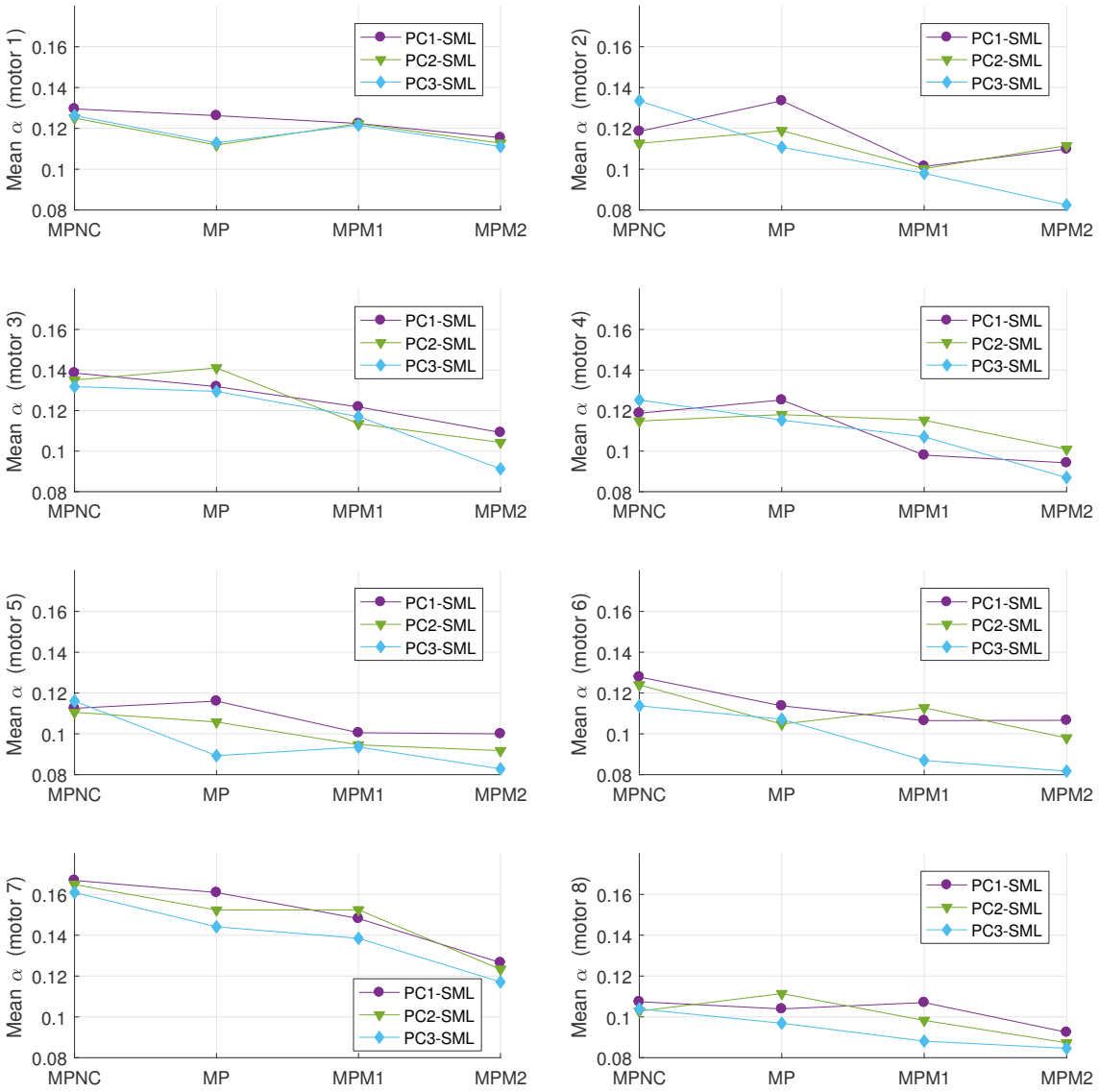

Figure 4.31: Evolution of the mean value of α for control schemes PC1, PC2 and PC3 with several payloads.

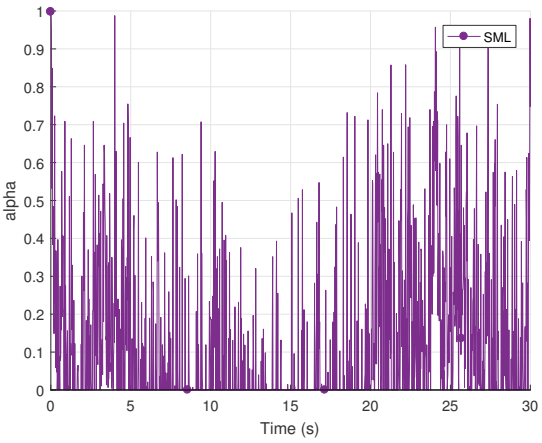

(a) Payload = MPNC (266 kg)

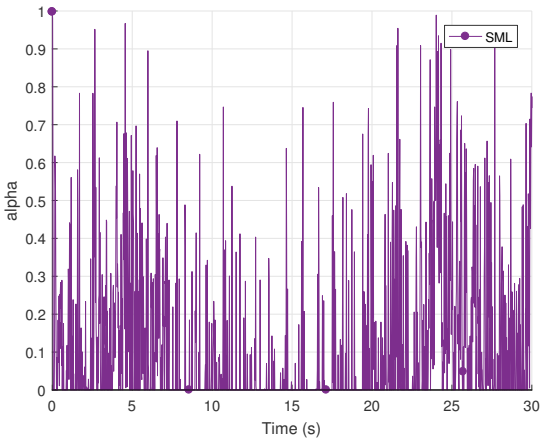

(b) Payload = MP (366 kg)

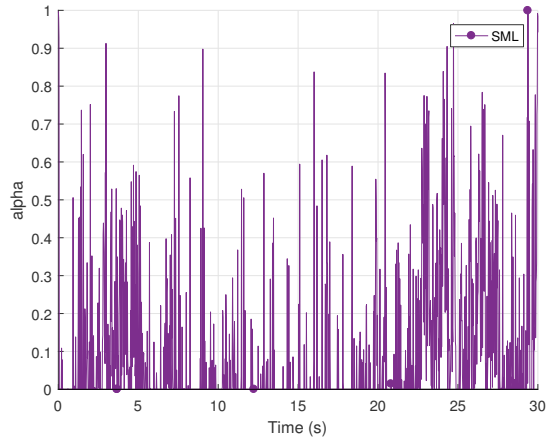

(c) Payload = MPM1 (488 kg)

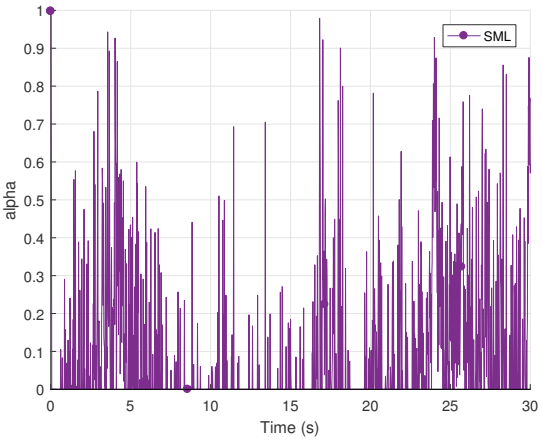

(d) Payload = MPM2 (615 kg)

Figure 4.32: Value of α versus time with PC1 control scheme for Motor 4.

4.5.6 PCE control architecture results

In the previous results, it was observed that the moving-platform was lower as the load increased. This is expected to be due to cable elongation due to elasticity. The objective of this section is to evaluate the effect of a cable elongation correction $\delta\mathbf{q}_E$ onto the final position accuracy of the platform.

The cable elongation compensation architecture (PCE) has been experimented on ROMP along the test trajectory for three loads: MP (366 kg), MPM1 (488 kg) and MPM2 (615 kg). The correction term $\delta\mathbf{q}_E$ is based on the linear cable model presented in Sec. 4.2.4 and the force sensors readings. The performance of the PCE are compared to those obtained by the architecture PC2$^+$. Recall that PC2$^+$ is based on PC2 for which the mass provided given to the feedforward term is equal to the real mass (m_{MP},m_{MPM1} and m_{MPM2}, respectively). However PC2$^+$ does not consider the cable elasticity. In this experiment, both PCE and PC$^+$ use the SML controller, which is the most robust towards load changes.

The platform pose along the test trajectory has been tracked using the HTC VIVE. The position of the platform center P along the vertical axis z_b has been computed from the tracker measurements. Figure. 4.33 presents an overview of the measured platform trajectories with PCE and PC2$^+$ for the three loads. Figures 4.34a and 4.34b show the platform position error along the vertical axis.

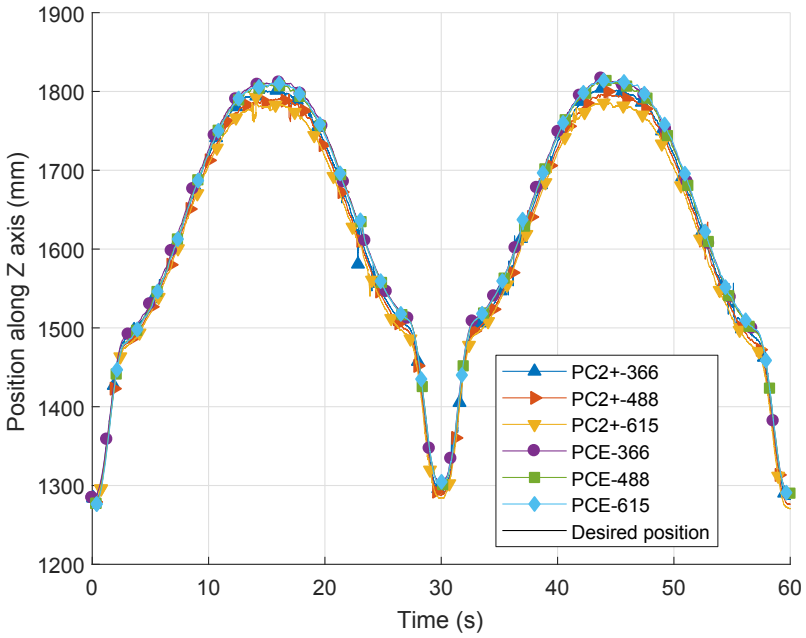

Figure 4.33: MP center P position along Z axis (mm) with control schemes PC2$^+$ and PCE, along the test trajectory.

The error between measured and desired position of the platform at the beginning of the trajectory is presented in Fig. 4.34a. Initially, the cable elongation correction $\delta\mathbf{q}_E$ is not yet applied; so the platform starts at the same set of motor positions with both PC2$^+$ and PCE. Since the cable elasticity is still not compensated, the impact

of the load on the platform position is clearly visible. The initial error of PC2$^+$ and PCE is around -15 mm for the 366 kg mass, -23 mm for 488 kg and -28 mm for 615 kg. However, once the motion starts the PCE control scheme applies the motor angular correction $\delta\mathbf{q}_E$ to the desired motor position $\mathbf{q}_d$, and the errors measured for the three different loads converge. After 15 seconds, the PCE errors are within 4 mm of each other, between 6 and 10 mm, while PC2$^+$ leads to a difference of around 20 mm between the platform position with the 366 kg compared to 615 kg.

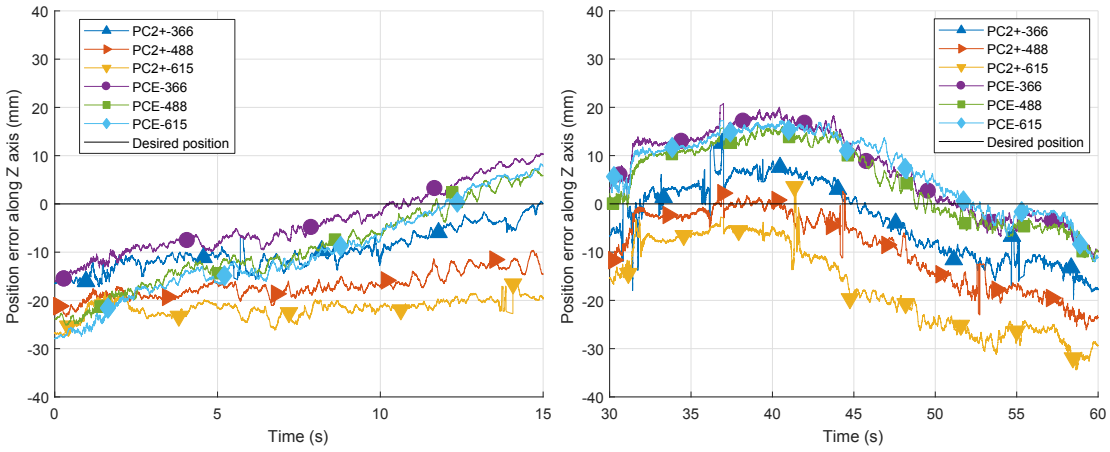

(a) Trajectory first 15 seconds. (b) Trajectory last 30 seconds.

Figure 4.34: MP center P initial position error along Z axis (mm) with control schemes PC2$^+$ and PCE, for the first 15 seconds and last 30 seconds of the test trajectory.

Figure 4.34b is focused on the last 30 seconds of the trajectory. It appears that, with the PCE architecture, the platform position repeatability despite the load variation is greatly improved: the curves PCE-366, PCE-488 and PCE-615 are very close during the entire second half of the trajectory. On the other hand, for the PC2$^+$ that does not include the elasticity compensation, the platform ends the trajectory with the same errors than in the beginning, with a spread of 15 mm between the 366 kg and the 615 kg cases.

Finally, Fig. 4.35 displays the mean pose error along the second part of the trajectory for the three loads obtained with PCE and PC2$^+$. The repeatability of the error is greatly improved with the cable elasticity compensation, and should therefore be used for the handling application.

Some modeling errors are still to be corrected in order to reduce error along the trajectory, but automated trajectories can now be more reliable as the platform position is now robust to the mass variation. Another solution for cable elasticity compensation could be to use the stiffness matrix to determine the displacement due to the wrench $\mathbf{w}_g$ applied onto the platform by gravity. From this information, it is the Cartesian desired pose that can be adjusted. This approach should be compared in future work with the results obtained with the PCE.

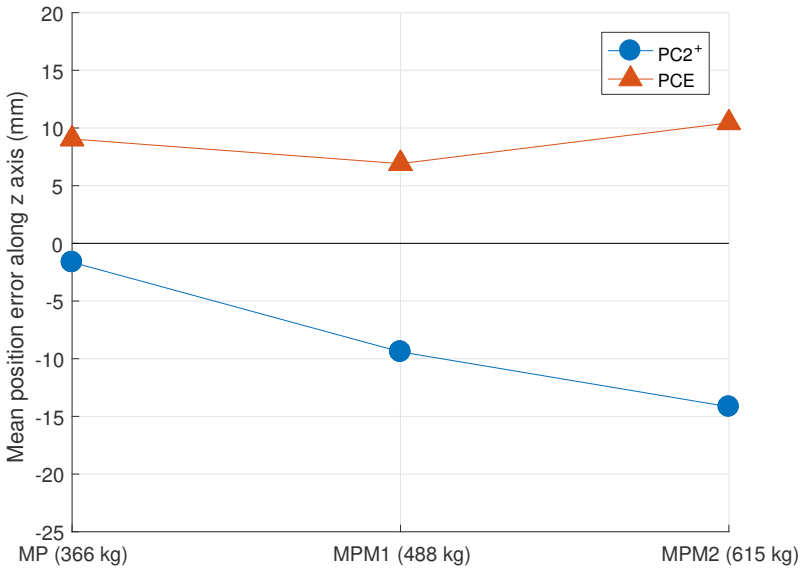

Figure 4.35: Mean Cartesian position error P along axis z_b (mm) with control schemes PC2$^+$ and PCE along the second half of the trajectory.

4.6 SOTDA simulation results

The proposed stiffness oriented tension distribution algorithm (SOTDA) has been tested in simulation for the ROWC prototype in MATLAB in a static pose of the platform and along the trajectory presented in Sec. 1.4.2. In both cases, a constant external wrench $\mathbf{w}_e$ has been applied onto the platform to simulate impact of the water jet pressure. The simulation is realized using the values given in Tab. 4.6. The Young modulus of the cable is set to 100×10^9 GPa, according to values proposed for ROWC Dyneema SK78 cables in [BMB08]. The cable tensions upper and lower boundaries are set to 10 N and 150 N, respectively.

Table 4.6: Simulation parameters

Variable	Parameter	Value	Unit
Number of cables	m	8	
Grid resolution	R_{res}	100	
Platform mass	m_p	14	kg
Platform initial position	$\mathbf{p}_0$	$\begin{bmatrix}1.5 & 0.350 & 0.590\end{bmatrix}^{\mathrm{T}}$	m
Platform orientation	ϕ	$\begin{bmatrix}0 & 0 & 0\end{bmatrix}^{\mathrm{T}}$	degrees
Tensions lower boundary	t_{lb}	10	N
Tensions upper boundary	t_{ub}	150	N
Gravity wrench	$\mathbf{w}_g$	$\begin{bmatrix}0 & 0 & -m_p g & 0 & 0 & 0\end{bmatrix}^{\mathrm{T}}$	N/N m
External wrench (water)	$\mathbf{w}_e$	$\begin{bmatrix}0 & 30 & 0 & 0 & 0 & 0\end{bmatrix}^{\mathrm{T}}$	N/N m
Cable Young Modulus	E	100×10^9	GPa
Cable cross section	S	0.81×10^{-6}	m^2

4.6.1 Static pose

In order to compare SOTDA and barycenter method (BMTDA), their cable tensions solutions were first computed in simulation for the static pose shown in Fig. 4.8. The estimated platform displacements depending on the selected cable tension sets are also analyzed.

The force $\mathbf{f}$ applied on the platform considered for the computation of the feasible polygon (Eq. (4.11)) is defined as

$$\mathbf{f} = \mathbf{w}_g + \mathbf{w}_e \tag{4.37}$$

$$= \begin{bmatrix} 0 & \mathrm{w}_{e,y} & -m_p g & 0 & 0 & 0 \end{bmatrix}^{\mathrm{T}} \tag{4.38}$$

$$= \begin{bmatrix} 0 & 30 & -137.34 & 0 & 0 & 0 \end{bmatrix}^{\mathrm{T}} \tag{4.39}$$

with $\mathbf{w}_e$ the external wrench, included in the computation of the feasible polygon.

The small external wrench $\delta\mathbf{w}_e$ must be in the same direction as the axis in which the stiffness should be maximized. In this simulation, $\delta\mathbf{w}_e$ is chosen equal to the external wrench due to water pressure $\mathbf{w}_e = \begin{bmatrix} 0 & 30 & 0 & 0 & 0 & 0 \end{bmatrix}^{\mathrm{T}}$ applied to the platform. By this way, the platform displacement computed from the robot stiffness matrix should be indicative of the actual platform displacement. However, since the stiffness matrix $\mathbf{K}$ was expressed for an infinitesimal displacement, the corresponding displacement is only accurate in a very small range of amplitude.

Using MATLAB *meshgrid* function, the platform feasible polygon in pose $\mathbf{p}_0 = \begin{bmatrix} 1.5 & 0.350 & 0.590 \end{bmatrix}^{\mathrm{T}}$ has been discretized and the platform displacement along the y axis, δp_y is computed across all intersections from the stiffness matrix, as detailed in Sec. 4.3.3.

Figure 4.36 introduces a new colormap, the vertical axis representing the displacement of the platform δp_y depending on the values of λ_1 and λ_2, the coordinates of the point selected in the feasible polygon. Blue area represents the part of the feasible polygon leading to the lowest displacement, and yellow area the highest one.

It is noteworthy that with the current values for the external effort and cable Young modulus, the computed displacements are reduced with a 0.6 mm amplitude between the lowest and highest values. From the simulation results, it appears that the passive part of the stiffness matrix $\mathbf{K}_p$ far outweighs the active part $\mathbf{K}_a$. As a consequence, the nature of the cables is much more impactful than the cable tensions. It can also be noticed that the current cable configuration is not optimal for maximizing the stiffness since only four of the eight cables of the CDPR are crossed.

4.6.2 Along path

Simulations have been performed to compare the solution obtained from the barycenter method (BM) to the solution selected according to the stiffness maximization criteria (SOTDA) along the test trajectory defined in Sec. 1.4.2. Recall that the

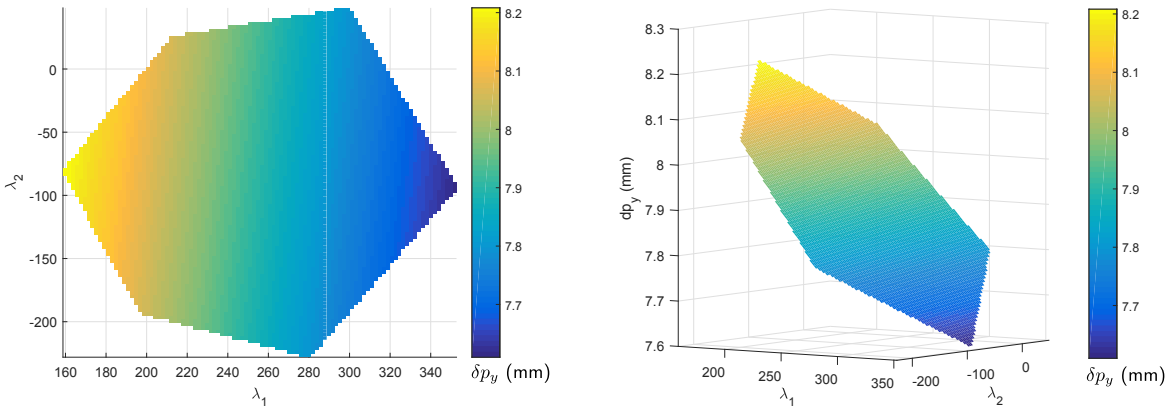

(a) Top view (b) Side view

Figure 4.36: Surface of feasible polygon with platform displacement δp_y (mm) as vertical axis.

desired path is a simple linear motion along the x-axis at a constant height, representative of a simple window cleaning motion.

Figure 4.37 shows the prototype, its cable configuration, the desired trajectory, and the external wrench applied by water pressure at the platform center P. The desired trajectory is centered in the workspace of the robot, at around mid-height of the wrench feasible workspace.

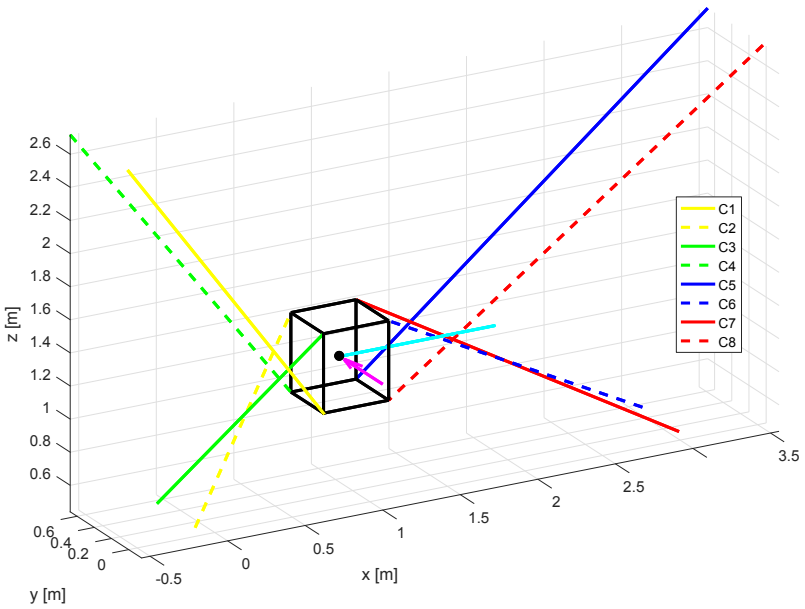

Figure 4.37: Simulated ROWC model, with test trajectory (cyan) and external wrench in (magenta)

The platform displacement δp_y along the y-axis under the small external wrench $\delta \mathbf{w}_e$ is computed along the trajectory. The minimum (SO) and maximum platform displacements found at each time step are plotted in Fig. 4.38, along with the displacement obtained from the barycenter (BM). Two values of $\delta w_{e,y}$ are considered

to observe the difference in evaluated displacements.

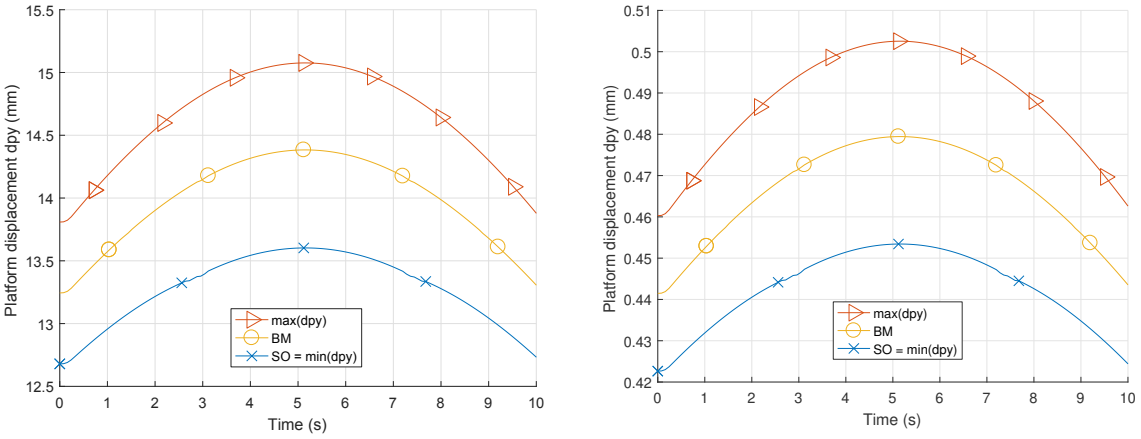

(a) $\delta w_{e,y} = 30$ N (b) $\delta w_{e,y} = 1$ N

Figure 4.38: Effect of small external wrench amplitude δw_e (N) on platform displacement δp_y (mm).

Considering the 30 N case for $\delta w_{e,y}$, the displacement obtained from the BM equals 14.4 mm, and the minimum displacement obtained with the SOTDA equals 13.6 mm. From this figure, it appears that the BM generates an intermediate value of the platform displacement between the minimum and maximum displacements. While it is not possible to achieve a null displacement of the platform, its value is slightly reduced by around 5.5% by selecting the SOTDA solution. The effectiveness of SOTDA is improved if the upper tension cable tension boundary is set to a higher level. As shown in Fig. 4.39 with an upper limit of 400 N, the estimated displacement is reduced by 19% with the SOTDA compared to the BM, from 11.86 mm down to 9.6 mm.

The cable tensions obtained with the BM and the SOTDA for the 30 N lateral wrench and 150 N upper tension limits are presented in Fig. 4.40. As expected, two cables are saturated at all time, reaching the maximum admissible tension levels.

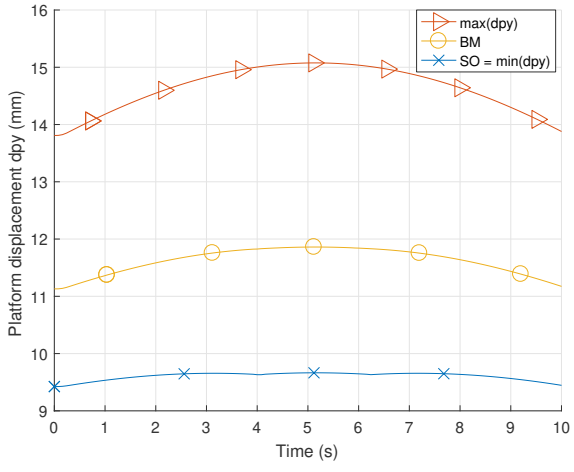

Figure 4.39: Platform displacement δp_y (mm) with upper tension limit set to 400 N.

Cables 3 and 6 are the least tensed ones along the trajectory. From Fig. 4.37, it makes sense since those cables have the largest contribution in the same direction as the external wrench to counteract. As a result, their tensions are set to the maximum acceptable level still maintaining the platform static equilibrium.

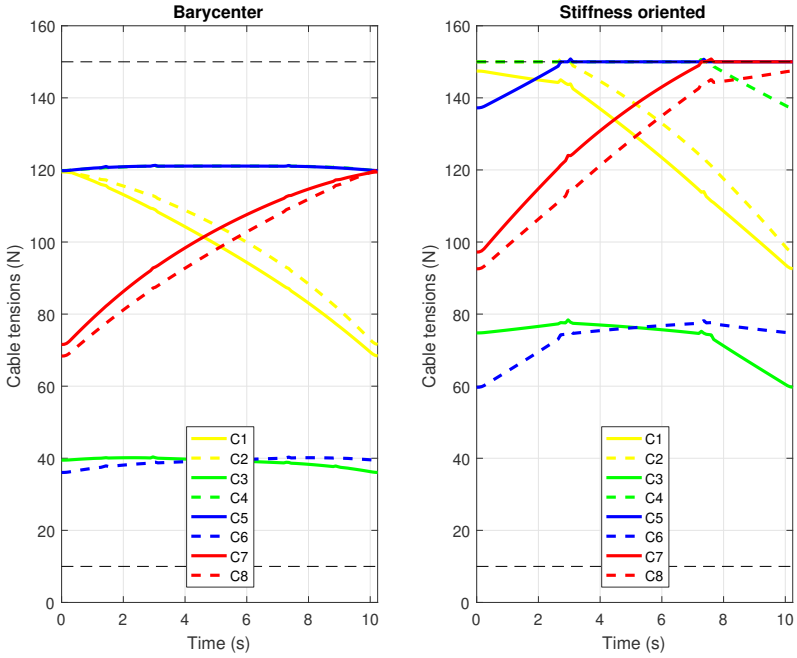

Figure 4.40: Simulated tension distributions along the test trajectory subject to a 30 N lateral force.

4.7 SOTDA experiments (ROWC)

Control scheme TC2-PD has been implemented on ROWC prototype, considering a static pose and the test trajectory. Both the barycenter method (BM) and the stiffness oriented (SO) tension distribution algorithms have been implemented in order to compare the platform stability and generated motor torques.

The proportional-derivative (PD) controller is selected in this control scheme, as the twisting sliding mode controller could lead to high values of the control signal τ_c in opposing cables (see Appendix C).

As described in Sec. 4.3.3, the SOTDA has been implemented based on the consideration of the feasible polygon corners only in order to minimize the computation time. The stiffness coefficient ν was also implemented in order to ensure an operational margin with regards to the edge of the feasible polygon. The implementation of ν also allows for an observation of the CDPR behavior based on the chosen value of the coefficient. As expected, the higher ν, the larger the cable tensions and the CDPR stiffness.

4.7.1 Static pose

The SOTDA is first applied in a static pose of the platform. The objective is to experimentally validate the reduction of the platform displacement under a constant lateral wrench with the SOTDA compared to the BM. In this experiment, the value of the external force and the upper limits are raised in order to improve the effects of the tensions distributions. The external wrench equals $\mathbf{w}_e = \begin{bmatrix} 0 & 50 & 0 & 0 & 0 & 0 \end{bmatrix}^{\mathrm{T}}$ and the upper tension limit is set to 200 N instead of the typical 150 N. The experimental setup is presented in Fig. 4.41.

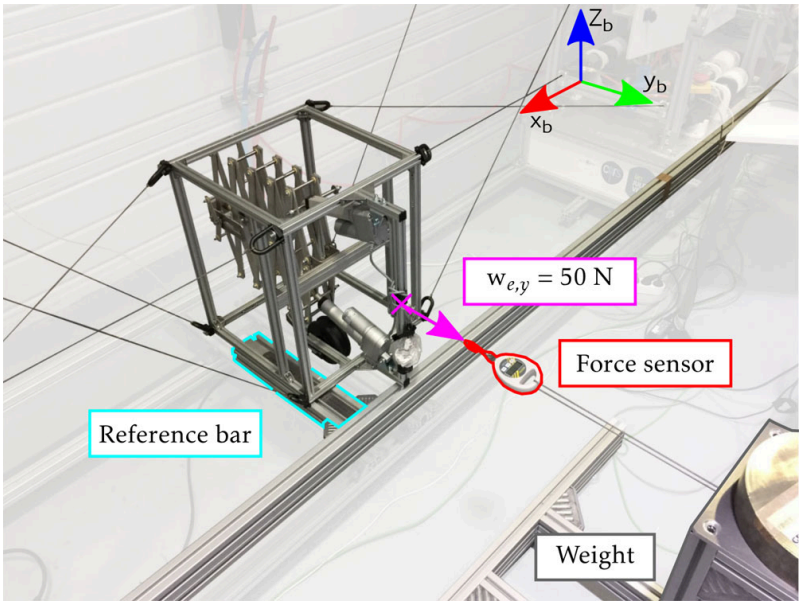

Figure 4.41: Static pose setup with 50 N force applied along along y_b axis

The experiment process is as follows:

1. the platform is positioned next to a fixed reference bar;
2. using a steel scribe, the resting position of the platform is marked on the reference bar when no external wrench is applied;
3. for each value of $\nu = \{0, \quad 0.1, \quad 0.2, \quad \ldots, \quad 0.9\}$;
   (a) the wrench (force) of 50 N is applied in the positive direction of y_b-axis and measured with a Kern HDB 10K10N force sensor;
   (b) the new steady position of the platform is marked on the bar.

The reference bar and recording platform position under the different values of ν are shown in Fig. 4.42a. The resulting displacement of the platform depending on the value of ν compared to the initial position in the absence of external force is plotted in Fig. 4.42b. It is apparent that the increase of the value of ν reduces the platform displacement. From these results, the SOTDA induces a reduction of up to 24.8% of the platform displacement due the lateral force compared to the BM, while a linear regression indicates a slope of 8.7 mm for this curve.

It is noteworthy that the measured platform displacement of Fig. 4.42b are larger than the estimated ones, presented in Fig. 4.38a. This difference is due to the

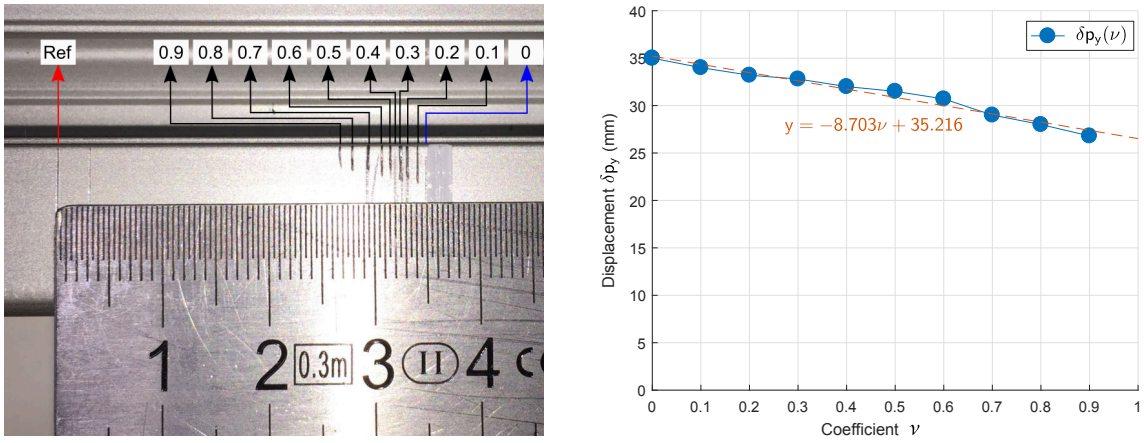

(a) Marks on reference bar

(b) Measured displacement dp_y

Figure 4.42: Measured platform displacement δp_y under a 50 N force along y_b axis depending on value of ν.

modeling simplifications while neglecting the pulleys geometry and the choice of a linear elastic cable model. The simulation results also only considers the elasticity of the cable, while neglecting the compliance of the controller and the elasticity of the frame. As a consequence, the complete system equivalent Young Modulus should be lower than the considered one, leading to larger displacements of the platform than the simulated ones.

4.7.2 Along path

The platform now follows the same linear trajectory as in the previous simulations, with the upper cable tension limit set back to the nominal 150 N.

An external force of 30 N was applied on the platform by manually pulling on the same wire than in the static case, but while the platform moved along the desired path. The force sensor is again used as a reference to ensure that the average force is constant. Figure 4.43 presents the resulting force generated along the y-axis by the motor controllers to counteract the lateral force applied on the platform. The mean value of $f_{c,y}$ is about 20 N in the presence of the external wrench $\mathbf{w}_e$. This difference between force measured with the sensor, and $f_{c,y}$ is mainly attributed to friction in the gearmotors, similarly to the observations made for ROMP prototype in Sec. 2.7.

The cable tensions obtained with both the BM and the SOTDA for $\nu = 0.9$ are presented in Fig. 4.44. The shape of the cable tensions are similar to those obtained in simulation in Fig. 4.40. For the SOTDA, the highest cable tension are close from the upper tension limit, but never reach it. As expected, Cables 3 and 6 have the smallest contribution for both tension distributions. Cables 1 and 2 have a slightly lower contribution than anticipated, which can be due to friction in the gearmotor.

Individual motor torques $\boldsymbol{\tau}_m$ generated by the TDA are plotted in Fig. 4.45 for three values of ν: 0 (BM), 0.5 and 0.9. It is clear that for all motors, the higher

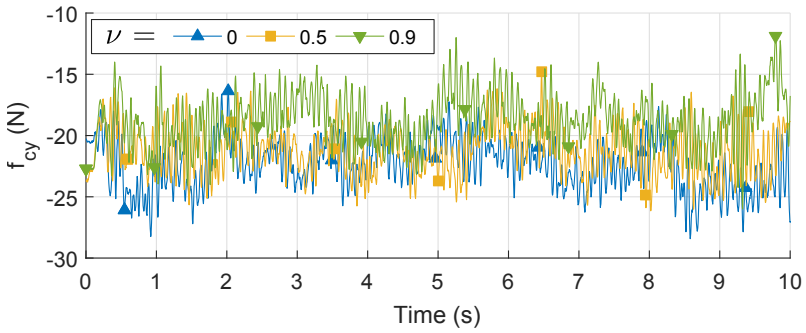

Figure 4.43: Component $f_{c,y}$ of the resulting force applied by the PD controllers onto the platform in the presence of the external wrench $\mathbf{w}_e$, for $\nu = \{0, 0.5, 0.9\}$.

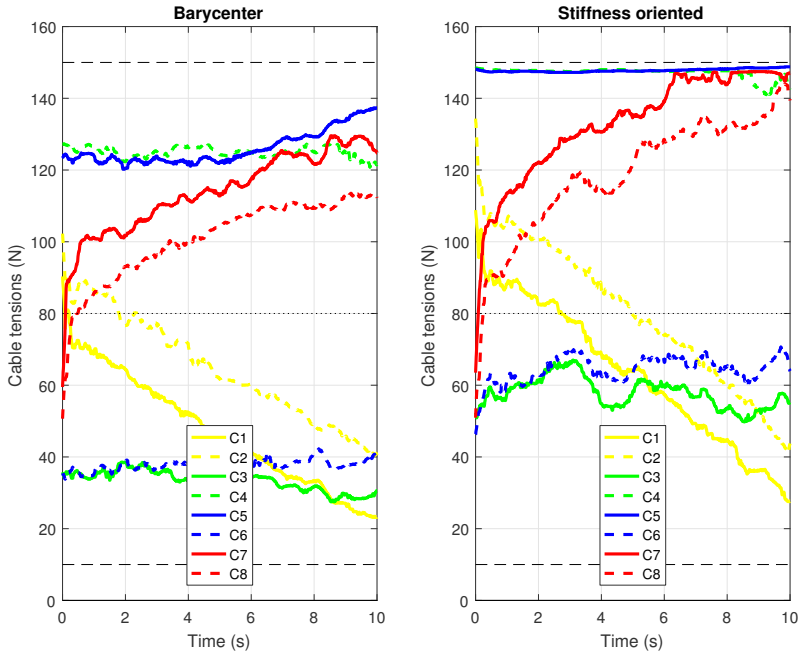

Figure 4.44: Experimental results of tension distributions along the test trajectory under a 30 N lateral force.

the value of ν, the higher the desired torque. The upper and lower cable tensions limits have been converted to torque limits and are plotted in dotted black lines. It is interesting to see again that, in the case of $\nu = 0.9$, the torque values for Motors 4 and 5 are very close but never reach the maximum admissible value, respecting the desired security margin.

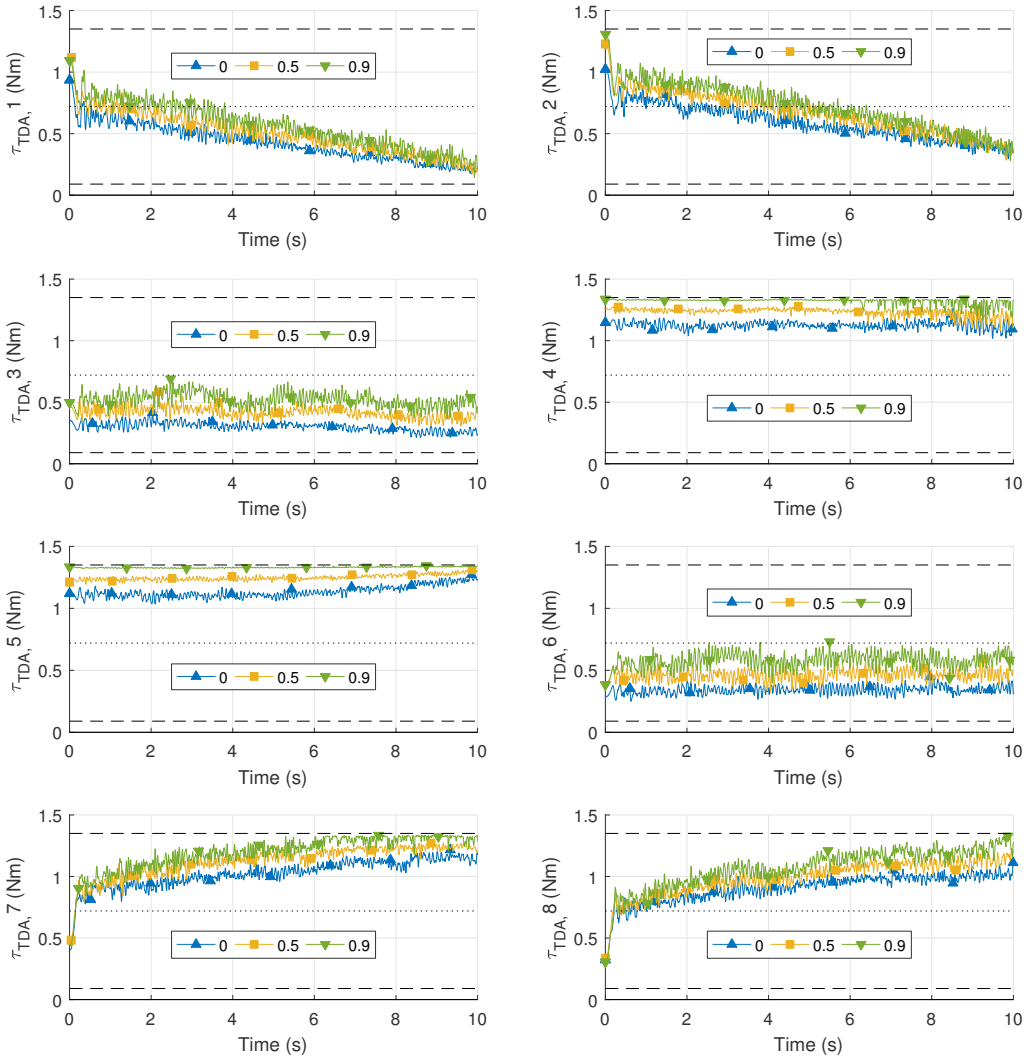

Figure 4.45: Distributed torques $\boldsymbol{\tau}_{TDA}$ as a function of coefficient ν.

Finally, the effects of tension distribution on motor position accuracy can be observed in Fig. 4.46 presenting the motor position errors, depending on the value of ν. It can be observed that the implementation of the TDA in the control scheme leads to larger motor position errors compared to the position control architectures (PC1 to PC3). For window cleaning, the maximization of the robot stiffness is more important than accurate control of the platform positioning, which makes this behavior non critical for the considered application. However, if accuracy at the motor level is required a different kind of control architecture might be needed. Tracking measurements should be realized in future work to evaluate the platform positioning accuracy in the Cartesian space along a path.

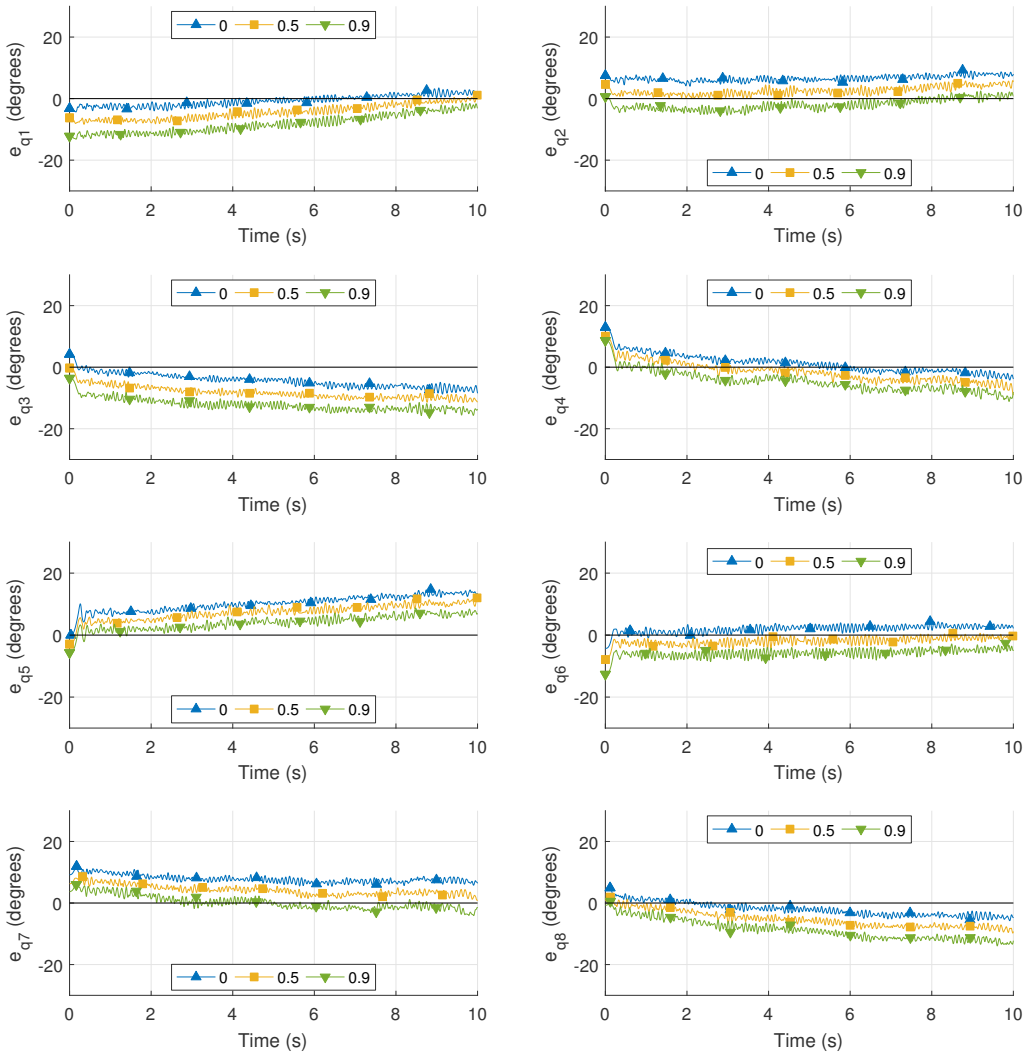

Figure 4.46: Motor position errors $\mathbf{e}_q$ as a function of coefficient ν.

4.8 Conclusion

Chapter 4 has been dedicated to the design of the control architectures for the two applications considered in the thesis. The metal plate handling application of ROMP is demanding in terms of accuracy and repeatability, while the window cleaning application of ROWC requires safe cable tensions and good stiffness, to resist against forces in an external environment. Decentralized control architectures have been considered, *i.e.* each cable of the robot is separately controlled by an independent controller. Both prototypes are controlled through the motor torques with motor positions and velocity feedback.

Figure 4.47 summarizes the choice between control architectures PC1, PC2 and PC3, and controllers PD and SML for an industrial application such as metal plate handling. In the most favorable conditions, *i.e.* when the total payload is known, the PC2$^+$-PD architecture can be applied for its good accuracy and smooth control signal. This scheme, however, is very restrictive due to the knowledge of the carried mass. If the CDPR is equipped with force sensors the mass estimation can be implemented. In this case, the PC3-PD appears more appropriate than the PC3-SML due to platform vibration if the mass must be continuously estimated in real-time. Nonetheless, if no information is available on the load mass or cable tensions, SML based architecture is a good option for its robustness towards uncertainties and stability. Both PC1-SML and PC2-SML achieve high accuracy once the controller has reached steady state. Notice that the SML controller could easily be further tuned for ROMP in order to increase the correction speed. The sliding mode based control architecture being the most robust, their application to the more favorable cases should also be considered, with the possibility of implementing higher order control laws to go towards control smoothness.

While a good accuracy is achieved with these controllers in the joint space, cable elasticity introduces nonlinearities between the motor and platform positions. Moreover, the higher the load, the larger the error which is detrimental to the precise control of the platform positioning. From the linear cable elasticity model expressed in Sec. 2.4, the cable elongation can be estimated. ROMP being equipped with force sensors located at the cable anchor points, a feedback loop has been implemented to compensate in real-time for the estimated cable elongation. This external control loop has a great interest for the platform positioning, with a significant improvement in the repeatability of the platform height for all considered loads. As a consequence, cable elongation should be taken in consideration for the handling of such heavy objects.

In the case of ROWC, the fully-constrained configuration requires the implementation of a tension distribution algorithm (TDA) in order to ensure that cable tensions are both feasible and safe. Since the stiffness of the platform is a critical

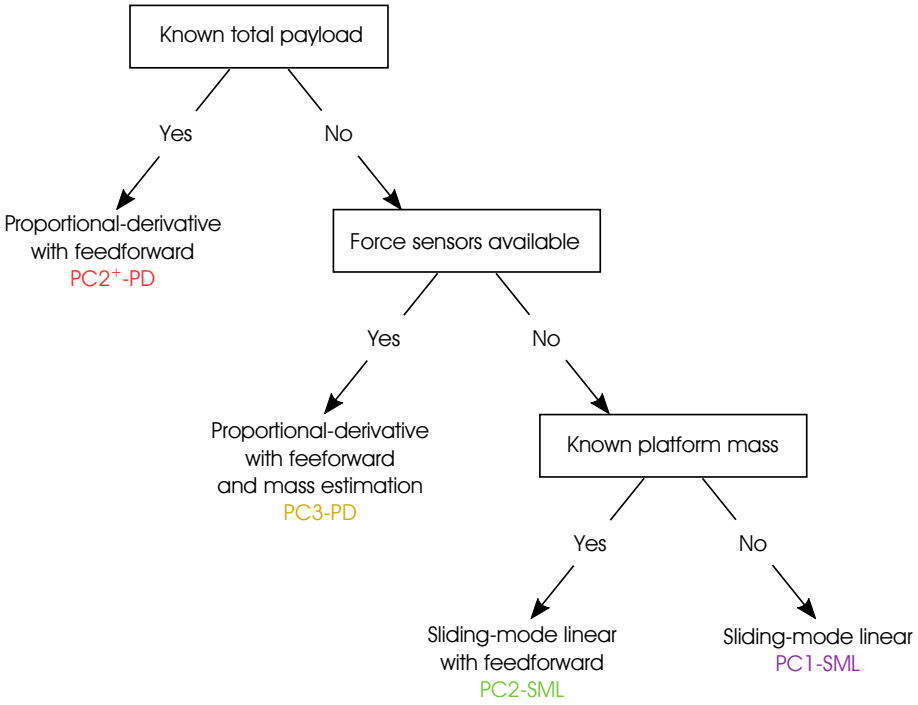

Figure 4.47: Applicable control architectures on ROMP.

aspect of the application, a tension distribution algorithm is proposed in order to select the set of cable tensions minimizing the platform displacement due to the lateral force due to water pressure. The set of feasible cable tensions provided by the feasible polygon is discretized; then the stiffness matrix expressed in Sec. 2.6 is used to compute the small-displacement screws of the moving-platform throughout the feasible polygon. Then, the set of cable tensions that leads to the smallest displacement is applied to the CDPR. The proposed TDA is compared in simulation to the solution provided by the barycenter selection method. As expected, the stiffness oriented TDA provides the largest stiffness of the moving-platform along a prescribed direction. This algorithm has been experimentally tested on the prototype and leads to a reduced platform displacement of around 24% in the considered experimental conditions. The introduction of the stiffness coefficient ν for the selection of an intermediate point successfully allows for the implementation of the SOTDA while maintaining a margin with respect to the maximum feasible tensions.

5. Emergency stop

In this chapter, a discussion is initiated on the emergency stops of CDPRs in an industrial context. To the author's best knowledge, some developments have been made in the field of security in the case of CDPRs, but the legislation on their implantation is still to be defined. Knowledge on the stopping time and travel distance of a CDPR in the event of an emergency stop is necessary to determine the safety process. This fact being a main concern for an industrial application, experiments have been made in the context of this thesis to provide initial results to the industrial partners of the ROCKET project, on the behavior of CDPRs during emergency stops.

Using the CAROCA prototype and the ROMP metal plate handling platform, two strategies and their influence on the platform behavior are compared: a direct power off that immediately activates the motor brakes, and a deceleration profile in a 500 ms time window, followed by a power off. Finally, the evolution of cable tensions on ROWC using the proposed SOTDA is observed when an increasingly large external force is applied to the platform.

5.1 Recovery after cable failures

One of the main concerns about the use of a CDPR in an industrial environment is a cable failure. While this scenario was not actively studied in this thesis, the subject of cable failures is a critical point in the safety of CDPRs and should be mentioned.

Cable breakage induces several safety concerns: first, the risk caused by the cable itself; secondly, the behavior of the platform until a new static equilibrium is found.

Due to the use of metal cables, the ROMP prototype is surrounded by an *Axelent*

X-Guard® safety fencing. All elements of the ROMP prototype have been sized with a security factor of at least 7 with regards to the maximum expected payload. As such, ROMP cables are rated for 1 t, while the robot load limit is set to 800 kg. This factor is based on the current legislation on overhead cranes under which the current prototypes at IRT Jules Verne operate, until dedicated CDPRs safety standard are established. In the window cleaning application, it is obviously not possible to install fences around the CDPR. As such, the use of a tension distribution algorithm is particularly important. ROWC uses polymer cables for their lower mass, and consequently lower risk in the event of a collision.

In the context of the ROCKET project, only redundant CDPRs with an actuation redundancy of 2 have been considered, reducing the risk of platform instability after a cable break compared to non-redundant CDPRs, combined with the symmetrical position of the cable exit points on the frame. Figure 5.1 presents the new workspace of the ROMP prototype after a cable failure. As in Sec. 1.3.1, the static workspace is computed using the software ARACHNIS [Rui+15] for maximum cable tensions of 2667 N. It is clearly visible that a single cable failure can have a large impact on the static workspace of the prototype, even in the case of a redundancy of two. In [RGL98], a method is proposed to evaluate the fault tolerance of redundant cable-suspended robots, which is the capacity of the robot to *survive* a cable break without suffering an instability of the platform.

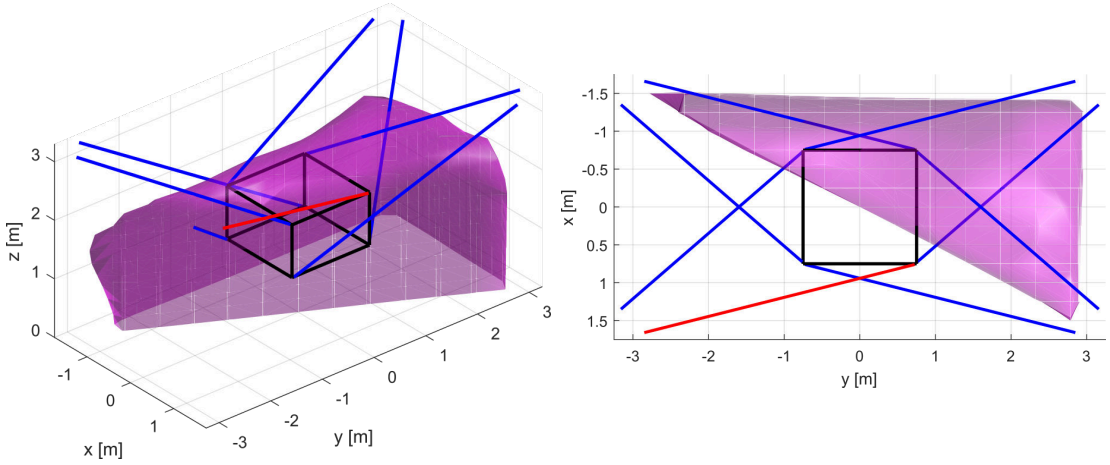

Figure 5.1: ROMP static workspace after failure of cable 1 (in red).

However, if the platform pose is not tolerant towards a cable break and becomes unstable, a new static equilibrium based on the remaining cables should be sought. A typical application for this type for emergency strategies is the case of skycams (suspended cameras used in stadiums) and illustrated in Fig. 1.5. This kind of CDPR can cover a very large workspace, but the travel distance to reach a new static equilibrium after a cable break can be substantial. If no emergency strategy is applied, the camera might naturally fall on the ground.

Emergency strategies for the dynamic recovery after a cable failure have been

actively studied in order to find a the optimal trajectory leading to a new static equilibrium. The strategy proposed in [BGC18] generates a trajectory from an unstable pose that is outside the current static workspace to a novel static equilibrium, in a safe manner. This algorithm has been tested in simulation for a point-mass platform actuated by 4 cables. The generation of the recovering trajectory is based on earlier work on the dynamic trajectory planing of 3 DoF suspended CDPRs [Gos13].

Recent work [PZB19] extends this method by generating an oscillatory trajectory that guarantees positive and bounded tensions in the remaining cables along the recovering trajectory. In [BB19], two strategies are based on a model-predictive approach and the minimization of the kinetic energy of the platform, and potential fields based method.

5.2 CDPR emergency stops

In the sequel, the focus will be on the behavior of CDPRs in the case of a standard emergency stop, in the absence of a cable break.

Hardware and software safety components

On industrial hardware, safety modules can be used to implement customized shutdown strategies. A safety module checks that the equipment is following the pre-determined behavior, based on certified sensors. If an something wrong occurs, an immediate stop is initiated. The B&R Automation hardware used for ROMP and ROWC can provide the safety functions listed in Tab. 5.1. These industrial standards determine the strategies available for the emergency stop of the system.

Table 5.1: Standard safety functions provided by B&R Automation hardware.

B&R Automation safety functions	Acronym
Safe Torque Off	STO
Safe Operating Stop	SOS
Safe Stop 1 and 2	SS1/SS2
Safely Limited Speed	SLS
Safe Maximum Speed	SMS
Safe Direction	SDI
Safely Limited Increment	SLI
Safely Limited Acceleration	SLA
Safe Brake Control	SBC
Safely Limited Position	SLP
Safe Maximum Position	SMP
Safe Homing	-
Safe Brake Test	SBT
Remanent Safe Position	RSP

Due to their hardware, ROMP and ROWC can currently only implement the *Safe Torque Off* (STO) safety mode, that leads to an immediate stop of the system and

the application of the motor brake if the motor torques become too close from a set value. However if *safe* motor encoders certified for use in safety functions modes are available, other functions such as *Safely Limited Position* (SLP) or *Safe Maximum Position* (SMP) can be implemented, and should be considered for future industrial CDPRs.

5.2.1 Immediate top and controlled deceleration

The objective of an emergency strategy is to dissipate energy in the system and stop any moving part in a short time, without additional risk for the environment.

Emergency stops can be requested for a number of reasons. An emergency stop can be request for maintenance, by opening a door of the robot enclosure, due to of a software error/hardware deficiency, or by pressing the emergency stop button. The response to and emergency stop request can differ depending on the preferred behavior of the robot.

An immediate stop is necessary in required to protect people or material. The end-effector must stop its course in a minimum amount of time and travel distance. When requesting an emergency stop, most systems will be powered off immediately and stopped with mechanical brakes.

On the other hand, a soft stop is better if there is no immediate danger and the robot. More time is allowed for the deceleration of moving parts in order to reduce strain on the system. Some equipment involving large revolving elements and high momentum require a progressive deceleration. The emergency shutdown strategy must then take into account the specificities of the system.

5.2.2 CDPR emergency stop

CDPR emergency shutdown strategies must be adapted according to their configuration. During the ROCKET project, some possible emergency strategies for redundant CDPRs have been identified (Fig. 5.2). It is expected that in a suspended configuration, blocking all motors in their positions might lead to tension variations in some of the cables. However, once all motion of the platform is stopped, the only energy left in the system is the potential energy due to the mass of the platform. In the case of a fully-constrained CDPR, cables might still be in tension even after stopping all motors. The proper strategy should at the same time maintain the position and stability of the platform, and reduce cable tensions to the minimum ensuring its static equilibrium. The use of a tension distribution algorithm is then beneficial.

CDPRs usually benefit from a low moving weight, due to motors being located on the ground and the use of cables to move the effector. Consequently, they do not require specific mechanical systems to slow down before coming to a full stop.

However, it can be considered that, at 266 kg, ROMP platform has a non negligible

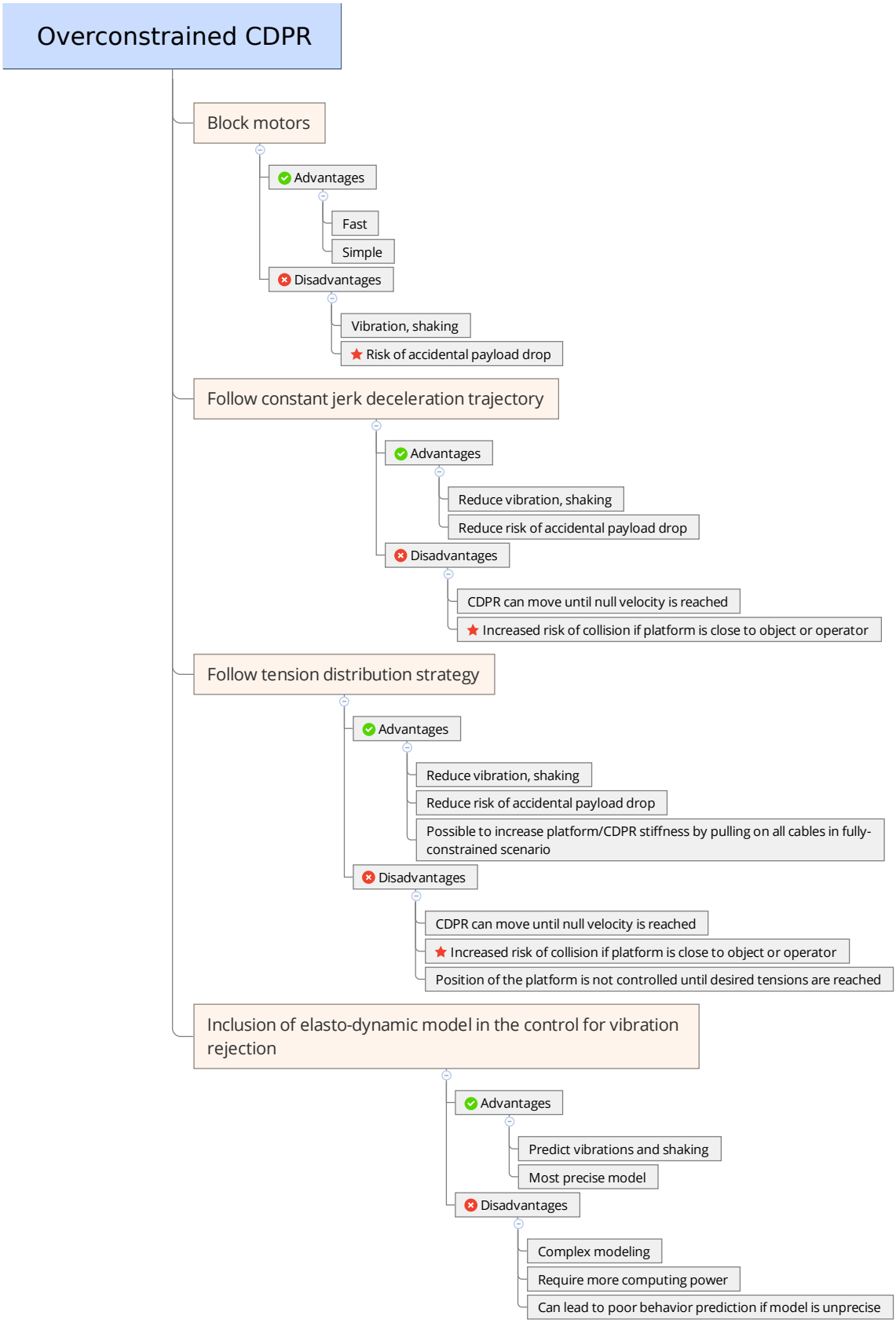

Figure 5.2: Identified possible emergency strategies for redundant CDPRs.

mass. Moreover, a sudden stop can lead to platform shaking that can be harmful to the structure, cables and attachment points. In the case of a pick and place application such as the ROMP prototype, a jolt could induce an accidental release of the object by the magnets. As such, a deceleration strategy is considered.

5.3 Constant jerk deceleration of a suspended CDPR

In order to reduce the platform kinetic energy before blocking the motors, a constant jerk deceleration trajectory is computed from the current position and speed of the platform. The behavior of the platform is compared between an immediate stop of the motors, and the constant jerk deceleration trajectory. The mains objectives consists to quantify the displacement of the platform in each case after the emergency stop request, and to study the impact on the cables tensions, including stabilization time.

The soft emergency stop strategy takes as input the current position and speed of the platform, and replaces the current trajectory generation. A new trajectory is generated to bring the platform to a stop in 500 ms. The value of the jerk used in this soft stop depends on the hardware of the robot. In the case of ROMP, a value of 10 $m.s^{-3}$ was chosen for the maximum jerk and 10 $m.s^{-2}$ for the maximum deceleration.

5.3.1 Experimental setup

The lightest version of the ROMP platform (MPNC) is used for this test, with a mass of 266 kg. The platform is set along a linear trajectory with a speed equal to -0.4 $m.s^{-1}$. The platform position is tracked using the VIVE tracker. Motor positions and velocities are recorded as well as cables tensions. The platform starts from position $\mathbf{P}_0 = \begin{bmatrix} 0 & 0.5 & 1 \end{bmatrix}^T$ with a null orientation. The platform moves along the y axis and the desired positions along the x-axis and the z-axis are constants.

Figure 5.3 presents the soft stop complete test trajectory: first, an acceleration phase to reach the necessary platform speed for the test, followed by the emergency stop request at $t = 1.5$ s leading to the platform deceleration in 500 ms:

a) the platform accelerates from $t = 0$ s until it reaches its maximum speed at $t = 0.5$ s;
b) the platform moves along the y-axis at -0.4 $m.s^{-1}$;
c) the emergency deceleration is automatically requested once the platform reaches the center of the workspace, at $t = 1.5$ s;
d) the platform then decelerates in 500 ms to reach a full stop at $t = 2$ s, according to the desired strategy.

Note that the proposed deceleration strategy only consist of the part from $t = 1.5$ s to $t = 2$ s. It is expected with the parameters of the deceleration strategy that the

platform will move for another 100 mm after the emergency stop request with the soft stop strategy.

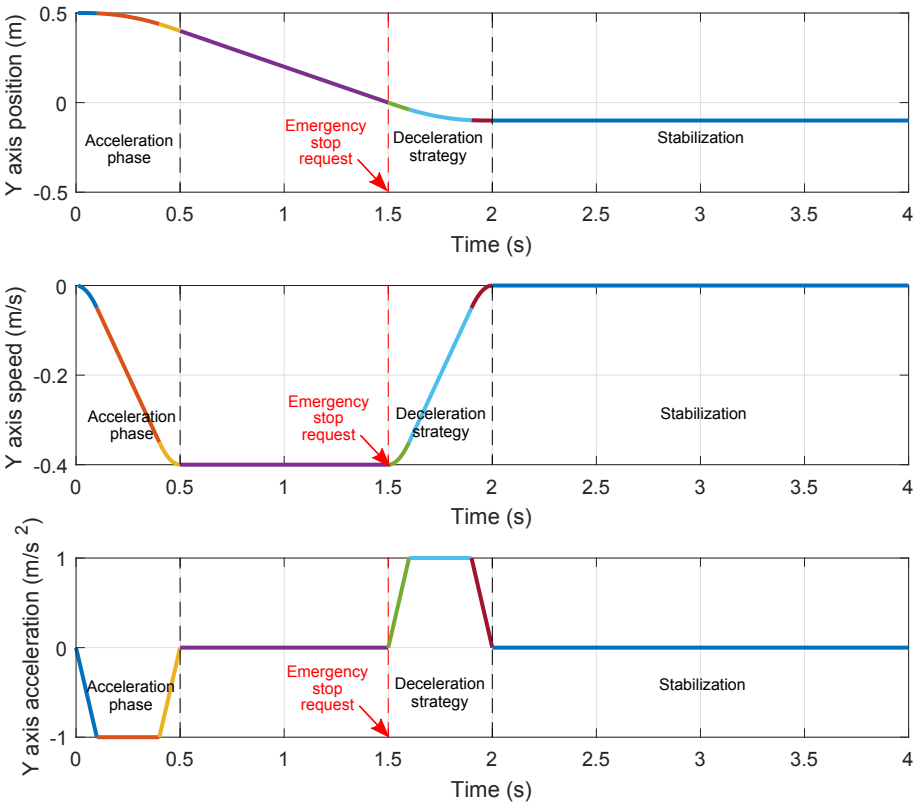

Figure 5.3: Generated trajectory along y-axis for soft stop in a 500 ms time window.

5.3.2 Results

In the following tests, the emergency stop request is made at $t = 1$s.

Figure 5.4 shows the absolute values of motor velocities during trajectory with the two strategies. The immediate stop is clearly identifiable compared to the soft stop that continues for a longer period. It appears that the deceleration greatly reduces the motor velocities until the measurement stopped due to the the power off at $t = 1.5$ s.

The platform tracking results are plotted in Fig. 5.5. Considering the immediate stop, it appears that the platform is shaken. This is particularly visible along the x and z axes. These oscillations of the platform position have a magnitude of a few millimeters and can be attributed to cable elasticity. The platform moves for around 7 millimeters along the y-axis before coming to a full stop, in a time of about 0.1 second. Note that the platform position along the x-axis presents a 10 mm error, that is attributed to the same modeling and measurement errors sources identified in Chapter 4.

On the other hand, the soft stop leads to an expected larger displacement along the y axis while the platform stops, with an additional stopping distance of 88 mm compared to the immediate stop. This distance is substantial in the case of a

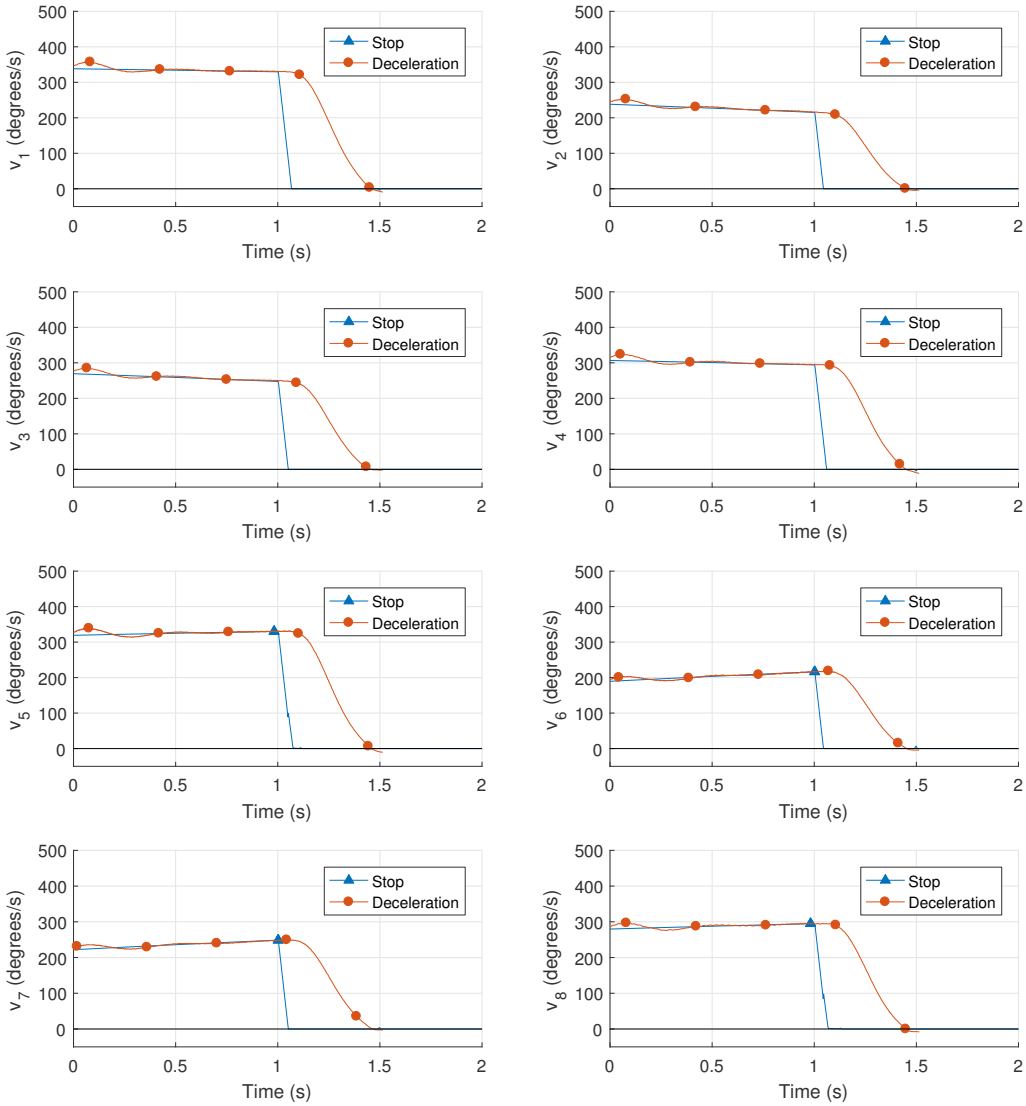

Figure 5.4: Absolute values of motors velocities after emergency stop request at $t = 1$ s with immediate stop and deceleration.

serious emergency situation. On the other hand, oscillations in the platform position disappeared, or are indistinguishable from measurement noise, confirming effectively softly stopping the 266 kg platform.

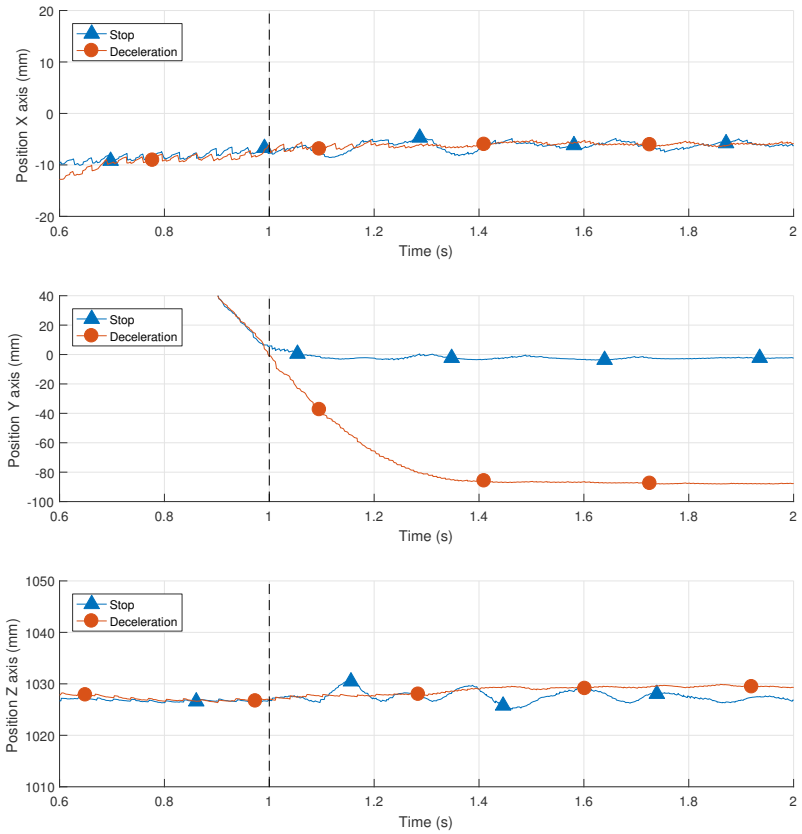

Figure 5.5: Platform trajectory tracking for and immediate stop and a soft.

Finally, cable tensions are plotted in 5.6, with the emergency stop request at $t = 1$s. The difference between the two strategies is clearly visible: in the case of the immediate stop, cable tensions peaks reach 66% of the nominal cable tension before the stop, while the increase is only 15% at most for the soft stop.

The two strategies have their own benefits depending on the user objectives. If the platform must stop in the fastest possible way, the immediate motor stop is a simple yet effective way. However the cable tensions transiently become high, and could be problematic. On the other hand, the simple constant jerk deceleration stopped the platform reduced effect on cable tensions, but with a longer stop distance. Future experiments should aim at reducing this overrun by experimenting with a larger jerk for a smaller time window. A compromise must be found between the maximum deceleration speed achievable while maintaining low cable tension variations. The implementation of model-predictive control for the kinetic energy reduction as in [BB19] also constitutes a perspective to consider.

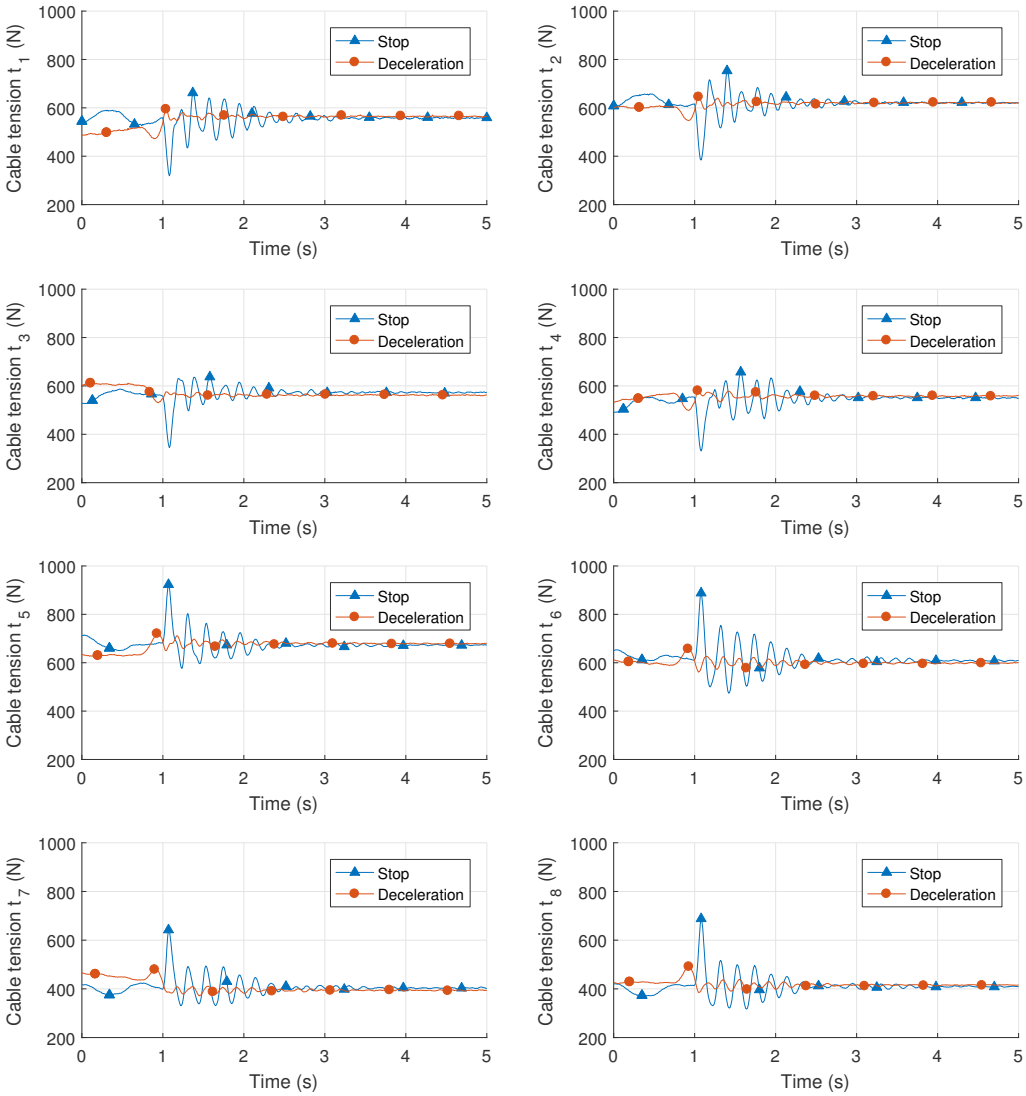

Figure 5.6: Cables tensions after emergency stop request at $t = 1$ s with immediate stop and deceleration.

5.4 SOTDA and overwhelming force

The behavior of ROWC in the event of an overwhelming external wrench was experimentally tested. As discussed in Sec. 4.3.3, in the current implementation of the TDA an emergency stop is requested if the desired force to be applied onto the platform is unfeasible. In this experiment the prototype was controlled using the TC2 architecture and the stiffness oriented TDA with a coefficient ν equal to 0.9. As before, choosing the value of ν determines the proximity to the feasible polygon edge.

After placing the platform at position $\mathbf{p} = \begin{bmatrix} 1.5 & 0.35 & 1.2 \end{bmatrix}^{\mathrm{T}}$ the external wrench effort was applied by hand onto the platform in the y axis negative direction until the emergency stop was triggered. The y component of the controller force, $f_{c,y}$, and the set of cable tensions found by the SOTDA, $\mathbf{t}$, are presented in Fig. 5.7, with the application of the external wrench starting at $t = 1$ s.

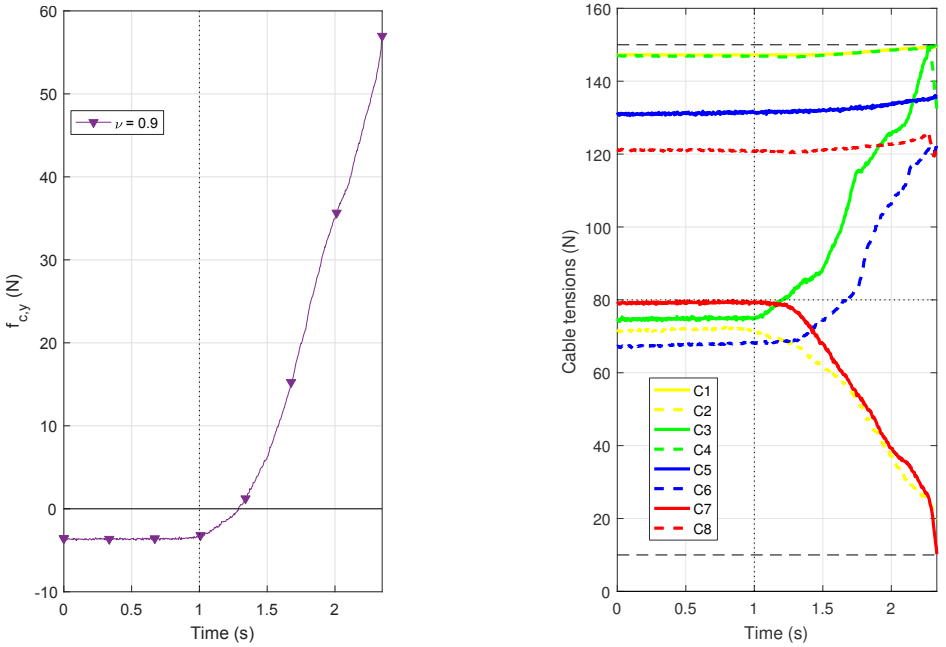

(a) Controller force $f_{c,y}$ (b) Cable tensions $\mathbf{t}$

Figure 5.7: Measurements when an external force is applied onto the platform starting at $t = 1$ s.

It can be observed that as the external wrench increases, so does $f_{c,y}$, while the cable tensions evolves over time in order to maintain the static equilibrium of the platform. The distributed cable tensions are continuous and respect the tensions upper and lower limits up to the triggering of the robot stop. It is noteworthy that during this experiment almost all cable tensions took the same time frame to reach the tension limits.

Figure 5.8 the feasible polygon of ROWC, computed in simulation for different values of the lateral wrench $w_{e,y}$. As the external wrench increases, the area of the feasible polygon decreases. As a consequence, the solutions corresponding to the

barycenter method (BM), to the stiffness oriented TDA (SO) and to the intermediate solution (IS) converge. Eventually, cable tensions tend either towards a minimum or maximum acceptable value, at which point the robot emergency stop is triggered.

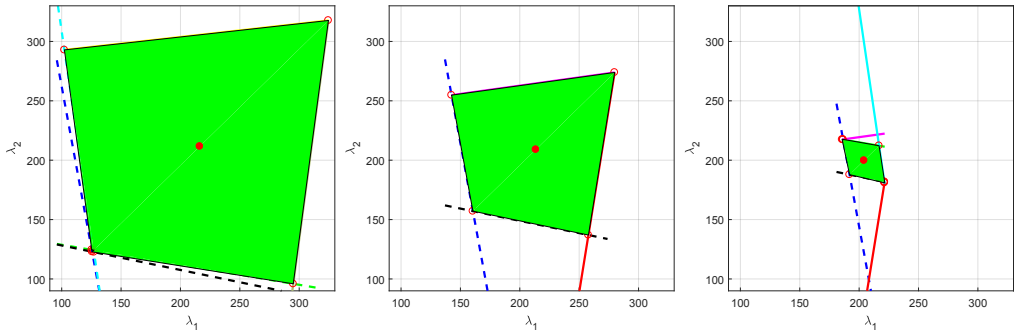

(a) $w_{e,y} = 0$ N (b) $w_{e,y} = 30$ N (c) $w_{e,y} = 57$ N

Figure 5.8: Evolution of feasible polygon depending on applied lateral wrench $w_{e,y}$.

In practice, this behavior can be leveraged to prevent the CDPR from applying a dangerous force on its environment. By this way, in the event of a collision with an obstacle, the CDPR will safely stop when the tension limits are reached.

5.5 Conclusion

Safety and emergency stop strategies are still a novel subject of research for CDPRs, that should be addressed for their deployment, especially for industrial applications. In this chapter, specifications of the desired behavior of CDPRs in an industrial environment have been discussed, then the behavior of ROMP and ROWC in emergency situations was recorded and discussed.

Experiments have been made on the prototype ROMP, in order to compare the effect of a simple motor stop with a deceleration profile. The immediate emergency stop produces shaking of the MP and oscillations in cable tensions, with peaks up to 66% of the nominal tension value. It has been possible to greatly reduce these variations effects by applying a deceleration profile over a short time frame. Future works could target emergency strategies over smaller time windows.

Based on the proposed stiffness oriented TDA, the application of an overwhelming force was experimented on ROWC. As the external force increased, cable tensions tended towards either the maximum or lower admissible. However cable tensions always respected the boundaries, and the robot was stopped when a solution could not be found. The next step will be to develop strategies to resume the motion of the CDPR after an emergency stop in a safe manner, by ensuring that cable tensions still respect those boundaries.

Part II: Conclusion

This second part has been dedicated to the robust control of prototypes ROMP and ROWC, and to the discussion on safety and emergency stops on CDPRs.

Chapter 4 focused on the control architectures implemented on the ROMP and ROWC prototypes. Without external sensors to measure the position of the platform, and since the resolution of the forward kinematics of the robot has been set aside in Part I, the considered control architectures are based on the errors in the joint space. The CDPR modeling written in Part I are used for trajectory generation. In particular for the ROMP prototype, the model including the pulleys geometry has been used to improve accuracy.

Several control architectures have been compared for the control of ROMP, the objective being to ensure robustness towards the mass variations. The mass estimation method introduced in Part I has been also leveraged in a feedforward term updated in real-time. A proportional-derivative controller (PD) and a controller balancing between sliding mode and linear control (SML) have been experimented in each architecture, along the test trajectory of ROMP. The recently developed SML controller achieved good accuracy even in the case of an entirely unknown payload. This is an advantage towards robustness, as this controller can be applied on CDPRs where the cable tensions cannot be easily assessed. It has been however observed that even if good accuracy and repeatability is achieved at the motor level, the platform positioning has been still affected to the mass due to cable elasticity. An architecture compensating for cable elongation successfully reduced the robot sensitivity to payload changes in the Cartesian space, improving the platform pose repeatability. It is expected that the remaining errors are due to the current identification of the robot geometric parameters and to the precision of the calibration

process. These aspects will be investigated in future work art IRT Jules Verne.

Secondly, in the frame of the window cleaning application a stiffness oriented tension distribution algorithm (SOTDA) has been proposed in order to minimize the platform displacement in the presence of an external wrench. After an analysis of the distributed tension in simulation, this SOTDA has been tested experimentally on the ROWC prototype. With the proposed cable tension selection method, the robot deflection when subjected to a lateral force could be reduced by up to 24% compared to the barycenter method. A safe operational margin could be maintained with respect to the maximum admissible forces thanks to the implementation of coefficient ν, that permitted the selection of an intermediate between the stiffness oriented and the barycenter solutions.

Since safety is a major concern for the deployment of CDPR in industrial applications, Chapter 5 discussed their emergency stop, based on the control architectures implemented in Chapter 4. The behavior of ROMP platform has been studied during two types of emergency stops: *i)* an immediate stop of the motors, the typical emergency strategy for systems of low moving weight *ii)* a platform deceleration in 500 milliseconds. The immediate stop of the motors leads to the shortest stop of the platform. However, oscillations in the cable tensions are consequent and vibrations of the platform are clearly visible. This type of stop can put strain on the structure of the CDPR, and requires to secure the payload to avoid an unwanted drop of the object in pick-and-place applications. On the other hand, the 500 millisecond time frame for the deceleration of the platform allows for a smooth stop and reduces the variations in cable tensions. However, with this second method the platform continues to move several centimeters after the emergency stop request, which would be problematic if the goal is to avoid collision with an object of operator. The choice between the two strategies can be dynamically chosen on a CDPR depending on the classification of the emergency types. Finally, the proposed SOTDA has been experimentally confronted to an unfeasible force to observe the evolution of cable tensions. As expected, as the force increases the feasible polygon area becomes smaller, until it becomes empty. The cable tension then tend towards a minimum or maximum value, but always respect the defined boundaries.

Perspectives

Perspectives

In order to meet a wider range of industrial applications, the next steps in the development of CDPRs at IRT Jules Verne is discussed in the sequel.

Modeling

From the experiments made during this thesis, the consideration of the pulleys geometry improve the accuracy of CDPR modeling maintaining a limited computation cost. Similarly, the linear cable elasticity model considered for evaluating the cable elongation, has shown its efficiency to ensure positioning repeatability of the platform in spite of load changes on the ROMP prototype. This elasticity model also allowed the definition of the stiffness matrix used in the stiffness oriented tension distribution algorithm (SOTDA) proposed for the window cleaning application.

The remaining positioning errors of the platform will need to be addressed. These are expected to result from the combinations of several factors. First, a better identification of the CDPR parameters and its geometry, as the nominal values from the CAD model where used in the trajectory generation in these experiments. Several small geometric variables are still neglected such as the cable angle between its exit point from the winches to its entry point onto the pulleys, that can account for errors in the orders of the centimeters. It is also expected for very large CDPRs that cable sagging will no longer be negligible. Future work at IRT Jules Verne could include the simulation of CDPRs with more elaborate cable models such as the sagging elastic cable model [Irv92; KZW06]. A dynamic simulator with such cable modeling is now necessary. Commercial solutions such as V-rep and its module Vortex are considered for this task.

Calibration

Lasting positioning errors of ROMP observed in the experiments are assumed to be due to the manual calibration process. Indeed, small error in the platform manual positioning during the calibration process might have a large effect on the platform accuracy, especially at the edges of the workspace. The need for a quick and repeatable calibration process is the main motivation for the implementation of an automatic calibration procedure.

The self-calibration method, based on the cable loop closure equations and the modeling including the pulleys geometry and cable elasticity must be experimented on the real prototypes. It will be particularly interesting to see which model provides the best results on each robot. The method has the advantage of simplicity of implementation and does not require additional sensors, however it might quickly lead to local

minima and it was found that slight changes in the model used for self-calibration could greatly impact the quality of the estimation. Parameter identifiability is also a concern as some parameters seem more difficult to estimate than others. A future improvement of the method would be the inclusion of the platform static equilibrium in the optimization problem to increase the total number of equations, and to better leverage the force sensors of prototype ROMP. In connection with the discussion on safety and regulation around CDPRs, certified calibration methods [Dit+14], in which the accuracy of the model can be quantified, should also be considered for future work on the calibration of industrial CDPRs. Lastly, while calibration methods based on external sensors were not considered in the ROCKET project due to environment constraints, vision-based calibration should be experimented in other projects at IRT Jules Verne to evaluate their efficiency.

Control

The retained architectures for ROMP are the SML based architectures, with or without knowledge of the platform mass, and the PD based control scheme with the mass assessment step. Some more work on the tuning of the SML controller will be realized in order to achieve a higher average value of the balancing parameter *alpha*, thus reducing platform shaking. A finer tuning of the SML controller should also lead to a reduced energy consumption compared to pure sliding mode approaches, this being a key point of the industry of the future and IRT Jules Verne roadmap.

The control schemes implemented on ROMP illustrated the differences between accuracy in the joint space and accuracy in the Cartesian space, as platform positioning errors still exist despite achieving low motor position errors. The evaluation of cable elasticity and its compensation helped with the repeatability on ROMP, but some errors still remain. In order to achieve a higher accuracy of the platform position, the robot model must be further improved or the error must be evaluated at the platform level. Vision based systems are more and more used for the direct measurement of the platform pose. Recent works at IRT Jules Verne have been focused on vision based control of CDPRs such as [Zak+19b; Zak+19a]. If the pose error of the platform is known, the SML controller can then be implemented in the Cartesian space. Combination with the SOTDA, the resulting control architecture could merge the robustness of the sliding mode control, the platform positioning accuracy offered by vision-based control, and the tension distribution maximizing the CDPR stiffness.

Stiffness oriented tension distribution

The proposed stiffness oriented tension distribution algorithm (SOTDA) has been successfully applied in real-time on the ROWC prototype. However, assumptions have been made on the location of the minimum in a corner of the feasible polygon. These assumptions could be validated if an analysis of the SOTDA objective function

proves that it is a convex or concave function. Moreover, efficient optimization methods would be applicable to quickly determine this minimum. If the objective function shape is not constant across the entire workspace, the assumptions might not always hold and general minimization algorithms will be required.

When defining the coefficient ν in Sec. 4.3.3, an assumption has also been made that the intermediate solution (IS) stiffness always leads to an improved robot stiffness compared to the barycenter (BM). Since the surface of the 3D feasible polygon presented in the simulation results (Fig. 4.36) is almost planar, the relationship between ν and the platform displacement appears to be close from a linear one. The platform displacement measurements in the static pose experiment of Sec. 4.7.1 seem to validate this behavior. This point remains to be analytically proven through the analysis of the objective function.

Safety and standardization

As discussed in Chapter 5, the safety regulations are currently a concern for CDPR acceptability in the industry and the standardization of CDPRs is an ongoing work at IRT Jules Verne. Following the experiment on emergency stop of ROMP and ROWC, future work could include the development of strategies to resume the motion of the CDPR after an emergency stop in a safe manner, by ensuring that cable tensions still respect those boundaries. A dynamically adaptive stiffness coefficient ν could also be experimented depending on the situation. The robot stiffness could be maximized only in the presence of an external force, allowing to reduce cable tensions in nominal operation conditions. It might also be interesting the future to implement a compliance of the CDPR in the event of a large external force to avoid cable over-tensions before the feasible polygon becomes empty.

Bibliography

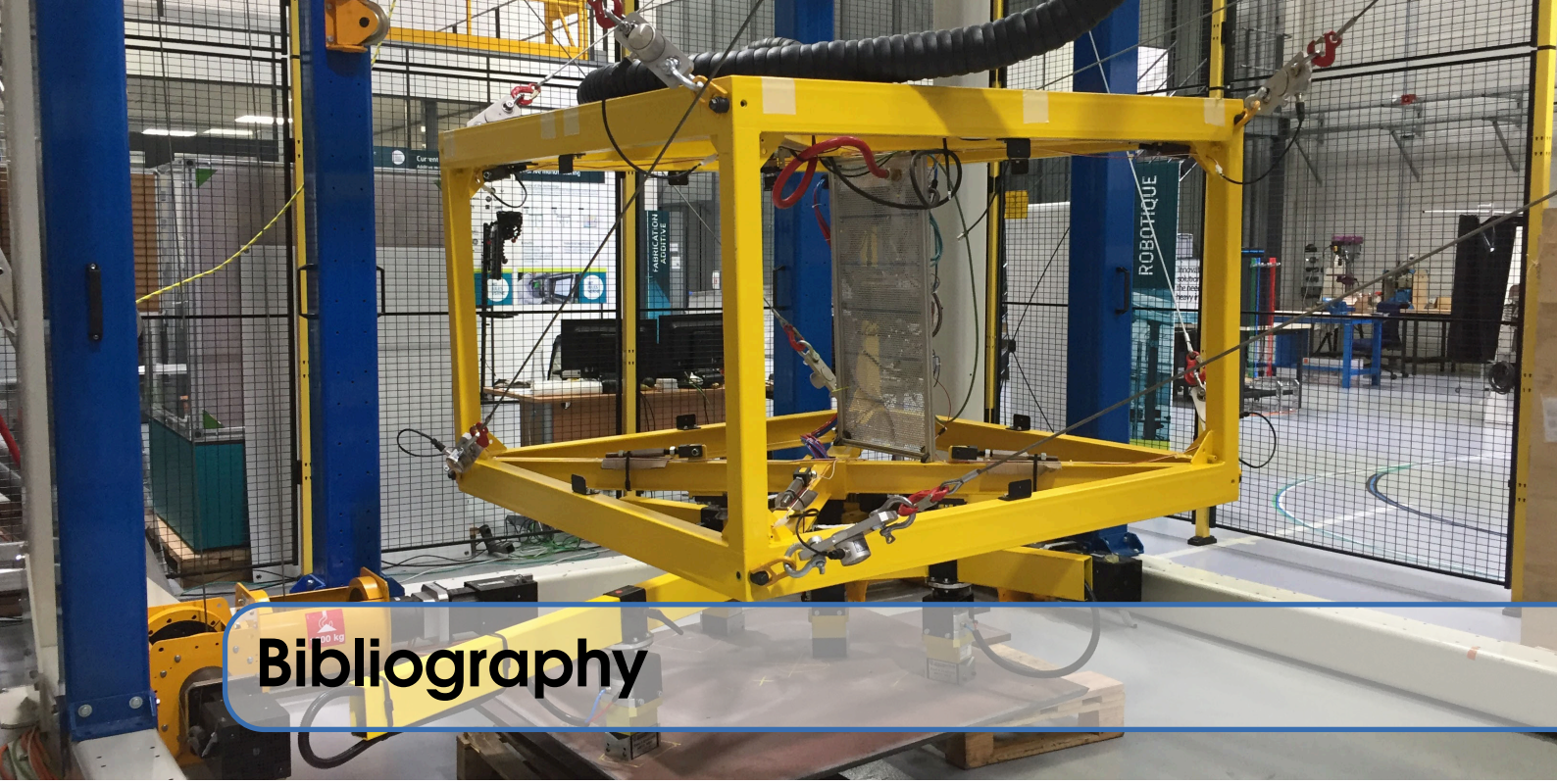

Bibliography

[AC15] Ghasem Abbasnejad and Marco Carricato. “Direct Geometrico-static Problem of Underconstrained Cable-Driven Parallel Robots With n Cables”. In: *IEEE Transactions on Robotics* 31.2 (2015), pages 468–478.

[ABD92] J. Albus, R. Bostelman, and N. Dagalakis. “The NIST SPIDER, A robot crane”. In: *Journal of Research of the National Institute of Standards and Technology* volume 97.3 (1992), page 373.

[ADG13] Julien Alexandre, David Daney, and Marc Gouttefarde. “Calibration of a Fully-Constrained Parallel Cable-Driven Robot”. In: 544.2007 (2013).

[AH17] Julien Alexandre dit Sandretto and Milan Hladík. “Solving over-constrained systems of non-linear interval equations – And its robotic application”. In: *Applied Mathematics and Computation* 313 (2017), pages 180–195.

[AV12] Alireza Alikhani and Mehdi Vali. “Sliding Mode Control of a Cable-driven Robot via Double-Integrator Sliding Surface”. In: *Conference on Control, Robotics and Cybernetics*. 2012.

[Ars13] Marc Arsenault. “Workspace and stiffness analysis of a three-degree-of-freedom spatial cable-suspended parallel mechanism while considering cable mass”. In: *Mechanism and Machine Theory* 66 (2013), pages 1–13.

[AH95] Karl J. (Karl Johan) Aström and Tore Hägglund. *PID Controllers: Theory, Design, and Tuning*. International Society for Measurement and Control, 1995, page 343.

[BCC18] Sana Baklouti, Stéphane Caro, and Eric Courteille. “Sensitivity analysis of the elasto-geometrical model of cable-driven parallel robots”. In: *Mechanisms and Machine Science* 53 (2018), pages 37–49.

[Bak+17] Sana Baklouti, Eric Courteille, Stéphane Caro, and Mohamed Dkhil. “Dynamic and Oscillatory Motions of Cable-Driven Parallel Robots Based on a Nonlinear Cable Tension Model”. In: *Journal of Mechanisms and Robotics* 9.6 (2017), page 061014.

[Beh06] Saeed Behzadipour. “Stiffness of Cable-based Parallel Manipulators With Application to Stability Analysis”. In: *Journal of mechanical design* (2006).

[BGC18] Alessandro Berti, Marc Gouttefarde, and Marco Carricato. “Dynamic Recovery of Cable-Suspended Parallel Robots After a Cable Failure”. In: (2018), pages 331–339.

[BMC16] Alessandro Berti, Jean Pierre Merlet, and Marco Carricato. “Solving the direct geometrico-static problem of underconstrained cable-driven parallel robots by interval analysis”. In: *International Journal of Robotics Research* (2016).

[Bor+09a] Per Henrik Borgstrom, Brett L Jordan, Bengt J Borgstrom, Michael J Stealey, Gaurav S Sukhatme, Senior Member, Maxim A Batalin, William J Kaiser, and Senior Member. “NIMS-PL : A Cable-Driven Robot With Self-Calibration Capabilities”. In: 25.5 (2009), pages 1005–1015.

[Bor+09b] Per Henrik Borgstrom, Brett L. Jordan, Gaurav S. Sukhatme, Maxim A. Batalin, William J. Kaiser, P H Borgstrm, Brett L. Jordan, Gaurav S. Sukhatme, Maxim A. Batalin, William J. Kaiser, Per Henrik Borgstrom, Brett L. Jordan, Gaurav S. Sukhatme, Maxim A. Batalin, and William J. Kaiser. “Rapid computation of optimally safe tension distributions for parallel cable-driven robots”. In: *IEEE Transactions on Robotics* 25.6 (2009), pages 1271–1281.

[BB19] Roland Boumann and Tobias Bruckmann. “Development of emergency strategies for cable-driven parallel robots after a cable break”. In: *Mechanisms and Machine Science*. Volume 74. Springer, Cham, 2019, pages 269–280.

[BT01] Mohamed Bouri and Daniel Thomasset. “Sliding control of an electropneumatic actuator using an integral switching surface”. In: *IEEE Transactions on Control Systems Technology* (2001).

[BMB08] J. G.H. Bouwmeester, R. Marissen, and O. K. Bergsma. “Carbon/Dyneema® intralaminar hybrids: New strategy to increase impact resistance or decrease mass of carbon fiber composites”. In: *ICAS Secretariat - 26th Congress of International Council of the Aeronautical Sciences 2008, ICAS 2008* 1 (2008), pages 3851–3856.

[CM11] Marco Carricato and Jean Pierre Merlet. “Direct geometrico-static problem of under-constrained cable-driven parallel robots with three cables”. In: *Proceedings - IEEE International Conference on Robotics and Automation* July (2011), pages 3011–3017.

[CCL17] R. Chellal, L. Cuvillon, and E. Laroche. “Model identification and vision-based H∞position control of 6-DoF cable-driven parallel robots”. In: *International Journal of Control* (2017).

[CCL15] Ryad Chellal, Loïc Cuvillon, and Edouard Laroche. “A kinematic vision-based position control of a 6-DoF cable-driven parallel robot”. In: *Mechanisms and Machine Science*. 2015.

[CLC14] Ryad Chellal, Edouard Laroche, and Loic Cuvillon. “An H∞ methodology for position control of 6-DoF Cable-Driven Parallel Robots”. In: *2014 European Control Conference, ECC 2014*. 2014.

[Che+13] Ryad Chellal, Edouard Laroche, Loïc Cuvillon, and Jacques Gangloff. “An identification methodology for 6-DoF cable-driven parallel robots parameters application to the INCA 6D robot”. In: *Mechanisms and Machine Science*. 2013.

[DS13] Alexandre Dit-Sandretto. “Certified calibration of parallel cable-driven robots”. In: (2013), pages 1–154.

[Dit+14] Julien Alexandre Dit Sandretto, Gilles Trombettoni, David Daney, and Gilles Chabert. “Certified calibration of a cable-driven robot using interval contractor programming”. In: *Mechanisms and Machine Science* 15 (2014), pages 209–217.

[EUV04] I. Ebert-Uphoff and P.a. Voglewede. “On the connections between cable-driven robots, parallel manipulators and grasping”. In: *IEEE International Conference on Robotics and Automation, 2004. Proceedings. ICRA ’04. 2004* 5.c (2004), pages 4521–4526.

[ES98] C Edwards and S Spurgeon. *Sliding mode control: theory and applications*. CRC Press, 1998.

[EGGC15] Gamal El-Ghazaly, Marc Gouttefarde, and Vincent Creuze. “Adaptive terminal sliding mode control of a redundantly-actuated cable-driven parallel manipulator: CoGiRo”. In: *Mechanisms and Machine Science*. Volume 32. Springer, Cham, 2015, pages 179–200.

[EP14] Antonio Estrada and Franck Plestan. “Second order sliding mode output feedback control with switching gains - Application to the control of a pneumatic actuator”. In: *Journal of the Franklin Institute* (2014).

[Fan+04] S. Fang, D. Franitza, M. Torlo, F. Bekes, and M. Hiller. “Motion Control of a Tendon-BasedParallel Manipulator Using Optimal Tension Distribution”. In: *IEEE/ASME Transactions on Mechatronics* 9.3 (2004), pages 561–568.

[FCCG14a] A Fortin-Coté, P Cardou, and C Gosselin. “An admittance control scheme for haptic interfaces based on cable-driven parallel mechanisms”. In: *Proceedings of the 2014 IEEE International Conference on Robotics and Automation (ICRA)*. Hong Kong, 2014, pages 819–925.

[FCCG14b] Alexis Fortin-Côté, Philippe Cardou, and Clément Gosselin. “An admittance control scheme for haptic interfaces based on cable-driven parallel mechanisms”. In: *Proceedings - IEEE International Conference on Robotics and Automation* (2014), pages 819–825.

[Gag+15] L Gagliardini, S Caro, M Gouttefarde, P Wenger, and A Girin. “A Reconfigurable Cable-Driven Parallel Robot for Sandblasting and Painting of Large Structures”. In: *Cable-Driven Parallel Robots*. Volume 32. Mechanisms and Machine Science. Springer, 2015, pages 275–291.

[Gag16] Lorenzo Gagliardini. “Discrete reconfigurations of cable-driven parallel robots”. PhD Thesis, Centrale Nantes. 2016.

[GGC18] Lorenzo Gagliardini, Marc Gouttefarde, and Stephane Caro. “Determination of a Dynamic Feasible Workspace for Cable-Driven Parallel Robots”. In: *Advances in Robot Kinematics 2016* volume 4 (2018), pages 361–370.

[Ger+13] Coralie Germain, Stéphane Caro, Sébastien Briot, and Philippe Wenger. “Optimal design of the IRSBOT-2 based on an optimized test trajectory”. In: *Volume 6A: 37th Mechanisms and Robotics Conference* (2013), pages 1–11.

[Gos88] Clément Gosselin. “Kinematic analysis, optimization and programming of parallel robotic manipulators”. PhD thesis. McGill University, 1988.

[Gos13] Clément Gosselin. “Global planning of dynamically feasible trajectories for three-dof spatial cable-suspended parallel robots”. In: *Mechanisms and Machine Science*. 2013.

[GW62] V. E. Gough and S. G. Whitehall. “Universal Tyre Test Machine”. In: *FISITA Proceedings* (1962).

[Gou+15] M Gouttefarde, J Lamaury, C Reichert, and T Bruckmann. “A Versatile Tension Distribution Algorithm for 6-DOF Parallel Robots Driven by n+2 Cables”. In: *IEEE Transactions on Robotics* 31.6 (2015), pages 1444–1457.

[GG16] Marc Gouttefarde and Marc Gouttefarde. “Cable-Driven Parallel Robots Content Overview Workspace and Wrench Feasibility A few Words on Design Tension Distribution and Basic Control”. In: March (2016).

[Gua+14] François Guay, Philippe Cardou, Ana Lucia Cruz-Ruiz, and Stéphane Caro. “Measuring How Well a Structure Supports Varying External Wrenches”. In: Springer, Dordrecht, 2014, pages 385–392.

[Ham+19] Marcus Hamann, Pauline Marie Nüsse, David Winter, and Christoph Ament. “Towards a Precise Cable-Driven Parallel Robot - A Model-Driven Parameter Identification Enhanced by Data-Driven Position Correction”. In: Springer, Cham, 2019, pages 367–376.

[HK09] M Hassan and A Khajepour. “Analysis of Large-Workspace Cable-Actuated Manipulator for Warehousing Applications”. In: *Proc. of the ASME Int. Design Eng. Tech. Conf. & Comput. and Inform. in Eng. Conf. (IDETC/CIE 2009)*. San Diego, CA, 2009, pages 45–53.

[HK11] Mahir Hassan and Amir Khajepour. “Analysis of bounded cable tensions in cable-actuated parallel manipulators”. In: *IEEE Transactions on Robotics* (2011).

[HC04] Cs Holland and Dj Cannon. “Cable array robot for material handling”. In: *US Patent 6,826,452* 1.12 (2004).

[Hu+14] Yongpan Hu, Limin Tao, Jun Jia, and Wei Lv. “Control and Simulation of Cable-Driven Parallel Robots in Offshore Cargo Handling”. In: *Proceedings of the World Congress on Intelligent Control and Automation (WCICA)* (2014), pages 2451–2455.

[Hus96] M. L. Husty. “An algorithm for solving the direct kinematics of general Stewart-Gough platforms”. In: *Mechanism and Machine Theory* (1996).

[IMC19] Edoardo Idá, Jean Pierre Merlet, and Marco Carricato. “Automatic self-calibration of suspended under-actuated cable-driven parallel robot using incremental measurements”. In: *Mechanisms and Machine Science*. 2019.

[Irv92] H. Max. Max Irvine. Irvine. *Cable structures*. 1992.

[Isi95] Alberto Isidori. *Nonlinear Control Systems*. Communications and Control Engineering. London: Springer London, 1995.

[Jin+18] Xue Jun Jin, Jinwoo Jung, Seong Young Ko, Eunpyo Choi, Jong Oh Park, and Chang Sei Kim. “Geometric parameter calibration for a cable-driven parallel robot based on a single one-dimensional laser distance sensor measurement and experimental modeling”. In: *Sensors (Switzerland)* 18.7 (2018).

[Kam+16] Kaveh Kamali, Ahmed Joubair, Ilian A. Bonev, and Pascal Bigras. “Elasto-geometrical calibration of an industrial robot under multidirectional external loads using a laser tracker”. In: *Proceedings - IEEE International Conference on Robotics and Automation* 2016-June (2016), pages 4320–4327.

[Kaw+95] S. Kawamura, W. Choe, S. Tanaka, and S. R. Pandian. “Development of an ultrahigh speed robot FALCON using wire drive system”. In: *Proceedings - IEEE International Conference on Robotics and Automation* 1 (1995), pages 215–220.

[Kaw+00] Sadao Kawamura, Hitoshi Kino, Choe Won, S Kamawura, Hitoshi Kino, and Choe Won. “High-speed manipulation by using parallel wire-driven robots”. In: *Robotica* 18.1 (2000), pages 13–21.

[KD04] W. Khalil and E. Dombre. *Modeling, Identification and Control of Robots*. Butterworth-Heinemann, 2004.

[KJ75] W P Koevermans and C J Jansen. “Design and performance of the four dof motion system of the NLR research flight simulator”. In: *Proc. of AGARD Conf.* 198. 1975, pages 11–17.

[KZW06] Kris Kozak, Qian Zhou, and Jinsong Wang. “Static analysis of cable-driven manipulators with non-negligible cable mass”. In: *IEEE Trans. on Robotics* 22.3 (2006), pages 425–433.

[Kra+13] Werner Kraus, Valentin Schmidt, Puneeth Rajendra, and Andreas Pott. “Load identification and compensation for a Cable-Driven parallel robot”. In: *Proceedings - IEEE International Conference on Robotics and Automation*. 2013, pages 2485–2490.

[Kra+14] Werner Kraus, Valentin Schmidt, Puneeth Rajendra, and Andreas Pott. "System identification and cable force control for a cable-driven parallel robot with industrial servo drives". In: *Proceedings - IEEE International Conference on Robotics and Automation*. 2014, pages 5921–5926.

[Kra+17] Werner Kraus, Valentin Schmidt, Puneeth Rajendra, and Andreas Pott. "System Identification and Cable Force Control for a Cable-Driven Parallel Robot with Industrial Servo Drives System Identification and Cable Force Control for a Cable-Driven Parallel Robot with Industrial Servo Drives". In: July (2017).

[Lam13] Johann Lamaury. "Contribution a la commande des robots paralleles a cables a redondance d'actionnement". In: (2013).

[LG13] Johann Lamaury and Marc Gouttefarde. "Control of a large redundantly actuated cable-suspended parallel robot". In: *Proceedings of the 2013 IEEE International Conference on Robotics and Automation (ICRA)*. Karlsruhe, Germany, 2013, pages 4659–4664.

[Lam+13] Johann Lamaury, Marc Gouttefarde, Ahmed Chemori, and Pierre Elie Herve. "Dual-space adaptive control of redundantly actuated cable-driven parallel robots". In: *Proceedings of the 2013 IEEE International Conference on Intelligent Robots and Systems (IROS)*. Tokyo, Japan, 2013, pages 4879–4886.

[Lar+13] Edouard Laroche, Ryad Chellal, Loïc Cuvillon, and Jacques Gangloff. "A preliminary study for H∞ control of parallel cable-driven manipulators". In: *Mechanisms and Machine Science*. 2013.

[Lau18] Darwin Lau. "Initial length and pose calibration for cable-driven parallel robots with relative length feedback". In: *Mechanisms and Machine Science*. Volume 53. 2018, pages 140–151.

[Lev93] Arie Levant. "Sliding order and sliding accuracy in sliding mode control". In: *International Journal of Control* 58.6 (1993), pages 1247–1263.

[Maj+10] Ana C. Majarena, Jorge Santolaria, David Samper, and Juan J. Aguilar. "An overview of kinematic and calibration models using internal/external sensors or constraints to improve the behavior of spatial parallel mechanisms". In: *Sensors (Switzerland)* 10.11 (2010), pages 10256–10297.

[Mer01] J.-P. Merlet. "Micro parallel robot MIPS for medical applications". In: *Proc. of the IEEE Int. Conf. on Emerging Technologies and Factory Automation (ETFA 2001)*. Volume 2. February 2001. Antibes-Juan les Pins, France, 2001, pages 611–619.

[Mer08a] J.-P. Merlet. “Analysis of wire elasticity for Wire-Driven parallel robots”. In: *Proceedings of the 2nd European Conf. on Mechanism Science (EUCOMES 2008)*. Cassino, Italy, 2008, pages 471–478.

[Mer08b] J. P. Merlet. “Kinematics of the wire-driven parallel robot MARIONET using linear actuators”. In: *Proceedings - IEEE International Conference on Robotics and Automation*. 2008, pages 3857–3862.

[MD10] J. P. Merlet and D. Daney. “A portable, modular parallel wire crane for rescue operations”. In: *Proceedings of the 2010 IEEE International Conference on Robotics and Automation (ICRA)*. 2010, pages 2834–2839.

[Mer06] J.-P. Jean-Pierre. Merlet. *Parallel Robots*. 2nd edition. Springer, 2006.

[Mer15] Jean Pierre Merlet. “The kinematics of cable-driven parallel robots with sagging cables: Preliminary results”. In: *Proceedings of the 2015 IEEE International Conference on Robotics and Automation (ICRA)*. Seattle, WA, USA, 2015, pages 1593–1598.

[MBN09] Gabriel Meunier, Benoit Boulet, and Mayer Nahon. “Control of an overactuated cable-driven parallel mechanism for a radio telescope application”. In: *IEEE Transactions on Control Systems Technology* 17.5 (2009), pages 1043–1054.

[Mie+16] Philipp Miermeister, Maria Lächele, Rainer Boss, Carlo Masone, Christian Schenk, Joachim Tesch, Michael Kerger, Harald Teufel, Andreas Pott, and Heinrich H. Bülthoff. “The CableRobot simulator large scale motion platform based on Cable Robot technology”. In: *IEEE International Conference on Intelligent Robots and Systems* 2016-Novem (2016), pages 3024–3029.

[MP12] Philipp Miermeister and Andreas Pott. “Auto calibration method for cable-driven parallel robots using force sensors”. In: *Latest Advances in Robot Kinematics*. 2012, pages 269–276.

[MPV12] Philipp Miermeister, Andreas Pott, and Alexander Verl. “Auto-calibration method for overconstrained cable-driven parallel robots”. In: *ROBOTIK 2012, 7th German Conference on Robotics 2012. Proceedings. CD-ROM* (2012), pages 301–306.

[Mik+08] Lars Mikelsons, Tobias Bruckmann, Manfred Hiller, and Dieter Schramm. “A real-time capable force calculation algorithm for redundant tendon-based parallel manipulators”. In: *Proceedings - IEEE International Conference on Robotics and Automation*. 2008.

[Ngu+13] Dinh Quan Nguyen, Marc Gouttefarde, Olivier Company, and Francois Pierrot. “On the simplifications of cable model in static analysis of large-dimension cable-driven parallel robots”. In: *IEEE International Conference on Intelligent Robots and Systems*. 2013.

[OA06] S.-R So Ryeok Oh and Sunil K. Agrawal. “Generation of feasible set points and control of a cable robot”. In: *IEEE Trans. on Robotics* 22.3 (2006), pages 551–558.

[OA05] So-ryeok Ryeok Oh and Sunil K. Agrawal. “Cable suspended planar robots with redundant cables: Controllers with positive tensions”. In: *IEEE Transactions on Robotics* 21.3 (2005), pages 457–465.

[PZB19] Chiara Passarini, Damiano Zanotto, and Giovanni Boschetti. “Dynamic trajectory planning for failure recovery in cable-suspended camera systems”. In: *Journal of Mechanisms and Robotics* 11.2 (2019).

[Pic+18a] Étienne Picard, Stéphane Caro, Fabien Claveau, and Franck Plestan. “Pulleys and Force Sensors Influence on Payload Estimation of Cable-Driven Parallel Robots”. In: *Proceedings of the 2018 IEEE International Conference on Intelligent Robots and Systems (IROS)*. Madrid, Spain, 2018, pages 1429–1436.

[Pic+18b] Etienne Picard, Stéphane Caro, Franck Plestan, and Fabien Claveau. “Control solution for a cable driven parallel robot with highly variable payload”. In: *Proceedings of the 2018 ASME Design Engineering Technical Conference*. Volume 5B-2018. Quebec City, QC, 2018.

[Pot+13] A Pott, H Mütherich, W Kraus, V Schmidt, P Miermeister, and A Verl. “{IPAnema}: a family of cable-driven parallel robots for industrial applications”. In: *Cable-Driven Parallel Robots*. Volume 12. Mechanisms and Machine Science. Springer, 2013, pages 119–134.

[Pot10] Andreas Pott. “An Algorithm for Real-Time Forward Kinematics of Cable-Driven Parallel Robots”. In: *Springer* (2010).

[Pot12] Andreas Pott. “Influence of pulley kinematics on cable-driven parallel robots”. In: *Latest Advances in Robot Kinematics*. 2012, pages 197–204.

[Pot14] Andreas Pott. “An improved force distribution algorithm for over-constrained cable-driven parallel robots”. In: *Mechanisms and Machine Science* 15 (2014), pages 139–146.

[PK16] Andreas Pott and Werner Kraus. “Determination of the wrench-closure translational workspace in closed-form for cable-driven parallel robots”. In: *Proceedings - IEEE International Conference on Robotics and Automation* 2016-June.June (2016), pages 882–887.

[PMV10] Andreas Pott, Christian Meyer, and Alexander Verl. “Large-scale assembly of solar power plants with parallel cable robots”. In: *Isr/Robotik 2010* (2010), pages 999–1004.

[Raf+04] Philippe A. Raffin, Robert N. Martin, Yau-De Huang, Ferdinand Patt, Robert C. Romeo, Ming-Tang Chen, and Jeffrey S. Kingsley. “CFRP platform and hexapod mount for the Array of MIcrowave Background Anisotropy (AMiBA)”. In: *Astronomical Structures and Mechanisms Technology*. 2004.

[Ras+18] Tahir Rasheed, Philip Long, David Marquez-Gamez, and Stephane Caro. “Available wrench set for planar mobile cable-driven parallel robots”. In: *Proceedings - IEEE International Conference on Robotics and Automation* (2018), pages 962–967.

[RGL98] Rodney G. Roberts, Todd Graham, and Thomas Lippitt. “On the inverse kinematics, statics, and fault tolerance of cable-suspended robots”. In: *Journal of Robotic Systems* 15.10 (1998), pages 581–597.

[RGM07] G Rosati, P Gallina, and S Masiero. “Design, implementation and clinical test of a Wire-Based robot for neurorehabilitation”. In: *IEEE Trans. on Neural Syst. and Rehabilitation Eng.* 15.4 (2007), pages 560–569.

[Rui+15] Ana Lucia Cruz Ruiz, Stéphane Caro, Philippe Cardou, and François Guay. “ARACHNIS: Analysis of Robots Actuated by Cables with Handy and Neat Interface Software”. In: Springer, Cham, 2015, pages 293–305.

[STD13] Julien Alexandre dit Sandretto, Gilles Trombettoni, and David Daney. “Confirmation of Hypothesis on Cable Properties for Cable-Driven Robots”. In: Springer, Dordrecht, 2013, pages 85–93.

[San+12] Julien Alexandre Dit Sandretto, David Daney, Marc Gouttefarde, and Cédric Baradat. “Calibration of a fully-constrained parallel cable-driven robot”. In: (2012).

[SCG19] João Cavalcanti Santos, Ahmed Chemori, and Marc Gouttefarde. “Model Predictive Control of Large-Dimension Cable-Driven Parallel Robots”. In: Springer, Cham, 2019, pages 221–232.

[SBM15] Christian Schenk, Heinrich H. Bulthoff, and Carlo Masone. “Robust adaptive sliding mode control of a redundant cable driven parallel robot”. In: *2015 19th International Conference on System Theory, Control and Computing, ICSTCC 2015 - Joint Conference SINTES 19, SACCS 15, SIMSIS 19* (2015), pages 427–434.

[Sch+18] Christian Schenk, Carlo Masone, Andreas Pott, and Heinrich H. Bülthoff. "Application of a differentiator-based adaptive super-twisting controller for a redundant cable-driven parallel robot". In: *Mechanisms and Machine Science*. Volume 53. 2018, pages 254–267.

[Sht+14] Yuri Shtessel, Christopher Edwards, Leonid Fridman, and Arie Levant. *Sliding mode control and observation*. Control Engineering. New York, NY: Springer New York, 2014, pages 1–356.

[STP12] Yuri Shtessel, Mohammed Taleb, and Franck Plestan. "A novel adaptive-gain supertwisting sliding mode controller: Methodology and application". In: *Automatica* 48.5 (2012), pages 759–769.

[SRB15] Dragoljub Surdilovic, Jelena Radojicic, and Nick Bremer. "Efficient Calibration of Cable-Driven Parallel Robots with Variable Structure". In: Springer, Cham, 2015, pages 113–128.

[Tah+18a] Elias Tahoumi, Malek Ghanes, Franck Plestan, and Jean Pierre Barbot. "A New Controller Switching between Linear and Twisting Algorithms". In: *Proceedings of the 2018 American Control Conference* (2018), pages 6150–6155.

[Tah+18b] Elias Tahoumi, Franck Plestan, Malek Ghanes, and Jean Pierre Barbot. "A Controller Switching between Twisting and Linear Algorithms for an Electropneumatic Actuator". In: *Proceedings of the 2018 European Control Conference (ECC)*. 2018, pages 2368–2373.

[Tem+19] Philipp Tempel, Dongwon Lee, Felix Trautwein, and Andreas Pott. "Modeling of elastic-flexible cables with time-varying length for cable-driven parallel robots". In: *Mechanisms and Machine Science*. 2019.

[Tre+19] Nicolas Tremblay, Kaveh Kamali, Philippe Cardou, Christian Desrosiers, Marc Gouttefarde, and Martin J.-D. Otis. "Eye-on-Hand Calibration Method for Cable-Driven Parallel Robots". In: Springer, Cham, 2019, pages 345–356.

[Utk92] Vadim I. Utkin. *Sliding Modes in Control and Optimization*. Springer, Berlin, Heidelberg, 1992.

[VAT10] Alaleh Vafaei, Mohammad M. Aref, and Hamid D. Taghirad. "Integrated controller for an over-constrained cable driven parallel manipulator: KNTU CDRPM". In: *Proceedings of the 2010 IEEE International Conference on Robotics and Automation (ICRA)*. 2010, pages 650–655.

[VXM05] Marcel Verner, Fengfeng Xi, and Chris Mechefske. "Optimal Calibration of Parallel Kinematic Machines". In: *Journal of Mechanical Design* (2005).

[WCG15] Xavier Weber, Loic Cuvillon, and Jacques Gangloff. “Active vibration canceling of a cable-driven parallel robot in modal space”. In: *Robotics and Automation (ICRA), 2015 IEEE International Conference on* 2 (2015), pages 1599–1604.

[YPP17] Xinming Yan, Franck Plestan, and Muriel Primot. “A New Third-Order Sliding-Mode Controller - Application to an Electropneumatic Actuator”. In: *IEEE Transactions on Control Systems Technology* 25.2 (2017), pages 744–751.

[Yao+10] Rui Yao, Xiaoqiang Tang, Jinsong Wang, and Peng Huang. “Dimensional optimization design of the four-cable-driven parallel manipulator in fast”. In: *IEEE/ASME Transactions on Mechatronics* 15.6 (2010), pages 932–941.

[YZX19] Han Yuan, Yongqing Zhang, and Wenfu Xu. “On the automatic calibration of redundantly actuated cable-driven parallel robots”. In: *Mechanisms and Machine Science*. 2019.

[Zak+19a] Zane Zake, Stéphane Caro, Adolfo Suarez Roos, François Chaumette, and Nicolò Pedemonte. “Stability Analysis of Pose-Based Visual Servoing Control of Cable-Driven Parallel Robots”. In: Springer, Cham, 2019, pages 73–84.

[Zak+19b] Zane Zake, Francois Chaumette, Nicolo Pedemonte, and Stephane Caro. “Vision-Based Control and Stability Analysis of a Cable-Driven Parallel Robot”. In: *IEEE Robotics and Automation Letters* 4.2 (2019), pages 1029–1036.

[ZK10] Meysar Zeinali and Amir Khajepour. “Design and application of chattering-free sliding mode controller to cable-driven parallel robot manipulator: Theory and experiment”. In: *Proceedings of the 2010 ASME Design Engineering Technical Conference*. 2010, pages 319–327.

[ZN95] J. G. Ziegler and N. B. Nichols. “Optimum settings for automatic controllers”. In: *InTech* volume 42.6 (1995), pages 94–100.

Appendix

A. HTC VIVE system

This chapter present the HTC VIVE and the VIVE Tracker used for the measurement of the position of the platform in the workspace.

A.1 Hardware

HTC VIVE™ is a virtual reality (VR) headset developed by HTC and Valve Corporation. While the VIVE is primarily sold as an entertainment product, it is also widely used for tracking application for academic purposes. The low cost of the system, the ease of setup and use and its availability are important advantages compared to traditional measurement systems such as laser trackers.

A standard installation for VR applications requires:

- One VIVE Head Mounted Device (HMD)
- Two VIVE Controllers
- Two VIVE Base Stations
- A computer running STEAM VR (available for Windows and Linux.)

It is also possible to purchase VIVE Trackers, sensors which can be attached to limbs or accessories to track additional points.

For a pure tracking application of the CDPR platform, the hardware configuration is composed of:

- Two VIVE Trackers
- Two VIVE Base Stations
- A computer running *Ubuntu 16.04* or later

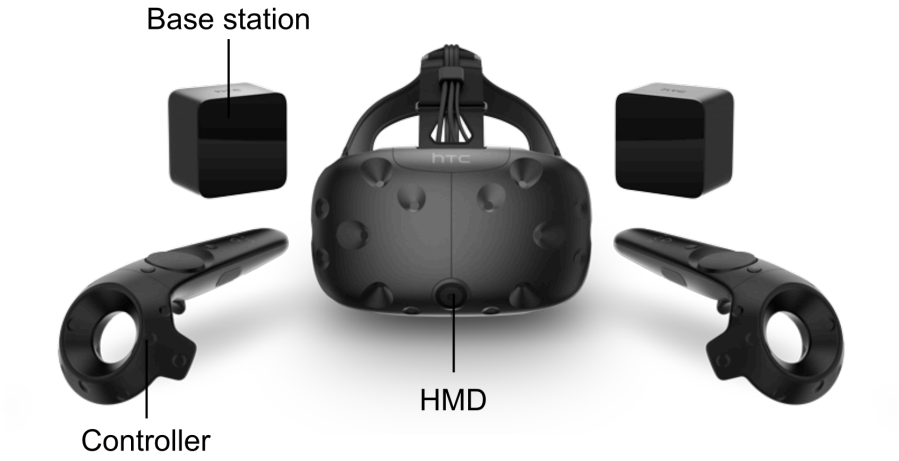

(a) VIVE standard kit including a HMD, two controllers and two base stations.

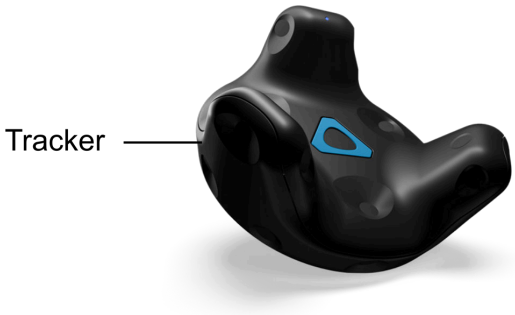

(b) VIVE tracker (2018 model)

Figure A.1: VIVE components

A.1.1 Software

The default software for VR applications is called SteamVR™. It is freely provided by Valve Corporation® through its distribution platform Steam®. Steam VR is itself based on OpenVR™, which offers an API for communication with the hardware to software developers. This solution was initially tested for tracking of the platform.

In standard operating conditions the VIVE tracker does data fusion between optical data from the base stations, at 60 Hz, and internal accelerometer data of the tracker, at 250 Hz. The accelerometer data is used between two optical measurements in order to smooth the tracker's trajectory during a motion. Although this is useful for fluid movements in virtual reality applications (games, simulation, etc.) this method can lead to very high perceived acceleration and displacements of the tracker in the event of a shock or collision. Moreover, slight drift of the tracker position over time was observed with the base software. This was attributed to the inner working of the poser algorithm and its reliability on accelerometer data.

For the CDPR platform tracking application, the repeatability of measurements is more important than very high frequency, especially for the test trajectory generated in Section 1.4.1. The open-source library *libsurvive* [1] which relies only on the optical measurement has been used for the platform tracking measurement of Chapter 4.

A.2 Tracking performances

The precision of the measurement obtained with a VIVE tracker is estimated around 2 millimeters, with a standard deviation of 0.3 mm along the two axis in the plane parallel to the front face of a base station. The standard deviation along the axis representing the distance between the tracker and the base is closer to the millimeter. It is possible to improve accuracy by placing the two base station so that their emitted light intercept with an angle in order to avoid alignment of the less precise axis.

The VIVE tracking cannot be considered as precise as a laser tracker. However, thanks to its repeatability and low measurement noise, the system provided good tracking results for the relative comparison of a control law to another.

[1] libsurvive GitHub web page (link)

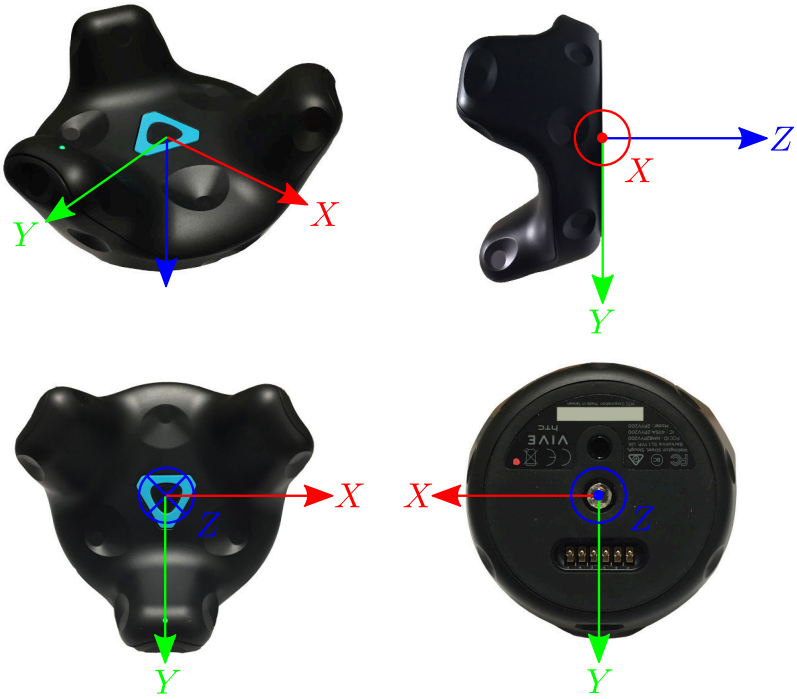

Figure A.2: VIVE Tracker coordinate systems

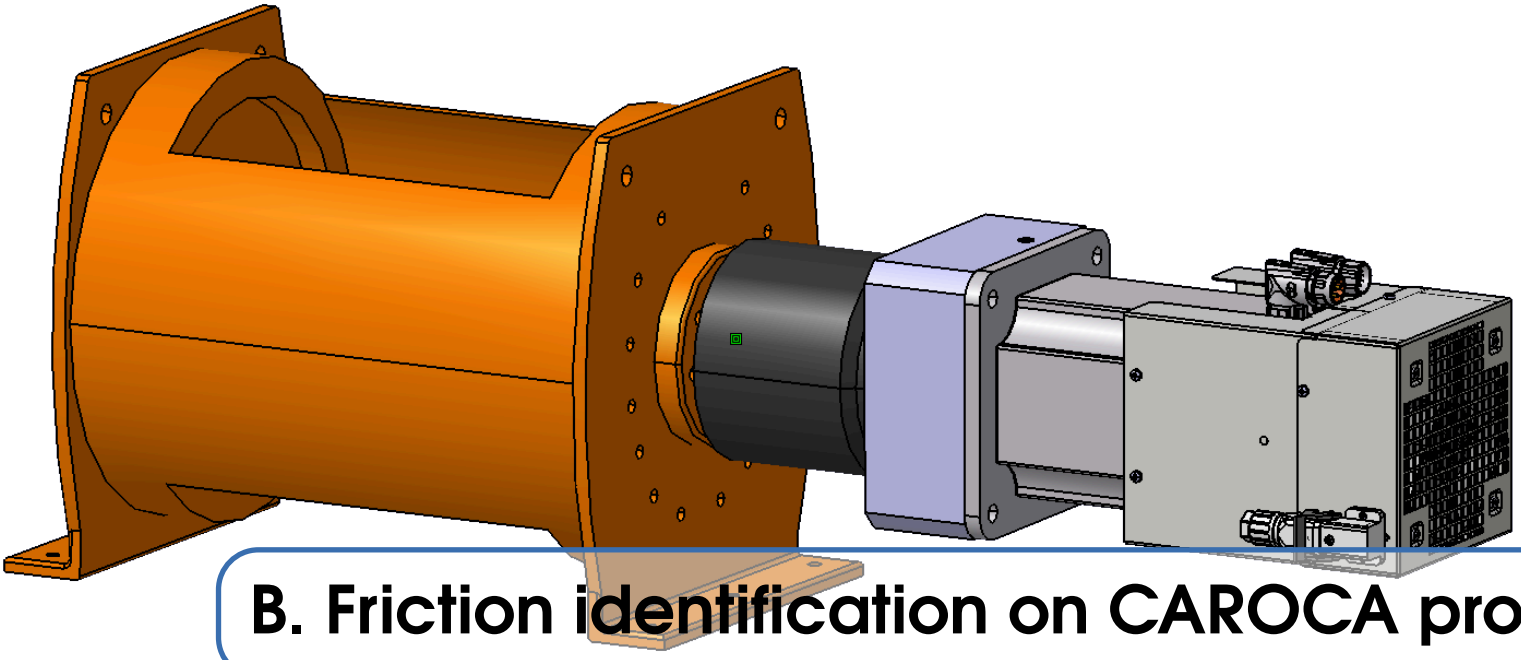

B. Friction identification on CAROCA proto

Friction in the motors can represent a significant portion of the total motor torque, which makes the system difficult to control. In order to improve stability, precision and speed, friction in the gearmotors can be estimated.

In the frame of ROMP, friction was identified in order to implement a feedforward friction compensation term in the control architecture. To estimate static and viscous friction coefficients motor torques are recorded for a range of velocities, from 0 to $200°.s^{-1}$, in the absence of a platform. The torque measurements were assessed by the B&R servo drives from the torque currents.

Two considered friction models are presented in Fig. B.1. $\mathbf{F}_c$ and $\mathbf{F}_v$ are respectively the vectors containing the static and viscous friction coefficients, separately identified for each motor, and F_{ci} and F_{vi} are their component corresponding to the i^{th} motor. In the friction Model A, the slope of the straight line defines the coefficient of viscous friction F_{vi} and intersects the vertical axis at F_{ci}. Model B represents the *Stribeck phenomenon*: an initially higher static torque F_{si}, then a slight drop at low rotational speed, due to fluid lubrication.

The torque measures for a set of different speed are traced in fig B.2. In this figure, the measured torque is plotted in blue and the friction model is traced in green, based on Model A. The identified friction coefficients F_{ci} and F_{vi} for the eight motors of ROMP are listed in Tab. B.1.

Based on Model A, the friction compensation torque for the i^{th} motor, $\tau_{fc,i}$ is defined as

$$\tau_{fc,i} = F_{ci}\text{sign}(\dot{q}_{d,i}) + F_{vi}\dot{q}_{d,i} \tag{B.1}$$

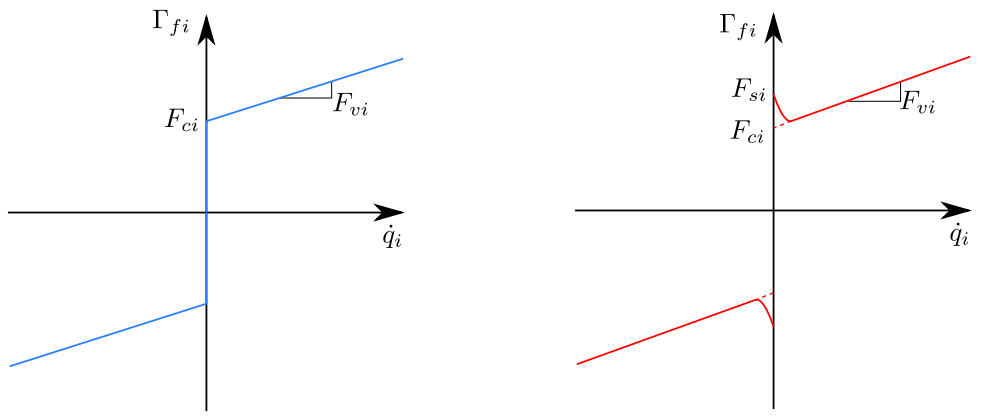

(a) Model A: linear model (b) Model B: Stribeck phenomenon

Figure B.1: Considered friction models.

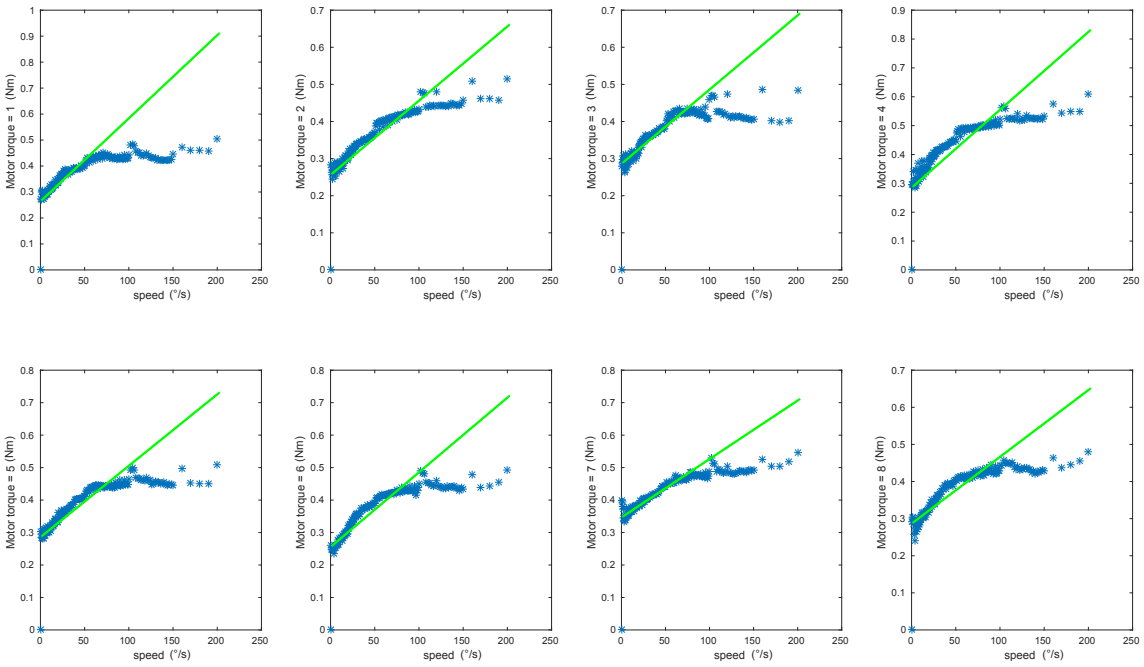

Figure B.2: Measured motor torques as a function of motor velocity.

where $\dot{q}_{d,i}$ is the desired rotation speed of the motor.

Table B.1: Static and viscous friction coefficient ROMP 8 motors

Motor	1	2	3	4	5	6	7	8
Static friction (F_{ci})	0.27	0.26	0.29	0.29	0.29	0.26	0.35	0.29
Viscous friction (F_{vi})	0.0022	0.002	0.002	0.0027	0.0022	0.0023	0.0018	0.0018

Figure B.3 compares for one motor the torque measured during a motion, and the estimated torque from the chosen friction model.

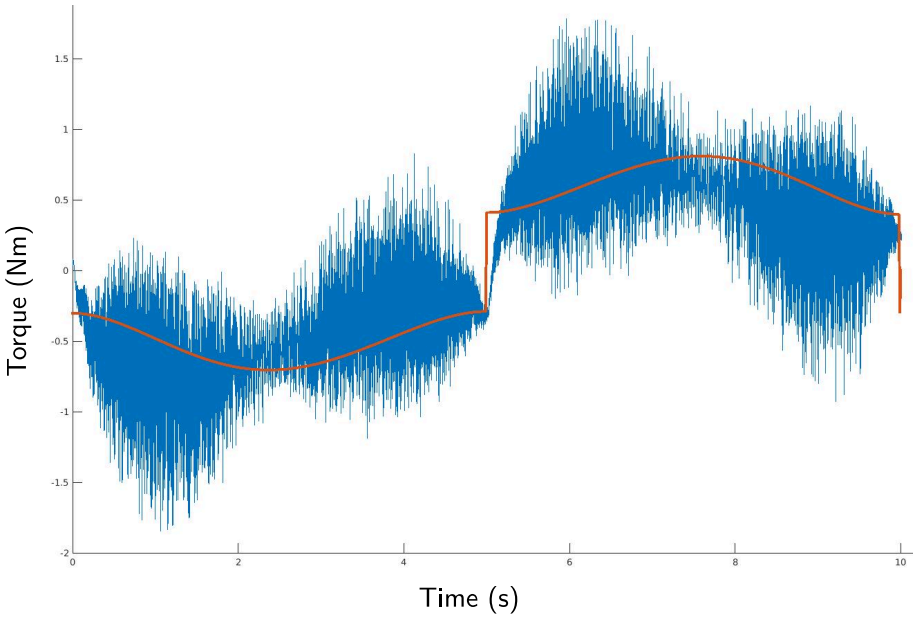

Figure B.3: Measured torque using motor speed control, in blue, and and torque from estimated friction model, in red.

It is noteworthy in Fig. B.2 that, while Model A gives a good approximation up to $100°.s^{-1}$, the model tends to overestimate friction at higher velocities. Since the CAROCA CDPR has a slow dynamics model, Model A is an acceptable approximation, but if friction estimation is critical a more refined model would be better suited, such as a polynomial estimation instead of a linear one.

C. SML behavior in TC2 architecture

The performance and behavior of the SML controller in the TC2 control architecture are discussed in the sequel. By design, the SML controller first generates $\dot{\mathbf{u}}$, the derivative of the controller signal $\boldsymbol{\tau}_c$. The benefits of this formulation is an improved smoothness of the control input and a reduced chattering phenomenon compared to directly working with $\mathbf{u}$. It was also observed in the PC1 architectures that the SML controller could achieve good accuracy even without feedforward in steady state. The stability of the SML controller is ensured by the values of the parameters, as discussed in Sec. 4.4.2.

However, while in the PC1 to PC3 control architectures the controller signal $\boldsymbol{\tau}_c$ was directly applied to the motors, the TC2 control architectures introduce additional nonlinearities between the controller and the motors. Indeed, the controller output $\boldsymbol{\tau}_c$ is converted into the resulting force requested by the controller onto the platform $\mathbf{f}_c$, which is then distributed by the TDA accordingly to the desired minimum and maximum cable tensions.

Moreover, ROWC is a fully-constrained CDPR with upper and lower cables applying opposite forces in all directions. Under these conditions, it was found that the SML controller could lead to increasingly high torque outputs $\boldsymbol{\tau}_c$, while maintaining a constant resulting force $\mathbf{f}_c$. As a consequence, the TDA could still find a feasible set of cable tensions and maintain platform stability, but due the large values of $\boldsymbol{\tau}_c$, a risk might arises. A sudden change in the motor positions errors can lead to unbalanced corrections for the controller, and the computed overall force $\mathbf{f}_c$ can momentarily take large values, before the SML controllers stabilize again.

In what follows, observations are made on the behavior of the SML controller inside the TC2 control scheme. The platform is placed in a static position of

coordinates $\mathbf{p} = [1.5,\ 0.35,\ 0.35]$, then the TC2-SML control architecture is applied and the platform is maintained at this position for ten seconds. The TC2-PD architecture results are also provided for comparison with the behavior of TC2-SML.

Figure C.1 shows the motor position errors $\mathbf{e}_q$ obtained with the TC2 control architecture with either the PD of the SML controller. It can be observed that for both the PD and the SML controller motors 2, 3, 6 and 7 all suffer from an static error of around 10C degrees. In the case of the PD controller, this error is almost constant during the recording. However in the case of the SML controller this errors slowly evolves along time, increasing for some motors and reducing for others, but never reaches zero in the ten seconds of the measurements.

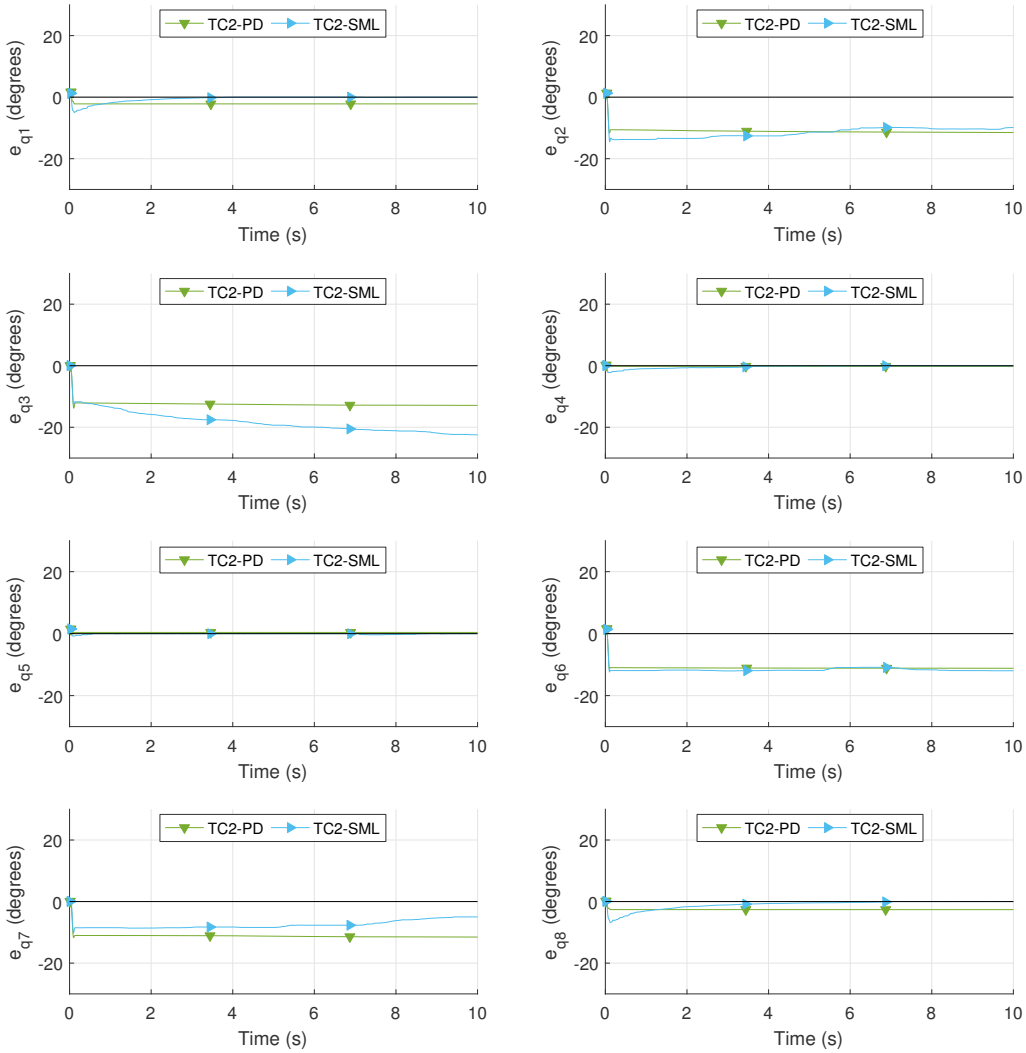

Figure C.1: Motor position errors $\mathbf{e}_q$ for PD and SML controllers with TC2 control architecture

In the case of the PD controller, a constant position error at a null speed leads to a constant controller torque output, the relationship between the two being directly defined by Eq. (4.15) However, in the case of the SML as proposed in Eq. (4.28), the integration of $\dot{u}$ leads to an increasing value of $\boldsymbol{\tau}_c$, as long as the motor position errors

$\mathbf{e}_q$ remains. Figure. C.4 shows this behavior: the controller output $\boldsymbol{\tau}_c$ of motors 2, 3, 6 and 7 increase over time.

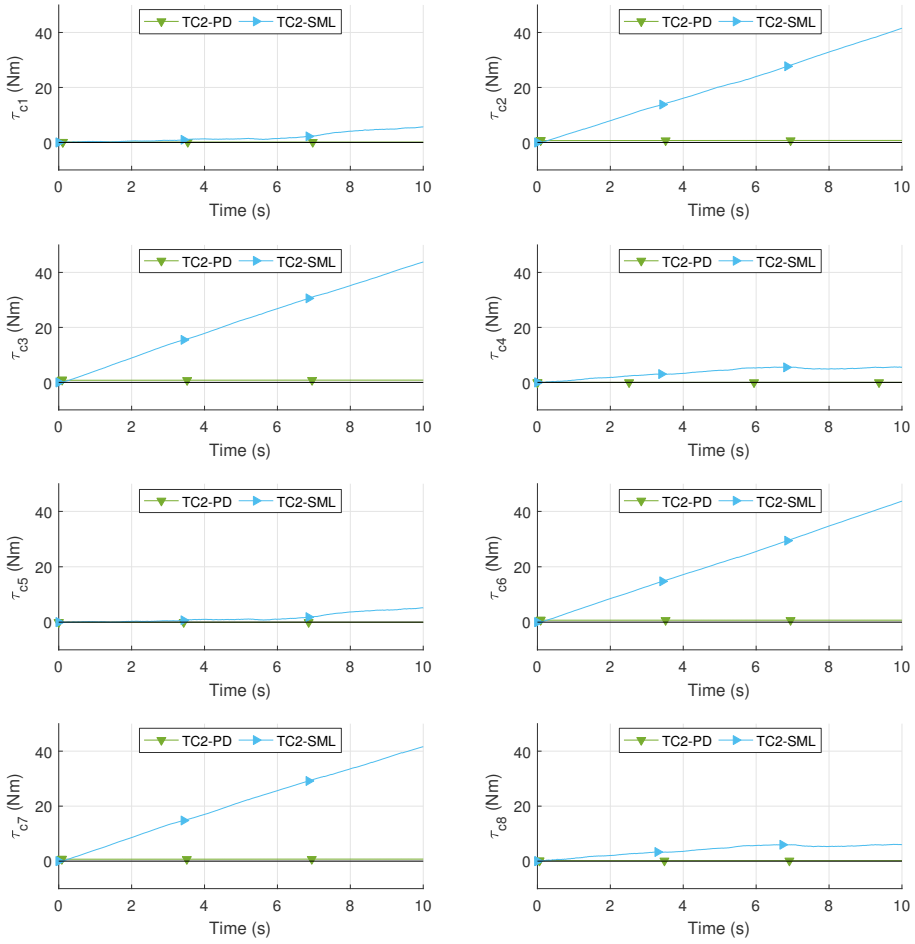

Figure C.2: Controller torque output $\boldsymbol{\tau}_c$ for PD and SML controllers with TC2 control architecture

it can be noted in Fig. C.3 that the computed force to be applied onto the platform by the controller is almost constant during the experiment. This can be explained by the CDPR fully-constrained configuration and its impact on the calculation of $\mathbf{f}_c$. As all controller outputs increase, the static equilibrium of the platform is maintained and the values of $\mathbf{f}_c$ remains stable and feasible. The tension distribution is still applied with a solution derived from the feasible $\mathbf{f}_c$.

The motor torque commands $\boldsymbol{\tau}_m$ obtained with the PD and SML controllers are shown in Fig. C.4. While the tensions obtained form the PD controller are almost constant, slight variations are visible in the tensions obtained when implementing the SML controller. All tensions still respect the boundaries defined for the TDA.

As a consequence, while the SML controller as defined in Sec. 4.4.2 worked well in the PC and PCE architectures, it has been set aside for TC2. Other sliding mode approaches that do not implement an integration step should be considered in the future. Experiments in a suspended configuration should also be made to verify if the behavior is the same.

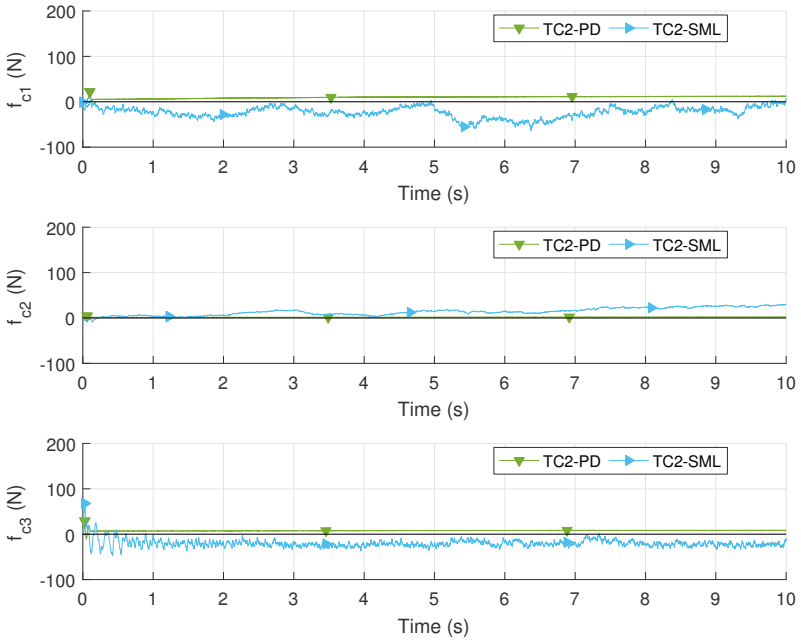

Figure C.3: Controller force $\mathbf{f}_c$ for PD and SML controllers with TC2 control architecture.

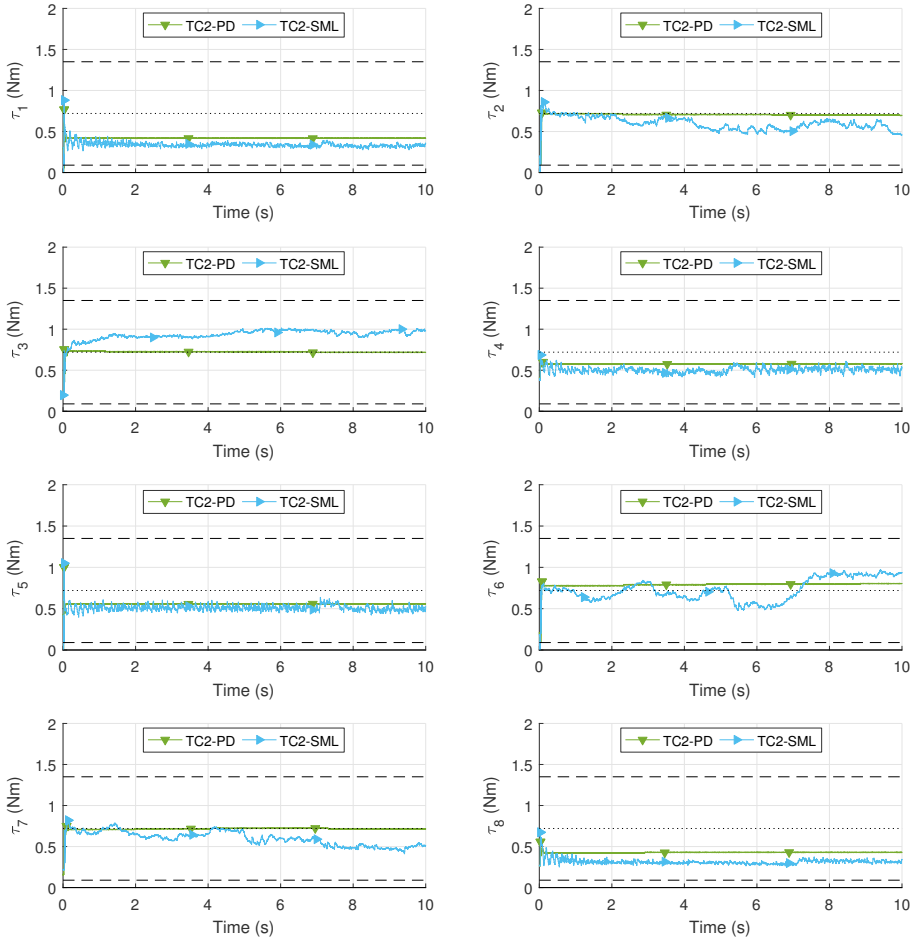

Figure C.4: Measured motor torques $\boldsymbol{\tau}_m$ with for PD and SML controllers with TC2 control architecture. Lower and upped limits are shown in dashed lines and middle in dotted line.

D. SOTDA: grid versus corner

A comparison has been realized between the use of a grid, or the consideration of the feasible polygon corners only, for the section of (λ_1, λ_2) in the SOTDA, with the same values of the simulation along the path of Sec. 4.6. Using MATLAB *meshrid* function, a 100×100 grid is defined to discretize the feasible polygon. The minimum and maximum values of λ_1 and λ_2 inside the feasible polygon are used to defined the edges of the grid. The two selection methods have been compared in simulation along ROWC test trajectory for an effort of 30 N and $\nu = 1$.

Figure D.1 presents the values of λ_1 and λ_2 with the grid (GD) and the corner (CR) methods. The difference $\Delta(\delta p_y)$ between the corresponding platform displacements $\delta p_y(GD)$ and $\delta p_y(IS)$ is plotted in Fig. D.2. It appears that the difference in platform displacement is less than 3×10^{-4} mm. Figure. D.3 presents the corresponding cable tensions along the path. It is interesting to see that the solution based on the corner provides smoother curves than the grid. The fact that the grid and corner solutions are extremely close reinforces the assumption the stiffness optimal solution is located in a corner of the feasible polygon.

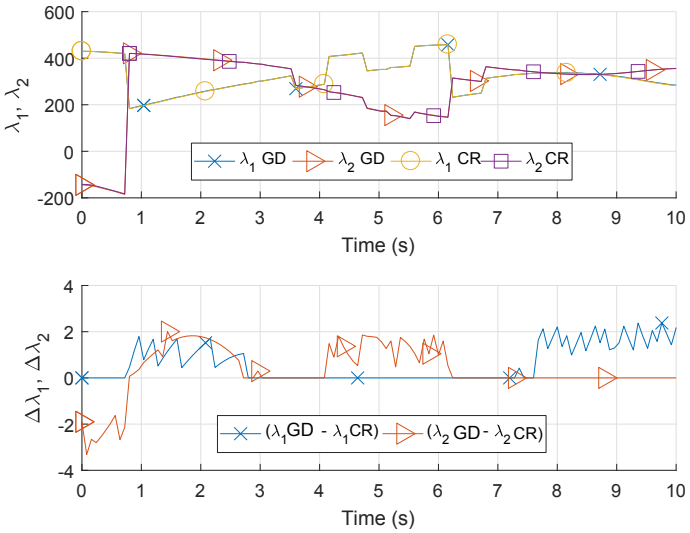

Figure D.1: Difference in selected λ_1 and λ_2.

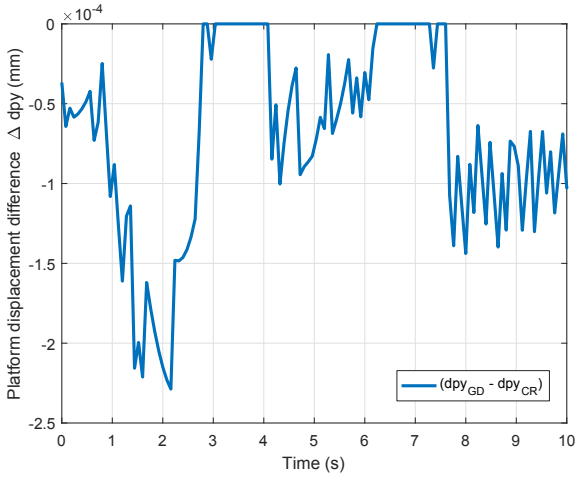

Figure D.2: Difference $\Delta(\delta p_y)$ between obtained displacements

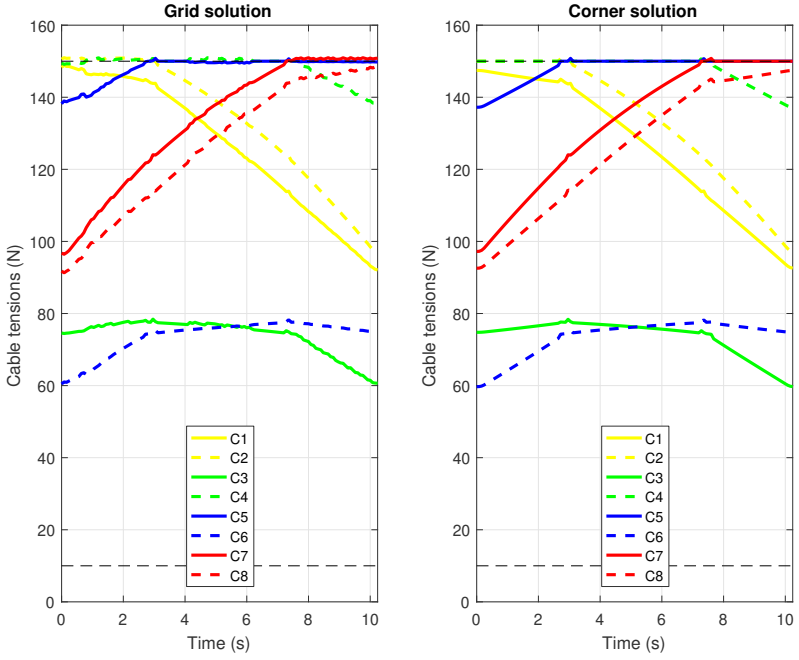

Figure D.3: Difference in cable tension solutions between grid and corners methods.

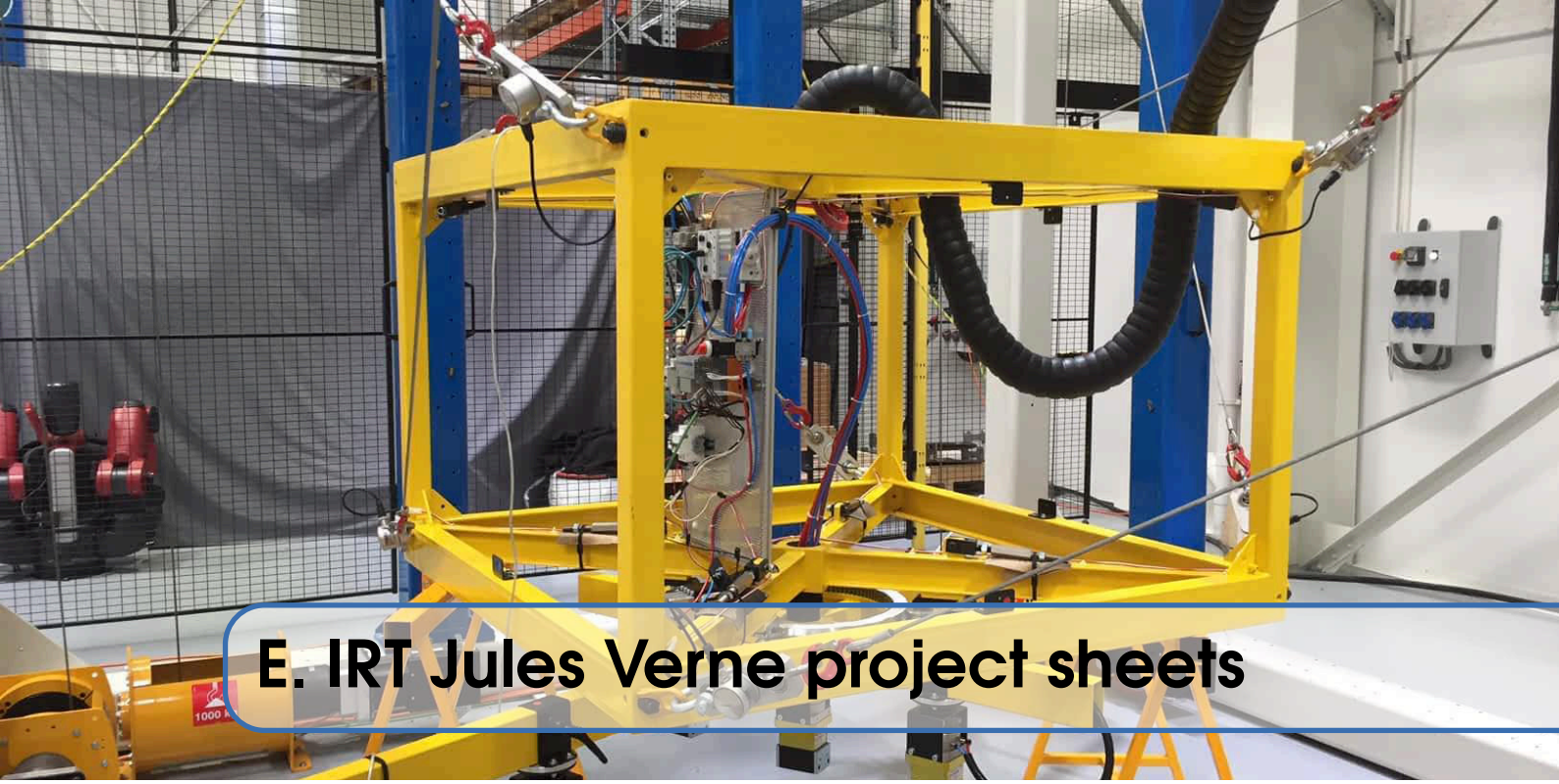

E. IRT Jules Verne project sheets

Cable driven parallel robots for manipulation and plate transport

ROCKET project

The project aims at developing an industrial CDPR for handling and sorting of parts by means of a man/machine interface with augmented reality.

IRT JULES VERNE

Technical and economic impacts

- Twice cheaper than the standard systems
- Handling parts can be faster than with standard systems
- Better control of the pieces: position, orientation, traceability

Keywords

Cable driven parallel robots
Augmented reality // Simulation
Models // Control system

Development of the gripper and the moving-platform
july 2016

Start of validation trials
march 2018

january 2016
Kick-off Meeting

july 2017
GO / No GO for prototype installation

january 2019
End of the project

INDUSTRIAL CONTEXT

CDPRs are complementary to the classical six-revolute industrial serial robots in terms of workspace size, stiffness, dynamic performance and heavy payload capacity. They are also cheaper and less bulky than the industrial serial robots. The most widespread CDPR in the world is the Skycam, which is maneuvered through three dimensions in the open space over a playing area of stadium or arena by computer-controlled cable-driven system. It brings video-game-like camera angles to television sports coverage.

INNOVATIVES FEATURES

- Adding augmented reality in the man/machine interface allowing the operator to use intuitively the technology, with a colour code for instance.
- Reliability of the robot models and the simulator, in order to assess the capacity of the robot to carry out heavy loads, in extreme outdoor environments and in large scale areas.
- Better control of the pieces, traceability, ergonomics
- Maintenance of the system: better accessibility to mechanical and electronical pieces as the motors, gearheads and winches are mounted to the floor.

INDUSTRIAL APPLICATIONS

At the end of the project, the robot could be installed in a large plant for handling and storing parts efficiently. The operator will control the robot thanks to a man-machine interface with augmented reality.

Partners

- IRT JULES VERNE
- B&R AUTOMATION
- CLARTE
- CLEMESSY
- STX FRANCE
- IRCCYN (UMR CNRS, CENTRALE NANTES, UNIVERSITÉ NANTES, MINES NANTES)

Equipment

- Large scale CDPR

Budget

- 1 223 k€

Sales contact
Philippe Piard
philippe.piard@irt-jules-verne.fr

Press contact
Sophie Péan
communication@irt-jules-verne.fr

www.irt-jules-verne.fr

JULES VERNE MANUFACTURING VALLEY
THE FRENCH INDUSTRIAL PLACE TO BE
SINCE 2010

INVESTISSEMENTS D'AVENIR

Figure E.1: IRT Jules Verne ROCKET project specification sheet.

ROCKET

CABLE-DRIVEN PARALLEL ROBOTS FOR HANDLING OPERATIONS

IRT JULES VERNE

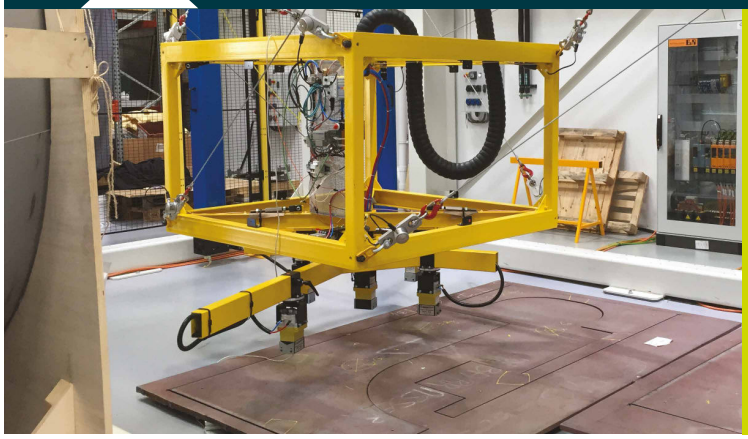

TECHNICAL AND ECONOMIC IMPACTS

- **Twice cheaper** than the standard systems
- **Faster pick-and-place** motions of steel plates than with standard systems
- **Agile manipulation** of the parts in a large workspace

KEY FEATURES

PICK-AND-PLACE OPERATIONS

- Displacement of heavy and variable steel plates with electromagnets
- Robust control of both position and orientation

REAL TIME MEASUREMENTS

- Motor positions, velocities and torques
- Cable tensions with dynamometers

HUMAN MACHINE INTERFACE

- Using joysticks and augmented reality
- Possibility of autonomous trajectories for the moving platorm

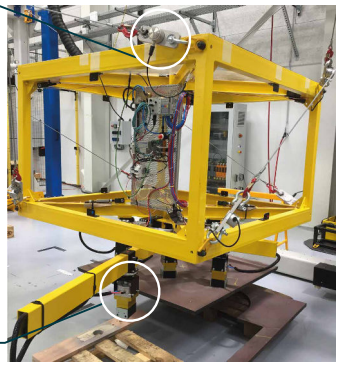

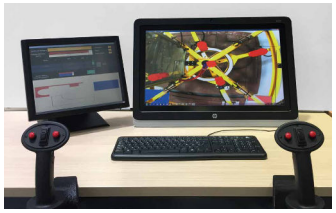

CDPR TECHNICAL DATA

Motor power x 8	2,7 kW
Gear box	40:01
Winch diameter	120 mm
Payload	800 kg
Max linear velocity	1000 mm/s
Max acceleration	500 mm/s²
Max cable tension	10000 N
Workspace	6m x 3,5 x 3,2 m

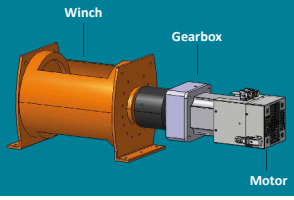

ROCKET PLATFORM

Platform size	1,5 x 1,5 x 1 m
Electromagnets x 5	Up to 147 kg per magnet
Additional axis	Manual rotation around vertical axis
Dynamometers x 8	Up to 25 000 N per dynamometer

EIFFAGE CLEMESSY CLARTE LS2N stx France

February 15, 2018

Figure E.2: IRT Jules Verne ROCKET presentation poster.

Cable-driven parallel robots

CAROCA project

Using methods like modelling, identification, simulation and prototyping, the project aims at identifying the industrial operations that can be handled by cable-driven parallel robots. This involves assessing the capabilities of cable-driven parallel robots to carry out different industrial operations, such as painting, shot blasting, part assembly, measurements and inspection of oversized parts.

IRT JULES VERNE

Technical and economic impacts

- Easy access to large structures
- Improved safety
- Optimized robot multi-tasking through reconfigurations

Keywords

Robotics // Cable-driven parallel robots
Reconfigurability
Large Volumes

Modelling and simulation december 2014
Robot reconfigurations tool june 2015
Experimental validations june 2016

january 2014 **Project launch**
january 2015 **Installation of a 1:50 scale demonstrator**
january 2016 **Installation of a 1:5 scale demonstrator**
january 2017 **End of project**

INDUSTRIAL CONTEXT

The processes considered thus far require moving operators or effectors over large distances in cluttered environments. The constraints for these heterogeneous processes are quite different in terms of robot accuracy, external wrenches and mass in motion. Therefore, there is a need, to develop robotic solutions to make these operations safer, less arduous and more efficient.

INNOVATIVE FEATURES

- Development of cable robots for shot-blasting and painting operations on offshore wind turbine jackets
- Development of a robotic system for moving and assembling heavy oversized parts
- Ideas: cable robots carrying another active system; reconfigurable cable robots
- Fast and accurate robotic systems covering a large workspace
- Robot reconfigurability for work/operations in congested areas

INDUSTRIAL APPLICATIONS

Optimizing the reconfiguration should make it possible to move the tools around oversized parts in order to perform a wide range of operations. This could be of interest to a number of industries.

Partners

- IRT JULES VERNE
- AIRBUS
- DCNS
- STX FRANCE
- CNRS (IRCCYN & LIRMM)

Equipment

- Two cable-driven parallel robots: the first 1 is one meter high, the second one is 5 meters high

Budget

- 605 k€

Sales contact
business@irt-jules-verne.fr

Press contact
communication@irt-jules-verne.fr

www.irt-jules-verne.fr

INVESTIR L'AVENIR

Figure E.3: IRT Jules Verne CAROCA presentation poster.

FASTKIT

Low cost and versatile cable-driven parallel robot solution for logistics

The objective of project FASTKIT is to develop a experiments aims at providing a low cost and versatile robotic solution for logistics using a unique combination of mobile robots and Cable-Driven Parallel Robot (CDPR).
FASTKIT prototype addresses an industrial need for fast picking and kitting operations in existing storage facilities while being simple to install, maintaining existing infrastructures and spanning large areas.

Industrial context

In the last 5 years, automated technical solutions for picking have emerged in the areas of production or logistics. These solutions are based on the coupling of polyarticulated arms and AGVs, however manufacturers have not yet succeeded in developing robust and versatile products (Tech robotics, Exotech ...). In this context, FASTKIT robot presents a new technical innovation that could help to bring more flexibility and versatility with respect to existing solutions.

Innovative features of the project

- Reconfigurability (depending on warehouse/factory) and flexibility (height, payload, speed)
- Lightweight and robust structure
- Low investment cost
- Mobile CDPR

Industrial applications and development

The targeted application for FASTKIT is the logistics industry, including intra-logistics operations within the retail automotive or aeronautics industries, where kitting bins have to be prepared. Indeed for automated kit preparation, specific bin picking algorithms and end effectors have to be developed. In order for the FASTKIT solution to be viable on the market, it must adapt to the requirements of several industries.

Technical and economic impacts

- Reduction in lead time of operations compared to robots based on AGV
- Reduction in investment costs
- Creation of start up

Planning

September 2016
- Project launch

May 2017
- AGV and trailer capable of obtaining desired position
- CDPR with end-effector capable of picking of box

October 2017
- CDPR integrated on mobile platform

February 2018
- End of project

TRL

1 2 3 4 5 6 7 8 9

Applications

Medias

www.fastkit-project.eu

@fastkitproject

Contacts

Alexis Girin
R&T Manager, Robotic and Cobotic
alexis.girin@irt-jules-verne.fr

Figure E.4: European project FASTKIT presentation poster.

Publications list

Modeling and Robust Control of Cable-Driven Parallel Robots for Industrial Applications

Etienne PICARD

International conference proceedings:

- E. Picard, S. Caro, F. Claveau and F. Plestan, "*Control Solution for a Cable Driven Parallel Robot with Highly Variable Payload*", IDETC/CIE 2018 ASME International Design Engineering Technical Conferences, Québec, Canada, 2018
- E. Picard, S. Caro, F. Plestan and F. Claveau, "*Pulleys and force sensors influence on payload estimation of cable-driven parallel robots*", IEEE/RSJ International Conference on Intelligent Robots and Systems IROS, Madrid, Spain, 2018

Accepted conference submissions:

- E. Picard, E. Tahoumi, F. Plestan, S. Caro and F. Claveau, "*A new control scheme of cable-driven parallel robot balancing between sliding mode and linear feedback*", accepted to the 21st International Federation of Automatic Control World Congress (IFAC 2020), Berlin, Germany, 2020
- E. Picard, S. Caro, F. Plestan and F. Claveau, "*Stiffness Oriented Tension Distribution Algorithm for Cable-Driven Parallel Robots*", accepted to the 17th International Symposium on Advances in Robot Kinematics (ARK 2020), Ljubljana, Slovenia, 2020

UNIVERSITE BRETAGNE SCIENCES LOIRE POUR L'INGENIEUR

CENTRALE NANTES

Titre : Modélisation et Commande Robuste de Robots Parallèles à Câbles pour Applications Industrielles

Mots clés : Robotique, parallèle, câble, modélisation, contrôle, étalonnage

Résumé : Cette thèse concerne la modélisation et la commande robuste de robots parallèles à câbles (RPC) pour deux applications du secteur naval : la prise et dépose de plaques métalliques à l'aide d'un RPC en configuration suspendue (ROMP), et le nettoyage de façades par un RPC pleinement-contraint (ROWC). Les travaux ont été réalisés à l'IRT Jules Verne dans le cadre du projet ROCKET.

La première partie de cette thèse se concentre sur la modélisation et la calibration des RPC. Les modèles géométriques incluant la géométrie des poulies et l'élasticité des câbles sont présentés, ainsi que la formulation de la matrice de raideur du robot. L'estimation de la masse transportée et de la position du centre de gravité de la plateforme, à partir des mesures de tensions dans les câbles et pour une trajectoire à faible dynamique, est expérimentée. Enfin, la calibration des RPC est discutée et une méthode de calibration automatique est étudiée en simulation selon les modèles considérés.

La seconde partie est dédiée au contrôle robuste des RPC par rapport aux perturbations de chaque application. Différents schémas de contrôle sont comparés suivant les informations disponibles sur le système. Deux familles de contrôleurs sont considérées pour ROMP : un contrôleur proportionnel-dérivée (PD) standard, et contrôleur récent balançant entre algorithmes de type mode glissant ou linéaire (SML). Un schéma compensant l'allongement des câbles par élasticité est également expérimenté pour améliorer la précision et la répétabilité du robot. Dans le cas de ROWC, l'intégration d'un algorithme de distribution des tensions dans les câbles dans le schéma de contrôle est nécessaire. Un nouveau critère de sélection des tensions est proposé afin de maximiser la raideur du robot face à l'effort dû à la pression du jet d'eau. Enfin, l'arrêt d'urgence des RPC est discuté et le comportement des prototypes ROMP et ROWC est observé dans le cas d'un arrêt d'urgence.

Title: Modeling and Robust Control of Cable-Driven Parallel Robots for Industrial Applications

Keywords : Robotics, parallel, cables, modeling, control, calibration

Abstract: This thesis covers the modeling and robust control of cable-driven parallel robots (CDPRs) for two industrial applications for the naval sector: pick and place of metal plates (ROMP) using a suspended CDPR, and window cleaning (ROWC) by a fully constrained CDPR. The work was carried out in the context of the ROCKET project at IRT Jules Verne.

The first part of this thesis focuses on the modeling and calibration of CDPRs. Models are written, including the consideration of pulleys geometry and cable elasticity. A linear model of cable elasticity introduced and used to write the robot stiffness matrix. A method for estimating the platform mass and center of mass position is proposed and experimented based on cable tension measurements, assuming a low-dynamic trajectory. Finally, the calibration of CDPRs is discussed and an automatic calibration method is tested in simulation based on the different models.

The second part is dedicated to the robust control of RPCs against the perturbations identified for both applications. Several control architectures have been experimented depending on the available information about the system. Two families of controllers are compared for the control of ROMP: a proportional-derivative (PD) controller and a recent controller automatically balancing between sliding mode or linear algorithms (SML). In the case of fully constrained CDPRs such as ROWC, the control architecture must include a tension distribution to ensure safety. A new tension selection criterion based on the stiffness matrix is proposed to reduce the displacement of the platform due to water jet pressure. Finally, CDPR emergency stops are discussed and the behavior of ROMP and ROWC prototypes was evaluated in emergency situations.